# UNIVERSITY OF SOUTHAMPTON

FACULTY OF NATURAL AND ENVIRONMENTAL SCIENCES

Chemistry

Volume I of I

**Supramolecular templating agents and Metal Organic Frameworks: control over crystal size and assembly**

by

**Lucia Lupica Spagnolo**

Thesis for the degree of Doctor of Philosophy

July 2016

**UNIVERSITY OF SOUTHAMPTON**

# ABSTRACT

FACULTY OF NATURAL AND ENVIRONMENTAL SCIENCES

Chemistry

Thesis for the degree of Doctor of Philosophy

**SUPRAMOLECULAR TEMPLATING AGENTS AND METAL ORGANIC FRAMEWORKS: CONTROL OVER CRYSTAL SIZE AND ASSEMBLY**

Lucia Lupica Spagnolo

Metal organic frameworks (MOFs) are an interesting class of microcrystalline materials constituted by metal ions or clusters connected by organic linkers characterised by their high porosity and tunable structures. Due to their chemical variability and numerous applications they have received great attention during the last few decades.

Recently also the control of their physical form or macroscopic structure, such as crystal size, morphology and the aggregation of the crystals into superstructures, have received more attention since it would further develop and enhance properties and applications of these materials. Indeed beside all the inherent properties derived from the chemical composition and microporosity of MOFs the higher level of order or the control over the dimensionality or shape of the particles should enrich their overall performance and open new fields of application, such as drug delivery or integration into electronic sensor devices.

In this context three prototypical MOFs were investigated, namely HKUST-1, ZIF-8 and ZIF-61; at first an overview of the behavior of HKUST-1 in presence of templating agents was performed, which involved the use of Pluronic-P123 ($HO(CH_2CH_2O)_{20}(CH_2CH(CH_3)O)_{70}(CH_2CH_2O)_{20}H$, $EO_{20}PO_{70}EO_{20}$, EO= ethylene oxide, PO= propylene oxide) and two carboxylic acids, namely octanoic acid and dodecanoic acid, on the synthesis of HKUST-1. As a proof of concept, this chapter underlined the importance of the synthetic conditions and of the interactions between MOF precursors and templating agents in directing the macroscopic structure of the MOF.

Thereafter the directional self-assembly properties of ZIF-8 in aqueous media with the templating agents SPAN-80 and/or dodecane for the formation of hollow capsule and colloidosomes was investigated, again in relation to optimize the synthetic conditions and understand the mechanism behind the hollow structure formation, which finally depended on the nature of the templating agent and the MOF precursors-templating agent interactions. Furthermore the etching effect of imidazole on the hollow capsule, which led to flower-like microcapsules was analyzed.

Furthermore the optimization of the synthesis of **zni** phase in aqueous media and the topological and morphological conversion from **zni** phase (ZIF-61) to **sod** phase (SALEM-2) promoted by the surfactant SPAN-80 was studied. The role of SPAN-80 was further investigated also in light of the variation of the composition of the two ZIFs and the thermodynamic of the system.

Finally the thesis was an attempt to rationalized the mechanism of MOF macroscopic structures formation, considering the structural features of the starting MOF, the synthetic conditions and the choice of the templating agents, envisioning a design *a priori* of the macroscopic structure of MOFs.

# Table of Contents

# List of Tables

# List of Figures

# List of Schemes

# List of Graphs

# DECLARATION OF AUTHORSHIP

I, Lucia Lupica Spagnolo

declare that this thesis and the work presented in it are my own and has been generated by me as the result of my own original research.

Supramolecular templating agents and Metal Organic Frameworks: control over crystal size and assembly

I confirm that:

1. This work was done wholly or mainly while in candidature for a research degree at this University;
2. Where any part of this thesis has previously been submitted for a degree or any other qualification at this University or any other institution, this has been clearly stated;
3. Where I have consulted the published work of others, this is always clearly attributed;
4. Where I have quoted from the work of others, the source is always given. With the exception of such quotations, this thesis is entirely my own work;
5. I have acknowledged all main sources of help;
6. Where the thesis is based on work done by myself jointly with others, I have made clear exactly what was done by others and what I have contributed myself;
7. Parts of this work have been published as:

   Bradshaw, D.; El-Hankari, S.; Lupica-Spagnolo, L., Supramolecular templating of hierarchically porous metal-organic frameworks. *Chem. Soc. Rev.* **2014,** *43* (16), 5431-43.

   <u>Abstract or Poster at Conferences:</u>

   11th International Conference on Materials Chemistry (MC11), Coventry, United Kingdom.

   4th International Conference on Metal-Organic Frameworks and Open Framework Compounds (MOF2014), Kobe, Japan.

Signed: .....

Date: .....

# Acknowledgements

Firstly, I would like to thank my supervisor Dr Darren Bradshaw for giving me the possibility to carry out this project research, for his advice and for his deep scientific knowledge.

I would like to thank also to members of my research group: Dr Jia Huo, Dr Ashesh Garai, Dr Samir El Hankari, Dr Mauro Chiacchia, Dr Jordi Aguilera Sigalat and India Willimott. Thanks for the many interesting discussion and the support in the lab.

I would like to thanks Amy for proof reading the thesis.

A big thank also to my family, my parents Caterina and Franco, my sister Marta and a special thought to my grandparents Nina and Sebastiano, for their constant support, advice and encouragement.

Also thanks to all my friends here in Southampton, Paco, Fra, Vale, Amy, Fra&Marta, Elena, Dani, Giacomo, Amir, Coralie and all the people that I met and made my stay here more enjoyable!

I thanks my friends in Italy Silvia, Iris, Simo, Davide, Carmi, Sao, Nadia which despite the time and the distance are always close to me.

Finally I thanks my friends around the word, which I am going to visit soon.

# Definitions and Abbreviations

| | |
|---|---|
| 2D | two dimensional |
| 3D | three dimensional |
| BB | Building block |
| BDC | 1,4-Benzenedicarboxylic acid |
| BET | Brunauer, Emmett, Teller |
| BTC | 1,3,5-Benzenetricarboxylic acid |
| CTAB | Cetrimonium bromide |
| DA | dodecanoic acid |
| DMA | N,N-dimethylacetamide |
| DEF | N,N-diethylformamide |
| DFT | Density functional theory |
| DMF | N,N-Dimethylformamide |
| FT | Fourier transformation |
| HKUST-1 | Hong-Kong University structure 1 |
| Im | Imidazole |
| IR | Infrared |
| IRMOF | Isoreticular metal-organic framework |
| IUPAC | International Union of Pure and Applied Chemistry |
| MeIm | 2-Methylimidazole |
| MIL | Matériaux de l'Institut Lavoisier |
| MOF | Metal-organic framework |

| | |
|---|---|
| OA | octanoic acid |
| Pluronic-P123 | $HO(CH_2CH_2O)_{20}(CH_2CH(CH_3)O)_{70}(CH_2CH_2O)_{20}H$, $EO_{20}PO_{70}EO_{20}$, EO= ethylene oxide, PO= propylene oxide |
| PSM | Post-Synthetic-Modification |
| RT | Room temperature |
| SALE | Solvent-assisted ligand exchange |
| SBU | Secondary building unit |
| SDA | Structure directing agent |
| SDS | Sodium dodecyl sulfate |
| SEM | Scanning electron microscopy |
| **sod** | Sodalite |
| SPAN-20 | sorbitan monolaurate |
| SPAN-80 | sorbitan monooleate |
| SPAN-85 | sorbitan trioleate |
| TEM | Transmission electron microscopy |
| TGA | Thermogravimetric analysis |
| TWEEN-85 | polyethylene glycol sorbitan trioleate |
| XRD | X-ray diffraction |
| ZIF | Zeolitic Imidazolate Framework |

# Chapter 1: Introduction

## 1.1 Porosity and porous materials

Porosity is a characteristic of numerous materials that influences physical properties such as density, strength and thermal conductivity.[1] This concept is related to the texture referring to the pore space in the material. In particular it is a measure of the void (i.e., "empty") spaces in a material, and is typically expressed as the apparent fraction of the volume of voids over the total volume. The interest in porous materials results from their outstanding properties and their manifold applications. Porous materials are classified by their pore size and three categories have been designated by the International Union of Pure and Applied Chemistry (IUPAC)[2] as shown in Figure 1.1:

- Macroporous: pores with widths exceeding 50 nm
- Mesoporous: pores of widths between 2 nm and 50 nm
- Microporous: pores with widths below 2 nm

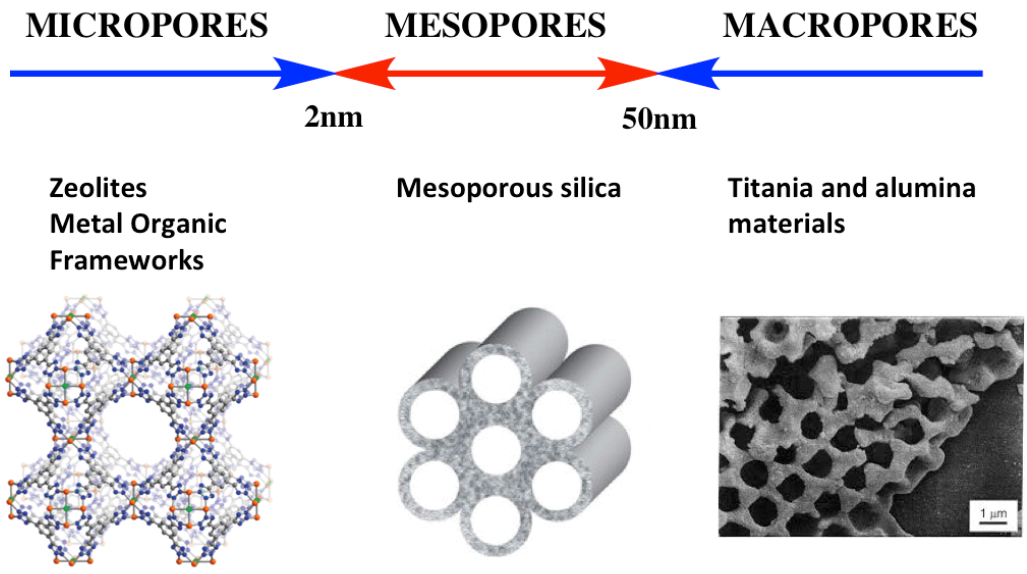


**Figure 1.1 Classification of porous solids according to the IUPAC definitions and some examples of materials within these categories.**

Figure 1.1 also shows some examples for each class of porous materials; for instance zeolites are microporous materials with high thermal stability and crystallinity, they are widely employed as catalysts[3] in the petrochemical industry, ion exchangers in detergents[4] and as molecular sieves in separation technology[5]. A more recent class of crystalline microporous materials, the metal-organic frameworks (MOFs) enables the introduction of organic components within the

framework, which allows a higher tunability and versatility of the materials and they show interesting application for instance in gas storage[6] and catalysis.[7] Mesoporous silicas, such as MCM-41,[8-9] are amorphous materials with high thermal stability and larger pore diameters (20 - 40 Å), which enable host-guest chemistry with larger molecules *i.e.* metal clusters[10] and proteins possible.[11] Finally examples of macroporous materials are alumina and titania, the former is employed in applications such as adsorbent,[12] catalyst,[13] and catalyst support[14] due to its thermal, chemical, and mechanical stabilities as well as catalytic and textural characteristics,[15] while the latter has been widely studied due to its accessible band gap in the UV region[16] and its ability to degrade organic compounds[17] and transfer energy such as in solar cells.[18]

## 1.2 Metal Organic Frameworks

Metal organic frameworks are an interesting class of crystalline hybrid porous materials comprised of infinite ordered three-dimensional networks, analogous to 3D polymeric network,[19-20] where metal ions or clusters are bridged by organic linkers through coordination bonds forming a network structure, as illustrated in Scheme 1.1.[21-23]

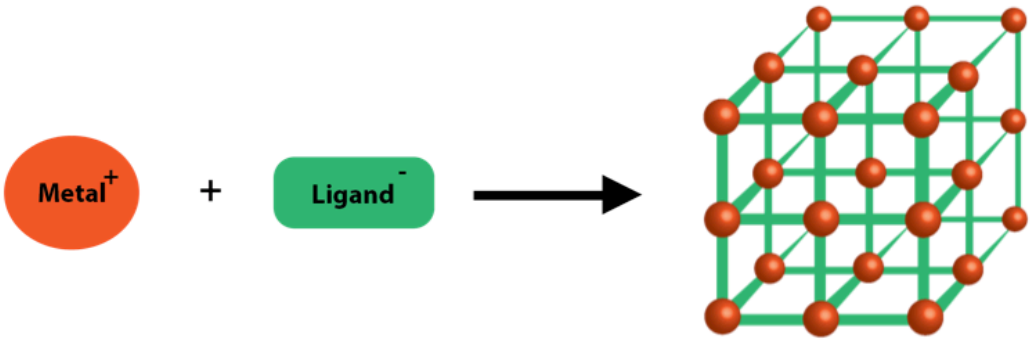


**Scheme 1.1 Representation of MOFs formation: metal ions or clusters and organic ligands react forming 3D ordered network.**

MOFs have attracted tremendous attention over the past years because of their useful properties, such as high porosity, large internal surface area, structural and thermal stability,[24] crystallinity, tunable pore size and topologies[25-29] and linking units available for post modification synthesis.[30] The robustness of the framework ensures their permanent porosity, which usually falls in the micropore range and can lead to very large surface areas, in some cases extending beyond 6000 $m^2/g$, with correspondingly large free volumes. Furthermore the pore size tuneability, the topology and the adjustable internal surface properties of MOFs increases their chemical versatility compared to other natural microporous materials, such as zeolites, which arises from their hybrid composition and modular nature.[29] Therefore the structural variety of those materials comes from the choice of the connectors and linkers and the number and orientations

of their binding sites (*viz*. coordination numbers and coordination geometries), as shown in Figure 1.2. Transition-metal ions are often utilized as connectors because their coordination numbers can range from 2 to 7 and carboxylates as typical linkers because of their rigidity.[31]

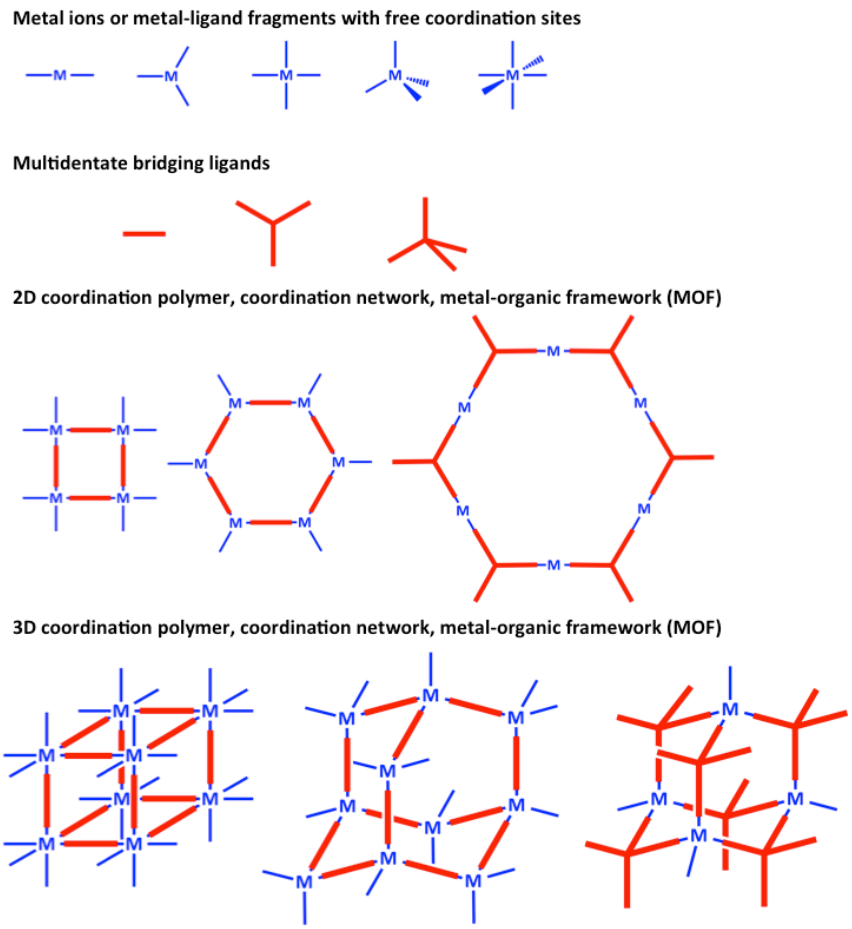


**Figure 1.2 Variety in MOFs synthesis: depending on the coordination number and the geometry of the metal ion and the organic ligand different network are formed.**

Usually, MOFs are synthesized under relatively mild reaction conditions by hydrothermal or solvothermal synthesis where the main reaction parameters can be classified as compositional, *e.g*. molar ratios of starting materials, metal source, pH, solvent, and by process parameters, such as reaction time, temperature and pressure. These parameters greatly influence the nature of the resulting products in terms of phase purity, framework topology, yields, particle size and morphology of the crystals[23] and their study is an area in MOF research, since such manipulation allows optimization of their physical properties (*e.g.* diffusion, adsorption).[22, 32] Furthermore beside the classical solvothermal methods, new routes are currently being developed for the synthesis of MOFs: room temperature synthesis, conventional electric (CE) heating, microwave (MW) heating, electrochemistry (EC), mechanochemistry (MC), and ultrasonic (US) methods have all been employed.[32-33]

Because of their desirable properties MOFs are good candidates for many applications, such as gas storage, molecular separations, chemical catalysis, chemical sensing, ion exchange, drug delivery, luminescence, non-linear optics and magnetism, as shown in Figure 1.3.[6-7, 34-38]

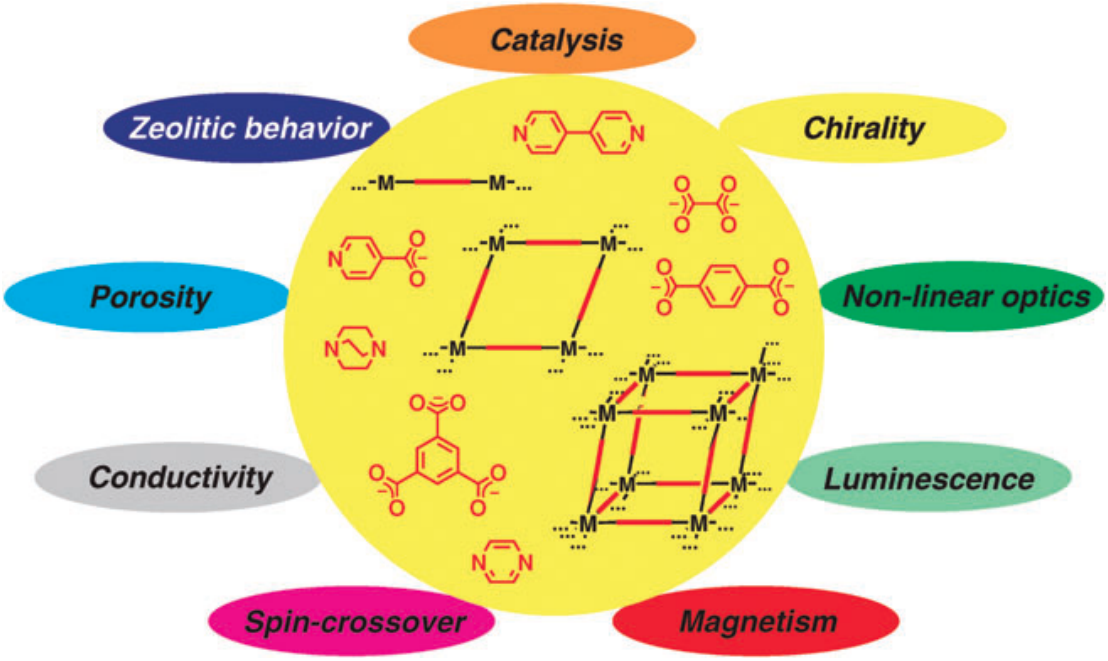


**Figure 1.3 Schematic presentation of application-oriented properties of MOFs. Reprinted with permission from ref.[29]**

### 1.2.1 Reticular chemistry

As previously mentioned MOFs are particularly interesting because of the tailorability of their structure. In particular reticular synthesis is defined as "*the process of assembling judiciously designed rigid molecular building blocks into predetermined ordered structures (networks), which are held together by strong bonding*".[26] Reticular chemistry implies control over the formation of defined building blocks and their assembly into an ordered network.[23, 39] The building blocks are also called secondary building units (SBUs) and they are the geometrical units used to design/assemble the MOF frameworks.[27] Usually SBUs are transition-metal carboxylate clusters generated in-situ under the correct chemical conditions, where the metal ions are locked into their positions by the carboxylate groups, giving sufficient rigidity to produce extended frameworks of high structural stability.[40] The neutrality of the framework allows the removal of solvent guest molecules from their cavities without any loss in porosity and crystallinity.[31] Therefore reticular chemistry has been useful for rationalizing the topologies of MOF structures, which are largely represented by a small number of simple, high symmetry structures, and *vice-versa* it can be used for the foresight of the topology adopted by a given set of SBUs.[39] Furthermore since the topology represents the network connectivity of the building units, which

largely determines the porous properties of a MOF, reticular chemistry is a useful strategy to achieve materials with predetermined structures, compositions and properties.

The concept of reticular synthesis is well explained by the work of Yaghi et al. where MOF-5 ($Zn_4O(BDC)_3$, $BDC^{2-}$=1,4-benzenedicarboxylate)[24] was used as a prototypical framework for the formation of an isoreticular series of MOFs (IRMOF)[25] (Figure 1.4).

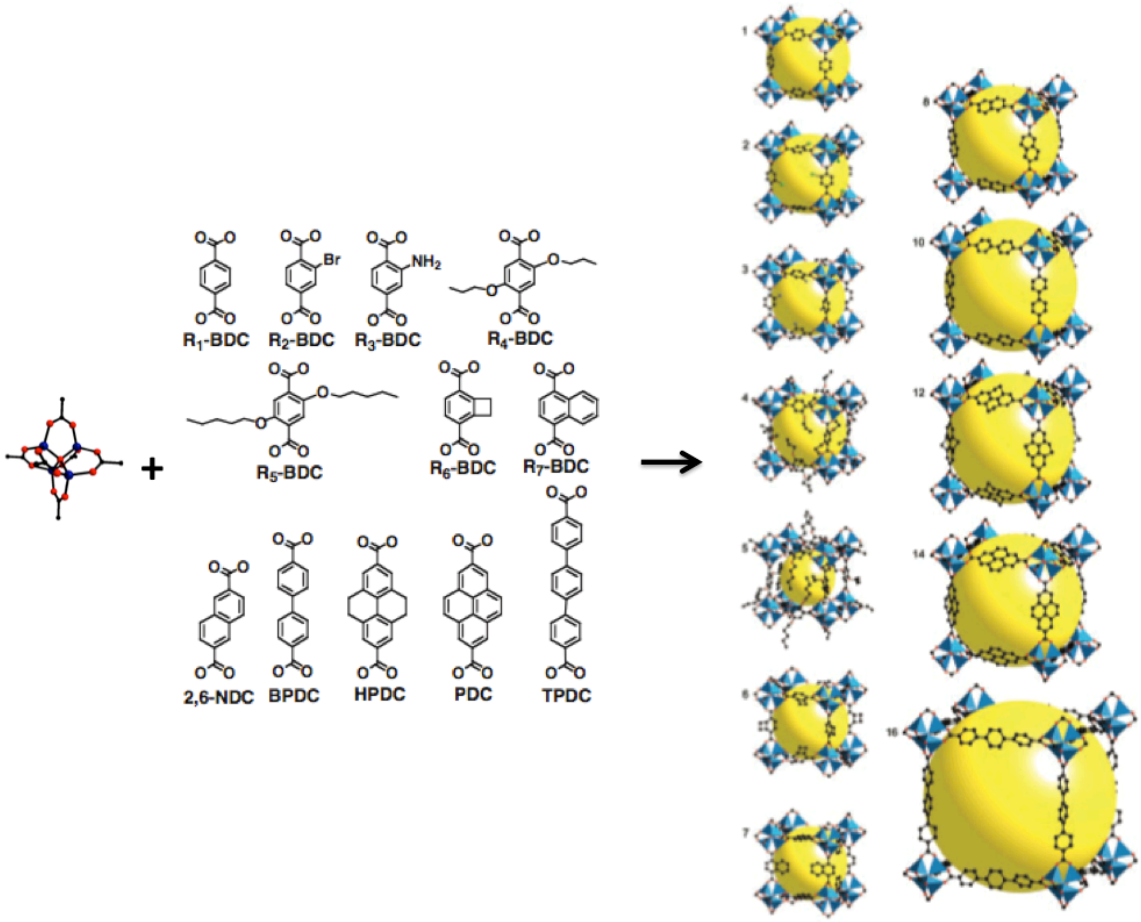


**Figure 1.4 Reaction between the zinc cluster and the organic linkers with different length which form the isoreticular series of MOF-5. Reprinted with permission from ref.[25]**

First the reaction conditions necessary to produce the SBUs are determined, in which an oxide-centered $Zn_4O$ tetrahedron is edge-bridged by six carboxylates to give the octahedral-shape, characteristic of MOF-5. The replacement of BDC with analogous ditopic carboxylate links under closely related conditions leads to the formation of frameworks with the original primitive cubic topology wherein the pore functionality and size of the accessible voids are readily modulated.

### 1.2.2 Prototypical MOFs

#### 1.2.2.1 HKUST-1

HKUST-1 or $Cu_3(BTC)_2(H_2O)_3$ (BTC=benzene 1,3,5-tricarboxylate) was first reported by Chui *et. al*. in 1999.[41] It is formed by binuclear clusters of copper acetate paddle-wheel SBUs connected by tridentate BTC ligands. The framework is a three-dimensional cubic network or tbo (twisted boracites net by combination of 3- and 4-connected nodes) with an open pore system which contains a bimodal pore structure (with a diameter of 9 and 5 Å respectively) (Figure 1.5).

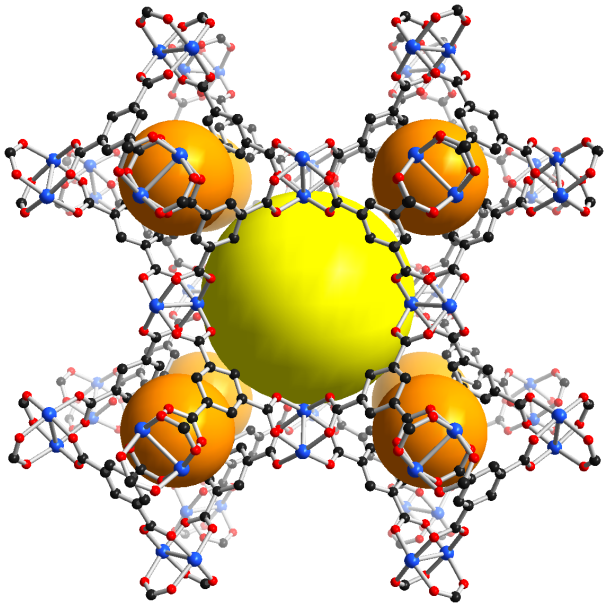

**Figure 1.5 Schematic illustration of HKUST-1 framework, the balls are placed in the structure for clarity and to indicate space in the cage. Reprinted with permission from ref.[42]**

HKUST-1 is usually synthesized solvothermally where it forms micron-sized octahedral crystals, and several other synthetic strategies have also been explored, including microwave, reflux, electrochemical and ultrasonic.[43-45] HKUST-1 is one of the most well-known MOFs because of its large surface area, high pore volume and high chemical stability, which makes it suitable for a wide range of applications. Indeed aside from $CO_2$, methane, and $H_2$ storage and separation applications,[46-47] HKUST-1 adsorption of environmentally toxic gases such as $NH_3$,[48] $H_2S$, $NO_2$,[49] and $SF_6$[50] have been also demonstrated. Furthermore HKUST-1 has also recently shown activity in a growing number of Lewis acid catalyzed reactions such as Friedländer quinoline synthesis,[51] isomerization of α-pinene oxide,[52] and the cyclization of citronellal.[53]

#### 1.2.2.2 UiO-66

UiO-66 (UiO =University of Oslo) is based on a $Zr_6O_4(OH)_4$ octahedral SBU,[54] forming face-centred cubic lattices by 12-fold connection through a 1,4-benzene-dicarboxylate (BDC) linker.[55]

Furthermore larger analogues can be synthesized through the use of extended linkers such as biphenyl- or terphenyl-dicarboxylic acids, leading to the formation of isoreticular UiO-67 and UiO-68 MOFs, respectively (Figure 1.6).[55] This series of MOFs is characterized by a high surface area and unprecedented thermal and chemical stability. Such high stability is related to the fact that each Zr octahedron is 12-fold connected to adjacent octahedral and to the strength of Zr-O bonds, making these materials very tolerant of polar solvents and elevated pressures.

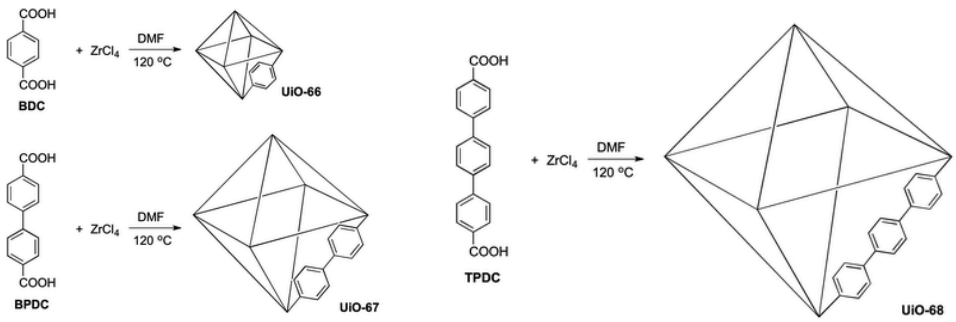


**Figure 1.6 Solvothermal synthesis of Zn(IV)-based MOFs: UiO-66, UiO-67, UiO68. Adapted with permission from ref.[56]**

The UiO family displays numerous potential applications in adsorption and separation: UiO-66 coated capillary columns have been used for gas chromatographic separation of alkane isomers and benzene homologues[57] and the properties of UiO-66 and UiO-66–2,5-$(OMe)_2$ in the vapor adsorption of $CO_2$, $CH_4$, $N_2$, and water were studied.[58] High photostability of the UiO-66 family under UV and visible light has also been reported.[59] Garcia and colleagues focused on photocatalytic hydrogen generation using UiO-66 and UiO-66-$NH_2$ in a methanol or a methanol/water mixture. The apparent quantum yield of UiO-66-$NH_2$ for $H_2$ gas generation was 3.5% using 370 nm monochromatic light in a methanol/water mixture.[60] Furthermore UiO derivatives have also been investigated as catalysts, for instance De Vos and co-workers demonstrated that UiO-66-$NH_2$ could catalyze cross-aldol condensations.[61]

### 1.2.2.3 MIL family

Porous metal carboxylates of the MIL-n type (for Materials Institute Lavoisier) were derived using trivalent cations, such as vanadium(III), chromium(III) and iron(III), aluminium(III), gallium(III) or indium(III). These open-framework MOFs resemble in part zeolite topologies, but they have an enhanced pore size (3-19 Å) and surface area (up to 5900 $m^2/g$).[29] MIL-53 [$(M^{3+}(OH)L$, Guest) with M = Al, V, Cr, Fe; L = terephthalate, naphthalene dicarboxylate, G: guest] is built up from chains of octahedra sharing OH vertices, that are linked in the two other directions by linkers in order to create 1D lozenge-shaped tunnels,[62] and MIL-101 $[Cr_3(O)F(H_2O)_2(BDC)_3]\cdot nH_2O$ (where n is ~25), has a SBU with a $\mu_3$-O oxide bridging three pseudo-octahedral $Cr^{3+}$ ions, with six bridging BDCs and

the final metal sites being taken up by two water molecules and a fluoride anion (Figure 1.7).[63] MIL-53 and MIL-101 are the most studied members of this family, the former because of the ability of the framework to expand and contract without making or breaking bonds while remaining highly crystalline in response of the temperature variation[62] or guests incorporation[64] and the latter because of its large pores, indeed it has hexagonal window of 16 Å opening and an inner free cage diameter of 34 Å.

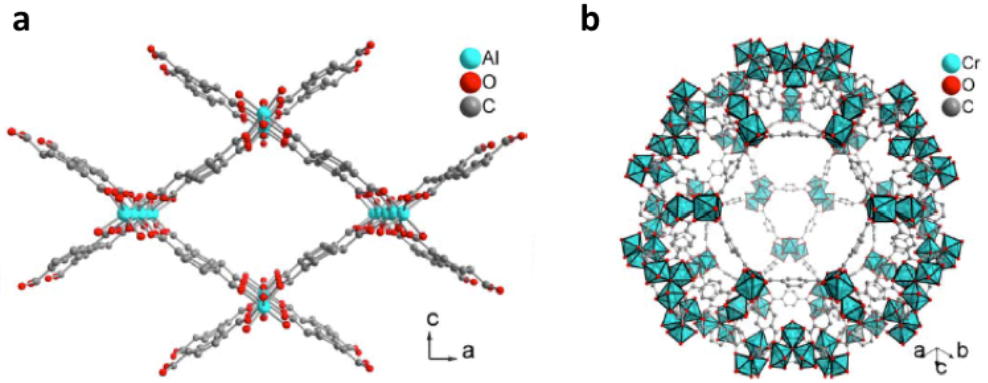


**Figure 1.7 Packing diagrams of (a) MIL-53(Al), [Al(BDC)(μ-OH)] (BDC = benzene-1,4-dicarboxylate, terephthalate) and (b) MIL-101, $[Cr_3(O)(BDC)_3(F,OH)(H_2O)_2]$. Reprinted with permission from ref.[65]**

MILs can function as containers for drug delivery: indeed the frameworks of the MIL series readily absorb anti-tumor and anti-AIDS active agents (*e.g.* busulfan, azidothymidine triphosphate, doxorubicin and cidofovir).[66] Furthermore MIL-101 has been tested for catalytic applications, such as cyanosilylation,[67] while MIL-53(Fe) exhibited adsorption properties[68] and efficient photocatalytic properties for methylene blue degradation under both UV-vis and visible light irradiation.[69]

#### 1.2.2.4 ZIF family

Zeolitic imidazolate frameworks (ZIFs) are a subclass of MOF materials formed by tetrahedral $Zn^{2+}$ and $Co^{2+}$ metal centres bridged by imidazolate linkers forming open network structures analogous to zeolites.[70-73] This topological similarity arises because the metal-imidazole-metal bridges in ZIFs have the same 145° bond angle typical of the Si-O-Si bridges found in zeolites as shown schematically in Figure 1.8.[74-75]

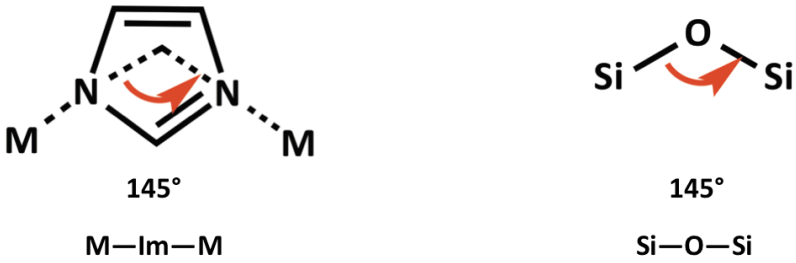


**Figure 1.8 The bridging angles in ZIFs and zeolites.**

Similar to MOFs, ZIF chemistry permits access to a large variety of compounds by virtue of the flexibility with which the linker and can be varied, and ZIFs bridge the gap between zeolite stability and the chemical versatility of MOFs.[76] Many ZIFs exhibit high chemical stability, for instance they can be refluxed in organic solvents, water and aqueous alkaline solution without loss of crystallinity and porosity.[70-71] Furthermore ZIFs display high thermal stability (up to 500 °C) due to the robustness of the frameworks and high porosity (up to 1800 $m^2/g$).[70-71, 76-77] These characteristics enable post synthetic modification of the frameworks and make them attractive candidates for many applications, especially the separation and storage of gases.[76, 78-79] Hereafter ZIF-8, which is a prototypical member of the ZIFs class is described further.

#### 1.2.2.4.1 ZIF-8

ZIF-8, $Zn(MeIm)_2$ (MeIm= 2-Methylimidazole) was first synthesized and characterized by Park *et al.* in 2006. It crystallizes in the cubic space group $I\bar{4}3m$, where each $Zn^{2+}$ ion is tetrahedrally coordinated by four nitrogen atoms from bridging imidazolates to furnish an infinite 3D framework. The secondary building units (SBUs) are $Zn_6(MeIm)_6$ and $Zn_4(MeIm)_4$ rings, from which the subunits of truncated octahedra are constructed when the MeIm ligands are regarded as spacers between the metal centers. The effective diameter of these cages is about 12.5 Å, while the effective hexagonal window size is about 3.3 Å.[80] The overall network resembles a regular zeolitic sodalite (SOD) topology ($4^26^4$) with a solvent-accessible volume of 47.0% of the crystal volume (Figure 1.9).[81]

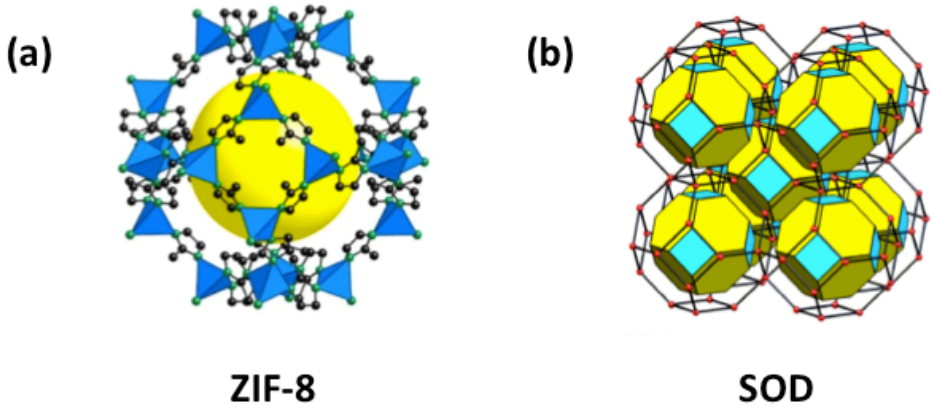


**Figure 1.9 Schematic representation of ZIF-8 (a) structure and (b) topology, the yellow balls are placed in the structure for clarity and to indicate space in the cage. Reprinted with permission from refs.[71, 82]**

ZIF-8 has been demonstrated to be thermally stable in ambient conditions up to 450 °C and chemically resistant when boiled in alkaline water and organic solvents,[70] which, together with the permanent porosity of ZIF-8 and high surface area, make it a prototypical compound for numerous industrial applications. For instance ZIF-8 shows an ability to confine hydrogen gas, and high capacity for methane and carbon dioxide adsorption.[83] Furthermore ZIF-8 nanocrystals have been used to fabricate porous composite nanofibers by electrospinning,[84] thin films with dual micro- and mesoporosity for selective adsorption and sensing of vapours[85] and membranes on titania and α-alumina supports exhibit selective gas separation abilities.[86-87] Further ZIF-8 nanocrystals have been used as a to coat silica capillary columns for chromatographic separation of mixtures of linear alkanes.[88] Esken *et al.* reported that the encapsulation of gold nanoparticles in the cavities of ZIF-8 can promote the catalytic oxidation of benzyl alcohol (or phenylmethanol) to methyl benzoate, where ZIF-8 alone does not exhibit catalytic activity in the oxidation of carbon monoxide.[89]

### 1.2.3 Porosity of Metal Organic Frameworks

MOFs are network structures formed from metal ions and organic linkers where the size of the building blocks used tends to restrict their porosity to the microporous range (less than 2 nm). However this porous range narrows their applications to small molecules; indeed the diffusion of large or bulky molecules in the framework is difficult and the mass transport properties can be limited.[7] One way to remedy this limitation is to incorporate mesopores inside the framework. This kind of hierarchically porous material, in which the walls of the mesopores are constructed by a microporous framework, would combine the advantages of microporosity, such as good stability, high surface activity and selectivity, with the benefits of a mesoscale pore network,

where the large pores can permit accelerated adsorption kinetics due to improved mass transport, with enhanced accessibility and overall storage capacity for large molecules. Therefore the hierarchical porous structure is expected to enhanced the typical application of porous materials, such as gas storage and separation, catalysis, drug delivery, separation and sensing, as in the case of hierarchically micro- and macroporous HKUST-1, which shows a significant enhancement in the liquid phase separation of aromatic molecules when used as a stationary phase in HPLC.[90] Mesoporosity would also enhance the catalytic performance of the material, especially for bulky molecules involved. The potential of such materials and their composites is great, and the challenge is to establish a successful strategy to reach this aim. Previously it has been attempted to form mesoporous MOFs by increasing the length of the organic ligand, but often interpenetrated networks with reduced porosity are formed or the frameworks collapse after removing the guest molecules.[28, 91] Therefore recently template-assisted synthesis approaches, consisting in using a template to direct the structure of MOFs have been employed.[92]

## 1.3 Controlling the macroscopic structure of MOFs

Although much MOF research is focused on the synthesis of new MOF structures and the exploration of their properties,[32] the macroscopic structure or physical form of MOFs, including their crystal size, morphology and the shape of the crystal aggregate, is receiving more attention.[93] The key point here is that enhanced MOF properties can be reached via manipulation of their physical form rather than altering their chemical components. For instance it is well known that the length scale of a material strongly affects its physical properties, for example, the reduction of the particle size from the bulk into the nanoscale range leads to intrinsic phenomena that are only observed at this scale.[94] Furthermore, the nanocrystals can be used as building blocks for the construction of higher-order superstructures, creating more complex architectures, again with collective properties and potential applications that are not observed for the bulk or single nanoparticles.[95-96] Starting from well-known MOF structures the manipulation of their physical form would even further develop and enhance properties and applications. Therefore besides all the properties derived from the inherent microporosity of MOFs, the higher level of order or the control over the dimensionality or shape of the particles should enrich their overall performance and open new fields of application, such as drug delivery or integration into electronic sensor devices.[38, 97] Indeed the self-assembly of MOF crystals is particularly useful in making advanced MOF-based architectures, the characteristics of which (e.g., size, shape, functionality, etc.) would be too complex to obtain by means of traditional chemical synthesis. Furthermore these MOF-based architectures might be self-assembled with

other materials to make MOF-composites, where the resulting superstructures can incorporate the respective properties of each component and exhibit synergic properties arising from the co-assembly. Therefore the control over the macroscopic structure of MOFs is a very powerful strategy to access unique systems and classes of structurally and functionally diverse materials. However, manipulating the macroscopic characteristics of MOFs is still challenging because of a lack of control over the crystallization process and the single-crystal characteristics (shape, size and crystallographic orientation), even though template-assisted synthesis has shown promising results.[98-99]

## 1.4 Template-assisted synthesis approach

Structure directing agents (SDAs) or templating agents, such as membranes, scaffolds and surfactants, represent a powerful tool to direct the structural evolution of inorganic materials.[100] In general template-assisted synthesis, the nucleation/growth of the targeted materials is allowed to occur either on or inside/within a suitable chosen or designed templating scaffold, typically displaying a completely different chemical nature and composition.[101] The template dictates both the shape and size of the desired material, meaning that the replication of one structure into another is accomplished under structural inversion. In the direct or "true" templating, the templated material is a 1:1 (but inverse) copy of the template structure, and no changes in order or length scale of the template structure occur. Templating therefore is a versatile technique also employed for the formation of nanostructured or porous materials, as the size and shape of the resulting pore structures can be easily tuned by choosing the appropriate template structures.[102] Templating agents are also distinguished between soft and hard templating. In the soft-templating approach, the template agents are typically surfactants, gels or biomolecules, whereas in the hard-templating approach inorganic materials, such as silica, metal oxide or organic polymers. In both cases the removal of the template without collapsing the inorganic structure is the final step. For soft templates generally thermal treatment or solvent extraction are the typical strategy, for hard templates etching agent such as strong acids are often used to remove them.

## 1.5 Supramolecular templating agents and MOFs

Surfactants have been widely used in the synthesis of MOFs as soft templating agents and they have been reported to play different roles depending on the system, the synthesis conditions and the supramolecular organization of their mesophase.[92, 98-99, 103] For instance surfactants can act as capping agents to modulate crystal growth rates,[104-105] providing steric stabilization that can allow the formation of nanoparticles[106] or affecting differently the distinct crystal faces, giving

rise to anisotropic growth of MOF crystals.[103] On the other hand, the surfactant-assisted synthesis of MOFs has also been reported to lead to the formation of mesostructured MOFs.[92] In this case, the MOF grows at the external surface of the micellar assemblies, which act as a molecular template leading to the formation of meso- and/or macropores, which together with the intrinsic microporosity of the MOF itself, give rise to particles with hierarchical porosity.[107-108] Furthermore surfactants or emulsion droplets (stabilized by surfactants) can direct the formation of MOF superstructures, leading to ordered assemblies of higher-dimensionality resulting from the self-assembly of nano or micron sized MOF building blocks (BBs).[98-99] The different roles that surfactants as supramolecular templating agents can play on MOFs are summarized in Figure 1.10. It is worth noting however that where there are not adequate interactions between surfactants and their assemblies with MOFs and/or MOF BBs, the two phases often grow independently.

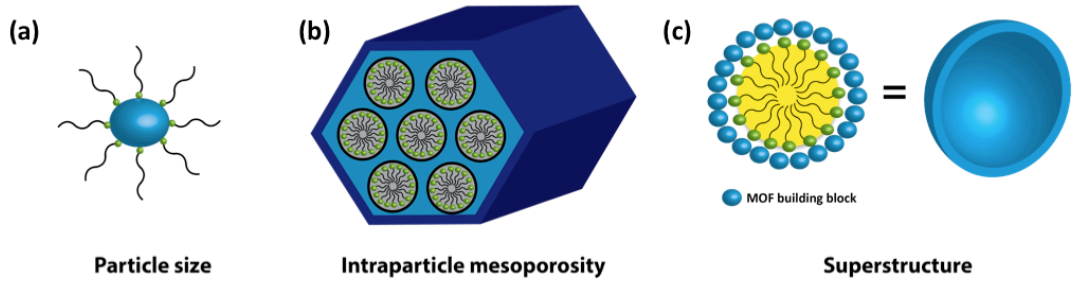


**Figure 1.10 Schematic representation of supramolecular templating agents on MOF: (a) surfactants acting on MOF particle size (b) surfactants directing intraparticle MOF mesoporosity and (c) colloids and surfactant directing the MOF superstructure formation.**

The following discussion is focussed on the different templating effects of surfactants on MOFs, control over particle size and morphology, intraparticle mesoporosity and superstructure formation, and key examples under each topic will are reported.

### 1.5.1 Control over the particle size and morphology

Control over the size and the shape of MOF crystals constitutes an essential step toward MOF specific applications: for instance MOF crystal down-sizing to the nanorange triggers a whole new set of properties compared to the bulk counterparts, such as reducing diffusion path lengths, increasing textural porosity and external surfaces, which are of utmost importance in catalysis and adsorption.[109] Moreover miniaturizing and controlling the crystal size and morphology of MOFs are key features to strengthen their contribution to the development of nanotechnology and device fabrication.[103]

The miniaturization and shape control of MOFs has already become one of the most prosperous disciplines in current MOF chemistry and different strategies have been adopted which usually involve compositional and process parameters, additives and reverse microemulsions.[110] Compositional and process parameters such as solvent, pH, metal source, time and temperature can be adjusted to manipulate the size and shape of MOF crystals.[111-112] Furthermore various additives have been tested to control the size and morphology of MOF crystals: capping agent, macromolecular additive, such as polymers or gelatin, and modulators through the coordination modulator method (CMM).[105-106]

CMM is a strategy to control the crystallization process of MOFs. It is based on the modulation of the interactions between the metal ions and a monodentate ligand that possesses the same organic functionality as the framework-forming multidentate linkers. The competition between the two organic species for the coordination of the metal ion modulates the nucleation process, and consequently the crystal growth. Thus, the size and morphology of the resulting crystals are greatly influenced.[104-105, 113]

Finally reverse nanoemulsions can be used to control MOF crystal size. These emulsions consist of nanodroplets which act as "nanocontainers" for the formation of the nanoparticles. The size and number of nanodroplets within the microemulsion can be tuned by adjusting the synthetic parameters and consequently also the size and morphology of the resulting crystals. Afterwards few examples regarding MOFs miniaturization and shape control are reported.

#### 1.5.1.1 Control over the particle size and morphology via additives

Regarding the use of additives Pan *et al.* gain control over the morphology and crystal size of ZIF-8 by employing the cationic surfactant CTAB as a capping agent, as shown in Figure 1.11.[106] Depending on the amount of CTAB introduced into the synthesis, the shape of the crystal varies from rhombic dodecahedral, truncated rhombic dodecahedral and truncated cubes without CTAB and with CTAB concentrations of 0.0025 and 0.01–0.025 wt.%, respectively. Moreover the size of the ZIF-8 crystals is also affected: in the absence of CTAB the crystals are 4 μm in size, while these are decreased to 100 nm when 0.025 wt.% of CTAB is employed. Molecular dynamics simulations show that the long hydrocarbon chain of the surfactant appears to play a crucial role in changing the morphology and the particle size of ZIF-8 crystals, indeed it is preferentially adsorbed on the [100] faces compared to the [110] and [111] facets leading to the observed anisotropic growth of the crystals.

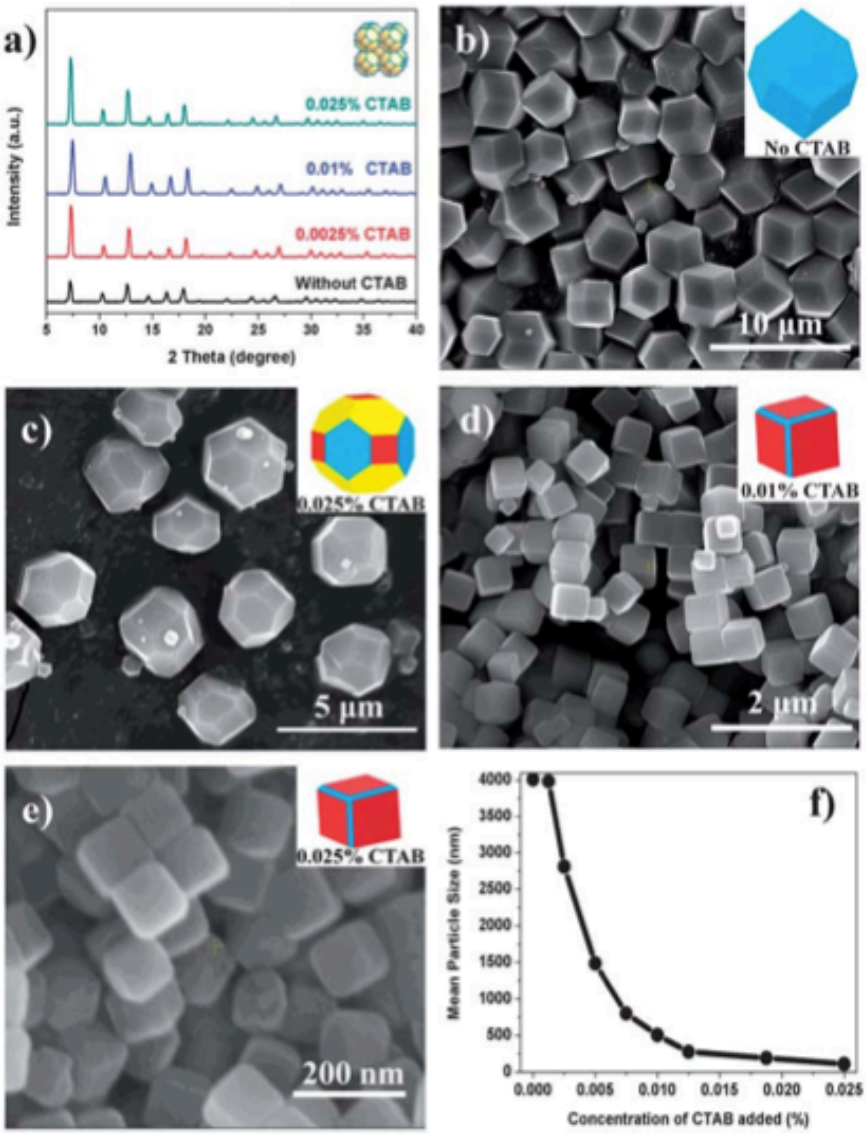


**Figure 1.11 PXRD patterns and SEM images of ZIF-8 crystal samples prepared with different amounts of CTAB. (a) XRD patterns, (b) no CTAB, (c) 0.0025 wt% CTAB, (d) 0.01 wt% CTAB, (e) 0.025 wt% CTAB, and (f) plot of the mean particle size of ZIF-8 crystals versus the concentrations of CTAB added. The insets in the SEM pictures are schematic sketches of the crystal morphologies. [110], [100] and [111] facets are represented in cyan, red and yellow color, respectively. Reprinted with permission from ref.[106]**

Furthermore in the work of Garai *et al.* a biomineral-inspired growth approach has been employed to control the crystal growth of ZIF-8 by introducing gelatin as a soluble macromolecular additive (Figure 1.12).[114] In particular small amounts of gelatin (0.005–0.1 wt%) were added to the hydrothermal synthesis of ZIF-8 at 120 °C: overall, addition of gelatin tends to reduce the ZIF-8 crystal size, which becomes more pronounced with increasing gelatin content. The crystal size is reduced from ~ 3.0 µm to 300 nm when, respectively, 0.005 and 0.1 wt% of gelatin is present, even though the particle size distribution remains relatively large. Therefore the biopolymer acts as an effective modifier to control particle size.

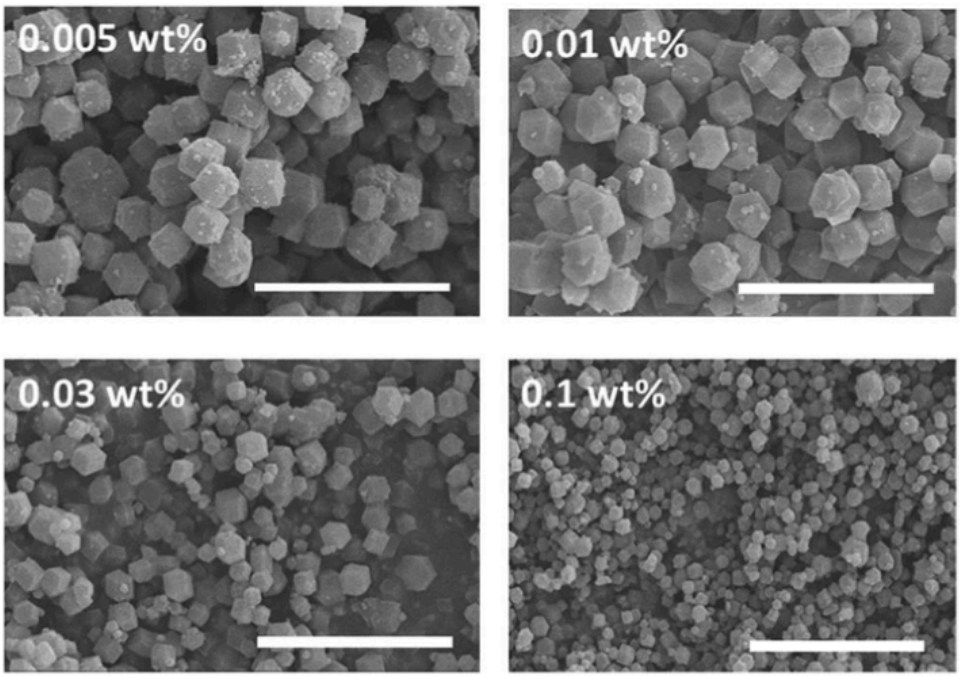


**Figure 1.12 SEM images of ZIF-8 prepared in aqueous solution at 120 °C in the presence of small amounts of gelatin (0.005–0.1 wt%) as a macromolecular crystal growth modifier. Scale bar in all images is 10 μm. Reprinted with permission from ref.[114]**

#### 1.5.1.2 Control over the particle size and morphology via coordination modulator method

Kitagawa *et al.* have employed the CMM in order to regulate the rate of framework extension and the crystal growth of $[Cu_2(ndc)_2(dabco)]_n$ (ndc =1,4-naphthalenedicarboxylate; dabco =1,4-diazabicyclo[2.2.2]octane), a MOF that exhibits the common pillared-layer type structure. (Scheme 1.2).[104] The anisotropic framework feature of $[Cu_2(ndc)_2(dabco)]_n$ is dominated by the two coordination modes: ndc–copper layers and dabco–copperpillars, which allows the selective modulation of one of the coordination modes (ndc–copper) by adding a monocarboxylic acid as the modulator. The presence of acetic acid as modulator in the framework synthesis impeded the ndc– copper interaction within the two-dimensional layer, because both ndc and acetate have the same carboxylate functionality, therefore, the selective coordination modulation method enhanced the relative crystal growth in the [001] direction forming $[Cu_2(ndc)_2(dabco)]_n$ nanorods rather than the bulk crystal morphology.

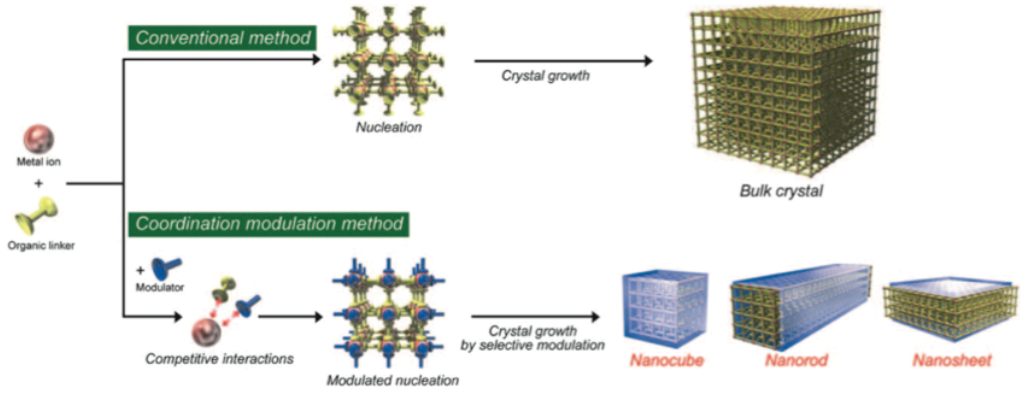


**Scheme 1.2 Coordination modulation method for fabricating porous coordination polymer (PCP) nanocrystals. Modulated nucleation is induced by the addition of modulators with the same functionality as organic linkers to impede the coordination interaction between metal ions and organic linkers. Selective coordination modulation in one of the coordination modes (illustrated as blue shells) to construct the framework then leads to anisotropic growth of the PCP crystals. Reprinted with permission from ref.[104]**

Furthermore the same group also present a method which combines microwave-assisted solvothermal conditions with CMM to achieve the size-controlled formation of HKUST-1, in the nano/micro regimes.[105] Indeed by adjusting the concentration of a dodecanoic acid additive in the reaction, they gain efficient control over the nucleation rate of HKUST-1 and thus the resulting crystal size: homogeneous nanocrystals of HKUST-1 with sizes ranging from few tens of nanometers up to a few micrometers could be successfully obtained. The ratio between the dodecanoic acid and benzene-1,3,5-tricarboxylic acid content was varied from r = 25 to r = 75, keeping the concentration of starting material constant, where the concentration of benzene-1,3,5-tricarboxylic acid is defined as c in Figure 1.13. In a second set of experiments, for a given ratio (r = 25, 50, or 75), only the volume of solvent changed, thus affecting the global concentration (Figure 1.13 (1)). For a given ratio r, the particles became smaller when the global concentration was decreased, while for a fixed concentration of starting materials, increasing the dodecanoic acid content promoted the growth of larger crystals. The proposed mechanism is the following: high concentrations of additive can provide a slow nucleation (fewer nuclei) of the HKUST-1 framework. A smaller number of crystals are indeed growing in line with the persistent nucleation during the heating process, leading to larger crystals with greater size polydispersity. With lower concentrations of modulator, the nucleation occurs faster. A large number of nuclei are formed and rapidly grow at the same time, while the available reagents are quickly depleted, affording smaller crystals with homogeneous size distribution (Figure 1.13 (2)).

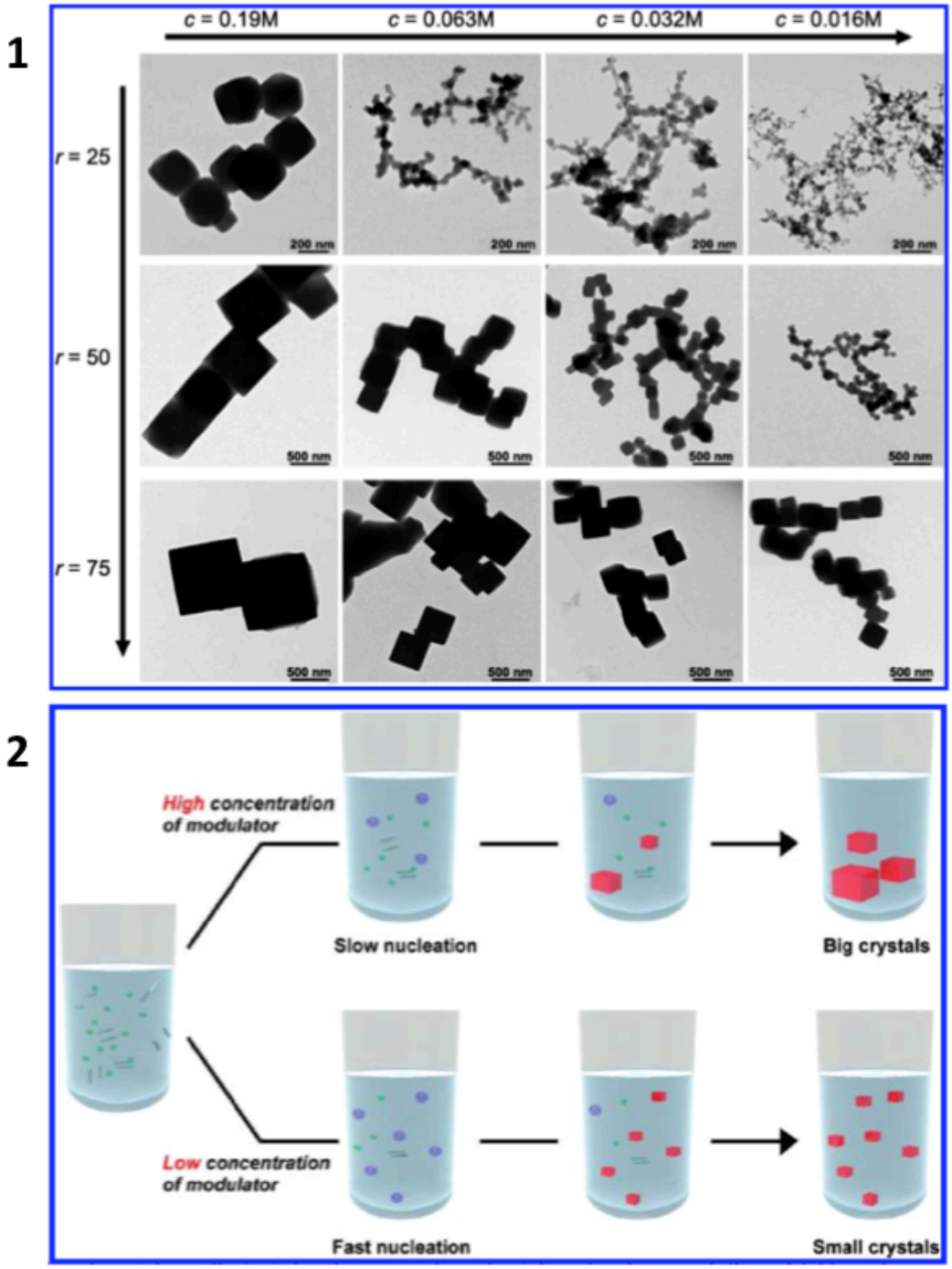


**Figure 1.13 (1) TEM images of samples obtained with various concentrations of dodecanoic acid and benzene-1,3,5-tricarboxylic acid. All samples were prepared under microwave irradiation (140 _C, 10 min). (2) Schematic Representation for the Nucleation-Controlled Formation of $[Cu_3(btc)_2]$ Nanoparticles, The precursors, nuclei, and crystals are illustrated as the green spheres (metal ions) and gray rods (ligands), blue spheres, and red cubes, respectively. Adapted with permission from ref.[105]**

### 1.5.1.3 Control over the particle size and morphology via microemulsions

Lin *et al.* reported the first examples of MOF nanoparticle synthesis in reverse microemulsions.[110] Uniform nanorods of $[Gd(BDC)_{1.5}(H_2O)_2]$ were prepared by stirring an optically transparent microemulsion of $GdCl_3$ and bis(methylammonium)benzene-1,4- dicarboxylate (molar ratio 2:3) in

CTAB/isooctane/1-hexanol/water system for 2 hours at room temperature. Higher water/CTAB molar ratios led to particles with higher aspect ratios, resulting from a decrease of nucleation sites within the microemulsion droplets and the particle size also decreased with lowering of reactant concentration (Figure 1.14 (1)). Furthermore the generality of the reverse microemulsions method was probed by carrying out the reaction of $GdCl_3$ and (1,2,4-BTC) in the same microemulsion system forming irregularly shaped, crystalline nanoplate of [Gd(1,2,4-BTC)$(H_2O)_3$]·$H_2O$ (Figure 1.14 (2)).

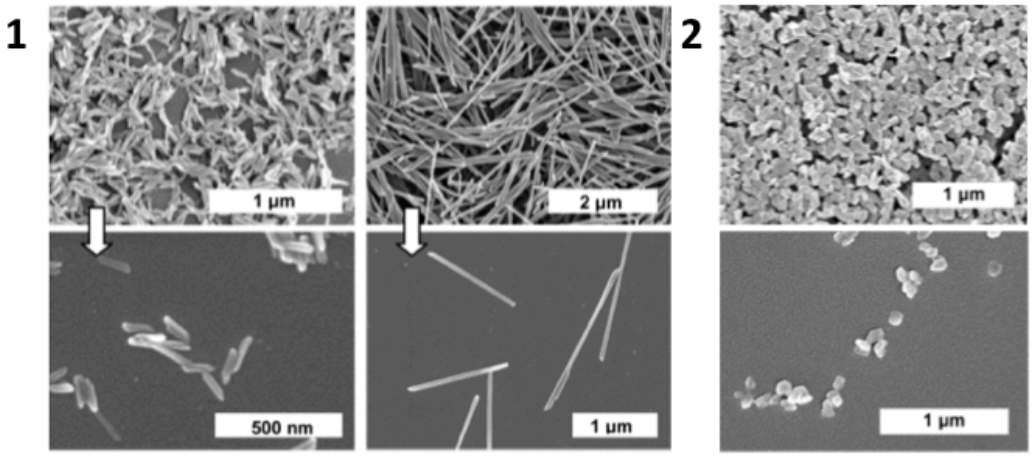


**Figure 1.14 SEM images of (1) $Gd(BDC)_{1.5}(H_2O)_2$ nanorods synthesized with *w* ) 5 (left) and *w* ) 10 (right) and (2) irregularly shaped, crystalline [Gd(1,2,4-BTC)$(H_2O)_3$]·$H_2O$ nanoplates. Reprinted with permission from ref.[110]**

Due to the presence of the $Gd^{3+}$ centers [$Gd(BDC)_{1.5}(H_2O)_2$] and [Gd(1,2,4-BTC)$(H_2O)_3$]·$H_2O$ have been tested as nanoscale contrast agents for magnetic resonance imaging (MRI). They exhibit enhanced relaxivities per mM of $Gd^{3+}$ compared to the clinically used OmniScan. Finally luminescent nanorods of [$Gd(BDC)_{1.5}(H_2O)_2$] have been synthesized by using $Eu^{3+}$ and $Tb^{3+}$ as dopants which can be used as potential contrast agents for multimodal imaging.

The reverse microemulsion approach has since been widely extended to a range of other systems including ZIF-8 and ZIF-67,[115] where extremely small crystals (particle size less than 5 nm) were synthesized or $Gd_2(BHC)(H_2O)_6$ (BHC= benzene hexacarboxylic acid), which exhibited blocklike morphology with dimension ranging in the nanoscale.[116]

### 1.5.2 Intraparticle mesoporosity

As previously mentioned the porosity of MOFs is often restricted to the microporous range limiting their applications to those involving small molecule separation and transformation. As a result the introduction of mesoporosity into MOFs would lead to significant improvements in mass transport and diffusion, and consequently widen the range of applications/substrates. Supramolecular templating strategies, which have already been applied to inorganic and hybrid

materials,[117] have been recently adopted for the formation of mesoporous MOFs. Ordered mesoscale arrays of surfactant molecules are used as scaffolds for the formation of the mesopores. In the process the surfactant acts as a SDA for the formation of a MOF mesostructure through co-assembly between a suitable surfactant mesophase, such as the hexagonal phase, and the MOF precursors leading to the positioning of the framework-building blocks. Then the cross-linking via metal–ligand bonding occurs to form an extended functional microporous coordination network punctuated by an array of mesopores[118] (Figure 1.15) where the surfactant mesophases potentially permit control over the dimension, shape, position and space distribution of the mesopores. However a few considerations must be taken into account for successful mesopore templating; for example, the formation of the mesostructure is determined by the co-assembly of the surfactant mesophase and the MOF precursors. Therefore suitably attractive interactions between them are vital. Typically such interactions are electrostatic or hydrogen-bonding, even though it is difficult to assign their specific nature due to the complexity of the self-assembly process of MOFs. However their strength is particularly important for the success of the mesostructure formation, where too weak interactions would lead to phase separation before co-assembly of the precursors and prevent effective templating by the SDA, whereas too strong interactions would lead to integration of the template into the framework and difficult removal. Furthermore the synthetic conditions should be carefully chosen to be compatible with the MOF formation and the co-assembly process, and in this respect pH, nature of the solvent, reaction temperature and the order of addition of the precursors are crucial factors. The final consideration is the removal of the SDA from the resulting mesostructured MOF in order to fully access the large templated pores within the structure. This commonly involves exhaustive solvent extraction or calcination but in some cases causes the mesopores to collapse, so stabilizing these is also a challenge.[118]

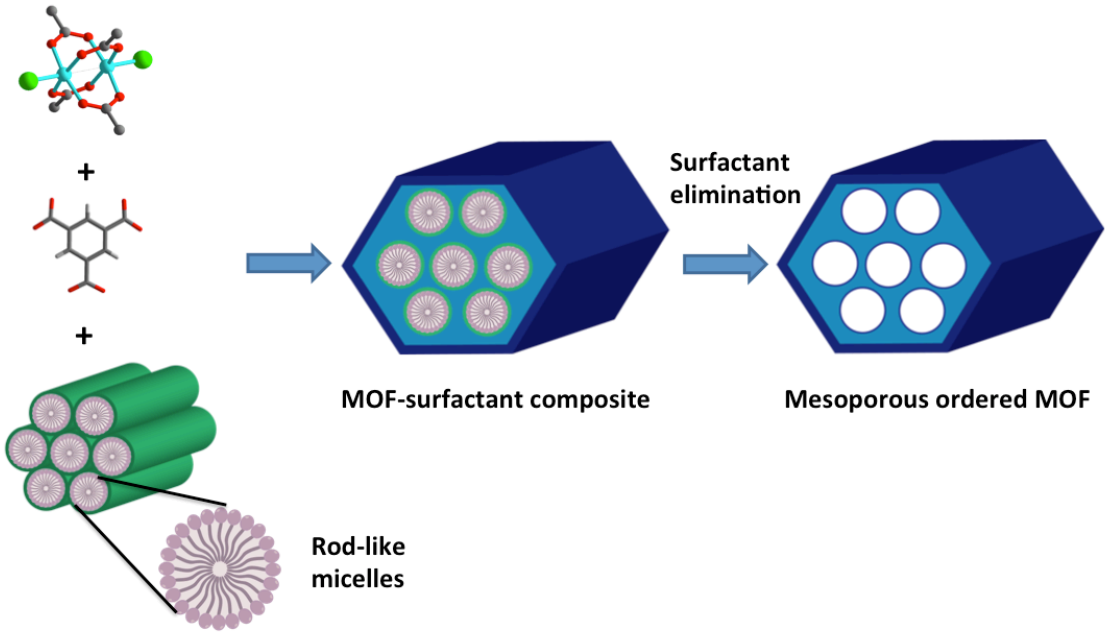


**Figure 1.15 Structure-directing approach illustrated for the formation of mesostructured HKUST-1: the surfactant mesophase acts as a template for the formation of the HKUST-1 mesostructure and after surfactant elimination a hierarchically porous solid is obtained.**

In the following text a few examples are presented showing the effect of the surfactant-templating approach using cationic, anionic, non-ionic block copolymer and non-ionic surfactants on the mesopores structuring of MOFs.

Wee *et al.* reported the synthesis of COK-15 ($(CTA)_1[Cu_{46}(C_9H_3O_6)_{24}$-$(OH)_{12}]$ $(PW_{12}O_{40})_3 \cdot xH_2O$, HPW= Keggin type phosphotungstate), a hexagonal variant of HKUST-1, with bimodal micro-/mesoporosity via a dual-templating approach.[108] The synthesis was performed at room temperature with a molar composition of Cu:BTC:HPW:CTAB:EtOH:$H_2O$= 18:10:1:1:170:2000, where the HPW anions serve as a molecular template for the structural motif of the MOF and CTAB acts as a SDA, directing these units into an ordered mesoporous structure giving rise to wide mesopores of 5 nm separated by microporous walls (Figure 1.16). The stability of the material is enhanced by the systematic occlusion of HPW anions in the cavities constituting the walls between the mesopores, while the structure directing role of CTAB is 2-fold: inclusion of CTA in the pores changes pore topology toward mesoporous and the externally present surfactant in solution controls the morphology of the crystals giving flat, extended sheets. Furthermore the catalytic performance of COK-15 was investigated for the alcoholysis of styrene oxide under mild reaction conditions (methanol at 40 °C). COK-15 showed remarkable catalytic activity compared to the reference compounds HKUST-1 and the microporous analogue with encapsulated Keggin ion HPW@HKUST-1, respectively 100, 2 and 40% conversion, suggesting that the acidic HPW ions are responsible for the catalysis and the mesoporous features of COK-15 efficiently reduced any mass transport limitations.

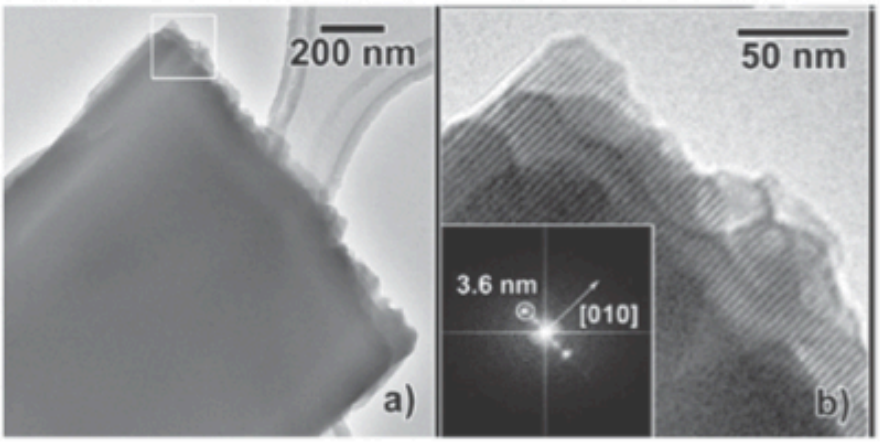


**Figure 1.16 TEM images of COK-15 showing (a) a typical bright-field image of the flat slab-like crystals. (b) An enlarged image of the region indicated in (a) showing the pore repetition. Inset: fourier transform demonstrating a pore spacing of 3.6 nm. Reprinted with permission from ref.[108]**

Yaghi *et al.* outlined a template strategy for producing hierarchically porous MOF-5 crystals in which a system of meso- and macropores either permeates the whole crystal to make sponge-like crystals (spng-MOF-5) or is entirely enclosed by a thick crystalline microporous MOF-5 sheath to make pomegranate-like crystals (pmg-MOF-5).[107] Depending on the amount of added DBA in the synthesis different results have been obtained: in the absence of DBA, the usual MOF-5 crystals were produced as in Figure 1.17 (a), in the presence of amounts of DBA equimolar to that of the organic linker (1,4-BDC), MOF-5 crystals are produced but with macroscopic pores being visible at the crystal surface to give an overall spongeous structure, spng-MOF-5, as illustrated in Figure 1.17 (b), and with 30 mol % of DBA to the organic linker, MOF-5 crystals are produced, but these have the pomegranate-type structure with a spongeous core and solid outer shell, pmg-MOF-5 (Figure 1.17 (c)). This demonstrates the decisive role of DBA in the formation of the hierarchically porous spng- and pmg-MOF-5, which has a dual purpose: the hydrophilic carboxylate head group is used for binding to the $Zn^{2+}$ ions required for framework formation while the long alkyl chain is used for space filling. Clearly the differing morphologies are strongly correlated to the availability of DBA during the crystal growth. Furthermore the $CO_2$ adsorptive properties of these structured MOFs have been studied demonstrating the higher uptake of pmg-MOF-5 compared to MOF-5, despite the fact that pmg-MOF-5 (3230 $m^2/g$) has slightly less surface area than MOF-5 (3410 $m^2/g$). This behavior is consistent with $CO_2$ uptake first through the microporous surface shell, followed by filling of the larger interior meso- and macropores under higher pressure followed by release through micropores as pressure is reduced.

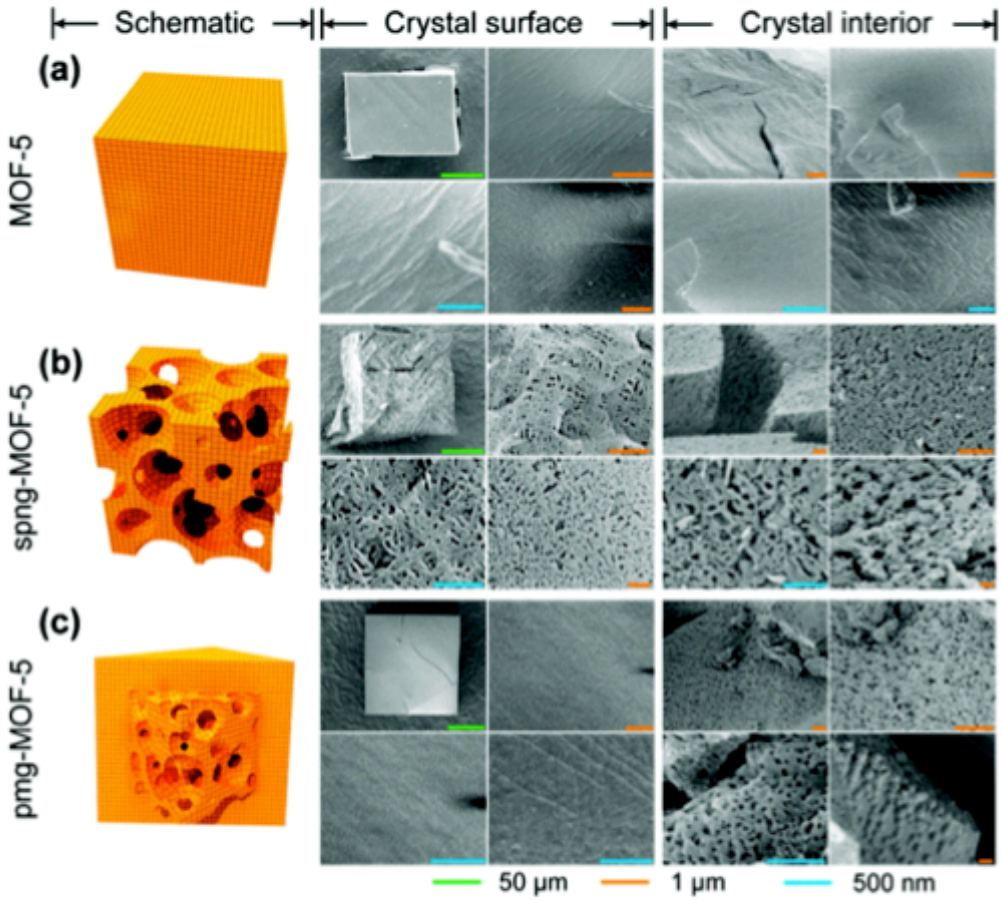


**Figure 1.17 Schematic illustration and SEM pictures of crystal surface and interior of (a) bulk, (b) sponge and (c) pomegranate MOF-5 structures obtained adding (a) no DBA or (b) DBA equimolar to of the organic linker, (c) 30 mol % of DBA to the organic linker. Reprinted with permission from ref.[107]**

Pham *et al.* synthesized hierarchically porous MOF nanocrystals via supramolecular templating using a non-ionic triblock copolymer, where the solvothermal reactions of the prototypical MOFs HKUST-1 and $[Cu_2(HBTB)_2]$ ($H_3BTB$ = 1,3,5-Tris[4- carboxyphenyl]benzene) were performed in the presence of F127 ($EO_{97}PO_{69}EO_{97}$) and acetic acid (AA) (Figure 1.18 (1)).[119] The proposed mechanism for the formation of MOF nanocrystals is the following: the presence of acetic acid and $Cu^{2+}$ ions probably leads to the formation of $[Cu_2(CH_3COO)_4]$ species. Upon the addition of the linkers, nanosized building blocks including MOF components are yielded. The nanosized building blocks coassemble with the surfactant micelles into mesostructures, and at high temperature (120 °C), the building blocks fuse to form MOF crystals, while maintaining the mesostructure (Figure 1.18 (2)). Therefore the AA acts as both competitor and deprotonator of the linker, slowing down the crystallization rate of the framework, permitting effective co-assembly with the triblock copolymer template by reducing framework growth and crystal size which prevents premature phase segregation, while F127 is employed to template mesopores within the MOF crystals. Higher crystallinity and more uniform wormhole-like mesostructures were obtained by

increasing the AA/$Cu^{2+}$ molar ratio, demonstrating its key role in the formation of both the micro- and mesopore structures within the MOF crystals.

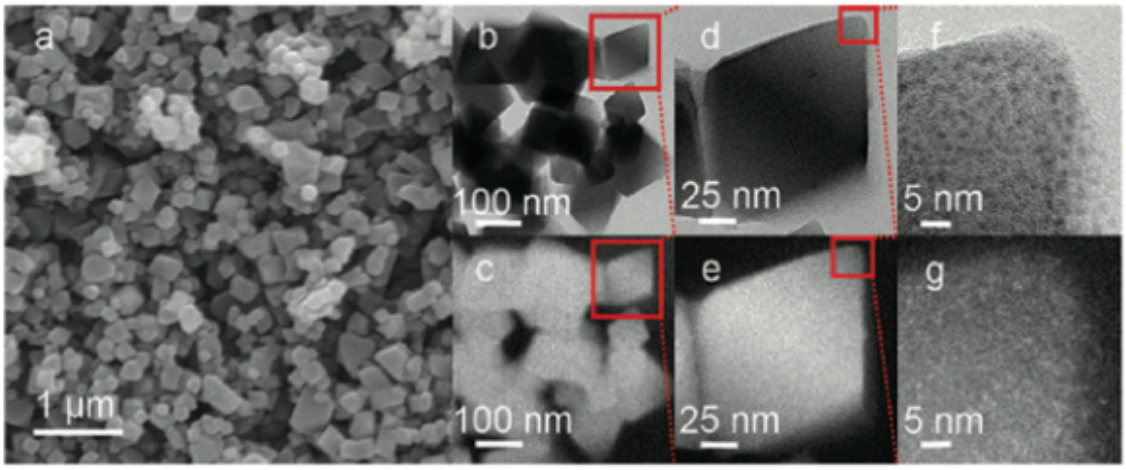


**Figure 1.18 (1) Electron microscopy images of UL1MOF-6. (a) SEM image showing the isolated octahedral mesoporous MOF crystals with the size in a range of 100–200 nm, (b, d, f) bright-field HRTEM images with different magnifications indicating a three-dimensional wormhole-like mesostructure, (c, e, g) dark-field HRTEM images obtained on the same area of the sample. The bright spots in the dark-field images correspond to MOF nanocrystal building blocks. Reprinted with permission from ref.[119]**

Zhao *et al*. reported the synthesis of MOF nanospheres with long-range ordered mesopores in an ionic liquid (ILs), supercritical $CO_2$ ($scCO_2$), surfactant emulsion system.[120] In a typical experiment, $Zn(NO_3)_2{\cdot}6H_2O$, 1,4-benzenedicarboxylic acid ($H_2BDC$), IL 1,1,3,3-tetramethylguanidinium acetate (TMGA), and surfactant N-ethyl perfluorooctylsulfonamide (N-EtFOSA) were added into a high-pressure cell, which was controlled at 80 °C, then $CO_2$ was charged into the cell to 16.8 MPa under stirring and the reaction was allowed to proceed for 48 h. Uniform nanospheres with diameter ~ 80 nm containing well-ordered mesopores were formed, where the walls of the mesopores are constructed by the microporous framework (Figure 1.19 (1)). The proposed mechanism for the formation of the novel MOF structure involves self-assembly of the surfactant molecules into cylindrical micelles with the fluorocarbon chain directed towards the inside of the micelles, and $CO_2$ exists as a core of the micelles. The IL, $Zn(NO_3)_2$, and $H_2BDC$ form a continuous phase. The $Zn^{2+}$ metal ions and BDC in the IL form a crystalline microporous framework because of the facile linkage property of $Zn^{2+}$ and BDC, which leaves cavities in the micelles. Therefore, MOFs with well-ordered mesopores and microporous structured walls were formed after removal of the IL, $CO_2$, and surfactant (Figure 1.19 (2)). The sizes of the micro- and mesopores determined by nitrogen adsorption isotherms were 0.7 and 3.0 nm respectively, with a mesopore wall thickness of 2.5 nm. Finally it is important to stress that the strong interaction between the fluorocarbon chains of N-EtFOSA and $scCO_2$ is vital to the formation of the mesopores, as materials prepared only in the IL have no mesoporous structure.

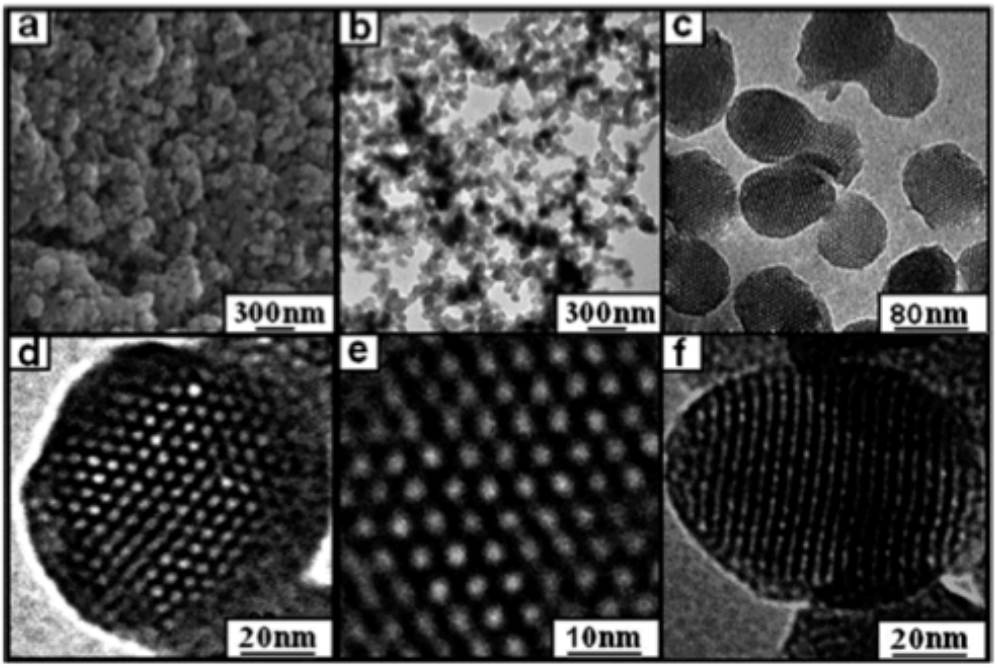


**Figure 1.19 (a) SEM and (b–f) TEM images of the MOF. Reprinted with permission from ref. [120]**

### 1.5.3 Superstructures

Superstructures are higher-dimensionality ordered structures resulting from the self-assembly of nano or micron sized building blocks (BBs). They have been mostly studied in inorganic nanoparticles,[121] while just a few pioneering studies have been conducted with MOFs.[98-99] MOF superstructures are promising materials because they would exhibit functionalities and architectures not provided by the individual BBs, where the properties of the material are tuned by designing their physical form rather than changing their composition. Indeed the superstructure, besides having the inherent properties of the BBs, displays new functions resulting from the higher-order architecture, improving the overall performance and leading to more advanced applications. For instance the control of crystal orientation would align the pore and maximise the separation capacities, therefore the self-assembly into a chain system may allow anisotropic molecular flow along the superstructure.[122] In the scheme below some examples of superstructures are shown.

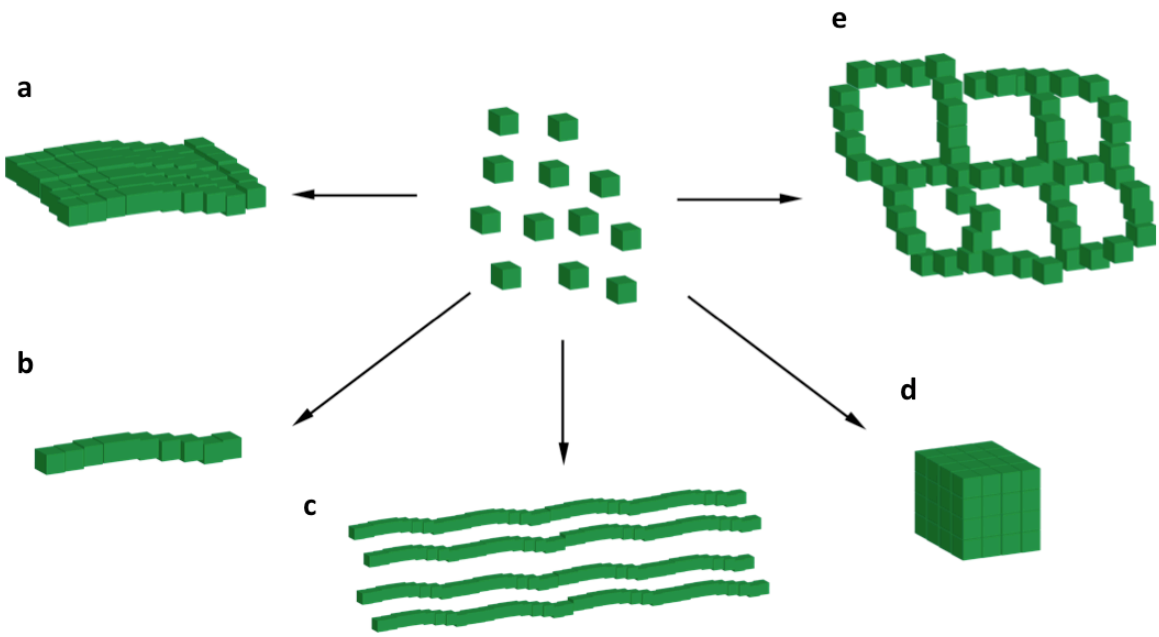


**Scheme 1.3 Schematic of the spontaneous organisation of MOF cubic crystals into (a) 2D superlattices, (b) chains (c) fishbone-like superstructures, (d) cubic structure (e) non-ordered, hierarchical superstructure self-assembled from the crystals.**

However it still remains a big challenge to synthesize well-defined MOF superstructures where the main requirements for higher level assembly are the uniformity of the nanocrystal BBs (shape, size and crystallographic orientation)[123] and spatial control over the crystallization process of MOFs. Hereafter a few examples of hybrid material superstructures are reported.

The first example is about the well-known Prussian blue (PB, $Fe_4[Fe(CN)_6]_3$) which can be viewed as a model for MOFs in this context. It is an important functional material and has many commercial and potential applications in the fields of molecular magnets, catalysis, sensor, and optics.[124-125] Well-defined PB nanocrystals with uniform morphologies, such as nanocubes and nanotubes, suitable for the formation of superstructures, have been obtained by a variety of solution-based routes and template techniques. For instance Wu *et al.* employed uniform PB nanocube building blocks to assemble rod-like superstructures, fishbone-like superstructures and 2D superlattices via a dynamic vacuum evaporation route.[126] In particular the pre-formed PB nanocubes with size of 120 nm were dispersed in aqueous solution and, by tuning the evaporation rate, different superstructures were obtained: at higher rates, the rod-like superstructures were favored, whereas at lower rates, the fishbone-like and 2D superlattices were favored (Figure 1.20).

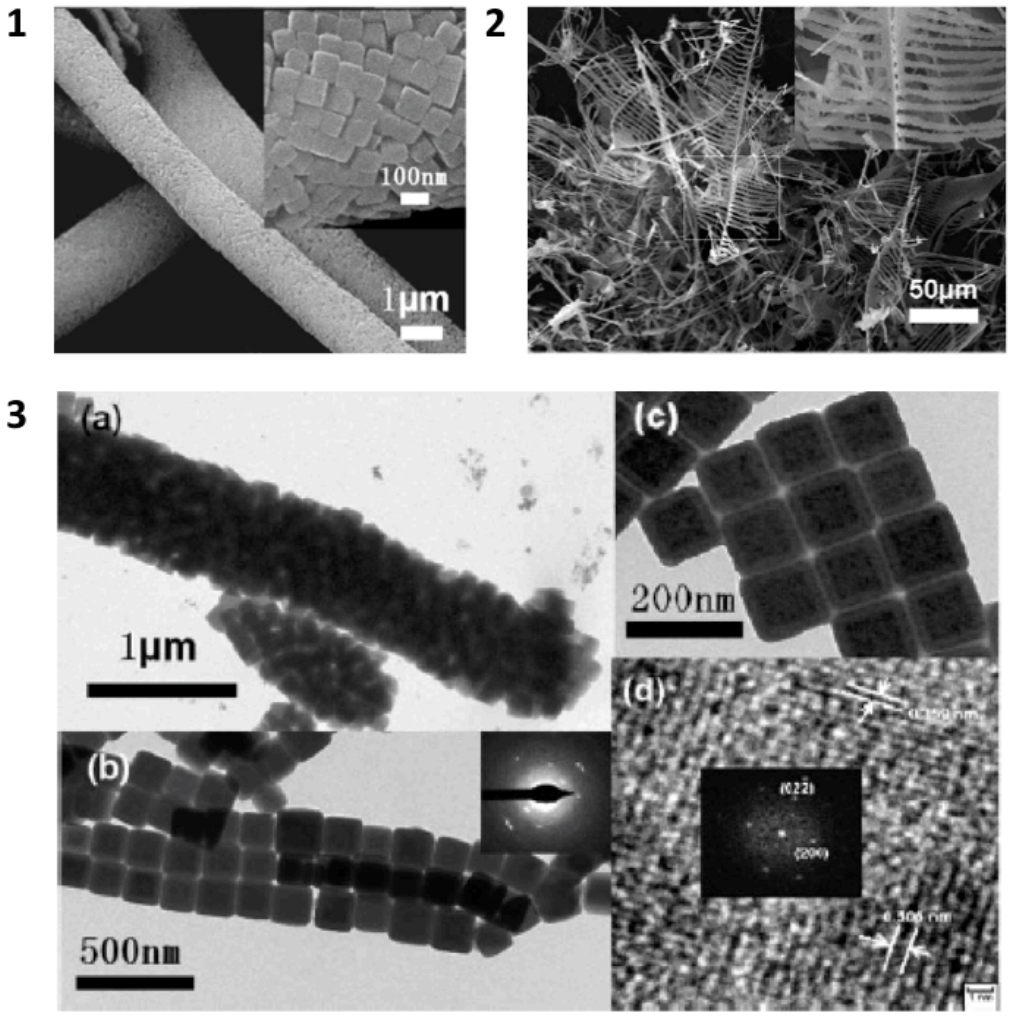


**Figure 1.20 SEM images of (1) microrods and the detail of PB nanocubes array in the microrod in the insert (2) fish-bone-like superstructure formed in a lower evaporation rate, the inset is a magnified view of the zone indicated by the pane. (3) TEM and HRTEM images of the PB nanostructures. (a) TEM image of the PB microrods. (b) TEM image showing a single layer of the rod-like superstructures, the inset is a SAED pattern taken from a nanocube. (c) TEM image of the uniform PB nanocubes assembling the microrods. (d) HRTEM image of a PB nanocube, inset is the corresponding fast Fourier transform (FFT). Reprinted with permission from ref.[126]**

Similarly Eddaoudi *et al.* used well-defined cubic micron-scale crystals of M-soc-MOF ($[M_3O(abtc)_{1.5}(H_2O)_3](H_2O)_3(NO_3)$, M= $In^{3+}$ and $Ga^{3+}$, abtc = 3,3',5,5'-azo-benzenetetracarboxylate, soc = square octahedron) as building blocks for self-assembled MOF superstructures (Figure 1.21).[127] Highly monodisperse cubic crystals of In-soc-MOF were obtained from a solvothermal reaction between $H_4ABTC$ and $In(NO_3)_3{\cdot}xH_2O$ in an $CH_3CN$:DMSO:DMF (2:1:1) solution containing poly-(vinylpyrrolidone) (PVP) and tetramethylammonium nitrate (TMAN), where PVP acts as a surfactant and TMAN as a structure-directing agents (SDAs). Interestingly increasing the amount of TMAN from 0.01 to 0.10 mL leads to an increment in the size of the In-soc-MOF cubes from 0.88 ± 0.03 to 1.50 ± 0.02 μm and the uniform cubic crystals self-assemble into a 2-D superlattice via the "oriented attachment" mechanism.

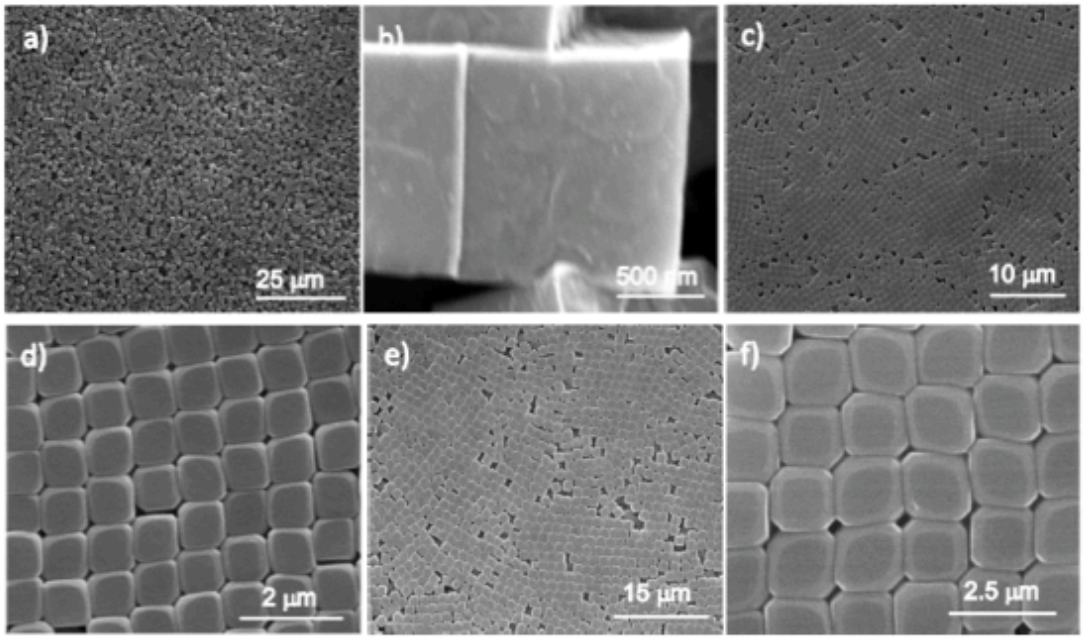


**Figure 1.21 SEM images of soc-MOF-1a crystals: (a,b) cubes, (c,d) edge- and corner-rounded cubes (TMAN= 0.01 mL), and (e,f) (110)-truncated cubes (TMAN= 0.10 mL). Reprinted with permission from ref.[127]**

Furthermore the formation of amorphous coordination polymers can also sometimes induce the spontaneous self-assembly of MOFs into superstructures. For instance the work of Dai *et al.* synthesized hierarchical microporous–mesoporous Zn-MOF-74 mixing zinc acetate and $H_2$DHBDC in DMF at room temperature (Figure 1.22).[128] In the initial stages of the reaction between the Zn precursors and ligands at room temperature, the bidentate-acetate-bridged $[Zn_2(CH_3COO)_4]$ units form. Upon the addition of the ligand precursor $H_2$DHBDC, nanosized MOF-74 crystals precipitate in addition to amorphous metal complexes, since the organic linkers compete with the carboxylate bridging ligands. At this stage, the formation of nanosized MOF-74 crystals possibly occurs via deprotonation of the linker precursors by the acetate groups. Thus, the acetate accelerates the MOF crystal formation through a ligand-exchange process. The precipitated material is composed of discrete nanosized Zn-MOF-74 particles embedded in an amorphous matrix. Therefore these superstructures show a bimodal pore size distribution: as a result of being formed by microporous Zn-MOF-74 crystals and a mesoporous amorphous matrix.

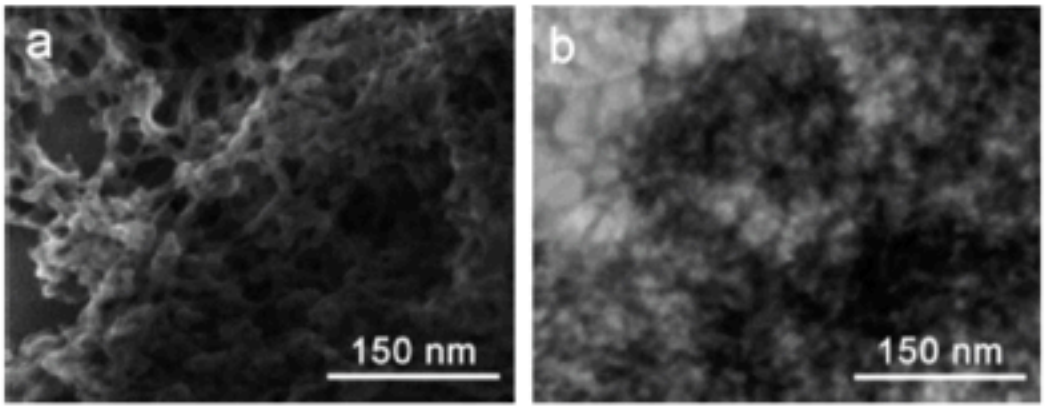


**Figure 1.22 (1) (a) SEM and (b) TEM images of the bimodal microporous–mesoporous material Zn-MOF-74/18 (2) Schematic Illustration of a Possible Mechanism for the Formation of the Bimodal Microporous–Mesoporous MOF Material and the Morphology Transformation by Solvent Etching (I–III). Reprinted with permission from ref.[128]**

Li *et al.* present the first example of the preparation of helically structured MOF nanomaterials from supramolecular assemblies of two low-molecular-weight bolaamphiphilic templates in a controlled manner (Figure 1.23).[129] The two bolaamphiphiles, based on either D- or L-glutamic acid functionalized with hydrophilic carboxyl groups at the surface (N,N-hexadecanedioyl-di-L-glutamic acid (L-HDGA) and its enantiomer D-HDGA), are used to form well-defined helical supramolecular aggregates. The functionalized surfaces show strong affinities for metal cations, and thus enable the nucleation, crystallization and growth of MOFs onto the curved helical aggregates. Indeed, after optimizing the conditions, the chirality of the helical supramolecular aggregates could be reliably expressed onto the formed HKUST-1, affording well-defined, helically nanostructured HKUST-1. Furthermore the diameters of the resultant L-HDGA@HKUST-1 nanomaterials can be gradually increased from 23 nm to 56 nm by stepwise addition of the HKUST-1 precursor (Figure 1.23 (2)). Moreover, in order to prove the generality of the method, MIL-100 was also chosen for the production of helical MOF constructs under similar conditions. In the case of MIL-100 more complex helical bundle superstructures were achieved through intertwining of a few helical MIL-100 nanofibers, which is probably due to the high coordination valency and high affinity of $Fe^{3+}$ relative to $Cu^{2+}$ (Figure 1.23 (3)). Finally these resultant HKUST-1 or MIL-100 superstructures with inherited chiralities showed additional optical properties and might be useful as precursors for the preparation of chiral nanocarbons.

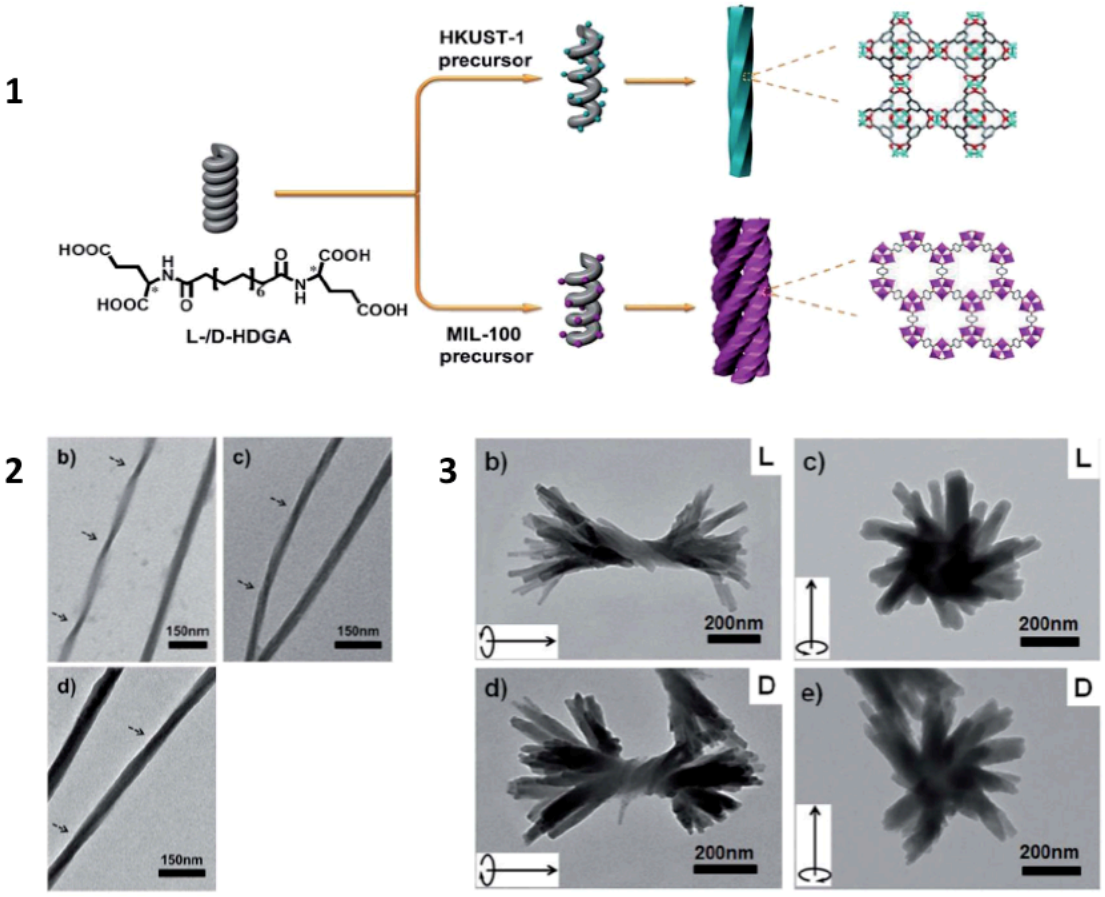


**Figure 1.23 (1) Schematic illustration of the fabrication of helical MOF nanostructures by using supramolecular assemblies as templates, (2) TEM images (b–d) of the resultant helical n-l-HDGA@HKUST-1 (n 1/4 1, 2, 3) nanomaterials with increased addition of the MOF precursor leading to evolution of the diameter (3) TEM images of the resulting right-handed (b and c) and left-handed (d and e) hierarchical MIL-100 superstructures. The arrow in the inset of each TEM image is to assist in the identification of the direction of the helicity of the formed superstructure. Reprinted with permission from ref.[129]**

Finally MOF superstructures can be formed by a coordination replication method starting from a pre-shaped dense metal oxide phase, as demonstrated by Reboul *et al.*.[130] In particular two-dimensional honeycomb and three-dimensional inverse opal oxide structures were prepared as model parent architectures and then converted by direct reaction with the organic ligand into the corresponding MOF superstructures (Figure 1.24 (1)). Diffraction measurements and microscopy studies confirmed complete conversion of an alumina architecture by forming cubic crystal of [Al(OH)(NDC)] (NDC= naphthalene dicerboxylate) with a dimension ranging from 10-200 nm when reacted with the NDC linker. The maintenance of the alumina support shape strongly supports a coupled dissolution-reprecipitation mechanism of formation where the metastable alumina dissolves in the fluid at the solid/liquid interface, and immediately crystallizes as a new stable MOF phase at the same site as the dissolved precursor. Furthermore the same strategy was applied to randomly oriented alumina aerogels, obtaining the related hierarchically porous MOF replicas with pores spanning the mesoporous (Meso-PCP) or meso-/macroporous (Macro-PCP)

regimes depending on the pore structure of the template (Figure 1.24 (2)). Breakthrough experiments performed with Meso-PCP or Macro-PCP for the separation of an equimolar binary water/ethanol mixture demonstrated the effect of the adsorbent architecture on the separation efficiency compared to the bulk powder and the increased selectivity in comparison to the parent macroscopic alumina aerogel.

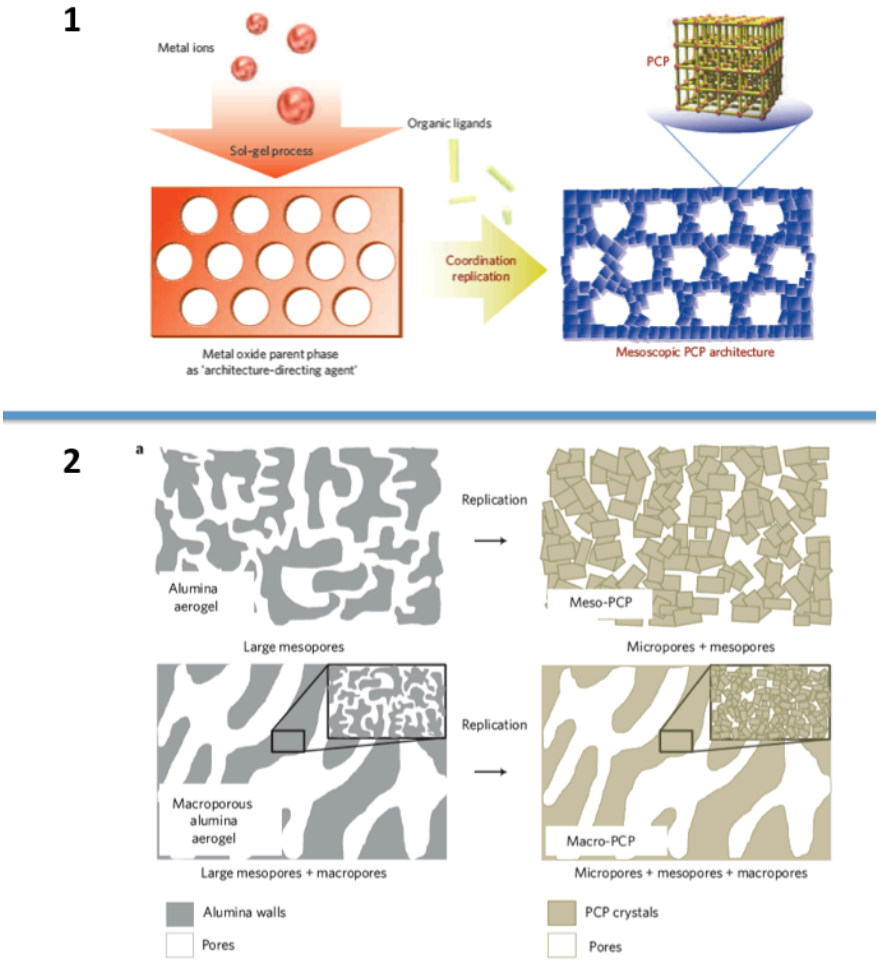


**Figure 1.24 Schematic illustration of (1) the coordination replication method based on the replacement of a metastable dense metal oxide phase (illustrated as a red honeycomb pattern) by more stable PCP crystals (blue honeycomb pattern) (2) the coordination replication from alumina aerogel and macroporous alumina aerogel parent structures to Meso-PCP and Macro-PCP analogous architectures, respectively. Adapted with permission from ref.** [130]

## 1.6 Aim of the project

The concept of the macroscopic structuring of MOFs has been explained within the previous chapter and some exemplar studies from existing work in this area of research have been introduced. Although there are already a number of studies on macroscopic MOF structures, many fundamental aspects of the mechanism as well as the interactions involved in the

organization of these materials are still not well understood, despite the significant potential for enhancing MOF applications through manipulation of higher level assembly.

Structural features of particular MOFs, such as the nature of the organic ligand and the metal that constitutes it and the morphology of the crystals, appear to promote different effects on the resulting macroscopic structures, as well as control over the particle size, interparticle mesoporosity and superstructure formation. The ability to control these effects is strongly dependent on the specific interactions between the MOF precursors and the desired templating agents.

In this work the focus is on directing the macroscopic structure and mesoporosity of MOF assemblies through soft templating strategies. Using a range of surfactants and amphiphilic block co-polymers we aim to investigate their effect on MOF crystal growth (size and shape) and assembly under a range of experimental conditions with a view to templating mesoporosity into MOF crystals and assemblies and the preparation of well-defined macroscopic MOF structures such as colloidosomes. Given the close need to match framework synthesis conditions with those of the template construct as outlined, this thesis will focus on prototypical MOFs such as ZIFs and HKUST-1 where a number of robust synthetic preparations under mild conditions have been reported. This should ensure that these frameworks could be prepared under conditions that are optimal for the template to increase chances of a successful (co)assembly process. Furthermore, having a number of reliable framework forming methods will allow the use of as diverse a range of templates as possible.

# Chapter 2: Methods and techniques

## 2.1 Instrumentation

### 2.1.1 X-ray Diffraction

X-rays are electromagnetic radiation with a wavelength range between 0.01 and 10 nm (*i.e.* it extends from ultraviolet light to gamma rays)[131-132] generated by hitting a cooled metal anode with a highly energetic, focused electron beam. X-rays with short-wavelength between 0.01 and 0.1 nm are utilized for diffraction as this range is comparable to the *d*-spacing in crystals. Therefore this type of radiation is of great application in the study of the structural arrangement of atoms, ions and molecules in a wide range of solid materials. In particular the ordered lattice of a crystal allows one to gain structural information by observing the symmetric diffraction patterns caused by constructive and destructive interference of X-rays scattered by the lattice planes (Figure 2.1).[133]

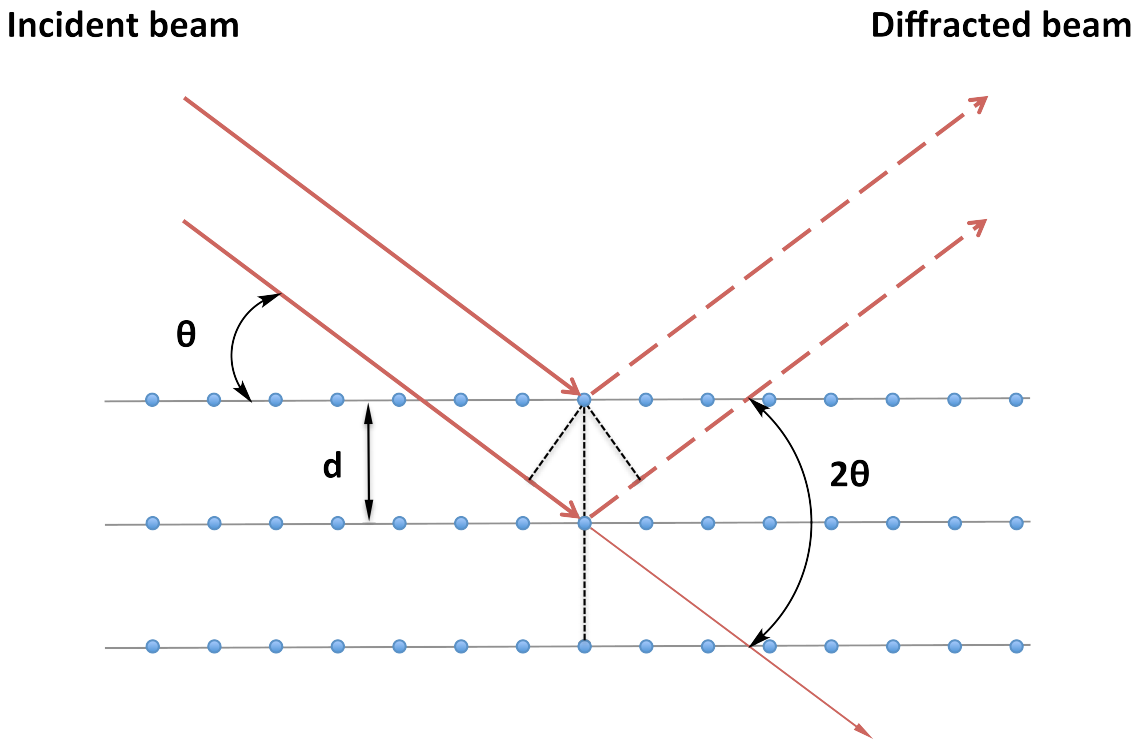


**Figure 2.1 Scheme illustrating the Bragg relation. Constructive interference is achieved when the path difference is a multiple integer of the X-ray wavelength.**

The path difference of two X-rays interacting with a crystal surface is defined as:

$$\Delta S = 2d_{hkl}sin\theta$$

where $\theta$ is known as Bragg angle and h, k, l are the Miller indices that are used to identify the lattice planes. Constructive interference of the scattered X-rays leads to the observation of diffraction peaks. According to Bragg's law, the diffracted beams show constructive interference if the path difference is a multiple integer of the applied wavelength:

$$n\lambda = 2dsin\theta$$

$n$: order of interference

$\lambda$: X-ray wavelength

$d$: lattice plane distance

$\theta$: angle of incidence

If $\theta$ is known, the distance *d* between the lattice planes can be readily deduced.

Monochromatic X-rays are employed for X-ray diffraction of single crystal and powder samples. The single crystal rotates in the beam, such that Bragg's law is fulfilled for each lattice plane at least once. Powder samples contain a large number of randomly oriented crystallites, so the resulting diffraction patterns are formed by a set of cones from all planes that satisfy the Bragg condition. Powder diffraction patterns allow the identification of crystalline phases by comparison with data bases.

### 2.1.2 Electron microscopy

Electron microscopy works on the same principle as optical microscopy, using a beam of accelerated electrons as the source of illumination. Because the wavelength of an electron is considerably smaller than visible light, the electron microscope has higher resolving power than a visible light microscope and can reveal the structure of smaller object. According to Abbe's law of limiting resolution

$$d = \frac{\lambda}{2NA}$$

$\lambda$ = wavelength of light illuminating the sample

$NA$ = numerical aperture

The maximum resolution of $d_{min}$ is $\lambda/2$, therefore the decrease of $\lambda$ leads to better resolution. In optical microscopy the resolution limit is $d_{min} \cong$ 200 nm while in electron microscopy it is ~ $10^5$ times smaller. Within this thesis two different microscopic techniques have been used, namely Scanning Electron Microscopy (SEM)[134] and Transmission Electron Microscopy (TEM).[135]

### 2.1.2.1 Scanning Electron Microscopy (SEM)

The schematic representation of a scanning electron microscope is shown in Figure 2.2. It is composed of two major parts: the microscope column and the electronic console. The microscope column consists of the electron gun (with the components cathode, Wehnelt cylinder, anode), one or two condenser lenses, two pairs of beam deflection coils (scan coils for *X*, *Y* deflection), the objective lens and some apertures. In the specimen chamber at the lower end of the microscope column are the specimen stage and the detectors for the different signals generated by the electron-specimen interaction. The microscope column and the specimen chamber are evacuated using a combination of pre-vacuum and high vacuum. The pressure in the specimen chamber is typically set to about $10^{-4}$ Pa, allowing the electron beam to travel from the cathode to the specimen with little interaction with the residual gas molecules.

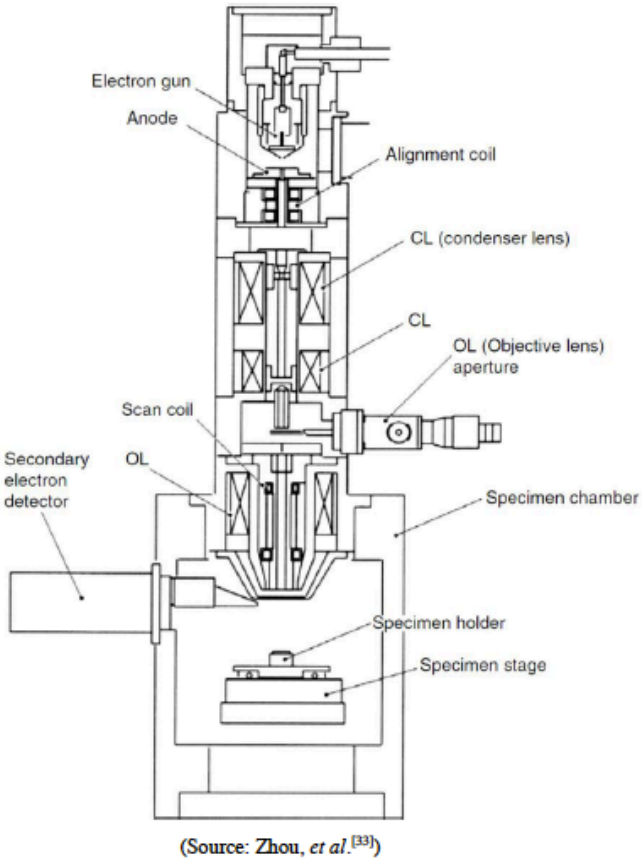


**Figure 2.2 Schematic representation of a scanning electron microscope. (Source: Zhou, *et al.*[136])**

There are several possible interactions between the electron beam and the sample as shown in Figure 2.3. However secondary electrons (SE) are the most commonly detected with SEM; they are generated from the collision between incoming electrons and loosely bound outer electrons.

They are low energy electrons, and when they are generated close to the surface of the sample they uncover valuable morphological and topological information of the sample.

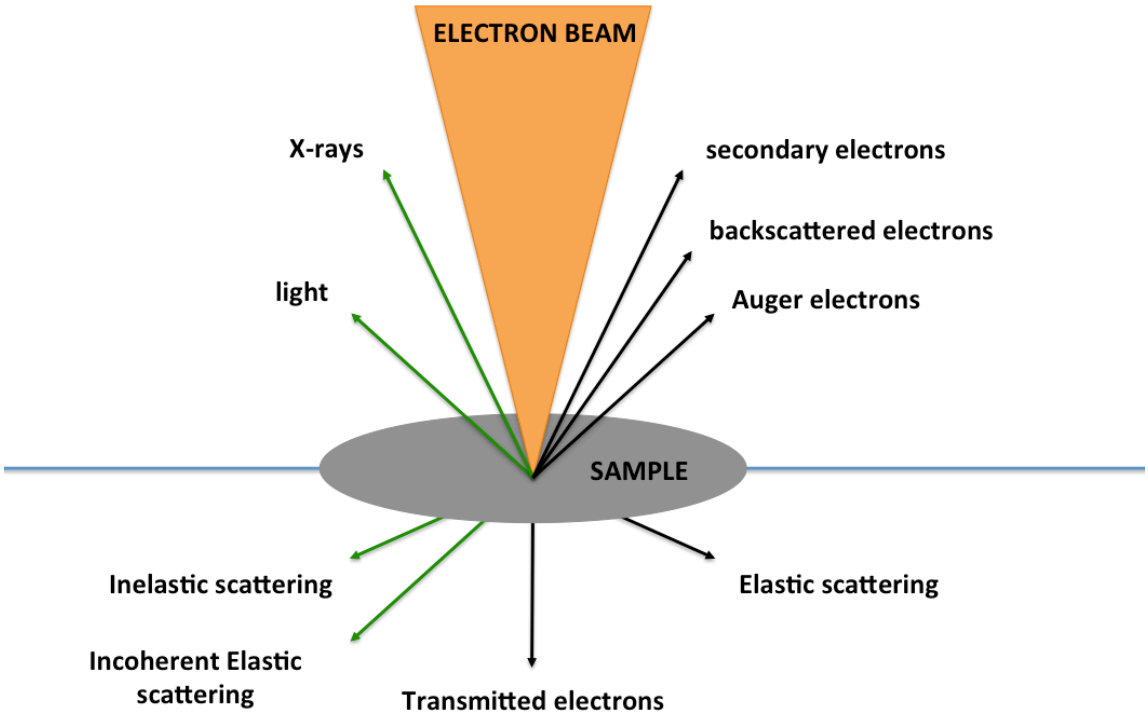


**Figure 2.3 Possible interactions between electron beam and sample.**

Another form of detection is from back-scattered electrons (BSE), which result from elastic scattering with the atomic nucleus and they can provide information about the composition of the scanned material, indeed their quantity is proportional to the atomic number of the elements present as well as on the acceleration voltage of the primary electron beam. Further collisions of primary electrons with core electrons from atoms in the sample result in excited atomic states. The re-occupation of the vacancy by an outer shell electron leads to emission of X-ray photons with characteristic wavelength distributions for different elements. Therefore, with the help of SEM we can also obtain information about the morphology and the elemental composition of a sample.

#### 2.1.2.2 Transmission Electron Microscopy (TEM)

Transmission electron microscopy uses a beam of highly energetic electrons, which are transmitted through an ultra-thin specimen that is in part transparent to electrons and in part scatters them out of the beam (Figure 2.3). An image is formed from the interaction of the electron transmitted through the specimen and collected onto an imaging device, such as a phosphorescent screen or a camera. In the region where electrons do not pass through the sample the image is dark. Where electrons are unscattered, the image is brighter, and there are a

range of contrasts in between depending on the way the electrons interact with and are scattered by the sample. The major disadvantage of the transmission electron microscope is the need for extremely thin sections of the specimens, typically about 100 nanometers.

### 2.1.3 Adsorption measurement

Gas adsorption measurements are widely used for determining the surface area and pore size distribution of a variety of different porous materials.[137] Adsorption is defined as the enrichment of one or more components in an interfacial layer, and physisorption occurs when a gas (the adsorptive) is brought into contact with the surface of a solid (the adsorbent) forming interactions between them, particularly van der Waals forces such as dipole-dipole, London forces or hydrogen bonding. Therefore physisorption is a completely reversible process, where the adsorptive is in equilibrium with the adsorbed gas molecules (adsorbate) dependent on the relative pressure $p/p^0$. Equilibrium isotherms are obtained by plotting the adsorbed volume as a function of $p/p^0$. Adsorption isotherms can be classified as one of six types according to the IUPAC[138] (Figure 2.4), which reflect the relationship between the porous structure and the sorption type.

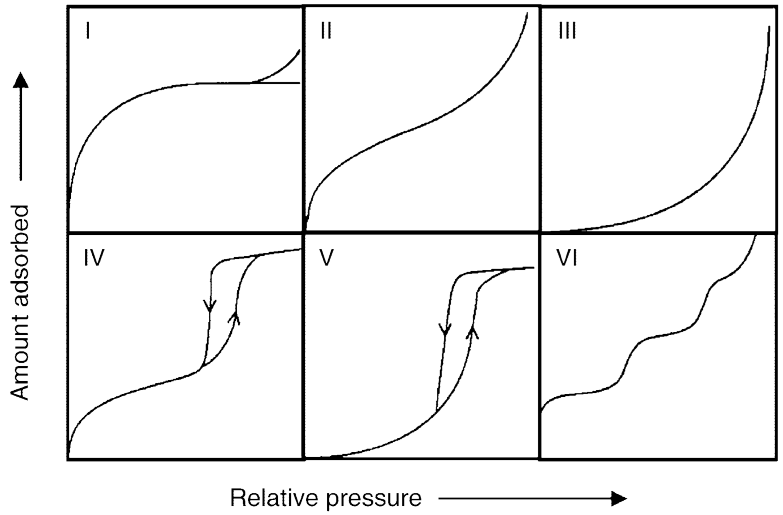


**Figure 2.4 IUPAC classification of adsorption isotherms.**

The reversible type I isotherms are typical for microporous solids having relatively small external surfaces, where the limiting uptake is governed by the accessible micropore volume rather than by the internal surface area. The reversible Type II isotherm is the normal form of isotherm obtained with a non-porous or macroporous adsorbent and it represents unrestricted monolayer-multilayer adsorption. The reversible Type III isotherm is characterised by heats of adsorption less than the adsorbate heat of liquification, where adsorption proceeds as the adsorbate interaction with an adsorbed layer is greater than the interaction with the adsorbent surface. Type IV

isotherms are characterized by hysteresis loops on desorption, which is associated with capillary condensation taking place in mesopores. The initial part of the Type IV isotherm is attributed to monolayer-multilayer adsorption of a non-porous form, analogous to the early part of Type II isotherms. The Type V isotherm is uncommon but is related to the Type III isotherm in that the adsorbent-adsorbate interaction is weak. The Type VI isotherm, in which the sharpness of the steps depends on the system and the temperature, represents stepwise multilayer adsorption on a uniform non-porous surface. The step-height now represents the monolayer capacity for each adsorbed layer.[137]

Hysteresis loops are principle characteristics of type IV and V isotherms, and their shape gives an indication of the nature of the mesoporosity, in particular if it arises from the textural porosity (intraparticle pores) or true mesopores (interparticle pores)[139] as shown in Figure 2.5.

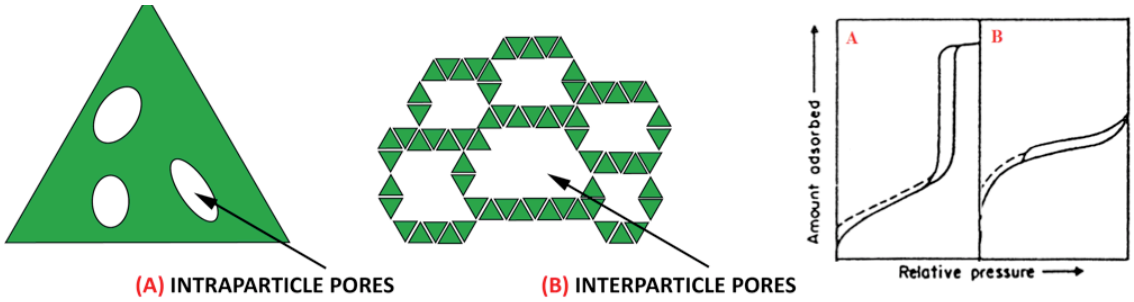


**Figure 2.5 Difference between intraparticle and interparticle pores.**

### 2.1.3.1 Brunauer, Emmett and Teller (BET) theory

For evaluation of the adsorption isotherms several different models exist. The Brunauer-Emmett-Teller (BET) theory is widely used for porous materials and is based on a number of simplifying assumptions in order to extend the Langmuir model[137] to multilayer adsorption.

- Adsorption of the first adsorbate layer can occur on a range of surface sites which have equal energy.
- The second layer of adsorption can only occur on the first layer of adsorbates, and the third can only occur on the second layer of adsorbate and so on. Therefore when the pressure equals the saturation pressure an infinite layer of adsorbate should be present.
- The rate of condensation and evaporation is equal at equilibrium for each layer.
- The first adsorbed layer will have an enthalpy of adsorption that is equal to the Langmiur case; however the following adsorbed layer will have equilibrium constants that are equal.

Therefore the BET equation is expressed as

$$\frac{p}{V(p-p^0)} = \frac{1}{V_m C} + \frac{(C-1)}{V_m C} \times \frac{p}{p^0}$$

$p$: pressure

$p^0$: the saturation pressure of the adsorptive

$p/p^0$: relative pressure

$V_m$: volume of gas required to from a monolayer

$V$: volume of gas adsorbed at pressure p

$C$: BET constant.

For low partial pressures ($p/p^0$< 0.3) the BET equation can be expressed in a linear form:

$$\frac{p/p^0}{n(p^0-p)} = \frac{1}{n_m C} + \frac{C-1}{n_m C} \times \frac{p}{p^0}$$

$n$: amount of adsorbate

$n_m$: monolayer capacity

$C$: BET constant.

From the obtained experimental data the monolayer capacity $n_m$ can be deduced and the surface area $A_S$ can be calculated according to:

$$A_S(BET) = n_m N_A a_m$$

$N_A$: Avogadro constant

$a_m$: cross-sectional area of the probe molecule.

In a strict sense, the BET method is not applicable for microporous solids, because the diameter of the micropores is too small to allow multilayer formation.[140] However, the BET theory is often used for microporous materials, such as MOFs, if the consistency criteria are satisfying:[141]

- Only a range where $n(p^0-p)$ increases monotonically with $p/p^0$ should be selected.
- The value of C resulting from the linear regression should be positive.
- The monolayer loading $n_m$ should correspond to a relative pressure $p/p^0$ falling within the selected linear region.

- The relative pressure corresponding to the monolayer loading calculated from BET theory $1/\sqrt{C}+1$ should be equal to the pressure determined in criterion 3. (For this criterion, Rouquerol *et al.*[142] suggested a tolerance of 20%).

#### 2.1.3.2 Barret-Joyner-Halenda (BJH) procedure and Kelvin equation

The BJH procedure is a computational method used to calculate the pore size diameters (PSD) over the mesopore and macropore range.

The basis for evaluation of PSD from nitrogen adsorption is the Kelvin equation which relates the nitrogen pressure to the size of pores in which capillary condensation/evaporation of the adsorbate takes place.

$$ln\left(\frac{p}{p^0}\right) = \frac{2\gamma V}{r_k RT} cos\theta$$

$\gamma$: surface tension of the adsorbate

$r_k$: kelvin radius

$V$: molar volume

The BJH model takes into account formation of liquid-like adsorbed layer of adsorbate on the pore walls which precedes capillary condensation or follows capillary evaporation (Figure 2.6).[143]

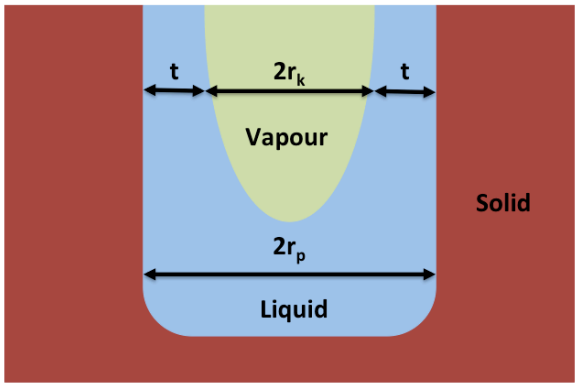


**Figure 2.6 Illustration of the condensation process considering the Kelvin equation ($r_k$= kelvin radius, $r_p$= pore radius, t= thickness).**

When this occurs there is already an adsorbed layer so $r_p$ no longer equal to pore size, thus need to use a correction ($t$) to account for this. Therefore the pore radius ($r_p$) can be obtained from the sum between the adsorbed layer ($t$) and the kelvin radius ($r_k$).

$$r_p = r_k + t$$

### 2.1.4 Thermogravimetric analysis (TGA)

Thermogravimetric analysis (TGA) is a technique that monitors the changes in weight that occur when a sample is heated. The measurement is normally carried out in a flowing atmosphere of air or $N_2$, and the weight is recorded as a function of increasing temperature or time. The sample is heated at constant or variable rates and the evolving weight changes are determined with the help of a thermobalance. Therefore TGA determines the thermal stability and the fraction of volatile components (solvent and organic ligands) of the sample.

TGA data of MOFs usually display two steps of weight loss; the first takes place between 30 and ~ 300 °C depending on the boiling point of the guest solvent(s) included within the MOF. The second step is between ~ 250 and 500 °C and corresponds to the removal of the organic components, which leads to the decomposition of the framework.

## 2.2 Methods and parameters used

In this study powder X-ray diffraction patterns were collected on a Bruker D2 phaser diffractometer typically in the angular range $2\theta$ = 5- 60° employing a Ni Kβ filter (detector side) producing Cu (Kα1/Kα2) radiation.

SEM measurements were made on a JEOL JSM 6500 thermal field emission scanning electron microscope at an accelerating voltage of 10 kV. Typically samples for SEM measurements were prepared by firstly placing a drop of sample suspension in absolute ethanol on a silica wafer attached to an aluminium substrate with a carbon paste, and then sputter-coated with a thin layer of conductive gold to improve electrical conductivity.

TEM images were obtained on a FEI Tecnai T12 transmission electron microscope operating at a bias voltage of 80 kV. Sample preparation involved deposition and evaporation of a 10µL droplet onto a grid (Formvar- and carboncoated 400 mesh copper grid).

$^1$H-NMR spectra were acquired using a Bruker DPX400 FT-NMR spectrometer. Fourier Transform Infrared (FTIR) spectra were collected on a Magna IR-560 Nicolet FTIR spectrometer equipped with a Mercure Cadmium Tellure detector. All experiments were run on a horizontal attenuated total reflectance (ATR) crystal (ZnSe) where powders were pressed. Content of metals was analysed using a Varian Vista MPX.

$N_2$ adsorption/desorption isotherm was measured at 77 K using a Micromeritics 3-Flex Surface Characterization Analyzer after the sample was first degassed at 100°C overnight. Surface areas were determined by the BET method in an appropriate pressure range, and total pore volume was

determined using the adsorption branch of $N_2$ isotherm curve at the $p/p^0$= 0.99 single point. Pore size distribution was determined using the adsorption branch of $N_2$ isotherms. Micropore size distribution analysis was carried out using the Horvath-Kawazoe method. Mesopore size distribution was calculated using the Barrett-Joyner-Halenda (BJH) method.

TGA was performed using a TG 209 F1 Libra (Netzsch) and typically the sample was heated from room temperature to 900°C at a rate of 10°C $min^{-1}$ under an air atmosphere.

# Chapter 3: HKUST-1

## 3.1 Introduction

Mesostructured MOFs would enhance the properties of the materials, as outlined in the general introduction. For example introduction of mesoporosity into MOFs would lead to significant improvements in mass transport and diffusion, and consequently widen the range of applications/substrates (Figure 3.1).[144] Hereafter a number of key examples in this area are presented.

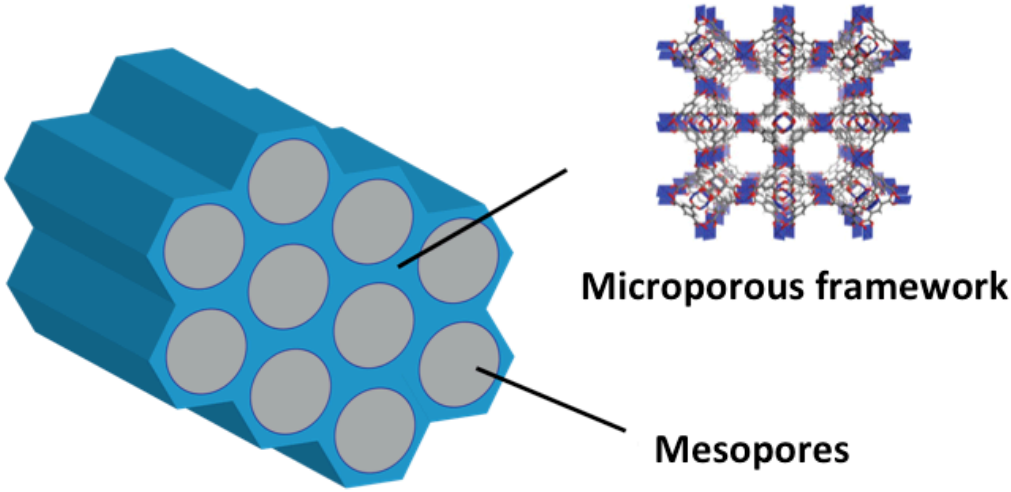


**Figure 3.1 Illustration of a hierarchical micro- and mesoporous HKUST-1 structure, where the micropores ensure the selectivity of the framework and the mesopores the mass transport.**

Qiu *et al.* used a supramolecular templating strategy for designing and synthesizing hierarchically micro- and mesoporous HKUST-1 with adjustable pore size, pore volume and surface area for the first time (Figure 3.2).[145] The cationic surfactant CTAB was used as the SDA to introduce mesoporority into the framework: the self-assembly of the framework precursors $Cu^{2+}$ and $BTC^{3-}$ directed by the surfactant micelles induced the formation of a disordered worm-like mesoporous structure with tunable diameters from 3.8 to 31.0 nm depending on the synthetic conditions. The solvothermal reaction was carried out in a mixture EtOH/$H_2O$ at 120° C for 12 hours varying the molar ratio of CTAB/$Cu^{2+}$ from 0.15 to 0.60; the mesopore diameters of the resulting HKUST-1 increased from 3.8 to 5.6 nm. Further when 1,3,5-trimethylbenzene was added to the synthesis as an auxiliary SDA to swell the CTAB micelles, the mesopore diameter could be increased up to 31.0 nm. According also to the assembly of MCM-41 silica, where the mesopore size could be tuned by incorporating TMB in the structure-directing surfactant CTAB.[9] In the proposed mechanism the

surfactant micelles act as SDAs for the assembly of the mesostructured MOFs. Firstly, the deprotonated organic ligand $BTC^{3-}$ may enter the solvent region to balance the cationic charge of the micelle surface. Electrostatic interactions between micelles of the cationic surfactant and the negatively charged $BTC^{3-}$ ions led to positioning of the framework-building blocks. Secondly, nucleation and crystal-growth processes lead to nanoparticles of the microporous MOF, which are self-assembled from the framework-building blocks (that is, $Cu^{2+}$ ions and the $BTC^{3-}$ ligand) in the continuous solvent region between micelles. After removal of the surfactant molecules from the solids by washing in EtOH, the hierarchically micro- and mesoporous MOFs were obtained.

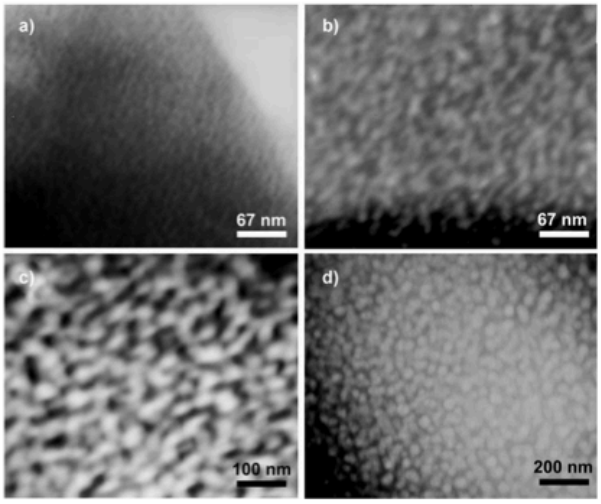


**Figure 3.2 TEM images of the mesostructured MOFs : a) CTAB/$Cu^{2+}$= 0.60, b) CTAB/$Cu^{2+}$= 0.60 and TMB/CTAB= 0.50, c) CTAB/$Cu^{2+}$= 0.30 and TMB/CTAB= 0.10, and d) CTAB/$Cu^{2+}$= 0.30 and TMB/CTAB= 0.50. Reprinted with permission from ref.[145]**

Huo *et al.* proposed a cooperative self-assembly strategy to obtain a highly ordered mesostructured MOF material with amorphous pore walls, namely Cu-(5-OH-BDC)-$C_{16}$ (Figure 3.3).[146] They emphasized the importance of the strength of the interaction between the MOF precursors and surfactant mesophase. Therefore they choose 5-hydroxy isophthalic acid (5-OH-BDC) as framework linker because it contained both weak and strong coordination sites for the metallic ions: the weak site (-OH) was liable to interact with the surfactant mesophase, while the strong carboxylate site combined with the metallic ions for framework assembly. The solvothermal synthesis was carried out with molar ratio CTAC/$Cu^{2+}$= 0.25 at 110° for 24 hours successfully formed Cu-(5-OH-BDC)-$C_{16}$ with an interlayer spacing of 41 A˚ determined from the PXRD data. Furthermore when surfactants with different chain lengths were employed in the synthesis, similar structures with a corresponding increase of unit cell size with increase of surfactant chain length were obtained.

In the proposed mechanism $Cu^{2+}$ and 5-OH-BDC form a chain structure, which also connected with the surfactants through the electrostatic interactions or hydrogen bonds to assemble the *P*6mm

mesostructured framework. The $NO_3^-$ ions and water molecule could play an important role in many aspects, such as assisting the process of self-assembly and/or connecting the remaining bonding sites of the framework.

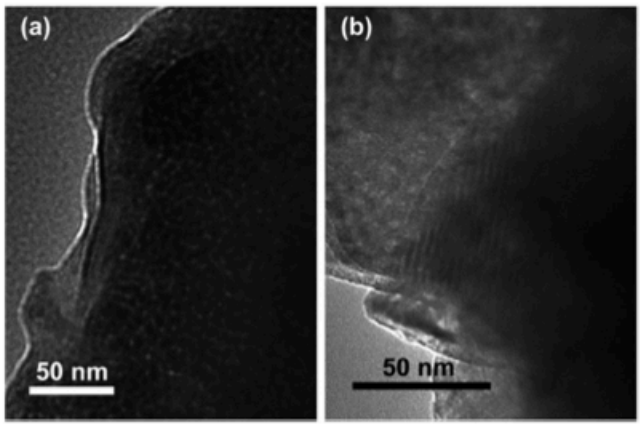


**Figure 3.3 Representative TEM images of Cu-(5-OH-BDC)-C16 frameworks (a) parallel to the channels, (b) perpendicular to the channels. Reprinted with permission from ref.[146]**

More recently a cooperative template system between the surfactant (CTAB) and the chelating agent citric acid (CA) was used to direct the synthesis of mesoporous HKUST-1 (Figure 3.4).[147] Here the CA was employed to establish an interaction between metal ions and surfactant molecules, i.e. between MOF precursors and micelles, through Coulombic attraction and coordination. The nucleation and crystal growth stages then proceed in the continuous solvent phase between micelles, leading to the formation of the mesoHKUST-1. Notably the structure-directing role of the surfactant was assisted by the chelating agent, which acted as a co-template. Indeed no mesoporosity is detected when the surfactant or the chelating agent are used individually. The synthesis was carried out in DMF at 75 °C for 24 hours varying the molar ratio $Cu^{2+}$: BTC: CTAB: CA = 1: 0.56: 0.54: 0-0.52 or 1: 0.56: 0-1.6: 0.26 leading to tunable amounts of mesopores depending on the ratio between the surfactant and chelating agent. In the proposed mechanism CA simultaneously interacts with the metal and surfactant, and a bridge-like chemical interaction between MOF precursors and micelles was built. This interaction led to the positioning of the building blocks of MOFs. The cooperative template thus played a directing role, making nucleation and crystal growth proceed in the continuous solvent phase between micelles. A mesostructured intermediate with the pores occupied by micelles had thus been fabricated. After the removal of templates, porous materials with hierarchical pores were produced, in which mesopore walls consisted of microporous frameworks. Further the use of CTAB as a single template did not form the mesoporous structure because too weak interactions between micelles and MOF precursors were formed, while CA did not form mesostructures when used alone because it was not amphiphilic thus did not form the required micellar assemblies.

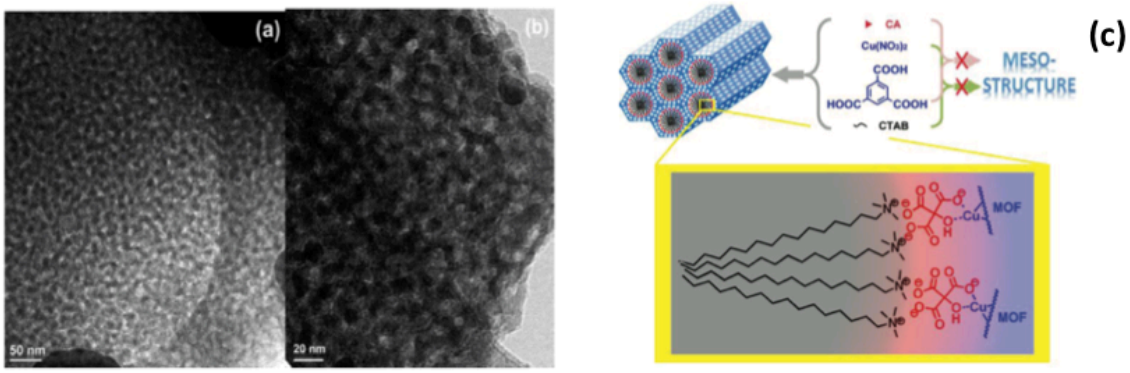


**Figure 3.4 (a,b) TEM images of the sample mesoporous MOF (molar ratio $Cu^{2+}$: BTC: CTAB: CA = 1: 0.56: 0.54: 0.52) at two different levels of magnification, (c) representation of the template direct synthesis mechanism. Adapted with permission from ref.[147]**

Finally the system poly(ethylene glycol) (PEG) and P104 ($EO_{27}PO_{61}EO_{27}$) was found to induce the formation of mesoporosity in HKUST-1 nanocrystals (Figure 3.5).[144] Here PEG worked as a reaction medium to induce the crystallization of nanosized HKUST-1 at room temperature and allowed controlling the crystallization rate of the framework, while the triblock copolymer P104 micelles templated the mesopores (pore size of 3-4 nm). Simultaneously, PEG molecules could be immobilized in the MOF pores through hydrogen bonding interactions with the organic linker $H_3BTC$, acting as a strut to prevent mesopore collapse during synthesis. Finally the mesoporous MOF nanocrystals stabilized by PEG were synthesized after removing the surfactant and solvent. In a typical experiment, $Cu(OAc)_2 \cdot H_2O$ and $H_3BTC$ were added into a P104/PEG solution. PEG-300, PEG-400 and PEG-600 were tested in the synthesis: PEG with the lower molecular weight yielded smaller MOF crystals but the mesopore size of all the three MOF detected was around 3.7 nm. Furthermore the catalytic performance of the as-synthesized HKUST-1 nanocrystals, for the oxidation of benzyl alcohol to benzaldehyde, was tested under mild conditions, using 2,2,6,6-tetramethyl-piperidine-1-oxyl (TEMPO) as a co-catalyst. The as-synthesized HKUST-1 showed an activity significantly higher than the commercial HKUST-1 (nearly 100% and 10% after 3 hours, respectively) and the catalyst could be easily recovered and reused. The increased catalytic activity was attributed to both the reduced particle size and the mesoporous HKUST-1, which are both favorable for the increased concentration of catalytically active sites and enhanced diffusion of substrates and products.

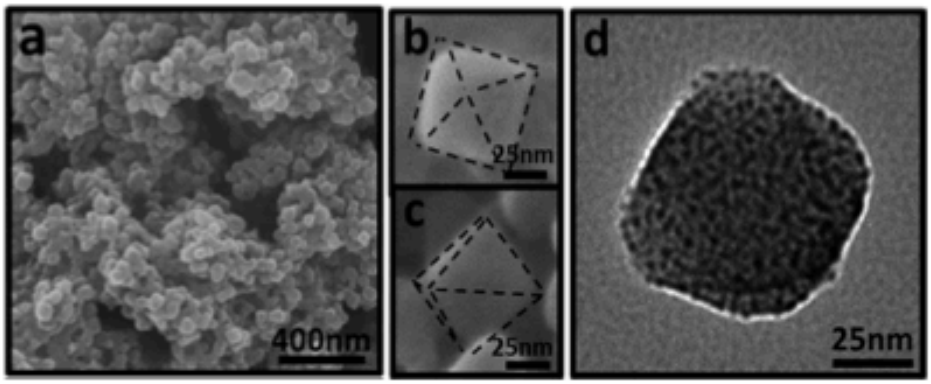


**Figure 3.5 SEM (a–c) and TEM (d) images of HKUST-1 nanocrystals synthesized in PEG-300. Reprinted with permission from ref.[144]**

The previously mentioned works underlined that it was not easy to form mesostructured frameworks, probably because the bridging ligands and metallic salt prefer to form crystalline MOF. The examples in which mesoporosity was induced were characterized by a careful design of the reaction and compositional parameters. Especially the templating properties of the surfactant and the strength of interactions between the surfactant and MOF precursors were crucial requirements for the success of the process.

This chapter was an attempt to find a suitable system for the control over the macroscopic structure of HKUST-1. Therefore the effects of compositional parameters and surfactants were investigated. In particular it involved a screening over the influence of pH, reaction solvent and the surfactants on the synthesis of HKUST-1. The surfactants used in this study were Pluronic-P123 ($HO(CH_2CH_2O)_{20}(CH_2CH(CH_3)O)_{70}(CH_2CH_2O)_{20}H$, $EO_{20}PO_{70}EO_{20}$, EO= ethylene oxide, PO= propylene oxide) and the two carboxylic acid based amphiphiles octanoic acid and dodecanoic acid.

## 3.2 Results and discussion

### 3.2.1 The effect of pH on HKUST-1

HKUST-1 was synthesized according to the literature:[52] an aqueous solution of copper nitrate (0.35g in 5.5 mL of $dH_2O$) was mixed with a solution of $H_3BTC$ (0.21 g in 5.5 mL of ethanol) and stirred for 30 minutes at room temperature, followed by a solvothermal reaction for 15 hours at 110 °C. It was reported that pH not just highly influenced the nucleation and crystallization of MOFs,[148] but also the stability and interactions between MOF precursors and surfactant mesophases, therefore the role of pH in the formation of HKUST-1 was investigated as part of this study.

Considering the assembly of HKUST-1 from $Cu^{2+}$ and BTC, higher pH would be expected to lead to faster deprotonation of the linker (higher availability for coordination with the metal ion), thus accelerating the nucleation rate and reducing overall crystal size. On the other hand, lower pH would slow down the deprotonation of the linker (lower availability) and nucleation rate promoting crystal growth leading to bigger crystals overall (Figure 3.6).[113]

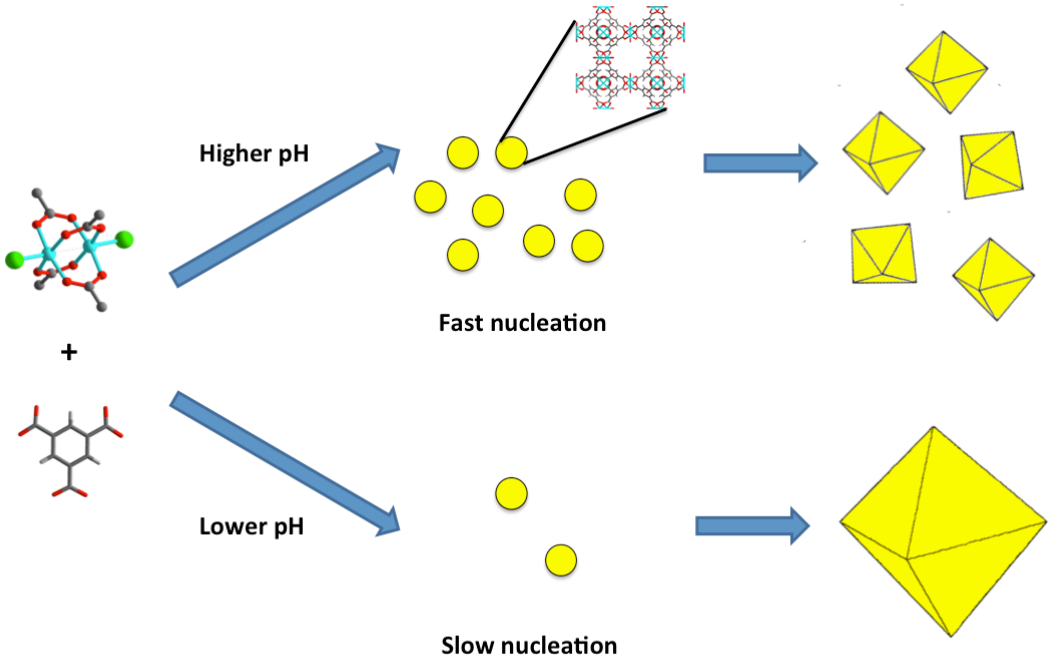


**Figure 3.6 The acid-base environment of the reaction medium governs the deprotonation of the organic linker, which influence its availability for coordination with the metal ion and therefore nucleation rate, the crystal size and crystal anisotropy: higher pH leads to fast nucleation and the formation of smaller crystals, while lower pH to slow nucleation and bigger crystals.**

Reaction studies of HKUST-1 showed that the nucleation process started at room temperature, indeed clouding was observed as soon as the two precursor solutions were mixed together.[149-150] Therefore in this study the pH was changed while the reaction was at room temperature. This implied to change the pH of the copper solution or when two precursor solutions are mixed together (synthesis solution). Changing the pH of the copper solution the speciation of the $Cu^{2+}$ was altered which may tune availability for binding, while changing the pH of the synthesis solution both the speciation of the $Cu^{2+}$ and $H_3BTC$ were affected.

At first the pH of the unadjusted synthesis was measured at the different steps: the copper solution had a pH of 3.5 units, then after mixing with the ligand solution the pH of the synthesis solution decreased to 1.5, due to the deprotonation of the linker during the framework formation.[113] Finally after the solvothermal synthesis the pH of the supernatant was 2.9 units.

The pH of the copper solution and synthesis solution were varied by addition of HCl (1 M) or NaOH (1 M). In the experiments the pH of the aqueous copper solution was varied from the unadjusted value of 3.5 to more acidic or basic values, respectively pH 1.8 and 4. Therefore leading to an overall pH on the synthesis solution of 1 and 3.4 respectively. The decrease of pH of the synthesis step accorded with the deprotonation of the linker for the framework formation. Furthermore the pH of the synthesis solution was varied from the unadjusted value 1.5 to more acidic or basic values, respectively pH 0.5 and 2.5. PXRD patterns and SEM images of the experiments were reported in Figure 3.7 and Figure 3.8.

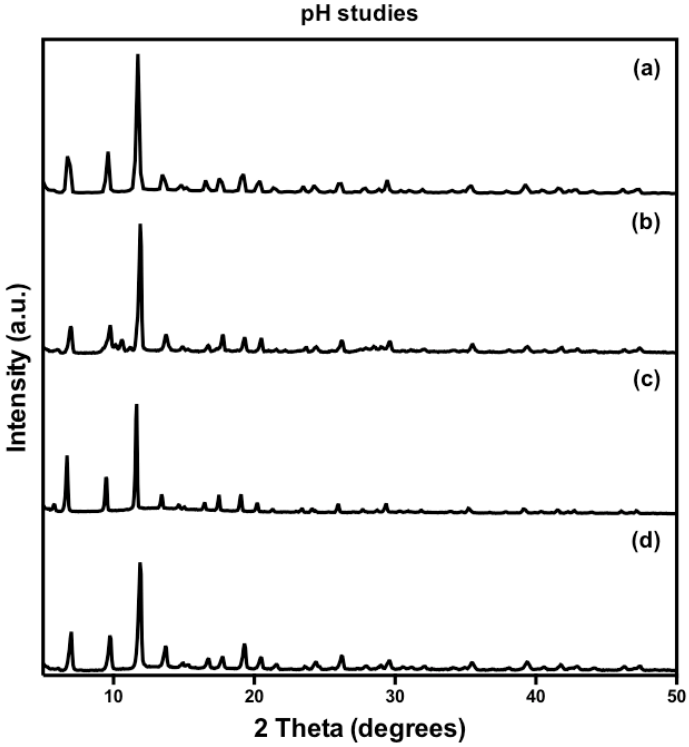


**Figure 3.7 PXRD patterns of HKUST-1 from (a) unadjusted synthesis (pH copper solution= 3.5 and synthesis solution= 1.6), variation of the pH of the copper solution to (b) more acidic value (pH= 1.8) or (c) more basic value (pH= 4) and (d) variation of the pH of the synthesis solution to more basic value (pH=2.5).**

As shown from the PXRD patterns the reactions lead to the formation of HKUST-1, except in the case of reducing the pH of the synthesis solution to pH=0.5 where no precipitate was detected; probably at very highly acidic conditions no deprotonation of the $H_3$BTC occurs or copper chloride complexes are formed and consequently no HKUST-1 was formed. Further in the reaction carried out decreasing the pH of the copper solution, Figure 3.7 b, an extra peak at θ= 10° was detected, which might be related to another phases of the copper(II)/$H_{3-n}$BTC system (n=1-3), but its amount was too low for a certain identification. Therefore decreasing the pH of the solution to more acidic conditions appeared less suitable for the formation of HKUST-1.

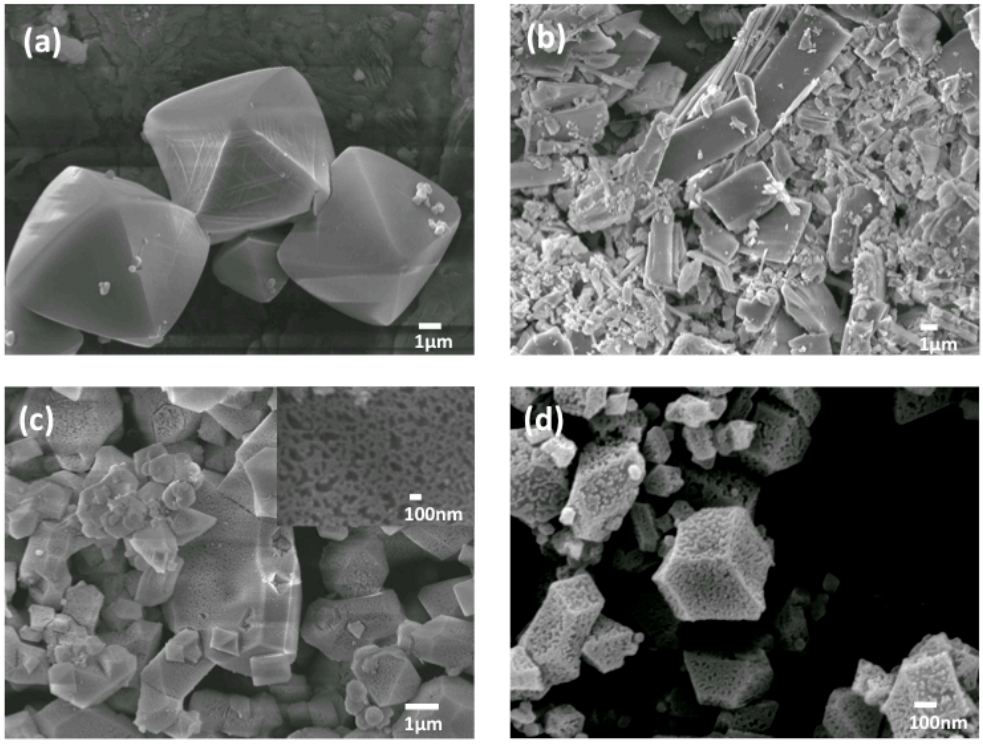


**Figure 3.8 SEM images of HKUST-1 from (a) unadjusted synthesis (pH copper solution= 3.5 and synthesis solution= 1.6), variation of the pH of the copper solution to (b) more acidic value (pH= 1.8) or (c) more basic value (pH= 4) with zoom-in of the surface features and (d) variation of the pH of the synthesis solution to more basic value (pH=2.5).**

SEM images showed that without any pH adjustment HKUST-1 formed the characteristic micron-size octahedral crystals consistent with previous studies[52] (Figure 3.8 a), which display surface features consistent with screw dislocations as reported by Attfield and co-workers.[151] Decreasing the pH of the copper solution led to crystals of poorly defined morphology and variable size (Figure 3.8 b). While increasing the pH of the copper solution led to crystals with less well-defined morphology and to the appearance of features on the surface of the crystals (Figure 3.8 c). The features were similar to those obtained on HKUST-1 crystals by the effect of guanidinium surfactants.[152] In the mentioned literature the etching was caused by the interaction between the atmospheric moisture and the crystal surface defects, which were due to the guanidinium species during framework formation, indeed the etching appears after 30 days of exposure to laboratory atmosphere. On the other hand in the experiment here reported the surface features appear in the crystals immediately following the synthesis, which indicated they depended on the pH increment.

When the pH of the synthesis solution was increased from 1.5 to 2.5 units, the crystals appeared to be more uniform in shape and size. The size was reduced from a few microns in the unadjusted synthesis to hundreds of nanometers. According to the previous experiments, increasing the pH of the synthesis solution formed features on the surface of the particles (Figure 3.8 d). As

mentioned before the nucleation process started in the synthesis solution,[149-150] which might be the reason of the higher control over the particles size and morphology reached.

These previous experiments showed the effect of pH variation on HKUST-1. In general the increase of the pH led to better results in terms of forming a pure phase of HKUST-1 (Figure 3.7 c, d). Instead decreasing the pH PXRD pattern showed the presence of an extra peak (Figure 3.7) or completely prevented the framework formation. Furthermore increasing the pH led to the formation of features on the crystal surface. Finally comparing the two experiments performed increasing the pH, the step in which the pH was change had an effect. Changing the pH of the synthesis solution, rather than the copper solution, led to more uniform crystals in shape and size.

### 3.2.2 The effect of P123 on HKUST-1

The system was further investigated adding the triblock copolymer Pluronic-P123 ($EO_{20}PO_{70}EO_{20}$) as a starting point to introduce mesoporosity into the framework. P123 was selected as it was previously successfully employed for the preparation of the large-pore silica SBA-15 in acidic media,[153] where the hexagonal mesophase forms by the surfactant acts as template for the mesoporous structure formation. As demonstrated above these conditions are also compatible with HKUST-1 assembly. As mentioned the pH changes would influence the availability and assembly of the surfactant,[154] protonating or not the EO groups, and thereafter the interactions between the micelle and the MOF precursors. The reaction was carried out by mixing an aqueous solution of copper nitrate (0.35 g, 1.5 mmol in 5.5 mL of $dH_2O$) with a solution of $H_3BTC$ (0.21g, 1 mmol in 5.5 mL of ethanol) and an aqueous solution of P123 (0.7 or 0.07g in 2 mL of $dH_2O$, ratio Cu:P123=1:$10^{-1}$ or 1:$10^{-2}$) and stirring for 30 minutes at room temperature, followed by a solvothermal reaction for 15 hours at 110 °C. In line with the previous experiments the pH of the copper solution or the synthesis solution were kept unadjusted or varied. In the unadjusted synthesis the pH of the copper solution was 3.5 units, which decreased to 1.5 units in the synthesis solution. Thereafter the pH of the copper solution was varied at values 1.8 or 4 units (3.2.2.1) and the pH of the synthesis solution was varied at value 2.5 units (3.2.2.2).

#### 3.2.2.1 The effect of P123 changing the pH of the copper solution

In this section the effect of variation of pH in the copper solution and/or the presence of the surfactant P123 were investigated. PXRD spectra and SEM images of the HKUST-1 samples were presented in Figure 3.9 and Figure 3.10.

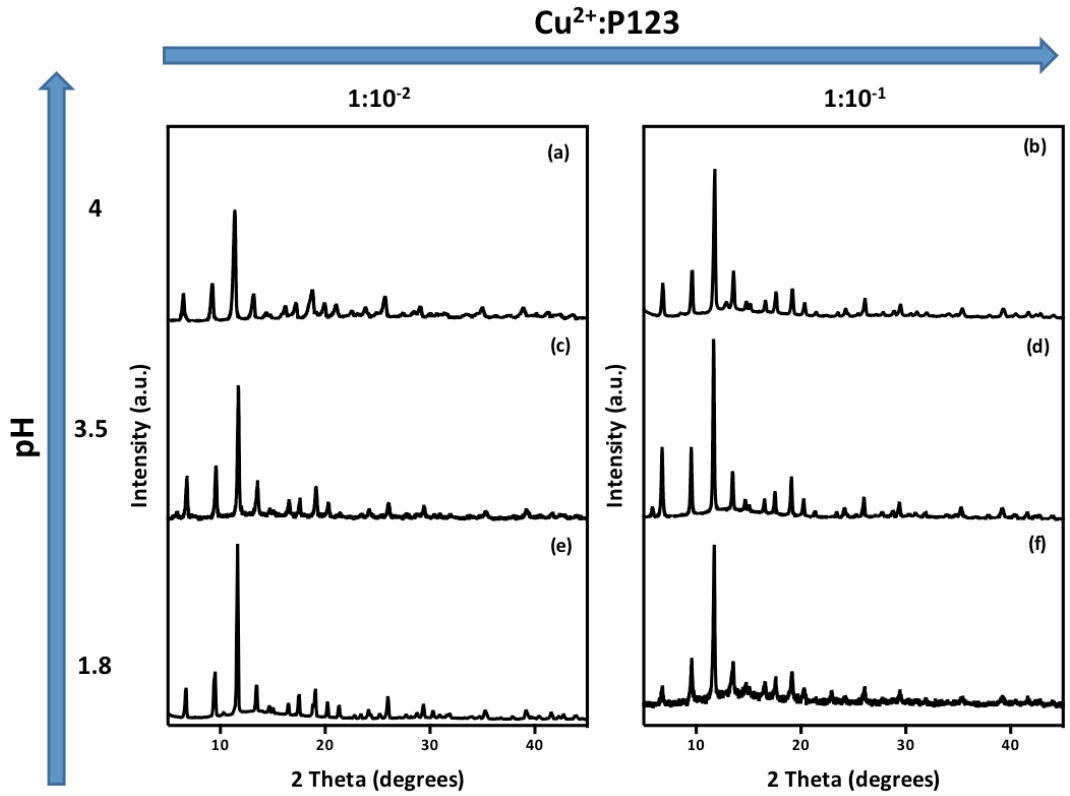


**Figure 3.9 PXRD patterns of HKUST-1 experiments performed in the presence of the surfactant Pluronic-P123 varying the pH of the copper solution.**

PXRD patterns of all the experiments performed varying the pH of the copper solution led to the formation of HKUST-1 (Figure 3.9). In the pH studies (3.2.1) the starting pH value of the copper solution influenced the pH of the synthesis solution. Therefore starting from pH 3.5, 1.8 and 4 units of the copper solution led to pH 1.5, 1 and 3.4 units respectively for the synthesis solution. On the other hand when P123 was added to the synthesis, starting from pH 3.5, 1.8 and 4 of the copper solution led to pH 1.5 in all the cases, indicating that P123 potentially acted as a buffer in stabilizing the pH, arising from an abundance of EO groups.

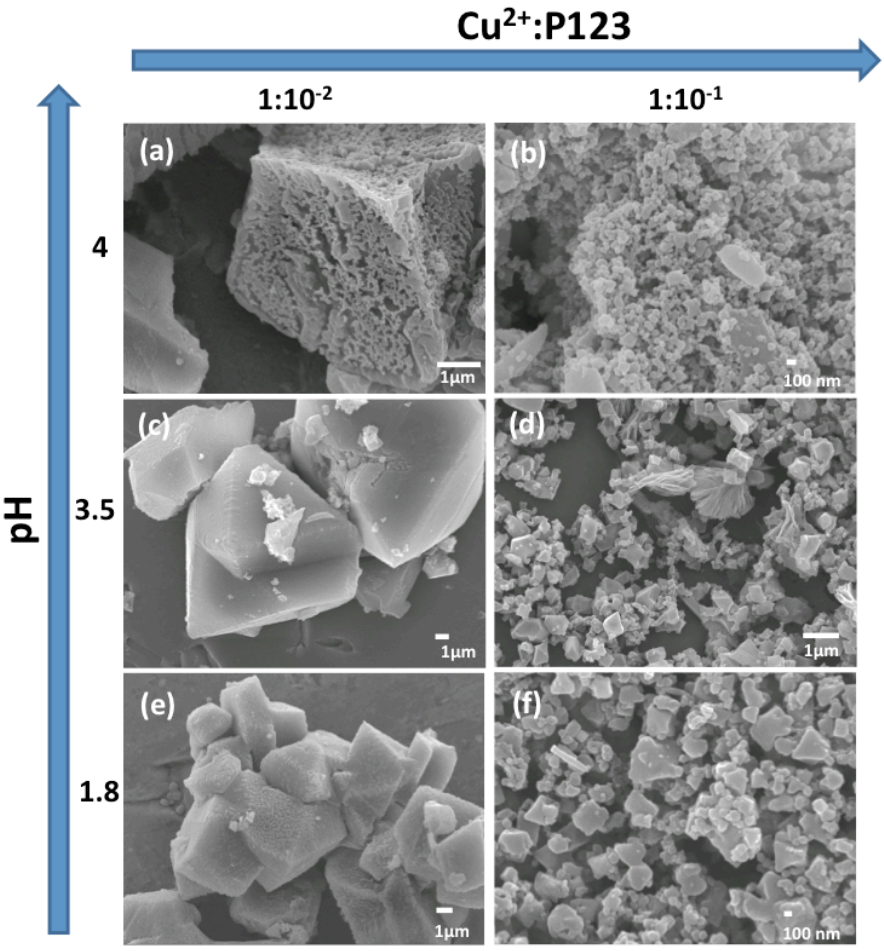


**Figure 3.10 SEM images of HKUST-1 experiments performed in the presence of the surfactant Pluronic-P123 varying the pH of the copper solution (a) pH=4, ratio Cu:P123=1:10$^{-2}$ (b) pH=4, ratio Cu:P123=1:10$^{-1}$ (c) pH=3.5 (unadjusted), ratio Cu:P123=1:10$^{-2}$ (d) pH=3.5 (unadjusted), ratio Cu:P123=1:10$^{-1}$ (e) pH=1.8, ratio Cu:P123=1:10$^{-2}$ (f) pH=1.8, ratio Cu:P123=1:10$^{-1}$.**

SEM images of all of the crystalline products are shown in Figure 3.10. In general at a ratio of $Cu^{2+}$:P123=1:10$^{-2}$ (Figure 3.10 a, c, e) the size of the crystals was comparable to the crystals of the reference synthesis presented in Figure 3.8 a. The experiment performed after increasing the pH to 4 units still presents features on the surface, which are likely related to the pH effect. On the other hand when the ratio of $Cu^{2+}$:P123 was increased to 1:10$^{-1}$ a decrease in the particle size into the nanorange was detected at every pH value tested. Therefore increasing the ratio metal to surfactant higher level of control on the macroscopic structure occurred, in this case on the particle size. This effect was reported also in the work of Huang *et al.*, where the control over the intraparticle mesoporosity of MIL-101 could be reached just at molar ratio $Cr^{3+}$: CTAB in the range 3.35-6 and not below.[155]

The porosity of the all the experiments performed with P123 was investigated by nitrogen sorption analysis (Figure 3.11) and the BET surface areas were reported in Table 3.1.

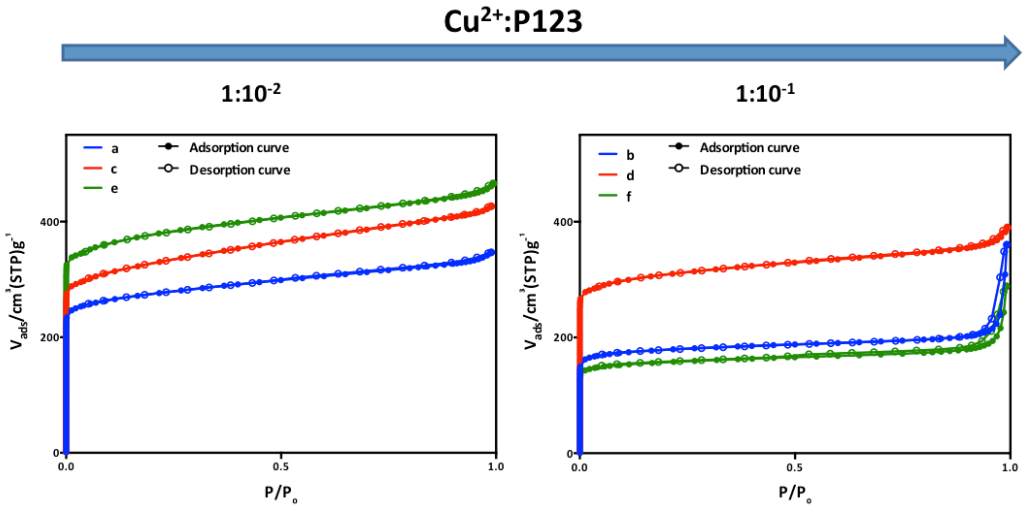


**Figure 3.11 Nitrogen sorption isotherms of the experiments performed in the presence of the surfactant Pluronic-P123 varying the pH of the copper solution measured at 77 K: (a) pH=4, ratio Cu:P123=1:$10^{-2}$ (b) pH=4, ratio Cu:P123=1:$10^{-1}$ (c) pH=3.5 (unadjusted), ratio Cu:P123=1:$10^{-2}$ (d) pH=3.5 (unadjusted), ratio Cu:P123=1:$10^{-1}$ (e) pH=1.8, ratio Cu:P123=1:$10^{-2}$ (f) pH=1.8, ratio Cu:P123=1:$10^{-1}$. Experiments performed at the same pH are reported with the same colour.**

| SAMPLE | BET surface area ($m^2/g$) |
|---|---|
| a | 1064 ± 0.3 |
| b | 703 ± 0.5 |
| c | 1242 ± 0.6 |
| d | 1197 ± 0.3 |
| e | 1450 ± 0.4 |
| f | 619 ± 0.5 |

**Table 3.1 BET surface area values of the HKUST-1 samples performed in presence of the surfactant Pluronic-P123 varying the pH of the copper solution: (a) pH=4, ratio Cu:P123=1:$10^{-2}$ (b) pH=4, ratio Cu:P123=1:$10^{-1}$ (c) pH=3.5 (unadjusted), ratio Cu:P123=1:$10^{-2}$ (d) pH=3.5 (unadjusted), ratio Cu:P123=1:$10^{-1}$ (e) pH=1.8, ratio Cu:P123=1:$10^{-2}$ (f) pH=1.8, ratio Cu:P123=1:$10^{-1}$.**

The surface area of the samples varied from 619 $m^2/g$ in sample f to 1450 $m^2/g$ in sample e, which was close to the value reported for the commercial HKUST-1 (1500 $m^2/g$). The isotherms of the experiments performed at ratio $Cu^{2+}$:P123=1:$10^{-2}$ displayed a type I behaviour, with a large uptake at very low pressure related to the presence of micropores typical of HKUST-1, with a BET surface area of 1064, 1242 and 1450 $m^2/g$, respectively for incremented, unadjusted and decremented pH. Therefore decreasing the pH there is an increment in porosity.

The isotherm of the experiments performed at ratio $Cu^{2+}$:P123=1:$10^{-1}$ also displayed a type I behaviour. Further samples d and f exhibited an intermediate behaviour between types I and IV, with a large uptake at low pressure and a hysteretic desorption profile. The large uptake at low pressure was related to the presence of the microporous HKUST-1, while the hysteresis in the desorption branch was characteristic of mesoporosity. In the present case this arose from textural

mesoporosity. However samples b and f displayed the lower surface area (703 and 619 $m^2/g$ respectively), considering they were synthesized with higher amount of P123 it might be P123 is still included in the framework.

However BJH adsorption and desorption pore distribution showed the presence of peaks just in experiment b (Figure 3.12).

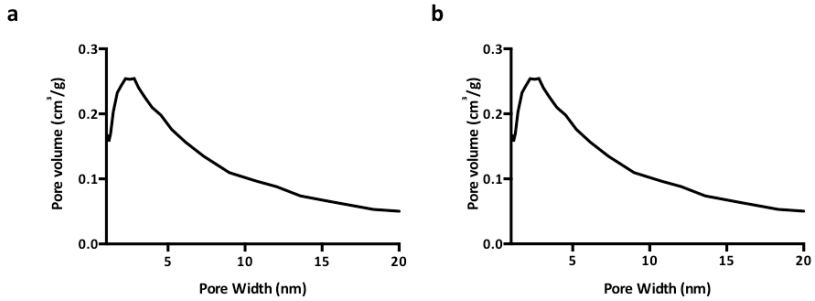


**Figure 3.12 Pore size of experiment (b) b performed at pH=4 and ratio Cu:P123=1:$10^{-1}$ determined by (a) BJH adsorption and (b) BJH desorption pore distribution.**

BJH adsorption and desorption graphs showed a mesopore size of 3-4 nm, due to the voids between the particles.

The experiments performed varying the pH of the copper solution showed that the effect of P123 increased increasing its amount. Indeed in the experiments performed at ratio $Cu^{2+}$:P123=1:$10^{-2}$ (Figure 3.10 a, c, e) the crystal size was comparable with the control experiment at unadjusted pH (Figure 3.8 a). Further increasing the pH of the copper solution the crystals showed etching on the surface (Figure 3.10 a), which is due to the pH variation (Figure 3.8 c). However increasing the ratio $Cu^{2+}$:P123 at 1:$10^{-1}$ the macroscopic structure of HKUST-1 was manipulated, decreasing the particle size. Further the conjunct effect of P123 and increment or decrement of the pH (sample b and f) led to the presence of textual mesoporosity, as detected by nitrogen sorption analysis (Figure 3.11).

### 3.2.2.2 The effect of P123 changing the pH of the synthesis solution

In this section the conjunct effect of variation of pH in the synthesis solution and the presence of the surfactant P123 was investigated. PXRD spectra and SEM images of the HKUST-1 samples were presented in Figure 3.13 and Figure 3.14.

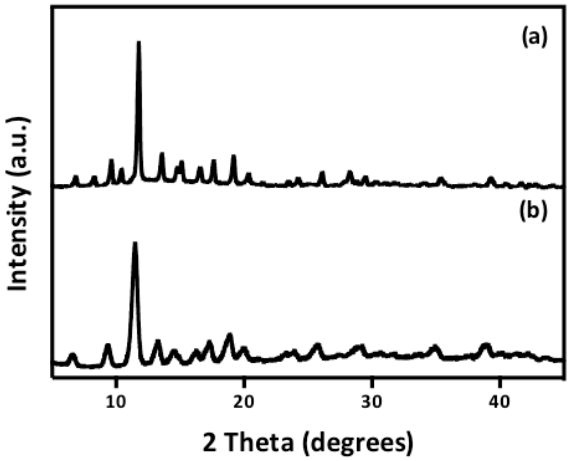


**Figure 3.13 PXRD patterns of HKUST-1 experiments performed in presence of the surfactant Pluronic-P123 changing the pH of the synthesis solution to 2.5 units at ratio Cu:P123 (a) $1:10^{-2}$ and (b) $1:10^{-1}$.**

The experiments performed increasing the pH of the synthesis solution to 2.5 units at ratio $Cu^{2+}$ to P123 $1:10^{-2}$ and $1:10^{-1}$ also led to the formation of HKUST-1 (Figure 3.13). However in sample a some extra peak at θ = 8° and 10° are detected, which are related to the phase $[Cu_2(BTC)(OH)(H_2O)]$.[44]

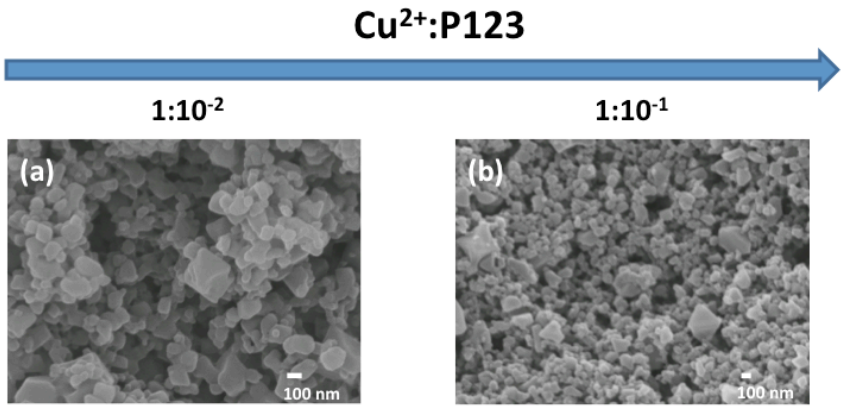


**Figure 3.14 SEM images of HKUST-1 experiments performed in presence of the surfactant Pluronic-P123 changing the pH of the synthesis solution to 2.6 units at ratio Cu:P123 (a) $1:10^{-2}$ and (b) $1:10^{-1}$.**

SEM images of both the experiments showed a decrement of HKUST-1 particles into the nanorange. Both at ratio $Cu^{2+}$:P123=$1:10^{-1}$ and $1:10^{-2}$ a decrement in the particle size into the nanorange was detected as shown from the SEM images (Figure 3.14). The size of the particles was further decreased compared to the control experiment (Figure 3.8 d), indicating the crucial role of P123. However in comparison with the experiment of the section 3.2.2.1, where the pH of the copper solution was varied, here it was noticed an effect on the particle size even at lower concentration of P123 (ratio $Cu^{2+}$:P123=$1:10^{-2}$). Therefore, as previously stressed, the step in which the pH was changed exert an effect on the final result.

The porosity of the experiments performed with P123 was investigated by nitrogen sorption analysis (Figure 3.15).

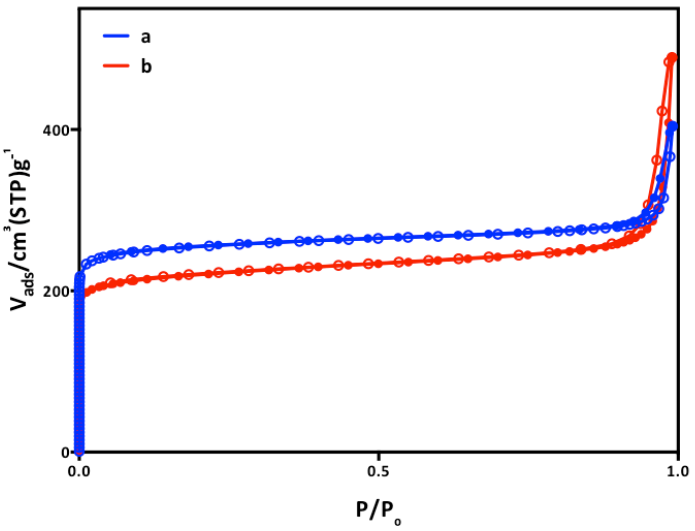


**Figure 3.15 Nitrogen sorption isotherms of the experiments performed in the presence of the surfactant Pluronic-P123 varying the pH of the synthesis solution to 2.6 units at ratio Cu:P123 (a) $1:10^{-2}$ and (b) $1:10^{-1}$ measured at 77 K.**

The isotherms exhibited an intermediate behaviour between types I and IV, with a large uptake at low pressure and a hysteretic desorption profile. The large uptake at low pressure was related to the presence of the microporous HKUST-1, while the hysteresis in the desorption branch is characteristic of mesoporosity. In the present case this most likely arose from the textual mesoporosity rather than templated mesopores. BET surface area detected for sample a and b were respectively 1009 ± 0.5 and 861 ± 0.3 $m^2/g$. The isotherms detected for samples a and b are similar to the ones detected in the previous section for samples b and f (Figure 3.11), and indeed also the particles obtained were comparable (Figure 3.14 and Figure 3.10 respectively). However the latter experiments were performed increasing or decreasing the pH of the copper solution and at ratio $Cu^{2+}$:P123=$1:10^{-1}$ respectively, while in the experiments of this section showed an effect at both ratio $Cu^{2+}$:P123=$1:10^{-2}$ and $1:10^{-1}$. This again support the importance of the step in which the pH was changed.

Nevertheless the isotherms of sample a and b reported hysteretic BJH adsorption and desorption graphs did not show any peak.

The surfactant pluronic P123 was previously used for the synthesis of MOFs, for instance stabilizing the synthesis of ZIF-8 in aqueous solution in the presence of ammonium hydroxide (molar composition $Zn^{2+}$ : MeIm : $NH^{4+}$ : P123 : $H_2O$ = 1 : 2 : 16 : (0.0029-0.014) : 547).[156] As with our results, in this case P123 did also not lead to intraparticle mesoporosity formation but its increment decreased the particle size and the BET surface area compared to reference ZIF-8 (<

1200 $m^2/g$). This was proposed to be related to the incomplete activation of the sample or the incorporation of small amounts of amorphous compounds.

On the other hand when P123 and F127 are employed together in the solvothermal synthesis of MIL-53 (Al) (molar composition $Al(NO_3)_3 \cdot 9H_2O$ : $H_2BDC$: DMF: $H_2O$: EtOH: SDA = 1.5 : 1 : 95 : 153 :35 0.3-0.15, $H_2BDC$ = benzenedicarboxylic acid or terephthalic acid and SDA = block copolymer P123 and F127) they led to micro- and meso- structured materials termed L-MOF. Indeed these materials displayed the micropores characteristic of the crystalline MIL-53(Al) framework and further contained up to two regular mesoporous systems, one with mesopore size around 4.0 nm, and the other one with mesopore size between 5.4 and 7.6 nm.[157] The authors stated that during the solvothermal synthesis the surfactants acted as a SDA forming rod-like micelle arrays around which the MOF precursors assembled to form mesostructured MOF materials.

The experiments performed here employing P123 in the synthesis of HKUST-1 under acidic conditions showed that the dominant effect of the surfactant was on reducing the overall particle size, which had been largely reported when surfactants were employed in the synthesis of MOFs.[103, 106, 158] Nevertheless the presence of P123 in the three systems gave different outcomes: in the case of ZIF-8 and HKUST-1 the surfactant affected the particle size, while in the case of MIL-53 it induced intraparticle mesoporosity, even though in this case F127 was employed as a co-surfactant. Starting from the same surfactant, factors as co-surfactant, synthetic condition and structural features of the particular MOF influenced the system, the interactions MOF (precursors)-surfactant and therefore the final result on the macroscopic structure.

### 3.2.3 Carboxylic acid derived surfactants

From the literature was stressed that introduction of mesoporosity into the MOF framework via supramolecular templating strategy depended on the MOF assembly process, the surfactant characteristics and the interaction between the MOF precursors and the surfactant mesophase.[92] The MOF assembly process was rationalized as the formation and organization of SBUs in the framework; therefore selecting a metal precursor, which had the same geometry of the SBU units, should facilitate the reaction course. This is known as the controlled SBU approach[159], and has previously been used to control the formation of defined building blocks and their assembly into an ordered network.[23, 39]

The MOF mesostructure formed because of the interactions between the surfactant mesophase and the MOF precursors, where the strength of the interaction was important, as shown in Figure 3.16. If the interactions were too weak phase separation occurred and the MOF and surfactant

mesophase grow independently, whereas if they were too strong the formation of the MOF could be prevented in favour of other species, such as surfactant/metal or surfactant/ligand complexes. Ideally the surfactant mesophase should be intimately associated with the MOF precursors through preferential and directional interactions. Furthermore the kinetics of the process was another key factor: the driving force for the MOF to form was very strong, and if this assembles too quickly there was inadequate time for its co-assembly with the mesophase. Therefore the assembly of the MOF mesostructure was expected to be composed of 2 steps: surfactant-precursor(s) interaction(s) and framework formation.

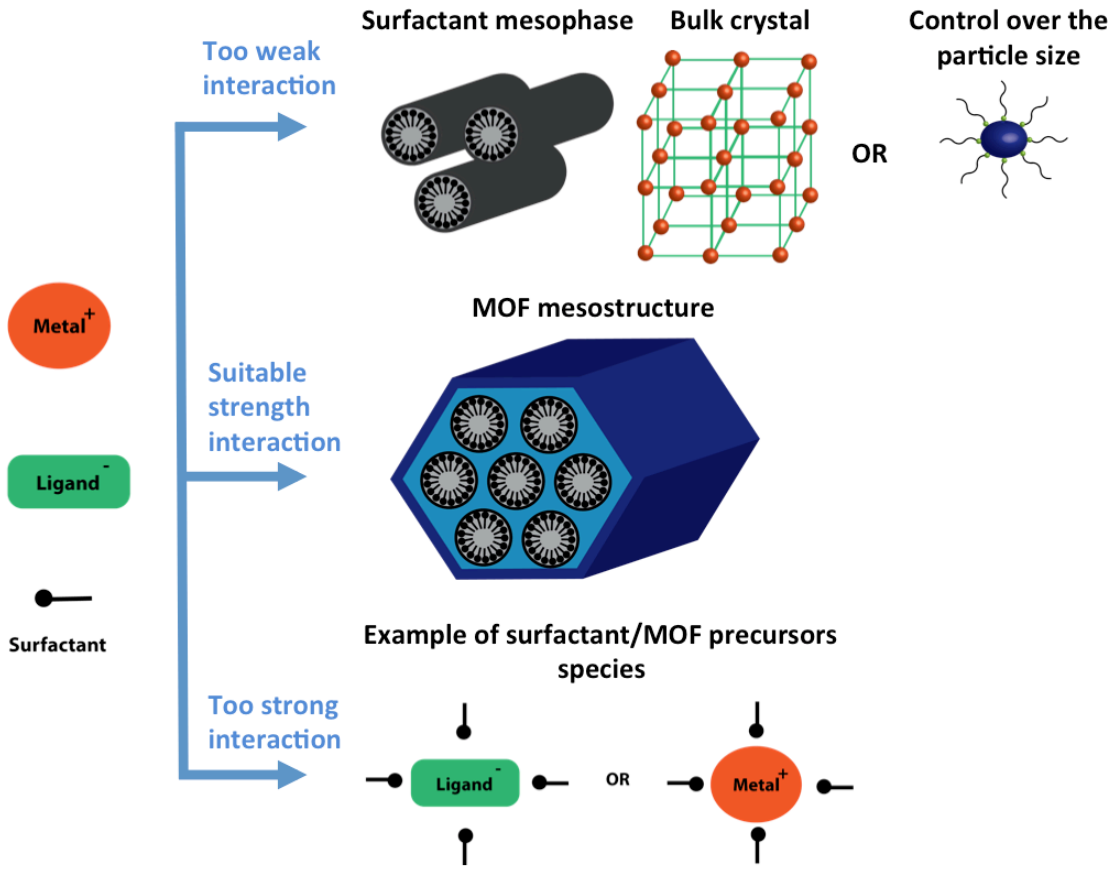


**Figure 3.16 Potential interactions between surfactant and MOF precursors: too weak interactions prevent the surfactant templating effect, suitable strength interactions form to the mesostructure MOF and too strong interactions prevent the formation of the framework.**

In the light of these considerations a number of changes to the synthetic procedure were made: copper acetate was selected as the metal precursor as this was already present as $[Cu_2(CH_3COO)_4(H_2O)]$ paddlewheel units,[160] which corresponded to the SBUs in the HKUST-1 framework. It was previously reported that ligand exchange of acetate by $H_3BTC$ acid led to efficient HKUST-1 assembly.[161] Furthermore surfactants with the same organic moiety of the linker, therefore potential modulators,[104, 162] were selected. This kind of surfactant might function in two ways: (1) acting on the external surface of the crystals on the morphology and

particles size[105] and (2) on the internal one forming the mesostructure. Furthermore the synthetic conditions used were carefully chosen in order to increase compatibility between surfactant mesophase formation and MOF assembly.

Starting from these considerations the long chain carboxylic acids octanoic acid (OA) and dodecanoic acid (DA) were employed as the amphiphilic modulators in the synthesis of HKUST-1. As mentioned before, the carboxylic moiety should ensure an interaction with the metal salt, while the difference in chain length would influence the micelle size.

#### 3.2.3.1 Experiments performed with order of solvent addition $H_2O$/EtOH

As a general method for the synthesis octanoic acid (0.5 or 1.8 g, respectively 3.5 and 12.5 mmol) or dodecanoic acid (0.7 or 2.5 g, respectively 3.5 and 12.5 mmol) was dissolved in 25 ml of distilled $H_2O$ and stirred for 30 minutes, then copper acetate hemi(pentahydrate) (0.16 g, 0.8 mmol) and 2 ml of distilled $H_2O$ were added and stirred for 2 hours. Finally $H_3BTC$ (0.1 g, 0.5 mmol) and 20 ml of ethanol were added. After one day stirring at room temperature the reaction was either left at room temperature or heated under solvothermal conditions at 90 or 120 °C for 17 hours. The surfactant was initially left under stirring alone in water in order to form the mesophase, then the metal salt was added and finally the organic linker, giving rise to the HKUST-1 formation. The reaction was carried out at different temperatures (room temperature, 90 or 120 °C): high temperatures should facilitate the formation of HKUST-1, while room temperature should be more suitable for the stability of the mesophase.

In the experiments performed, the modulator was put in a large excess compared to the ligand because of its weaker coordination property and because the critical micelle concentration under these conditions is unknown, in particular the ratio modulator/ligand was 5 or 25, however, since $H_3BTC$ has 3 acid groups the carboxylate excess/availability between surfactant and BTC is 5/3.

Control experiments were performed without adding any surfactant and PXRD patterns and SEM images were show below in Figure 3.17 and Figure 3.18.

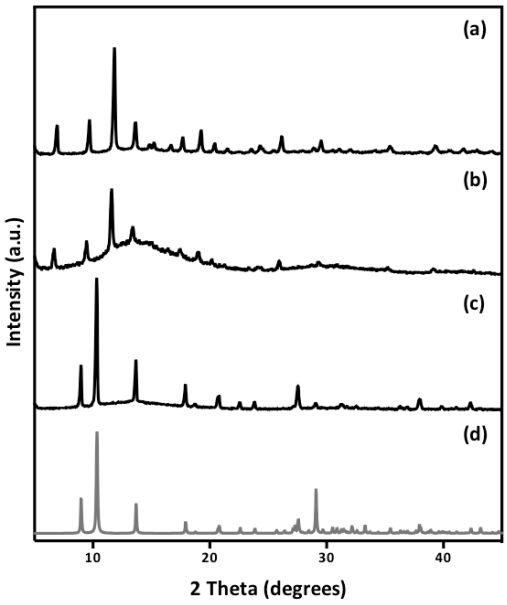


**Figure 3.17 PXRD patterns of control experiments performed with solvent introduction order $H_2O$/EtOH at (a) room temperature, (b) 90 °C and (c) 120 °C (d) simulated pattern of [$Cu_2$(BTC)(OH)($H_2O$)].**

PXRD patterns showed that HKUST-1 was formed at room temperature and in the solvothermal reaction carried out at 90 °C, while in the solvothermal reaction carried out at 120 °C the alternative phase [$Cu_2$(BTC)(OH)($H_2O$)] was obtained. This agreed with the work of Schlesinger *et al.*, where the solvothermal reaction performed under similar conditions ($Cu(OAc)_2 \cdot H_2O$ as precursor, ratio $H_2O$:EtOH = 3:2 and reaction temperature 180 °C), led to the formation of pure [$Cu_2$(OH)(BTC)($H_2O$)$\cdot 2nH_2O$]. Further, in the same work, [$Cu_2$(OH)(BTC)($H_2O$)$\cdot 2nH_2O$] was obtained in microwave-assisted synthesis in mixture $H_2O$:EtOH=4:3 employing $Cu(OAc)_2 \cdot H_2O$ as precursor.[44]

On the other hand, employing $Cu(NO_3)_2$ as metal salt, the optimized procedure reported for the preparation of HKUST-1 was performed in solvothermal condition at 120 °C.[52] This again confirmed the importance of the compositional parameters on the synthesis of HKUST-1.

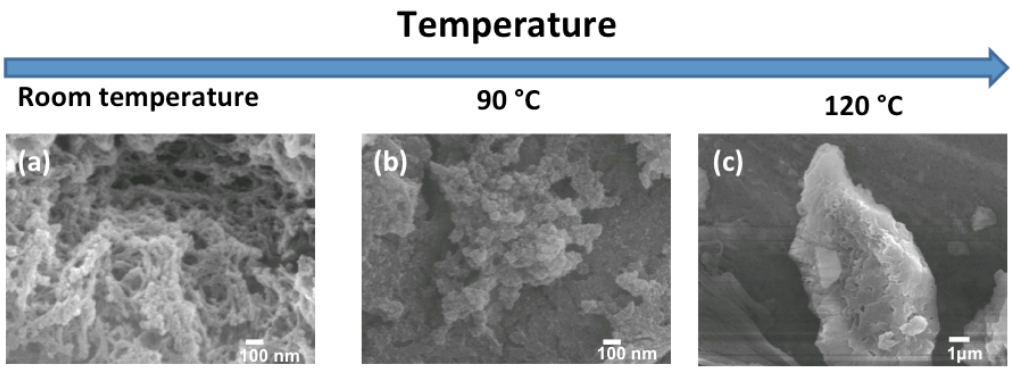


**Figure 3.18 SEM images of control experiments performed with solvent introduction order $H_2O$/EtOH at (a) room temperature and (b) 90 °C.**

Furthermore SEM images of the experiments performed at room temperature and at 90 °C showed that nanoparticles were formed, it might be due to the dilution of the solution (molar ratio $Cu^{2+}$: BTC : $H_2O$ : EtOH = 1: 0.65 : 1875 : 428), according to the work of Biemmi *et al.* where doubling the concentration of the starting solutions decreased the particle size by an order of magnitude.[148] Finally SEM image of the phase [$Cu_2$(BTC)(OH)($H_2O$)] is shown in Figure 3.18 c.

#### 3.2.3.1.1 Experiments performed with order of solvent addition $H_2O$/EtOH and octanoic acid

The control reactions were repeated in the presence of octanoic acid (ratio OA/BTC= 5 or 25) under the same conditions, and the PXRD patterns and SEM images of the obtained solids were shown in Figure 3.19 and Figure 3.20, respectively.

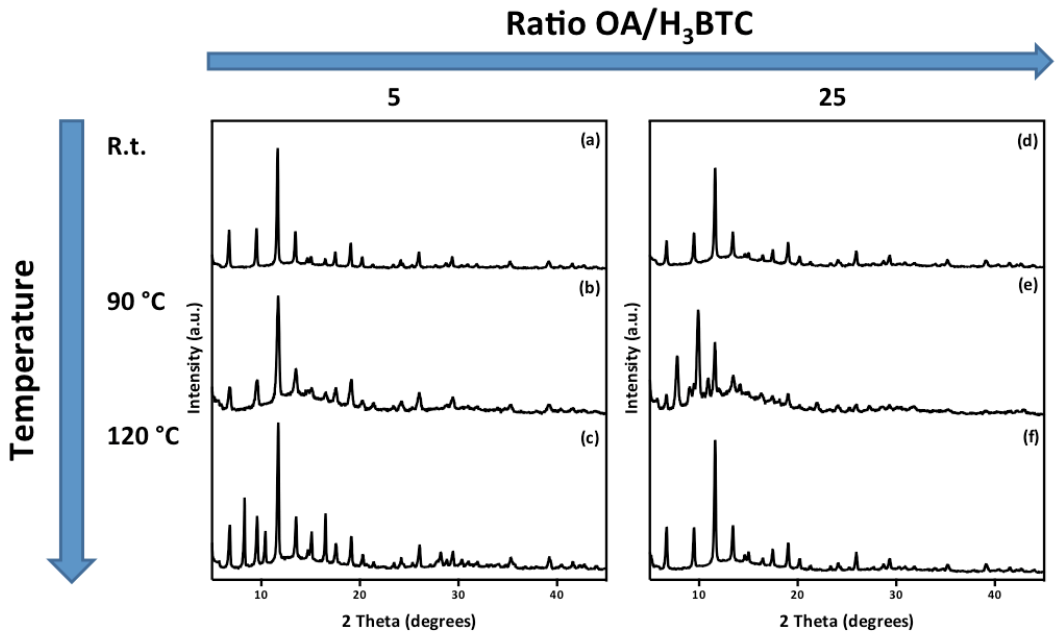


**Figure 3.19 PXRD patterns of the samples performed with solvent introduction order $H_2O$/EtOH at different temperature and amount of octanoic acid: at ratio OA/L=5 at (a) room temperature, (b) 90 °C and (c) 120 °C, at ratio OA/L=25 at (d) room temperature, (e) 90 °C and (f) 120 °C.**

PXRD patterns showed that HKUST-1 was not always formed as a pure phase (Figure 3.19). Both the experiments a and d, performed at room temperature, showed formation of pure HKUST-1 phase. However increasing the temperature at 90 °C, experiment b, performed at ratio OA/$H_3$BTC=5 showed a pure phase of HKUST-1, while experiment e, performed at ratio OA/$H_3$BTC=25 showed mostly the presence of extra peaks at 2θ= 8.5° and 11°. Those were identified respectively as [Cu(BTC-$H_2$)$_2$($H_2O$)$_2$]·3$H_2O$[43] and [$Cu_2$(BTC)(OH)($H_2O$)][44] phases. Finally in the experiments performed at 120°C, employing ratio OA/$H_3$BTC= 5 (sample c), two extra peaks at 2θ= 8.5° and 11° were detected, which again were related to [Cu(BTC-$H_2$)$_2$($H_2O$)$_2$]·3$H_2O$ and

$[Cu_2(BTC)(OH)(H_2O)]$ phases. Finally employing ratio OA/$H_3$BTC= 5 at 120°C (sample f) pure HKUST-1 was formed.

$[Cu(BTC–H_2)_2{\cdot}(H_2O)_2]{\cdot}3H_2O$ was characterized by Seo *et al.* but no indexing of the diffraction pattern and peak positions was given.[43] In particular both $[Cu(BTC–H_2)_2{\cdot}(H_2O)_2]{\cdot}3H_2O$ and $[Cu_2(OH)(BTC)(H_2O){\cdot}2nH_2O]$ were obtained as extra phases by microwave assisted synthesis employing $Cu(OAc)_2{\cdot}H_2O$ as metal salt. The intensities of the phases depended on the synthesis time, temperature and ratio $H_2O$/EtOH. Further the two phases were obtained from solvothermal synthesis ($H_2O$:EtOH = 1:1, $Cu(OAc)_2{\cdot}H_2O$ as metal salt), where increasing the temperature from 120 to 180 °C the intensity of the two phases increased.[148] Finally $[Cu(BTC–H_2)_2{\cdot}(H_2O)_2]{\cdot}3H_2O$ was obtained as a pure phase by mixing aqueous solution of $Cu(OH)_2$ with BTC at room temperature or 80°C.[163]

From the literature it appeared that employing $Cu(OAc)_2{\cdot}H_2O$ as metal salt, high temperature favored the formation of the $[Cu(BTC–H_2)_2{\cdot}(H_2O)_2]{\cdot}3H_2O$ and $[Cu_2(OH)(BTC)(H_2O){\cdot}2nH_2O]$. In the experiments performed with OA there was not such direct correlation. However both the experiments performed at room temperature led to the formation of pure HKUST-1, while increasing the temperature the result depended also on the ratio OA/$H_3$BTC employed, indeed at 90 °C HKUST-1 was obtained at ratio OA/$H_3$BTC = 5 and at 120 °C HKUST-1 was obtained at ratio OA/$H_3$BTC = 25.

Further, compared to the control experiments the surfactant appeared to promote the formation of other phases. This might be related to formation of the interaction between OA and the MOF precursors. Further in $[Cu(BTC–H_2)_2{\cdot}(H_2O)_2]{\cdot}3H_2O$ the ligand is not fully deprotonated, the excess of OA might decrease the pH of the solution and therefore prevent the deprotonation of the linker.

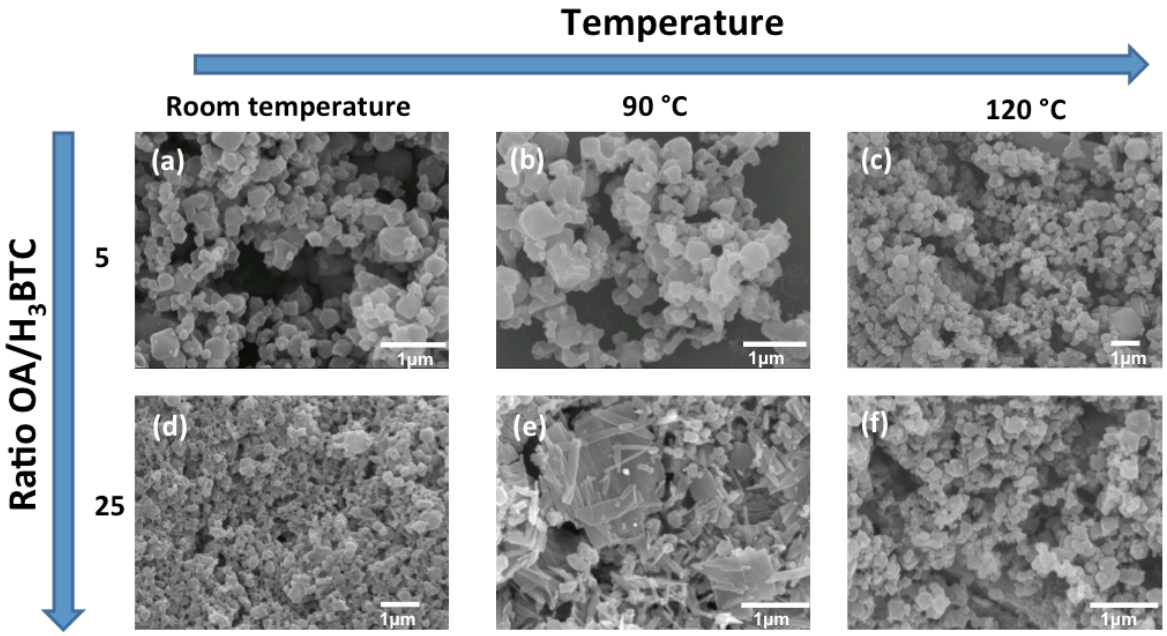


**Figure 3.20 SEM images of the samples performed with solvent introduction order $H_2O$/EtOH at different temperature and amount of octanoic acid: at ratio OA/L=5 at (a) room temperature, (b) 90 °C and (c) 120 °C, at ratio OA/L=25 at (d) room temperature, (e) 90 °C and (f) 120 °C.**

SEM images of the experiments were shown in Figure 3.20. Samples a, b, d and f were related to pure HKUST-1, the presence of the surfactant caused an increment in the particle size over one hundred nanometers compared to the control experiments (3.2.3.1). A similar effect was reported in the synthesis of HKUST-1 in the presence of the modulator dodecanoic acid. In this case the nucleation rate was slowed down by the modulator and therefore larger crystals with greater polidispersity were formed.[105] The PXRD pattern of sample c did not show a pure HKUST-1 phase, however the SEM image showed particles with size comparable to samples a, b, d and f, but none fibrous structures typical of the $[Cu(BTC\text{-}H_2)_2(H_2O)_2]\cdot 3H_2O$ phase.[43] However this might be due to the low amount of the extra-phases, as detected from the PXRD pattern. Finally the fibrous structures typical of the $[Cu(BTC\text{-}H_2)_2(H_2O)_2]\cdot 3H_2O$ phase appeared in sample e.

#### 3.2.3.1.2 Experiments performed with order of solvent addition $H_2O$/EtOH and dodecanoic acid

Thereafter the PXRD patterns and SEM images of the experiments performed with dodecanoic acid (ratio DA/BTC= 5 or 25) at room temperature or in solvothermal condition at 90 or 120 °C were shown (Figure 3.21 and Figure 3.22).

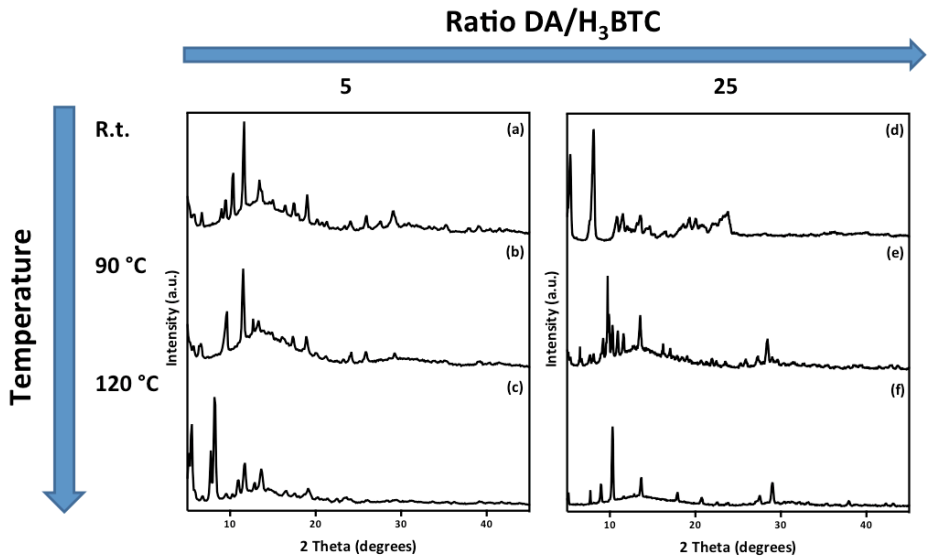


**Figure 3.21 PXRD patterns of the samples performed with solvent introduction order $H_2O$/EtOH at different temperature and amount of dodecanoic acid: at ratio DA/L=5 at (a) room temperature, (b) 90 °C and (c) 120 °C, at ratio DA/L=25 at (d) room temperature, (e) 90 °C and (f) 120 °C.**

PXRD patterns show HKUST-1 was formed only at ratio DA/$H_3$BTC = 5 at room temperature and at 90 °C (samples a and b), however both the patterns showed some small extra peaks and a large amorphous background. The PXRD patterns corresponding to the other experiments did not show the peaks characteristic of HKUST-1 but just a mixture of the other phases of the copper(II)/$H_{3-n}$BTC system (n=1-3); therefore under these conditions the excess of DA prevented the formation of the framework. As mentioned before (3.2.3.1.1) high temperature favored the formation of other phase rather then HKUST-1, as in the experiments performed at ratio DA/$H_3$BTC = 5. However in the experiments performed at ratio DA/$H_3$BTC = 25 HKUST-1 was not formed in any case. This implied the large excess of surfactant prevented the framework formation, maybe interacting too strongly with the MOF precursor(s), of affecting the pH and therefore the precursors availability.

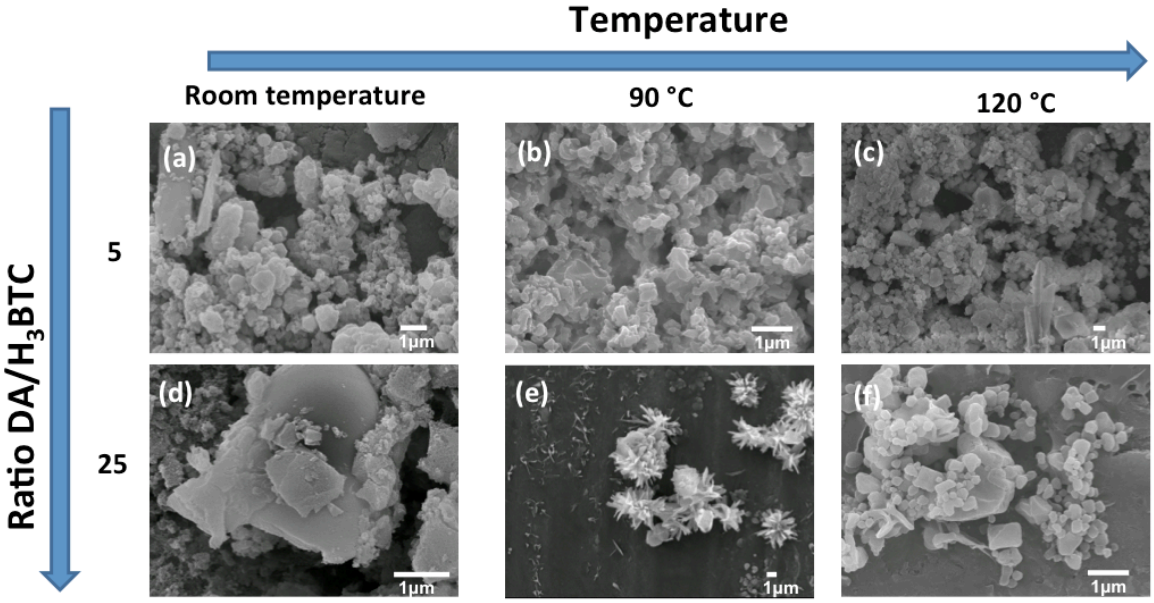


**Figure 3.22 SEM images of the samples performed with solvent introduction order $H_2O$/EtOH at different temperature and amount of dodecanoic acid: at ratio DA/L=5 at (a) room temperature, (b) 90 °C and (c) 120 °C, at ratio DA/L=25 at (d) room temperature, (e) 90 °C and (f) 120 °C.**

SEM images of HKUST-1 (Figure 3.22 a-b) showed aggregation of particles with increased size compared to the control experiments, therefore under these conditions dodecanoic acid showed a similar effect to octanoic acid and the reported literature.[105] The SEM images (c-f) are related to other phases of copper(II)/$H_{3-n}$BTC system (n=1-3) and they displayed powders with irregular particles or needle-like particles of few micron size (sample e).

In general the previous experiments showed the presence of extra phase in HKUST-1 patterns. In the control experiments high temperature (120 °C) favored the formation of $[Cu_2(BTC)(OH)(H_2O)]$, according to the literature.[44] However introducing the surfactants OA or DA in the syntheses two extra phases were detected, $[Cu(BTC\text{-}H_2)_2(H_2O)_2]\cdot 3H_2O$ and $[Cu_2(BTC)(OH)(H_2O)]$. It appeared that the presence of the surfactants further prevented the HKUST-1 formation, which might be related to the interaction surfactant-MOF precursors or to the pH change caused by them.

### 3.2.3.2 Experiments performed with order of solvent addition EtOH/ $H_2O$

The previous experiments showed the use of OA and DA mostly led to the formation of the phases $[Cu(BTC\text{-}H_2)_2(H_2O)_2]\cdot 3H_2O$ and $[Cu_2(BTC)(OH)(H_2O)]$ instead that HKUST-1. However DA had previously shown modulator property when employed with HKUST-1.[105] The synthesis was performed in butanol under microwave-assisted solvothermal conditions and led to size controlled formation of HKUST-1. Therefore starting from the consideration that compositional parameters, such as solvents, are crucial for the final results[163] the reaction was carried out with the opposite order of introduction of solvents.

In a typical synthesis octanoic acid (0.5 or 1.8 g, respectively 3.5 and 12.5 mmol) or dodecanoic acid (0.7 or 2.5 g, respectively 3.5 and 12.5 mmol) was dissolved in 25 ml of distilled ethanol and stirred for 30 minutes, then copper acetate hemi(pentahydrate) (0.16 g, 0.8 mmol) and 2 ml of ethanol were added and stirred for 2 hours. Finally $H_3BTC$ (0.1 g, 0.5 mmol) and 20 ml of $dH_2O$ were added. After one day stirring at room temperature the reaction was either left at room temperature or heated under solvothermal conditions at 90 or 120 °C for 17 hours. PXRD patterns and SEM images of the control experiments were shown in Figure 3.23 and Figure 3.24.

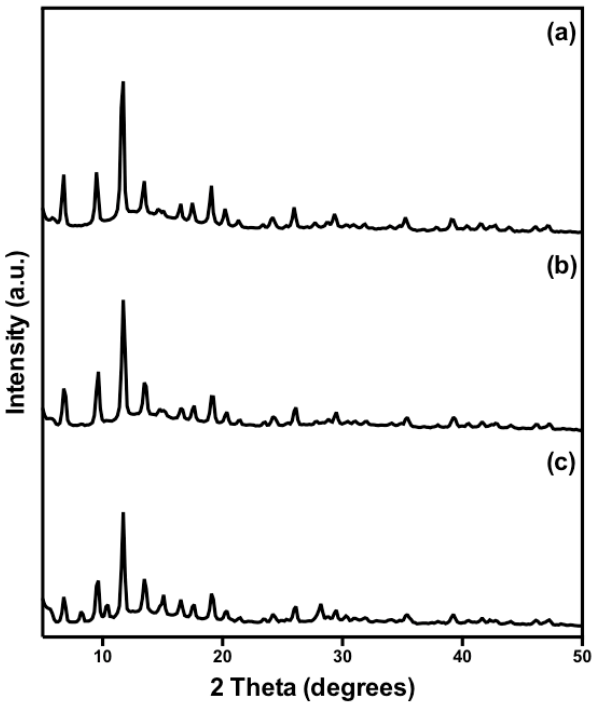


**Figure 3.23 PXRD patterns of control experiments performed with solvent introduction order EtOH/$H_2O$ at (a) room temperature, (b) 90 °C and (c) 120 °C.**

Similarly to the previous case the increase of the temperature led to the formation of other phases. The experiments performed at room temperature and 90 °C formed pure HKUST-1, while the experiment performed at 120°C showed two extra peaks at 2θ= 8.5° and 11°, which were related respectively to $[Cu(BTC\text{-}H_2)_2(H_2O)_2]\cdot 3H_2O$ and $[Cu_2(BTC)(OH)(H_2O)]$ phases.

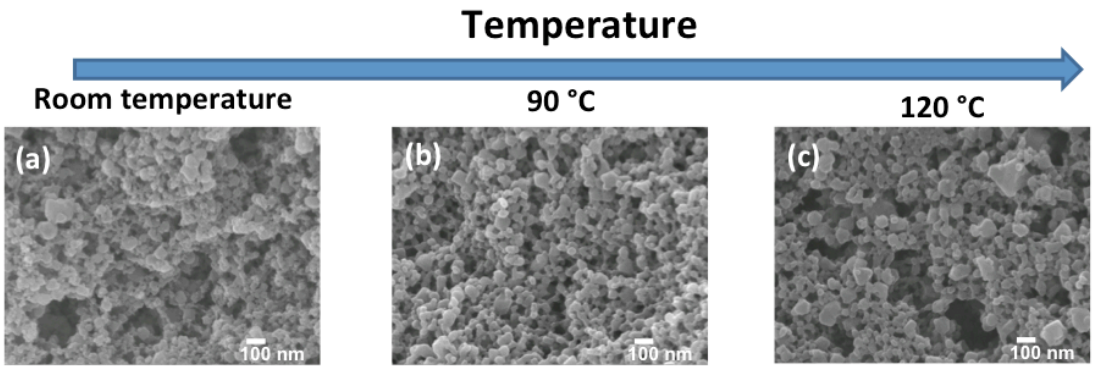


**Figure 3.24 SEM images of control experiments performed with solvent introduction order EtOH/$H_2O$ at (a) room temperature, (b) 90 °C and (c) 120 °C.**

SEM images showed the formation of HKUST-1 nanoparticles at all the temperatures tested, similar to the control experiments performed with order of addition of solvent $H_2O$/EtOH, which again might be due to the higher dilution of the synthesis solutions.

#### 3.2.3.2.1 Experiments performed with order of solvent addition EtOH/ $H_2O$ and octanoic acid

Thereafter the PXRD patterns and SEM images of the experiments performed with octanoic acid (ratio OA/BTC= 5 or 25) at room temperature or in solvothermal condition at 90 or 120 °C were shown (Figure 3.25 and Figure 3.26).

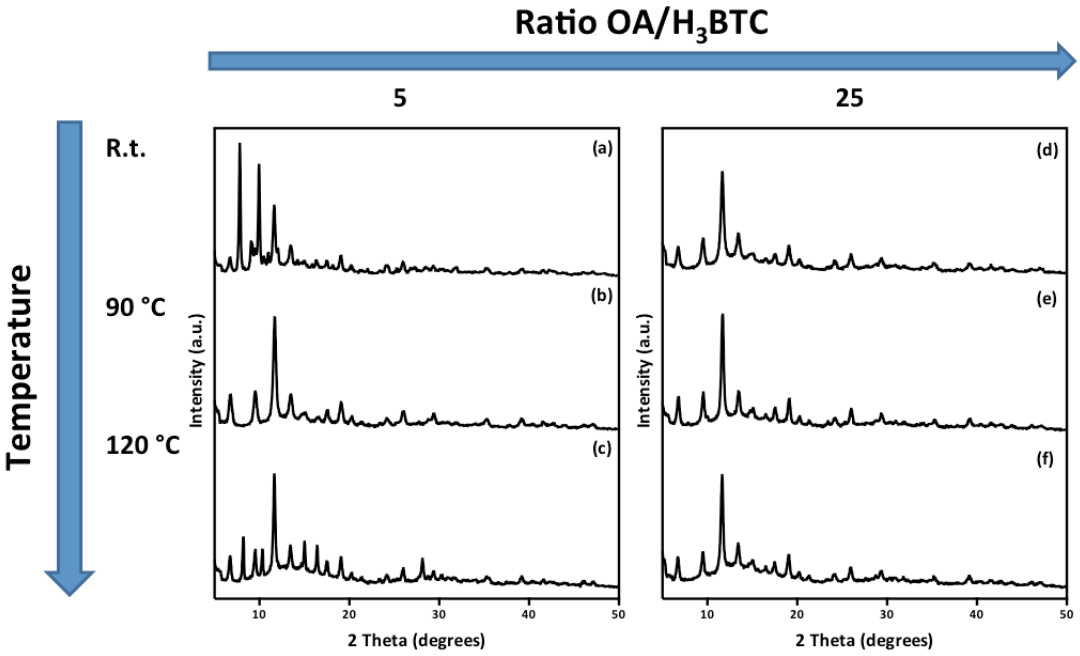


**Figure 3.25 PXRD patterns of the samples performed with solvent introduction order EtOH/$H_2O$ at different temperature and amount of octanoic acid: at ratio OA/L=5 at (a) room temperature, (b) 90 °C and (c) 120 °C, at ratio OA/L=25 at ratio OA/L=25 at (d) room temperature, (e) 90 °C and (f) 120 °C.**

PXRD patterns of the experiments performed at ratio OA/$H_3$BTC=5 showed presence of pure HKUST-1 just at 90°C, while [Cu(BTC-$H_2$)$_2$($H_2O$)$_2$]·3$H_2O$ and [$Cu_2$(BTC)(OH)($H_2O$)] phases were formed at room temperature and at 120 °C. Instead at ratio OA/$H_3$BTC=25 pure HKUST-1 was always formed. Comparing to the experiments performed with order of solvents addition $H_2O$/EtOH the trend was different. In that case the experiments performed at ratio OA/$H_3$BTC = 5 showed the presence of the two extra-phases at 120 °C, while the experiments performed at ratio OA/$H_3$BTC = 25 showed the presence of the two extra-phases at 90 °C.

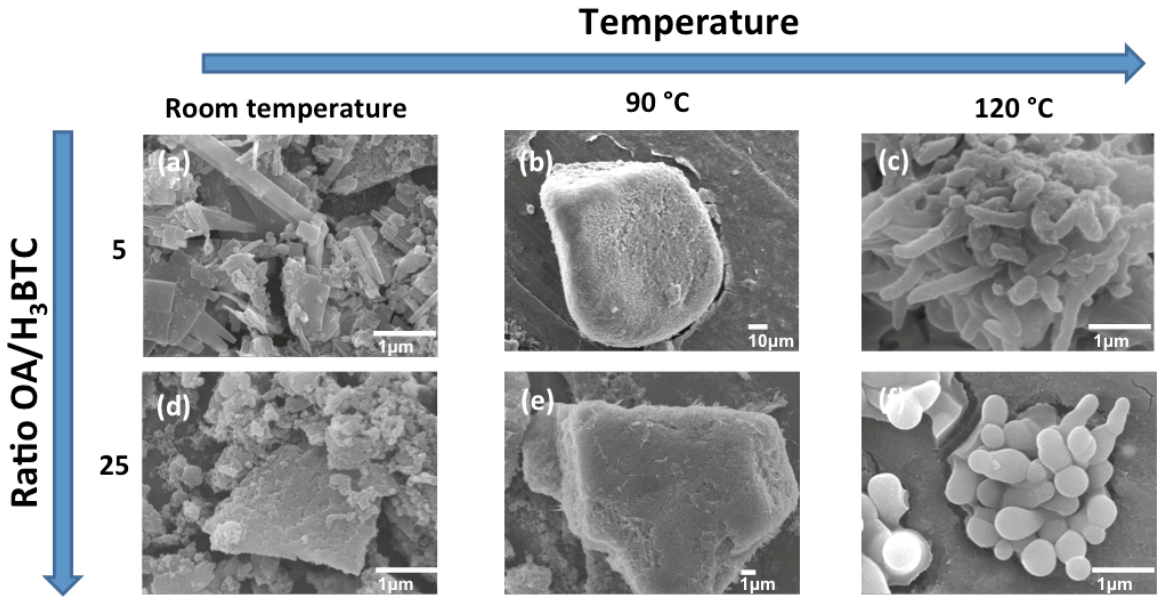


**Figure 3.26 SEM images of the samples performed with solvent introduction order EtOH/$H_2O$ at different temperature and amount of octanoic acid: at ratio OA/L=5 at (a) room temperature, (b) 90 °C and (c) 120 °C, at ratio OA/L=25 at (d) room temperature, (e) 90 °C and (f) 120 °C.**

SEM images of sample a showed the fibrous structure related to [Cu(BTC-$H_2$)$_2$($H_2O$)$_2$]·3$H_2O$, samples b, d, e were formed by aggregation of particles, while sample c, f showed micron size worm-like structures. Interestingly both experiments c and f were performed under solvothermal conditions at 120 °C for 17 hours and they just differ for the ratio OA/$H_3$BTC employed in the synthesis, respectively 5 and 25, which might suggest that, under these conditions, an increase in the surfactant concentration promoted the formation of HKUST-1 as a pure phase. Hereafter the system was further investigated keeping the ratio OA/$H_3$BTC at 25 and decreasing the reaction time (from 1 to 5 hours). PXRD patterns and SEM images were shown below in Figure 3.27 and Figure 3.28.

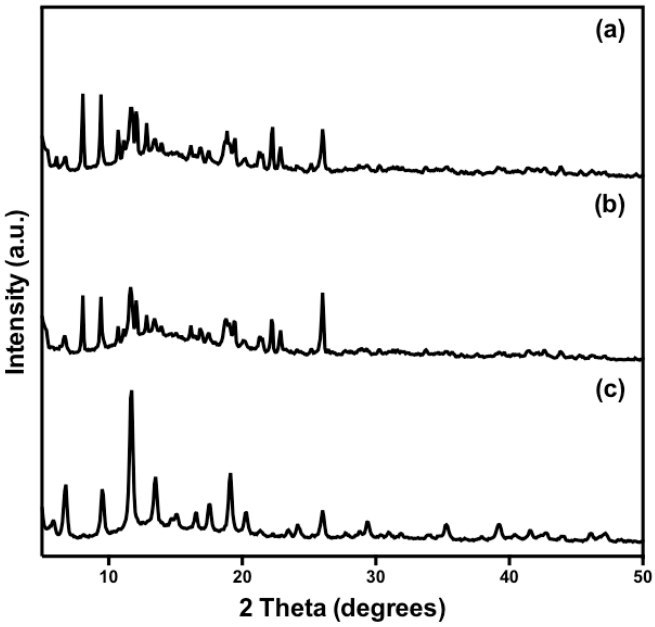


**Figure 3.27 PXRD patterns of the samples obtained in presence of OA (ratio OA/$H_3$BTC= 25) at 120 °C for (a) 1 hour, (b) 3 hours and (c) 5 hours.**

PXRD patterns of the reactions performed at time 1 and 3 hours showed the presence of the two phases Cu(BTC)$(H_2O)_3$[149] and HKUST-1, while at a reaction time of 5 hours only pure HKUST-1 was formed.

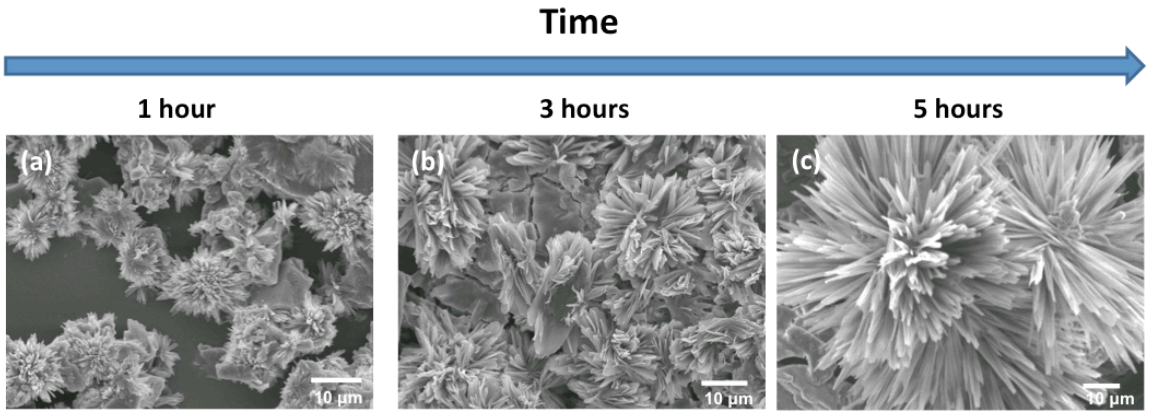


**Figure 3.28 SEM images of the samples obtained in presence of OA (ratio OA/$H_3$BTC= 25) at 120 °C for (a) 1 hour, (b) 3 hours and (c) 5 hours**

SEM images of the experiments performed at ratio OA to $H_3$BTC= 25 at 120 °C showed a needle-like structure, which dimension increased with time and belonged to the micronrange. Furthermore, comparing these results with the experiment performed at a reaction time of 17 hours (Figure 3.26 f), the thickness of the needles appeared to increase with the reaction time.

#### 3.2.3.2.2 Experiments performed with order of solvent addition EtOH/ $H_2O$ and dodecanoic acid

Finally PXRD patterns and SEM images of the experiments performed with dodecanoic acid (ratio OA/BTC= 5 or 25) at room temperature or in solvothermal condition at 90 or 120 °C were shown (Figure 3.29 and Figure 3.30).

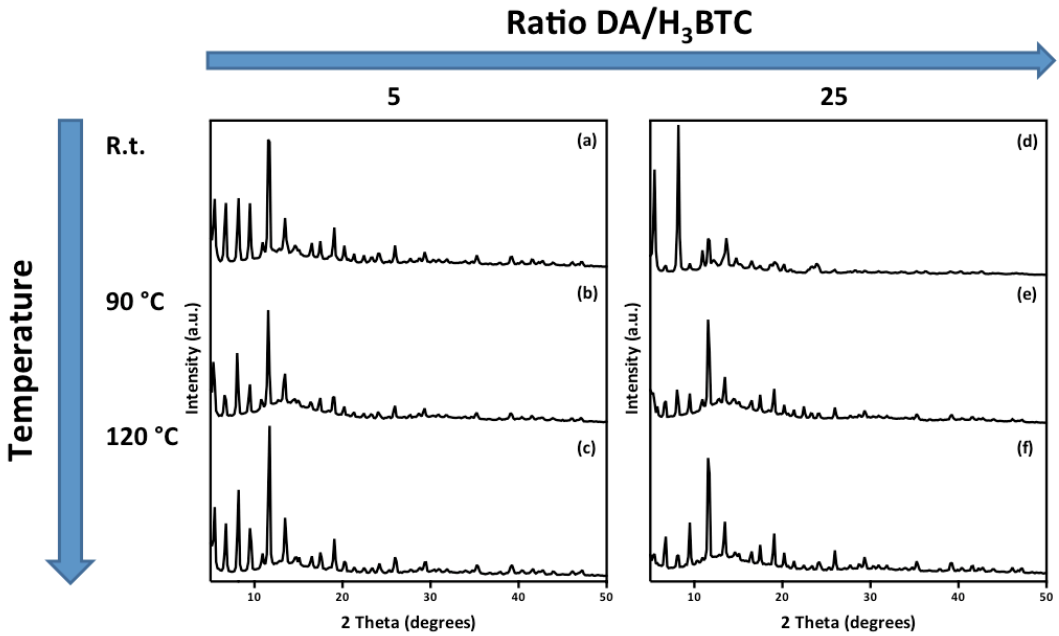


**Figure 3.29 PXRD patterns of the samples performed with solvent introduction order EtOH/$H_2O$ at different temperature and amount of octanoic acid: at ratio DA/L=5 at (a) room temperature, (b) 90 °C and (c) 120 °C, at ratio DA/L=25 at (d) room temperature, (e) 90 °C and (f) 120 °C.**

PXRD patterns of all the experiments showed the peaks related to the three phases HKUST-1, $[Cu(BTC\text{-}H_2)_2(H_2O)_2]\cdot 3H_2O$ and $[Cu_2(BTC)(OH)(H_2O)]$ just at different intensities, except the experiment performed at ratio DA to $H_3BTC$= 25 and at temperature 120 °C where just the phases HKUST-1 and $[Cu(BTC\text{-}H_2)_2(H_2O)_2]\cdot 3H_2O$ were present.

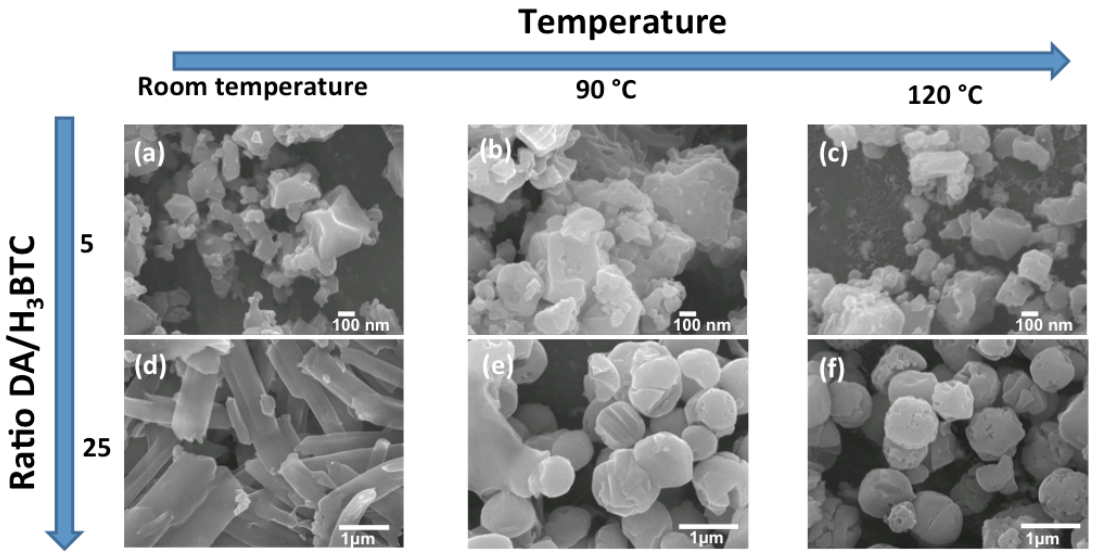


**Figure 3.30 SEM images of the samples performed with solvent introduction order EtOH/$H_2O$ at different temperature and amount of octanoic acid: at ratio DA/L=5 at (a) room temperature, (b) 90 °C and (c) 120 °C, at ratio DA/L=25 at (d) room temperature, (e) 90 °C and (f) 120 °C.**

SEM images of the experiments performed at ratio DA to $H_3BTC$= 5 showed the formation of irregular particles of hundreds of nanometer size. The experiment performed at ratio DA to $H_3BTC$= 25 at room temperature showed fibrous structure typical of the $[Cu(BTC\text{-}H_2)_2(H_2O)_2]\cdot 3H_2O$ phase,[43] while SEM images of the experiments performed at ratio DA to $H_3BTC$= 25 and temperature 90 and 120 °C formed rounded particles with hundreds of nanometers size. Even though the experiment performed at ratio DA to $H_3BTC$= 25 and temperature 120 °C showed the presence of $[Cu(BTC\text{-}H_2)_2(H_2O)_2]\cdot 3H_2O$, due to the rounded-like morphology of the particles, the sample was further investigated in the following section (3.2.3.2.3).

The series of experiments performed in solvent order EtOH/$H_2O$ showed the presence of extra phases in even more samples than the previous series. The two phases $[Cu(BTC\text{-}H_2)_2(H_2O)_2]\cdot 3H_2O$ and $[Cu_2(BTC)(OH)(H_2O)]$ were found in the control experiments performed at 120 °C and in the experiments performed with OA at ratio OA to $H_3BTC$= 5 and room temperature or 120 °C. In the experiments performed with DA, they were presented in all the samples performed at ratio DA to $H_3BTC$= 5 and at ratio DA to $H_3BTC$= 25 at room temperature and 90 °C, while at 120 °C just $[Cu(BTC\text{-}H_2)_2(H_2O)_2]\cdot 3H_2O$ was detected. Furthermore in the experiments performed with OA at ratio OA to $H_3BTC$= 25 and 120 °C at time 1 and 3 hours the phase $Cu(BTC)(H_2O)_3$ was detected. However when the order of introduction of solvents is EtOH/$H_2O$ the octanoic acid showed a stronger effect on the morphologies of the particles, such as forming worm-like structures.

The results obtained in the solvothermal synthesis (Paragraph 3.2.1) and the results obtained under these synthetic conditions differed in terms of purity of HKUST-1 phase obtained. However the solvothermal synthesis was optimized for the formation of HKUST-1[52] while the current

synthesis was designed in order to favour the interaction between the surfactant and precursors and to slow down the kinetics of the reaction. The presence of other phases related to the copper(II)/$H_{3-n}$BTC system (n=1-3) indicated that HKUST-1 was no longer the favoured product and that there was an increased variability in the synthesis products.

This system was considered as a sort of equilibrium between copper(II)/$H_{3-n}$BTC phases, where choosing the right set of conditions the manipulation of HKUST-1 in terms of macroscopic structure would be higher. On the other hand in the optimized synthesis the assembly of the MOF and the kinetics of the process was probably fast, in order to gain a pure phase of HKUST-1 and therefore reducing the degree of control on the physical form of the material.

This might explain the formation of worm-like structures and rounded particles with carboxylic acid amphiphiles, while in the experiments performed according to the optimized synthesis just an effect on the particle size was detected.

#### 3.2.3.2.3 Characterization of Rp-HKUST-1

The experiment performed at ratio DA to $H_3$BTC= 25 and temperature 120 °C (PXRD pattern showed in Figure 3.29 f), hereafter named rp-HKUST-1, where rp stands for rounded particles, was selected for further characterization analysis (SEM, TEM, BET). Further SEM and TEM images were shown below in Figure 3.31.

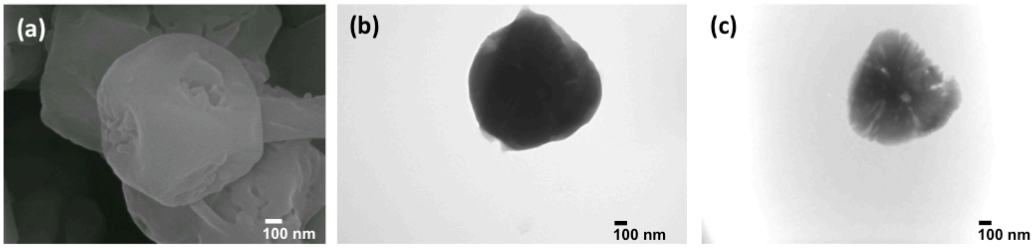


**Figure 3.31 SEM and TEM images of rp-HKUST-1.**

SEM images showed the rounded particles, where the average size distribution of the particles was around 800 nanometers (Graph 3.1). Further TEM images performed at different brightness showed the presence of channels that point into the centre of the rp-HKUST-1, which might indicate presence of mesoporosity (Figure 3.31 b and c).

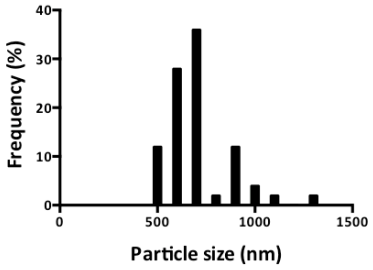


**Graph 3.1 Particle size distribution of rp-HKUST-1 calculated after measuring 50 capsules and expressed in percentage.**

Nitrogen sorption analysis of rp-HKUST-1 and BJH adsorption and desorption distribution are shown below (Figure 3.32 and Figure 3.33).

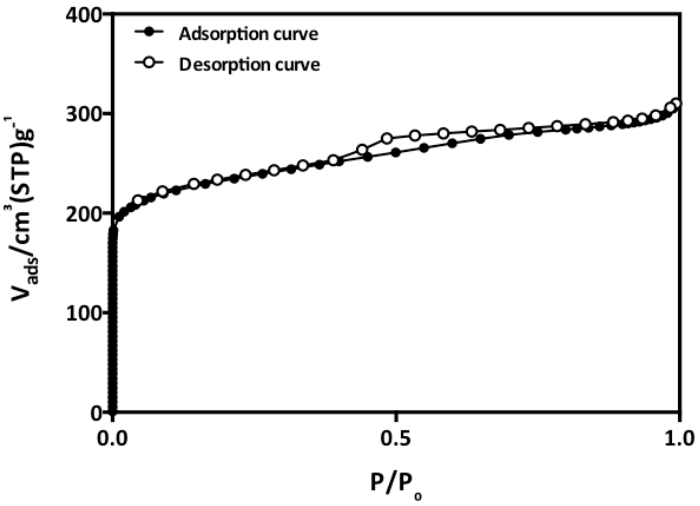


**Figure 3.32 Nitrogen sorption analysis of the rp-HKUST-1 sphere-like particles measured at 77K.**

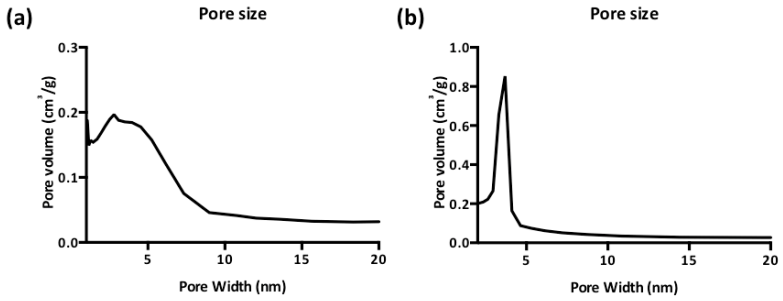


**Figure 3.33 The pore size determined by (a) BJH adsorption and (b) BJH desorption pore distribution.**

The isotherm of rp-HKUST-1 exhibited a behaviour between types I and IV, with a large uptake at low pressure and a clear hysteresis loop upon desorption. The large uptake at low pressure was related to the presence of the inherent micropores of the HKUST-1 framework, while the hysteresis in the desorption branch was characteristic of mesopores, according to the channels observed in the TEM images (Figure 3.31 b and c). The BET surface area detected showed a drop

compared to the commercial HKUST-1, which might be related to the presence of mesoporosity[145] and the presence of $[Cu(BTC\text{-}H_2)_2(H_2O)_2]\cdot 3H_2O$ (respectively 873 and 1500 $m^2/g$). Finally BJH graphs indicated the pore size: the peak of the adsorption graph is broader but both are pointed around 4 nm.

Due to the fact that DA showed both modulator and surfactant properties, the proposed mechanism for the formation of rp-HKUST-1 sphere-like particles was the following: DA formed micellar structures around which the inorganic phase could grow leading to the observed mesoscopic pores and it also acted on the external surface controlling the morphology and the size of the sphere-like particles, as shown in Figure 3.34. A similar effect on the crystal morphology and mesoporosity was observed by Pham *et al.* as discussed in the introduction.[119]

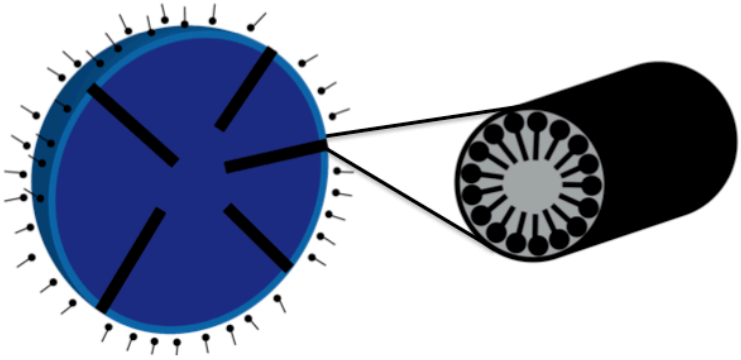

**Figure 3.34 Proposed mechanism for the formation of rp-HKUST-1 sphere-like particles: DA acts on both the external and the internal surface**

These results further underlined the importance of the synthetic conditions, which allowed or not the formation of the surfactant mesophase and the MOF mesostructure, therefore the same surfactant/modulator species could just act on the external surface of the MOF[105, 164] or also on the internal one, as demonstrated here.

3.2.3.2.3.1 Attempts of purification of Rp-HKUST-1

The PXRD pattern of rp-HKUST-1 (Figure 3.29 f) showed the presence of the phase $[Cu(BTC\text{-}H_2)_2(H_2O)_2]\cdot 3H_2O$ and different attempts in order to remove it were performed, including sample washing in different solvents and optimization of the reaction parameters (stirring time, order of introduction of the reagent, solvent, scale up of the reaction, variation of the heating time and temperature). Generally when the PXRD pattern showed HKUST-1 as a pure phase the rounded morphology was not maintained, while when the rounded morphology of the particles was kept the PXRD pattern showed the two phases, which occurred just under a narrow set of experimental conditions (increment of the reaction heating time to 20 hours). Due to the different

morphology and dimension reported for the two phases (rod-like shape crystals of few microns for $[Cu(BTC\text{-}H_2)_2(H_2O)_2].3H_2O$ and sphere-like particles of 500 nm sizes for HKUST-1), separation by centrifugation was attempted, but this proved to be unsuccessful.

A new strategy for the removal of the second phase was planned considering its chemical composition: $[Cu(BTC\text{-}H_2)_2(H_2O)_2].3H_2O$ is characterized by bi-protonated BTC, so increasing the pH should prevent its formation, however probably also altering the availability of the surfactant. Basic agents were added to the mixture, namely NaOH or $Et_3N$, or decreasing the water percentage in the synthesis mixture was performed (from 42 to 36%). Both the basic agents led to an increase of the impurity phase, according also to the literature.[163, 165] The decrement of water percentage led to the removal of the phase but the spherical shape of the particles was not maintained (Figure 3.35 and Figure 3.36).

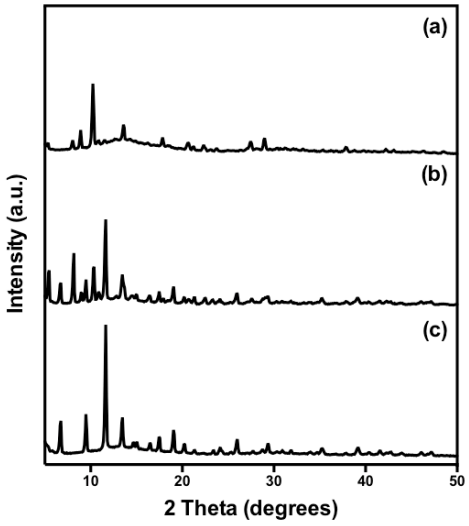


**Figure 3.35 PXRD patterns of the samples performed adding (a) sodium hydroxide, (b) triethylamine or (c) reducing the amount of $dH_2O$ from 42 to 36% to the reaction synthesis.**

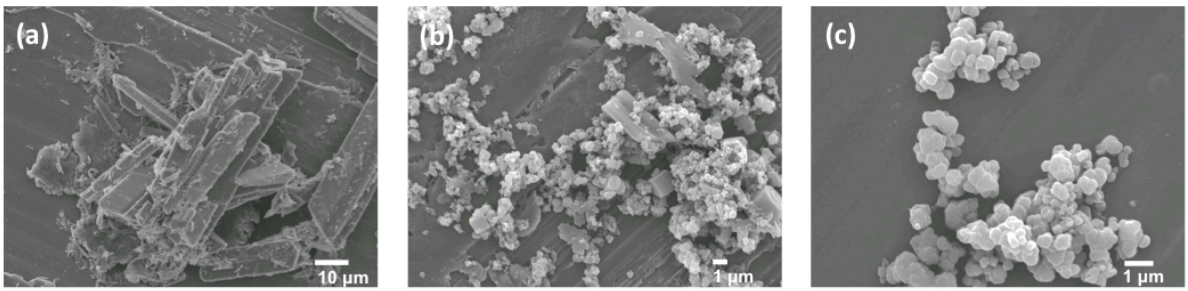


**Figure 3.36 SEM images of the samples performed adding (a) sodium hydroxide, (b) triethylamine or (c) reducing the amount of $dH_2O$ from 42 to 36% to the reaction synthesis.**

## 3.3 Conclusions

The strategy for the introduction of mesoporosity in MOFs framework was initially inspired by the synthetic method used for mesoporous silica.[154, 166] However in the case of MOFs the formation of mesostructured framework was not easy and the main requirement to fulfil was the co-assembly between the surfactant mesophase and the MOF precursors.[146] Especially the strength of the interactions were crucial for the formation of mesoporous materials. Too strong interactions would avoid the MOFs formation and too weak would prevent the templating effect of the surfactant mesophase. Ultimately also the other synthetic parameters, such as salt precursors, pH, solvent and reaction temperature strongly influenced the system therefore *a priori* designing the synthetic procedure was needed.

The effect of the surfactant Pluronic-P123 demonstrated those considerations: even though it was successfully used for the synthesis of mesoporous silica[166] it did not have the same effect on HKUST-1, where instead reduced the particle size, which indicated that an interaction had occurred, but the surfactant might interact with the external surface of the crystal rather than the internal part.[106]

Therefore the understanding of a more specific interaction surfactant mesophase/MOF precursors and the importance of the synthetic conditions led to make some change in the procedure, such as SBU-like precursor copper salt (copper acetate), surfactant with modulator properties (carboxylic acids) and synthetic conditions which favoured the surfactant-precursors interactions. In general this set of experiments was characterized by the formation of other phases of the copper(II)/$H_{3-n}$BTC system (n=1-3), but under the suitable conditions higher control over particle morphology and mesoporosity were reached (worm-like structure and rp-HKUST-1).

In summary in the previous chapter a wide range of synthetic conditions were tested, but just in a specific case it led to mesoporous HKUST-1, which underlines that the introduction of mesoporosity in MOF was not an easy target. It seemed to be just a small window of conditions in which the templating effect on MOFs can occur, therefore the choice of the surfactants and all the other synthetic parameters was crucial. A precise and rational design of all the parameters of the reaction was then needed to achieve the results.

## 3.4 Experimental part

**SOLVOTHERMAL SYNTHESIS OF HKUST-1:** a solution of $Cu(NO_3)_2 \cdot 2{,}5H_2O$ (0.3489 g, 1.5 mmol) in distilled water (5.5 ml) was stirred with a solution of $H_3$BTC (0.210 g, 1 mmol) in pure ethanol (5.5 ml) for 30 minutes and then put into a teflon-lined steel autoclave. After 15 hours at 110°C, the

autoclaves were immediately cooled down to room temperature. The product was filtered and washed 3 times with ethanol (20 ml) and dried in air. Finally it was extracted twice with ethanol for 4 hours at 60°C.

**ROOM TEMPERATURE SYNTHESIS OF HKUST-1:** $H_3BTC$ (0.03g, 0.16 mmol) and ethanol (15-X mL, X=0, 3, 4.5, 6.5, 10.5, 12, 13.5, 14.25, 15) were added to an aqueous solution of $Cu(OAc)_2 \cdot 2.5H_2O$ (0.048g, 0.24 mmol, X mL) and stirred for 1 day. The product was filtrated and washed 3 times with ethanol (10 ml) and dried in air.

**SYNTHESIS OF HKUST-1 WITH CARBOXYLIC ACIDS**: Dodecanoic acid (0.7 or 2.5 g, respectively 3.5 and 12.5 mmol) or octanoic acid (0.5 or 1.8 g, respectively 3.5 and 12.5 mmol) was dissolved in 25 ml of distilled $H_2O$ (or EtOH) and stirred for 30 minutes, then copper acetate hemi(pentahydrate) (0.16 g, 0.8 mmol) and 2 ml of distilled $H_2O$ (or EtOH) were added and stirred for 2 hours. Finally $H_3BTC$ (0.1 g, 0.5 mmol) and 20 ml of ethanol ( or distilled $H_2O$) were added and stirred for one day. The reaction was carried out solvothermally (90 or 120°C) or at room temperature for 17 hours. The product was filtrated and washed 3 times with ethanol (20 ml) and dried in air.

**SYNTHESIS OF HKUST-1 WITH BASIC AGENTS:** Dodecanoic acid (2.5 g, 12.5 mmol) was dissolved in 25 ml of EtOH and stirred for 30 minutes, then copper acetate hemi(pentahydrate) (0.16 g, 0.8 mmol) and 2 ml of EtOH were added and stirred for 2 hours. Finally an aqueous solution of $H_3BTC$ (0.1 g, 0.5 mmol in 20 ml of distilled $H_2O$) and basic agent (NaOH=200 µL or $Et_3N$= 70 µL) was added and the resulting solution stirred for one day. The reaction was carried out solvothermally (120°C) for 17 hours. The product was filtrated and washed 3 times with ethanol (20 ml) and dried in air.

All the experiments where performed at least 3 times in order to ensure reproducibility.

# Chapter 4: ZIF-8 hollow capsules

## 4.1 Introduction

MOF superstructures, i.e. higher-dimensionality ordered structure obtained via self-assembly of nano- or micron sized building blocks (BBs), are promising materials for the improvement of the properties of the materials resulting from the higher-order architecture. For example the alignment of the pore given by the control over the crystal orientation would maximise the separation capacities,[122] as discussed in the introduction. In this chapter superstructures based on hollow spheres were considered: they were promising for many applications such as drug delivery, energy storage and chemical catalysis.[95, 167] Furthermore the intrinsic microporosity of MOFs would make them even more useful as permeable capsules with the potential to become size-selective reaction systems where molecules in either oil or water phases enter via the nanopores and react inside[168] and the encapsulation of functional species, e.g. nanoparticles or biomolecules, into them might enhance their potential as catalysis by protecting them from the external environment and improving recovery and recyclability.[169] Scheme 4.1 illustrates the most common strategies for the formation of hollow MOF-based capsules, which include templating using hard particles or surfactant-assemblies, Pickering-based emulsion droplet systems, spray-drying and liquid-liquid interfacial synthesis.

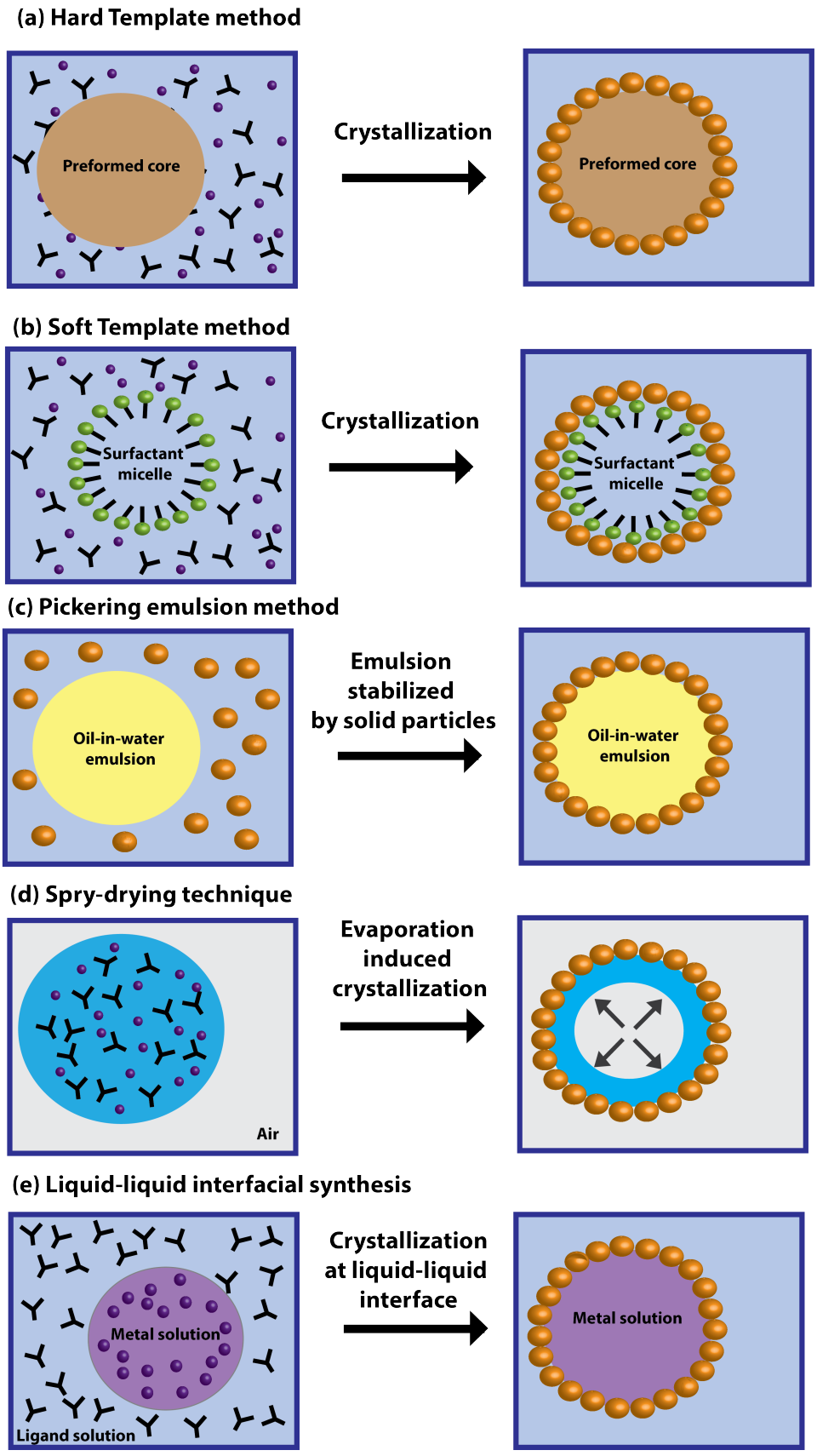


**Scheme 4.1 Synthetic strategies for the formation of MOF hollow spheres or capsules: (a) hard template method, (b) soft template method, (c) Pickering emulsion method, (d) spray-drying technique and (e) liquid-liquid interfacial synthesis**

In the hard template method the template usually a pre-shaped solid particle is used as a scaffold around which an external shell of the desired material is formed. Usually it is functionalized with appropriate active sites in order to promote the nucleation and growth of the MOF crystals onto its surface, or it can act as the metal source for MOF formation (also called liquid-solid interfacial reaction or sacrificial reaction). The resulting material is initially a composite of core-shell structure until the template is removed (e.g. by etching) to leave the desired hollow sphere. In the literature there are a few examples of the hard template method for the formation of hollow MOF spheres. Hollow ZIF-8 microspheres were formed by using spherical polystyrene (PS) spheres as templates.[170] PS@ZIF-8 core-shell structures were accessed by a stepwise solvothermal reaction, where carboxylate-terminated PS spheres were added to the standard ZIF-8 synthesis mixture. The functionalization on the PS spheres allowed the spatial control of the MOF crystallization, while the shell thickness was controlled by altering the number of growth cycles. The as-prepared PS@ZIF-8 core–shell microspheres were then immersed in DMF to selectively remove the PS cores and induced the formation of hollow ZIF-8 microspheres where the shape was maintained after removing the template (Figure 4.1).

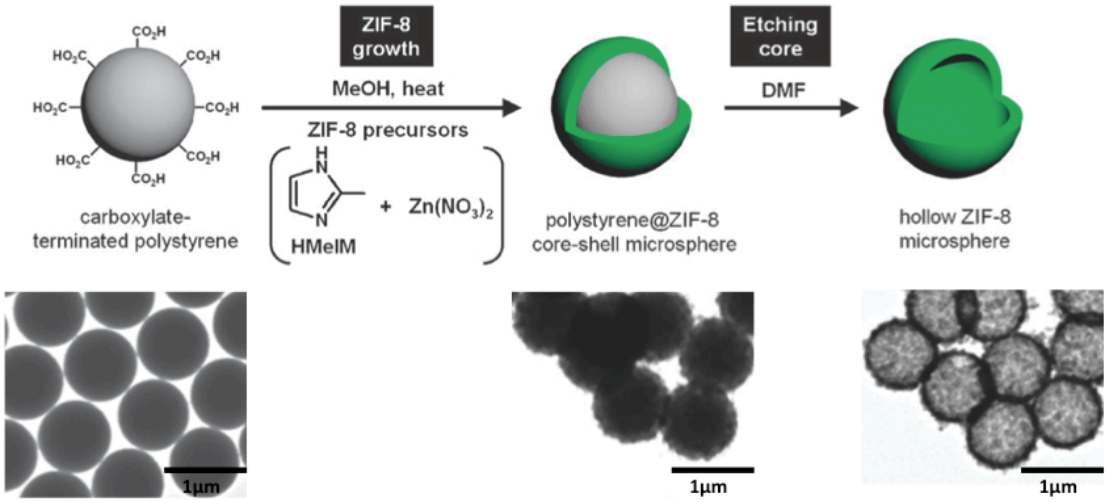


**Figure 4.1 Schematic representation of the preparation of polystyrene@ZIF-8 core–shell and hollow ZIF-8 microspheres from carboxylate-terminated polystyrene spheres with the related TEM images. Adapted with permission from the ref.[170]**

Recently Tsung and co-workers synthesized yolk-shell Pd@ZIF-8 nanostructures.[171] The synthetic strategy involved coating a Pd nanocrystal with a layer of $Cu_2O$ as a sacrificial template and then a layer of polycrystalline ZIF-8. $Cu_2O$ was spontaneously etched away during the ZIF-8 crystallization process due to imidazole protons liberated during the ZIF assembly process leading to the formation of the yolk-shell structure. The microporous shell, large internal cavity and encapsulated noble metal nanocrystal made this material suitable for size-selective catalysis of hydrogenation reactions (Figure 4.2).

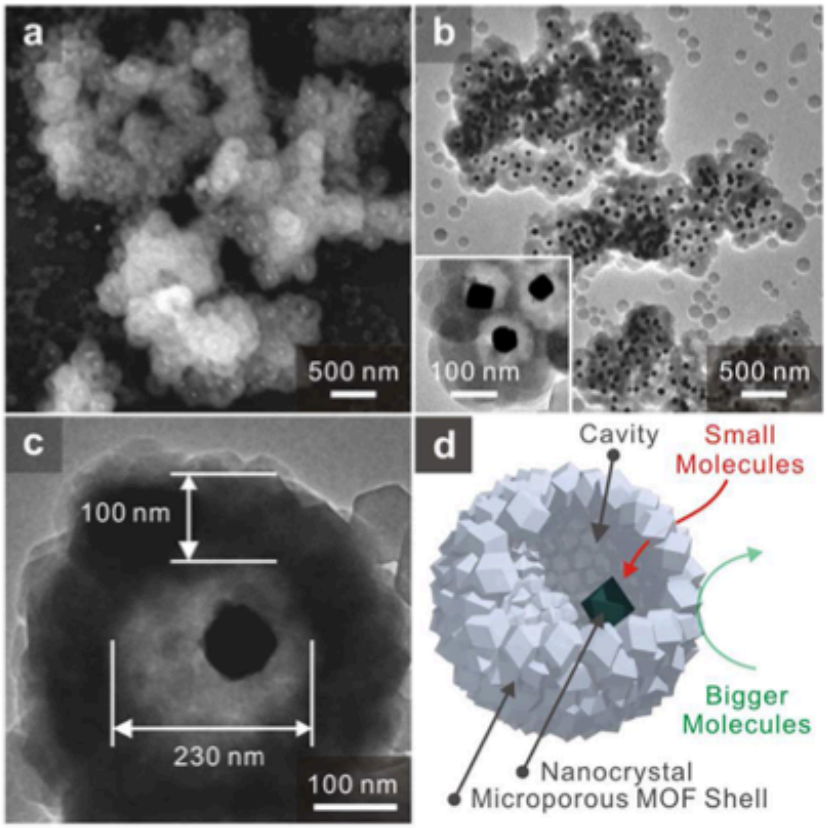


**Figure 4.2 Nanocrystal@ZIF-8 yolk-shell nanostructures. (a) SEM and (b, c) TEM images. The cores are Pd octahedra with edge sizes of 60 nm, and the shells are microporous ZIF-8 with thickness of ≈ 100 nm. (d) Schematic sketch of the yolk!shell nanostructure. Reprinted with permission from ref.[171]**

The soft template method generally involved the use of surfactants or other amphiphilic molecules which were assembled into superstructures by non-covalent interactions which could then act as templates for MOF formation. Also in this case the interaction between the surfactant and the MOF precursors should be of sufficient strength to ensure spatial control of the nucleation of MOFs and prevent phase segregation.[92]

ZIF-8 hollow nanospheres were synthesized by a surfactant-template strategy using sodium dodecyl sulfate (SDS).[172] The micelles formed by the surfactant acted as template for the formation of the hollow nanosphere, where the spatial control of the crystallization was ensured by the interaction between the $Zn^{2+}$ and the oxygen atoms of the hydrophilic groups of the surfactant. The surfactant template was removed simply by washing, ensuring the ZIF-8 would not be damaged. Furthermore the hollow ZIF-8 spheres were found to be suitable for the encapsulation of the anti-cancer drug 10-Hydroxy Camptothecin (HCPT). HCPT was directly added into the synthesis with SDS; the SDS assembly constructed into micelles with HCPT inside and when the zinc salt and 2-methylimidazole were added in sequence, HCPT@ZIF-8 hollow nanospheres were obtained as confirmed by confocal laser scanning microscopy.

The third method involved Pickering emulsions, which is an emulsion where the droplets (internal phase) are stabilized by solid particles adsorbed at the interface of the two phases, and the resulting hollow spheres are called colloidosomes.[173] Colloidosomes are self-assembled hollow capsules with sizes ranging from micrometers to millimeters. The capsule surfaces are typically composed of close-packed layers of colloidal particles, linked together to form a solid shell, where the interstices between the particles form an array of uniform pores.[95] Colloidosomes were previously prepared using particles of diverse composition including latex, silica, clay, metal oxides and gold nanoparticles.[174] MOF based colloidosomes were reported by Huo *et al.* who demonstrated that oil-in water (o/w) Pickering emulsions could be formed using MOF particles displaying suitable wettability and mid-range zeta potentials allowing their efficient partitioning to the oil-water interface. This was exploited to prepare PS@ZIF-8 composite colloidosomes using a two-step emulsion-based method.[175] The o/w Pickering emulsions were first stabilized by the assembly of pre-formed ZIF-8 nanoparticles at the o/w interface and when the organic inner phase contains monomers, cross-linkers and an initiator these stable "MOF-somes" could act as polymerisation microreactors to form the desired composite microcapsules via polymer-induced phase separation of a cross-linked polystyrene (PS) membrane which locks the MOF particles into the external surface of the resulting hollow composite capsules (Figure 4.3).

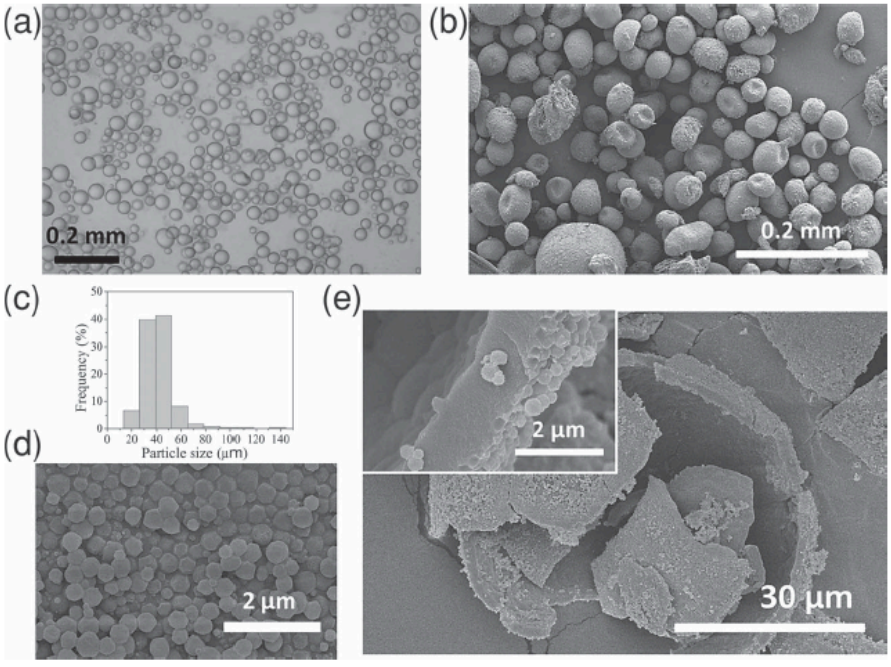


**Figure 4.3 a) Optical microscopy image of a typical o/w emulsion stabilized by ZIF-8 NPs. b) SEM image of intact ZIF-8@PS microcapsules. c) Size distribution of the microcapsules shown in (b). d) SEM image of the surface of a single microcapsule showing embedded ZIF-8 NPs. e) SEM image (and inset) of a single broken capsule revealing the hollow interior. Reprinted with permission from ref.[175]**

The method was demonstrated to be relatively general and different MOF@polymer capsules (MOF = ZIF-8, MIL-101 and UiO-66) were readily formed. Finally ZIF-8@PS was loaded with the dye molecule oil red O in order to evaluate the shell permeability.

Extending this work to reverse-phase emulsions the encapsulation of biomolecules within MOF-based microcapsules was also demonstrated.[168] Indeed agarose hydrogel droplets Pickering-stabilized by UiO-66 and magnetite nanoparticles were used as a templare around which to deposit a hierarchically structured ZIF-8 shell. Robust, highly microporous microcapsules readily attracted to a magnet were fabricated. Furthermore the hydrogel core provides a facile means to encapsulate large biomolecules, such as enzymes, for recyclable size-selective biocatalysis.

Furthermore *Eddaoudi et al.* described the fabrication of 3D hollow Fe-soc-MOF $[Fe_3O(abtc)_{1.5}(H_2O)_3](NO_3)(H_2O)_3$ (abtc = 3,3',5,5'-azobenzenetetracarboxylate) colloidosomes by a one-step emulsion technique.[176] The solvothermal reaction was carried out in the presence of *tert*-butylamine and TWEEN-85 (polyethylene (20) sorbitan trioleate), where the amine acted as a modulator for the formation of cubic monodisperse BBs of the Fe-soc-MOF and the TWEEN-85 simultaneously formed emulsion droplets around which the BBs spontaneously self-assemble into the observed colloidosomes. The colloidosomes shell was constructed from a monolayer of BBs, whose dimensions could be precisely controlled by varying the amount of emulsifier used in the synthesis (Figure 4.4). While these structures were very well defined overall, large gaps remain between particles in the shell, which may limit their practical use in molecular encapsulation technologies.

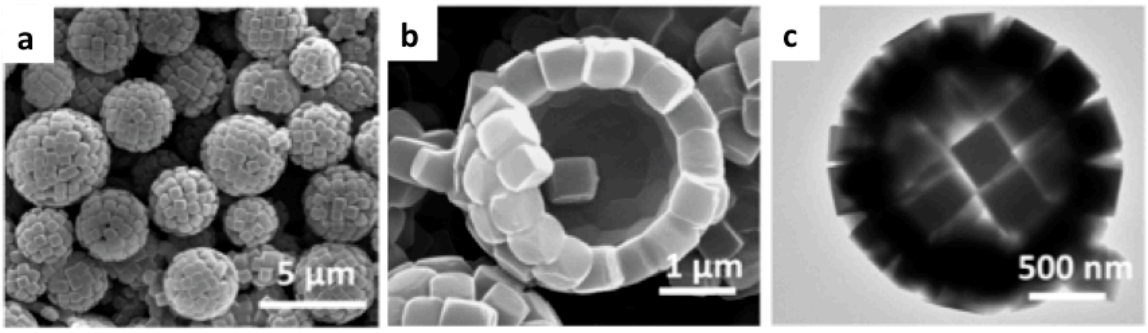


**Figure 4.4 Small Fe-soc-MOF hollow colloidosomes prepared by adding TWEEN-85: (a–e) SEM and (f) TEM images. Adapted with permission from ref.[176]**

The spray-drying technique is a method of producing a dry powder from a liquid by rapidly drying with gas.[177] If MOF precursors are contained in the liquid phase by controlling the evaporation location and speed at the air–liquid interface crystallization would start and the superstructures would form adopting the shape of the interfaces. Maspoch *et al.* reported the use of this technique as a versatile methodology for the synthesis and self-assembly of nanoMOFs into

spherical hollow superstructures.[178] By inducing the solvent evaporation in the microdroplet, the precursors were radially diffused to the droplet surface and were concentrated at the surface region. Once the concentration reached a critical value, the MOF crystallization occurred at the droplet surface and the resulting crystals were accumulated to form a hollow spherical superstructure. This was demonstrated for a number of prototypical MOFs and sonication broke up the superstructures to leave MOF nanoparticle dispersions. Furthermore the spray-drying technique allowed the construction of multicomponent MOF superstructures and the encapsulation of guest species within the hollow spheres by carefully choosing the starting materials and the reaction conditions (Figure 4.5).

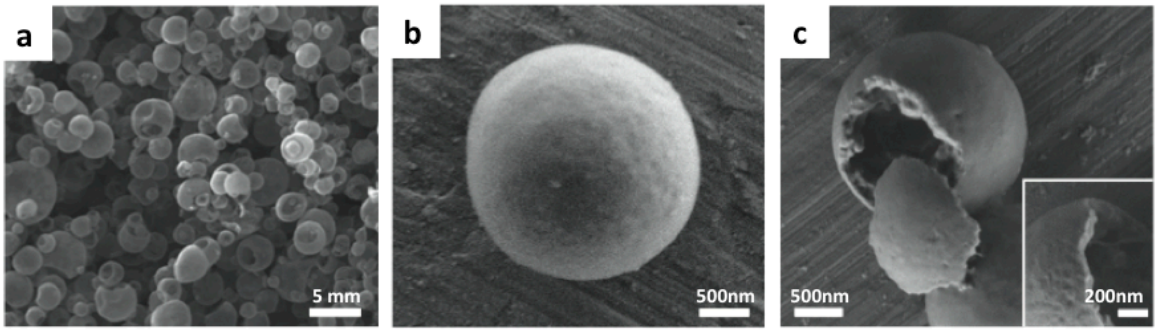


**Figure 4.5 SEM images of hollow HKUST-1 superstructures synthesized by spray-drying technique: (a) general view of the spherical HKUST-1 superstructures, (b) the wall of a single HKUST-1 superstructure showing the assembly of nanoHKUST-1 crystals and (c) a mechanically broken hollow superstructure showing the internal cavity and the thickness of its wall. Adapted with permission from ref.[178]**

Synthesis of MOFs at a liquid-liquid interface relied on the ability to dissolve the metal ions and organic linkers for framework formation into two immiscible liquids. In such biphasic reaction systems framework nucleation occurred only at the interface where the resulting MOF takes on the shape of the interface. De Vos *et al.* reported the direct synthesis of hollow HKUST-1 capsules via a droplet-templating route.[179] The injection of water by a syringe produced the water droplet in the organic phase under continuous flow conditions and the size of the resulting hollow capsules was controlled by adjusting the ratio of the inner and outer flows, and thus the injection speed of each phase. In particular hollow capsules with uniform diameter of 375 (± 15) µm and uniform shell thickness of 1.5-2 µm were obtained (Figure 4.6).

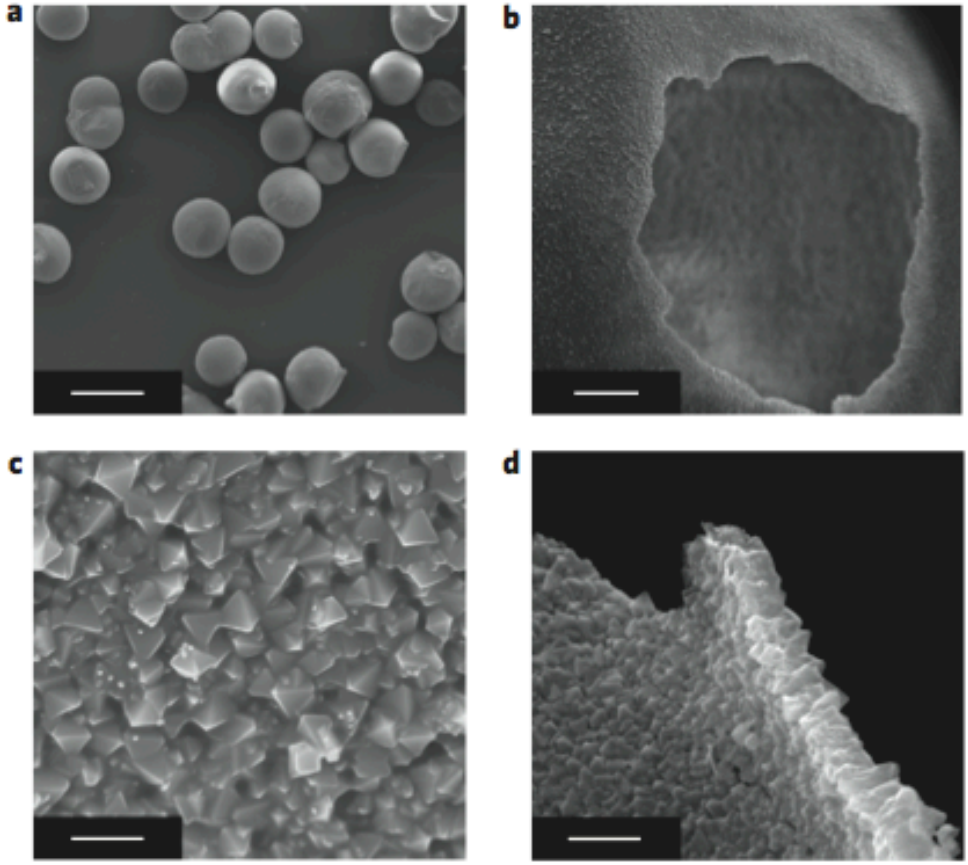


**Figure 4.6 Scanning electron micrographs of hollow [$Cu_3(BTC)_2$] capsules. a, Overview of several capsules illustrating their monodispersity. The capsules retain their spherical shape upon drying. Scale bar, 500 mm. b, Capsule crushed with a needle tip showing its hollow interior. Scale bar, 25 mm. c, Detail of the defect-free capsule wall. Gaps between larger crystals are sealed by intergrown smaller ones. Scale bar, 2 mm. d, Cross-sectional view of the capsule wall, showing its thin and uniform thickness. Scale bar, 2 mm. Reprinted with permission from ref.[179]**

Moreover the hollow capsules demonstrated selective permeability directly related to the micropore size of the MOF crystallites forming the capsule wall: molecules of different sizes were included in the inner phase of the capsule during synthesis and it was demonstrated that small molecules such as ethylene glycol were able to diffuse freely through the MOF membrane but large dyes such as Rose Bengal were not.

Moreover hollow ZIF-8 nanospheres with controllable shell thickness were also obtained by emulsion-based interfacial reaction methods.[169] The nucleation and growth of ZIF-8 nanocrystals and their formation of continuous shells took place at the water/1-octanol interface stabilized by polyvinylpyrrolidone (PVP), where the nanosized emulsion droplets acted as soft-templates. Furthermore Pd nanocubes could be encapsulated during the emulsification process into the hollow ZIF-8 nanospheres and used for heterogeneous catalysis.

Despite the advances outlined above, it is noted that successful and controlled superstructure formation is still challenging. In this regard the self-assembly properties of ZIF-8 crystals were

further investigated in this chapter. ZIF-8 was selected as a prototypical MOF because its crystals have already shown directional self-assembly properties forming ordered supracrystals without the use of template (due to van der Waals attractions between the flat faces of the crystals) or under an external electric field [122, 180] and beyond the aforementioned hollow capsules other superstructure have already been formed by ZIF-8, such as hollow ZIF-8 nanoworms by template-directed synthesis from block copolymers.[181] ZIF-8 is also readily prepared under a range of synthetic conditions, including in aqueous solution at rt, which should further ensure compatibility with soft-templating assembly approaches.

Hereafter the synthesis of ZIF-8 in aqueous media at room temperature[182] in the presence of the surfactant SPAN-80 (sorbitan monooleate) and/ or dodecane has been fully investigated. At first a preliminary study on the effect of SPAN-80 in the synthesis of ZIF-8 is described, then the conjunct use of dodecane and SPAN-80 was analysed. The dodecane and dodecane/SPAN-80 emulsion preparation was optimized employing a shear force instrument, which ensures higher homogeneity and stability, and ZIF-8 hollow capsule prepared. Finally the hollow capsules obtained previously via dodecane or dodecane/SPAN-80 emulsion were treated with imidazole leading to flower-like microcapsule.

## 4.2 Results and discussion

### 4.2.1 Preliminary studies

SPAN and TWEEN are two classes of related surfactants (sorbitan esters and ethoxylated SPANs, Figure 4.7, Appendix A), which were already used in the synthesis of MOF leading to interesting results on the macroscopic structure, such as control over the particle size of ZIF-8 [183] and superstructure formation of Fe-soc-MOF.[176]

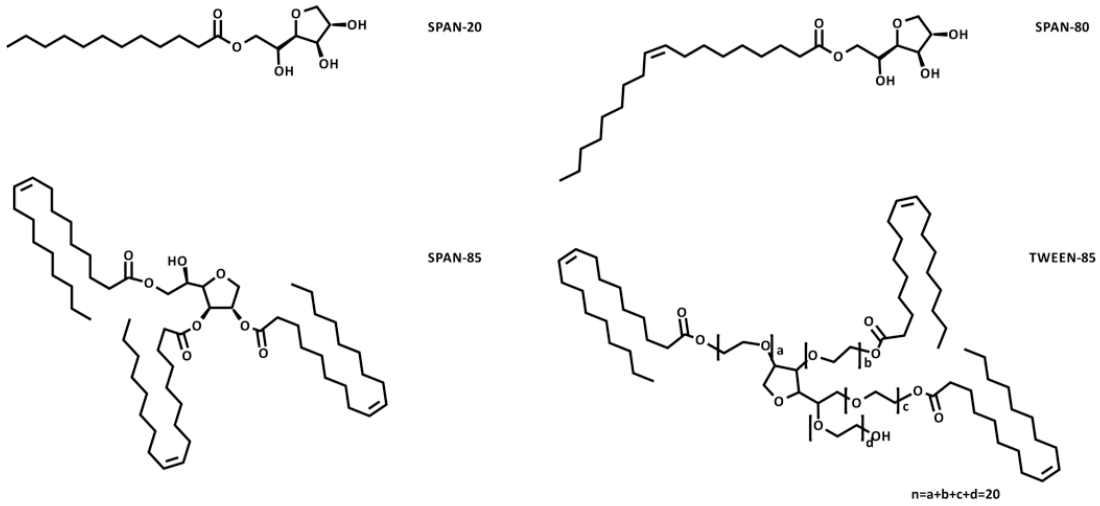


**Figure 4.7 Illustration of SPAN-20, SPAN-80, SPAN-85 and TWEEN-85.**

Therefore ZIF-8 was chosen as prototypical MOF and its macroscopic structure investigated through the use of the surfactant SPAN-80. The synthesis conditions were chosen in order to facilitate the supramolecular organization of the surfactant. In a typical synthesis SPAN-80 was dissolved in 5 mL of water and stirred for variable times at room temperature, then a zinc nitrate solution (29 mg in 0.5 mL $dH_2O$) and methylimidazole solution (560 mg in 2 mL $dH_2O$) were added and left under stirring for a further two hours. In general the reaction can be classified as being a two step process: the dissolution of SPAN-80 in water, also called emulsion step, and the addition of zinc and methylimidazole solution, which leads to the MOF formation, also called ZIF-8 synthesis step. Hereafter the two steps were investigated under different aspects: firstly the concentration of SPAN-80 in the solution was varied in order to have a first screen of its effect on the synthesis. PXRD patterns and SEM images of the experiments performed at different concentrations, where respectively 18, 54, 90, 126 and 162 mg of the surfactant were dissolved in 5 mL of water and stirred for 1 hour, are shown below in Figure 4.8 and Figure 4.9.

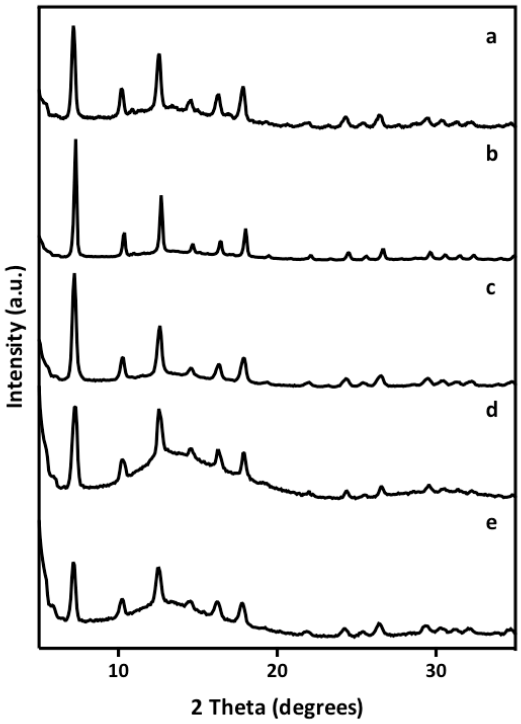


**Figure 4.8 PXRD patterns of the ZIF-8 experiments performed in aqueous solution at room temperature with respectively (a) 18, (b) 54, (c) 90, (d) 126, (e) 162 mg of SPAN-80.**

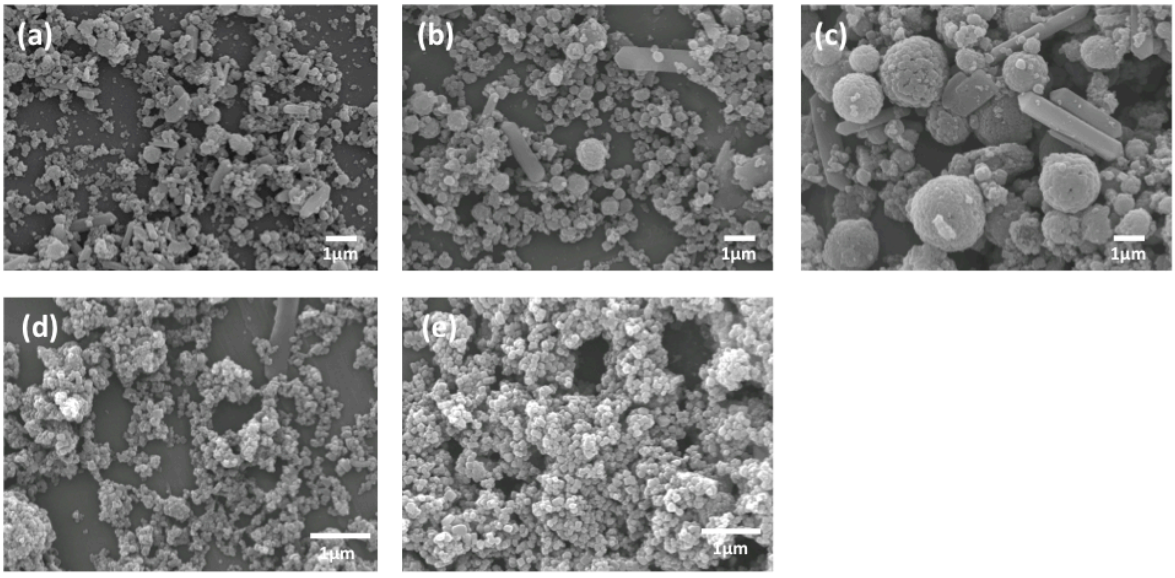


**Figure 4.9 SEM images of the ZIF-8 experiments performed in aqueous solution at room temperature with respectively (a) 18, (b) 54, (c) 90, (d) 126, (e) 162 mg of SPAN-80.**

As indicated from the PXRD patterns all the experiments successfully formed ZIF-8, meaning that the introduction of SPAN-80 did not interfere with the MOF synthesis (Figure 4.8). Interestingly the variation of SPAN-80 concentration appeared to influence the morphology of the resulting ZIF-8 particles.

When only 18 mg of SPAN-80 was added polydisperse particles, from nanoparticles to micron-sized rod-like particles were formed (Figure 4.9 a). Increasing the amount of SPAN-80 to 54 mg, led to the same types of particles observed at the lower SPAN-80 concentration, but now a few spherical colloidosome-type assemblies were also present (Figure 4.9 b), which increased in number as more SPAN-80 was added; e.g. at 90 mg of surfactant mostly colloidosomes and micronsize rods were detected (Figure 4.9 c). Finally when the SPAN-80 concentration was $\geq$ 126 mg (Figure 4.9 d, e), just nanoparticles were detected, which might indicate a variation in the supramolecular organization of SPAN-80, even though to the best of our knowledge no data about the behavior of SPAN-80 in these conditions have been reported. It was further noted that when greater levels of SPAN-80 were employed, the PXRD patterns showed in Figure 4.8 exhibited a higher amorphous background which probably arose from the lower amount of products obtained from the synthesis.

The reaction carried out in the presence of 90 mg of SPAN-80, which led to the formation of colloidosomes (Figure 4.9 c), was further investigated analyzing the two reaction steps and compositional parameters in order to gain a better understanding of the reaction mechanism with a view to optimizing the colloidosome assembly. Regarding the first step, i.e. the formation of the emulsion, SPAN-80 dilution and stirring time and the combined effect of SPAN-80 with the surfactant CTAB were tested. In the ZIF-8 synthesis step the synthesis time, the effect of the stirring and the addition of imidazole as a competitor ligand were explored and compositional parameters such as solvent and MOF precursor were varied.

#### 4.2.1.1 Emulsion step

Emulsions and supramolecular organization of surfactants depend also on concentration of the surfactant in solution, nature of the surfactant itself and time,[184-185] therefore in the next section these parameters were investigated.

At first the effect of SPAN-80 dilution as a factor that could influence the supramolecular organization was investigated. The amount of SPAN-80 was kept constant at 90 mg and was dissolved in 5 mL $H_2O$, as in the previous synthesis, or decreased to 2.5 or increased to 10 mL and stirred for 5 hours at room temperature. The stirring time was increased from 1 to 5 hours in order to facilitate the supramolecular organization of SPAN-80, then zinc nitrate solution and methylimidazole solution were added and the reaction carried out for 2 hours. PXRD patterns and SEM images are shown below in Figure 4.10 and Figure 4.11.

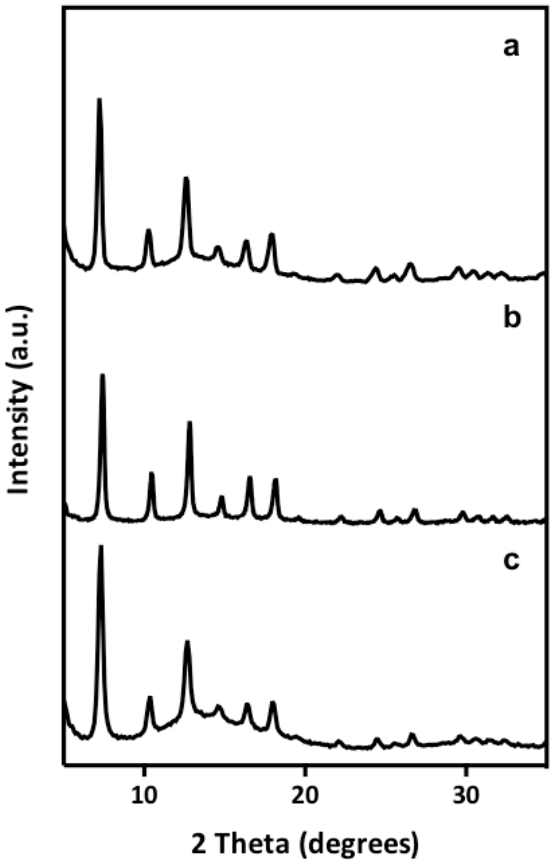


**Figure 4.10 PXRD patterns of the ZIF-8 experiments performed in aqueous solution at room temperature with 90 mg of SPAN-80 at different diluitions: respectively (a) 2.5, (b) 5, (c) 10 mL of $H_2O$.**

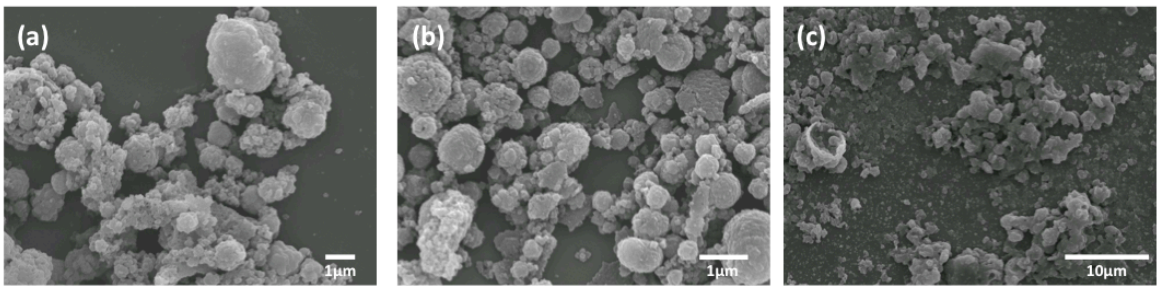


**Figure 4.11 SEM images of the ZIF-8 experiments performed in aqueous solution at room temperature with 90 mg of SPAN-80 at different dilutions: respectively (a) 2.5, (b) 5, (c) 10 mL of $H_2O$.**

PXRD patterns confirmed that pure ZIF-8 phase was formed in all the experiments (Figure 4.10), while SEM images revealed that the best conditions for colloidosome assembly were obtained when SPAN-80 was dissolved in 5 mL of $H_2O$ (Figure 4.11 b). When the surfactant was dissolved in 2.5 or 10 mL of $H_2O$ (respectively Figure 4.11 a and c) a larger number of unaggregated ZIF-8 nanoparticles were detected, probably due to the transition to different mesophases of SPAN-80 supramolecular organization. Furthermore the longer stirring of the surfactant (5 hours) enhanced the number of colloidosomes formed compared to the initial study where stirring was only carried out for 1 hour.

The reaction was then investigated by varying the surfactant composition, where SPAN-80 was mixed with the cationic surfactant CTAB. As discussed in the introduction, CTAB can tune the morphology of ZIF-8 crystals[106] and maybe imparting a shape which makes them more suitable for the superstructure formation. Furthermore in mixed surfactant system the surfactants often exhibit synergism in their effects on the properties of the system, such as in substantially lower the CMC and interfacial tension.[186]

90 mg of SPAN-80 (0.21 mmol) and respectively 38, 8 and 4 mg of CTAB (respectively 0.105, 0.02 and 0.01 mmol, ratio SPAN-80:CTAB=1:0.5, 1:0.1, 1:0.05 respectively) were dissolved in 5 mL of $H_2O$ and stirred for 5 hours, then the zinc nitrate solution and methylimidazole solution were added and the reaction carried out for 2 hours. PXRD patterns and SEM images are shown below in Figure 4.12 and Figure 4.13.

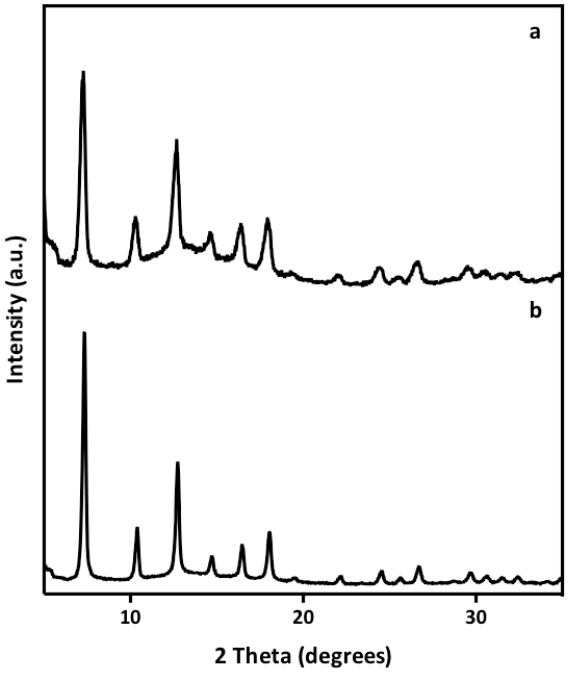


**Figure 4.12 PXRD patterns of the ZIF-8 experiments performed in aqueous solution at room temperature with SPAN-80/CTAB surfactants in ratio (a) 1:0.1, (b) 1:0.05.**

PXRD patterns confirmed that pure ZIF-8 phase was formed in all the experiments except in the ratio SPAN-80:CTAB = 1:0.5. Under these conditions the combination of SPAN-80 and CTAB appeared to suppress ZIF-8 formation, yielding only a clear and transparent solution. The surfactant CTAB has previously been employed in the synthesis of ZIF-8. As previously mentioned *Pan et al.* have tuned the crystal morphology and size of ZIF-8 in aqueous solution using CTAB as a capping agent.[106] While the ratio zinc precursor to MeIm and the dilution of the solutions were comparable ($Zn^{2+}$:MeIm:$H_2O$=1:56:4581 vs 1:70:4294 respectively for the mentioned literature and the present work), they carried out the reaction under solvothermal conditions and using

lower amounts of CTAB (range between 0.0055 and 0.055 mmol versus 0.105 mmol in the present work).

On the other hand in the work of *Wang et al.* ZIF-8 was prepared from stoichiometric metal and ligand solutions at room temperature in the presence of the triblock copolymer P123 and ammonium hydroxide (overall reaction composition $Zn^{2+}$:MeIm:$NH_4^{2+}$:$H_2O$=1:2:16:546). When P123 was replaced by CTAB (2.8 mmol) however, no solid product was obtained (ratio MeIm:CTAB=1:0.23).[156] Probably the higher concentration of CTAB and the synthetic conditions used allowed strong interactions between the cationic surfactant and the deprotonated MeIm to occur which prevented the network formation, even though the ratio methylimidazole to CTAB was an order of magnitude lower than in the reported literature (ratio MeIm:CTAB=1:0.015). However by increasing the SPAN-80:CTAB ratio to 1:0.1 or 1:0.05 and therefore the MeIm:CTAB to 1:0.003 or 1:0.0015 ZIF-8 was successfully formed (Figure 4.12 a and b), probably because decreasing the amount of CTAB an higher level of MeIm was available for the framework formation.

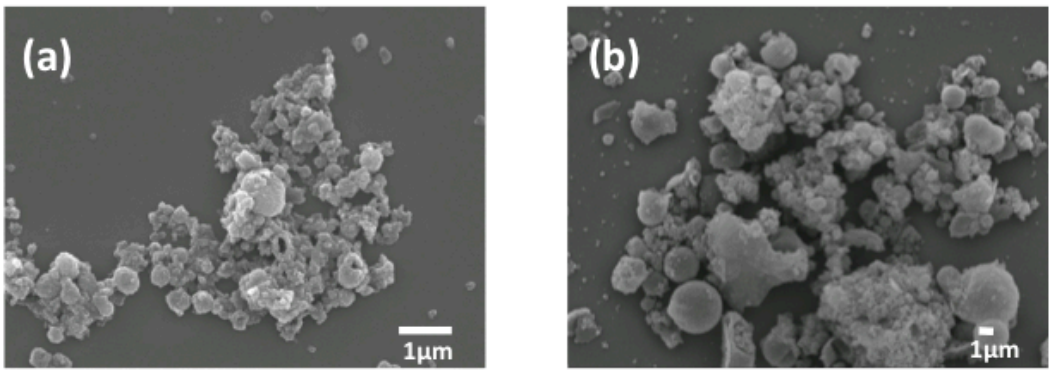


**Figure 4.13 SEM images of the ZIF-8 experiments performed in aqueous solution at room temperature with SPAN-80/CTAB surfactants in ratio (a) 1:0.1, (b) 1:0.05.**

The effect of the combined surfactants SPAN-80 and CTAB on the macroscopic structure of ZIF-8 is shown in Figure 4.13. SEM images displayed the presence of unaggregated nanoparticles and just a few colloidosomes, indicating that the combined effect of the two surfactants did not improve the superstructure formation at any condition performed.

#### 4.2.1.2 Synthesis step

Hereafter the ZIF-8 synthesis step was further investigated varying parameters such as the synthesis time, the effect of the stirring and the addition of imidazole as a competitor ligand. Indeed the nucleation and formation of ZIF-8 is clearly involved in the superstructure formation.

At first the synthesis time of ZIF-8 was performed at 0.5, 2 or 24 hours. PXRD patterns and SEM images of experiments are shown below in Figure 4.14 and Figure 4.15.

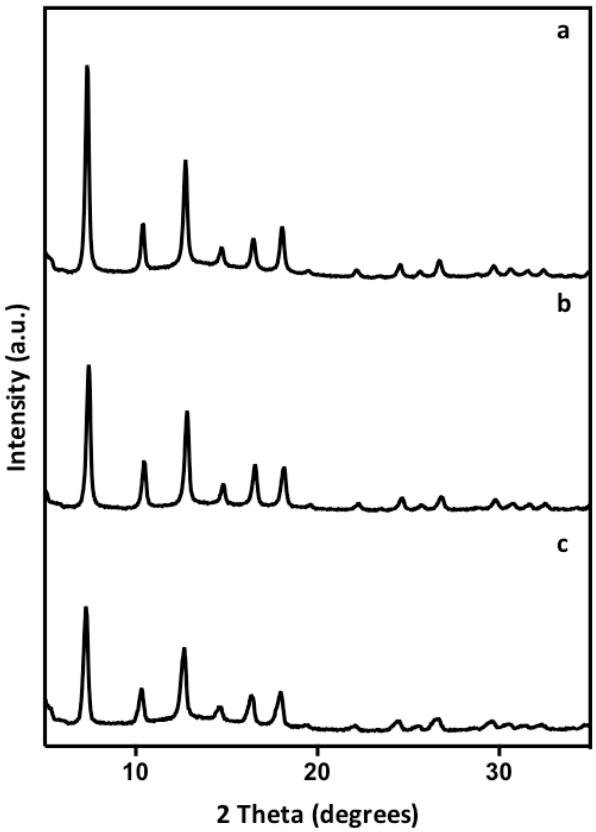


**Figure 4.14 PXRD patterns of the ZIF-8 experiments performed in aqueous solution at room temperature with SPAN-80 at different reaction time, respectively (a) 0.5h, (b) 2h, (c) 24h.**

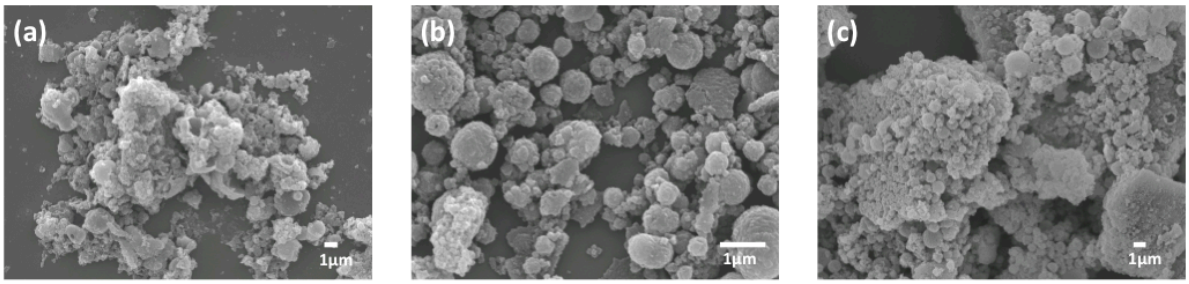


**Figure 4.15 SEM images of the ZIF-8 experiments performed in aqueous solution at room temperature with SPAN-80 at different reaction time, respectively (a) 0.5h, (b) 2h, (c) 24h.**

PXRD patterns confirmed that a pure ZIF-8 phase was formed in all the experiments (Figure 4.14). SEM images of the experiments performed following reaction times of 0.5 and 24 hours revealed that mostly nanoparticles were formed, while in the experiment performed at 2 hours mostly colloidosomes were formed. There appeared to be a range of time in which the MOF nanoparticles were organized into the observed superstructures, which is around 2 hours. Probably before this time the nanoparticles were unaggregated because they had not yet

interacted with the surfactant mesostructure (Figure 4.15 a) and after which the colloidosomes have been broken into the related nanoparticles by the collisions due to the stirring (Figure 4.15 c). In order to prove this and to have a higher degree of control over the colloidosome formation, the ZIF-8 synthesis time was performed without stirring; PXRD patterns and SEM images are shown below inFigure 4.16 and Figure 4.17.

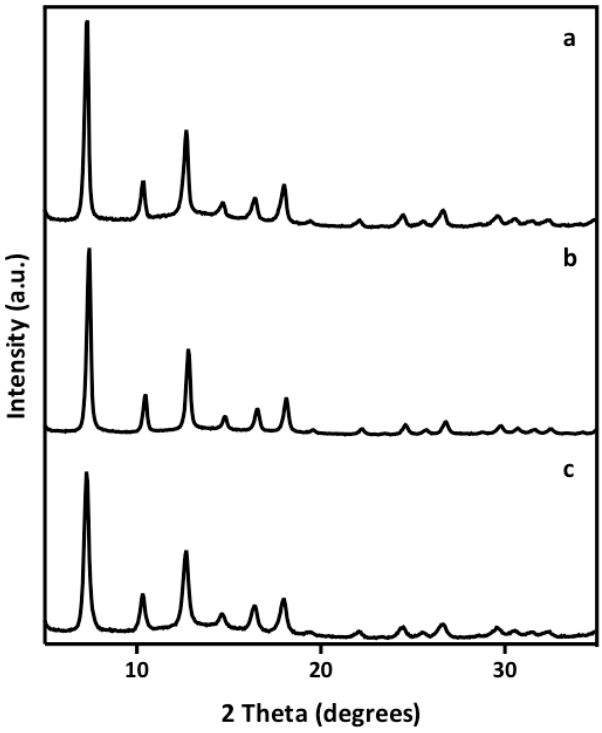


**Figure 4.16 PXRD patterns of the ZIF-8 experiments performed in aqueous solution at room temperature with SPAN-80 at different reaction time, respectively (a) 2h, (b) 18h, (c) 24h, where the reaction step was not stirred.**

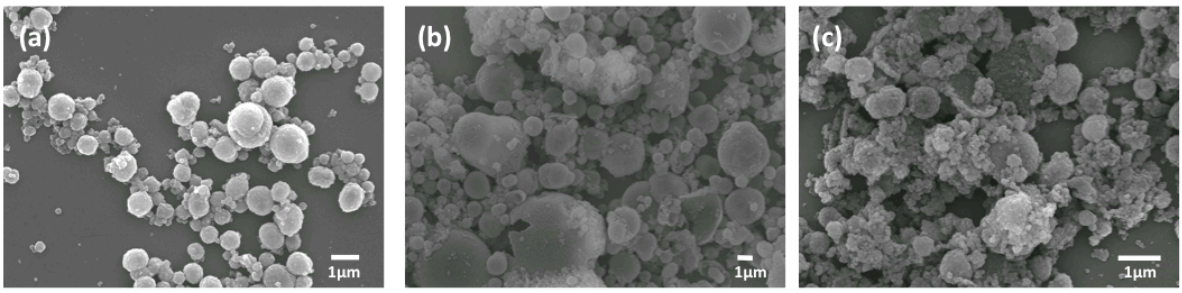


**Figure 4.17 SEM images of the ZIF-8 experiments performed in aqueous solution at room temperature with SPAN-80 at different reaction time, respectively (a) 2h, (b) 18h, (c) 24h, where the reaction step was not stirred.**

PXRD patterns confirmed that pure ZIF-8 phase was formed in all the experiments where stirring was not employed (Figure 4.16). SEM images revealed that colloidosomes were still present after reaction times of 18 and 24 hours, suggesting that long stirring times could decrease the quality of the colloidosomes formed. However the experiment performed at a ZIF-8 synthesis time of 2 hours appeared to be the most suitable in terms of unbroken colloidosomes and amount of

unaggregated ZIF-8 nanoparticles. Therefore the breakdown of the colloidosomes with time might be due to other causes rather than the stirring, such as the dynamic behaviours of the system at the interface.[174]

In general slowing down the MOF reaction kinetics facilitated macroscopic structure formation,[99] for instance through the competitive interactions arising from a judiciously selected modulator, i.e. a capping agent with the same chemical functionality as the framework linker, the crystal morphology could be controlled.[105] For instance employing various simple modulating monodentate ligands with different functionalities (sodium formate, 1-methylimidazole, n-butylamine) the size of ZIF-8 crystals could be tune between ~10 nm and 1 µm.[187] In this regard the reaction was carried out by adding imidazole to the ZIF-8 synthesis step as a competitor for the methylimidazole framework-forming component. After stirring SPAN-80 for 5 hours, different amounts of the two linkers methylimidazole and imidazole were used in the ZIF-8 synthesis (ratio Zn:MeIm:Im= 1:70:17.5, 1:70:35, 1:70:70) and the reaction carried out for 2 hours. PXRD and SEM were used in order to monitor the reaction outcomes (Figure 4.18 and Figure 4.19)

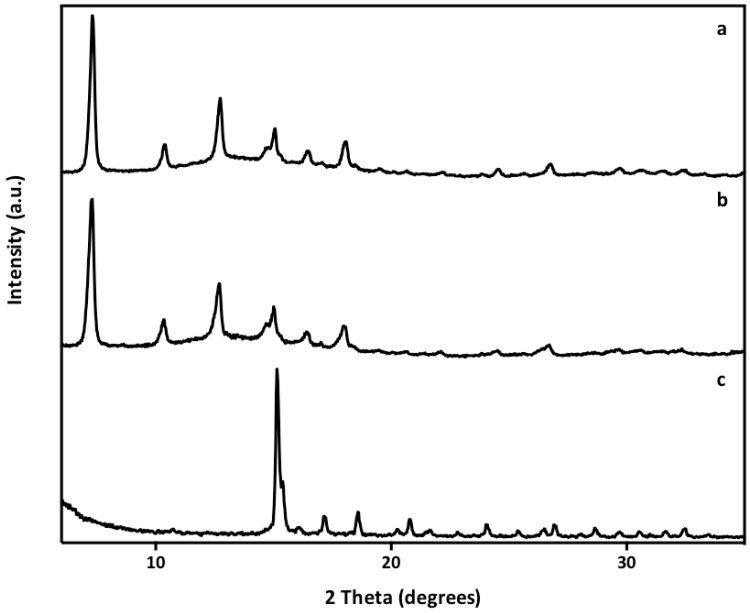


**Figure 4.18 PXRD patterns of the ZIF-8 experiments performed in aqueous solution at room temperature with SPAN-80 introducing imidazole as a competitor, ratio Zn:MeIm:Im= (a) 1:70:17.5, (b) 1:70:35, (c) 1:70:70, at reaction time 2 hours.**

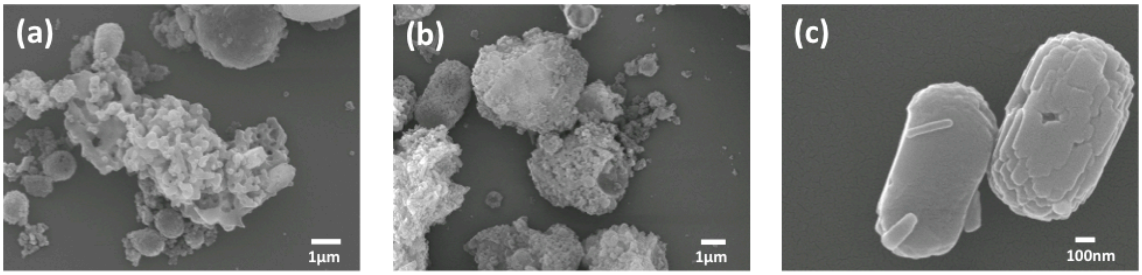


**Figure 4.19 SEM images of the ZIF-8 experiments performed in aqueous solution at room temperature with SPAN-80 introducing imidazole as a competitor, ratio Zn:MeIm:Im= (a) 1:70:17.5, (b) 1:70:35, (c) 1:70:70, at reaction time 2 hours.**

The experiments performed at ratio Zn:MeIm:Im= 1:70:17.5 and 1:70:35 (Figure 4.18 a and b) show, beside ZIF-8 formation, the appearance of another phase, as evidenced by the appearance of an additional peak detected at 2Θ = 15°, and this phase completely replaced ZIF-8 in the experiment performed at ratio Zn:MeIm:Im= 1:70:70 (Figure 4.18 c). Further the experiments showed a significant increment of the overall ratio metal to ligand(s), from 1:70 in the original synthesis to 1:140 in the latter case. The phase was identified as related to the dense **zni** topology that is often observed for Im-only or mixed MeIm-Im ZIFs and is typical of ZIF-61. The **zni** phase is further discussed in Chapter 5. The increase of the Im concentration clearly modified the morphology of the crystals obtained. As the ratio of MeIm:Im decreases the morphology of the particles varied from colloidosomes and unaggregated particles (Figure 4.19 a), unaggregated particles (Figure 4.19 b) and lozenge like particles typical of the **zni** phase (Figure 4.19 c).

#### 4.2.1.3 Compositional parameters

Compositional parameters such as solvents and precursors relevant to the ZIF-8 synthesis have also been investigated. In order to further explore the SPAN-80 supramolecular organization the reaction was carried out in the solvent mixture water/methanol (1:1). Methanol was chosen as co-solvent because it has already been employed for the synthesis of ZIF-8 nanoparticles at room temperature.[188] Different amounts of SPAN-80 (18, 54, 90, 126 and 162 mg) were dissolved in 5 mL of a water/methanol (1:1) mixture and stirred at room temperature for 5 hours, then zinc nitrate solution and methylimidazole solution were added and left to stir for a further 2 hours. PXRD patterns and SEM images are shown below in Figure 4.20 and Figure 4.21.

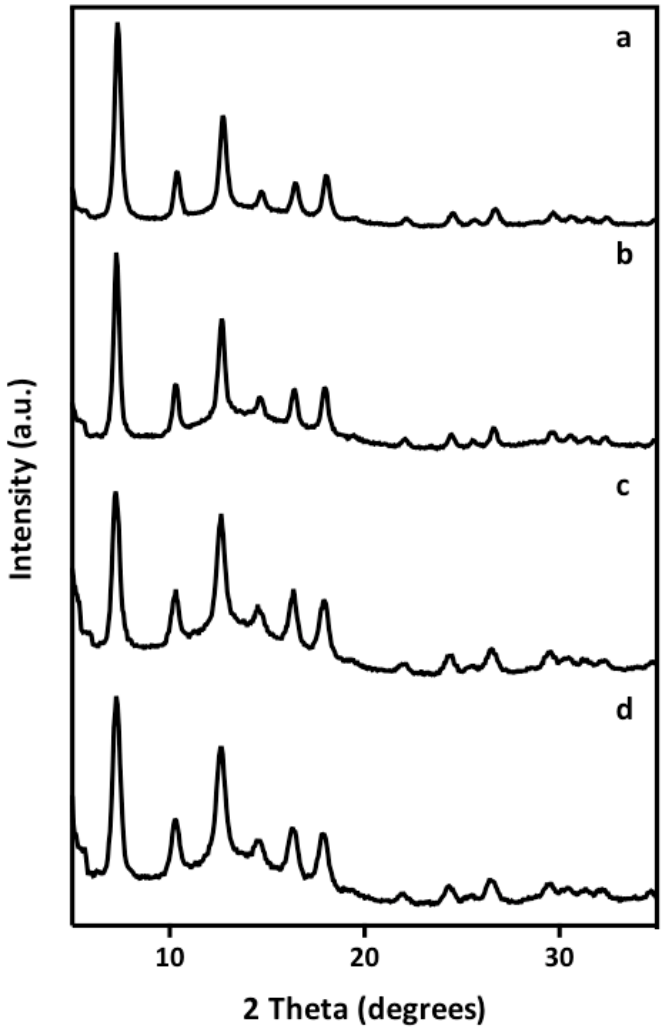


**Figure 4.20 PXRD patterns of the ZIF-8 experiments performed in MeOH/$H_2O$ (1:1) at room temperature at different concentration of SPAN-80, respectively (a) 54, (b) 90, (c) 126, (d) 162 mg.**

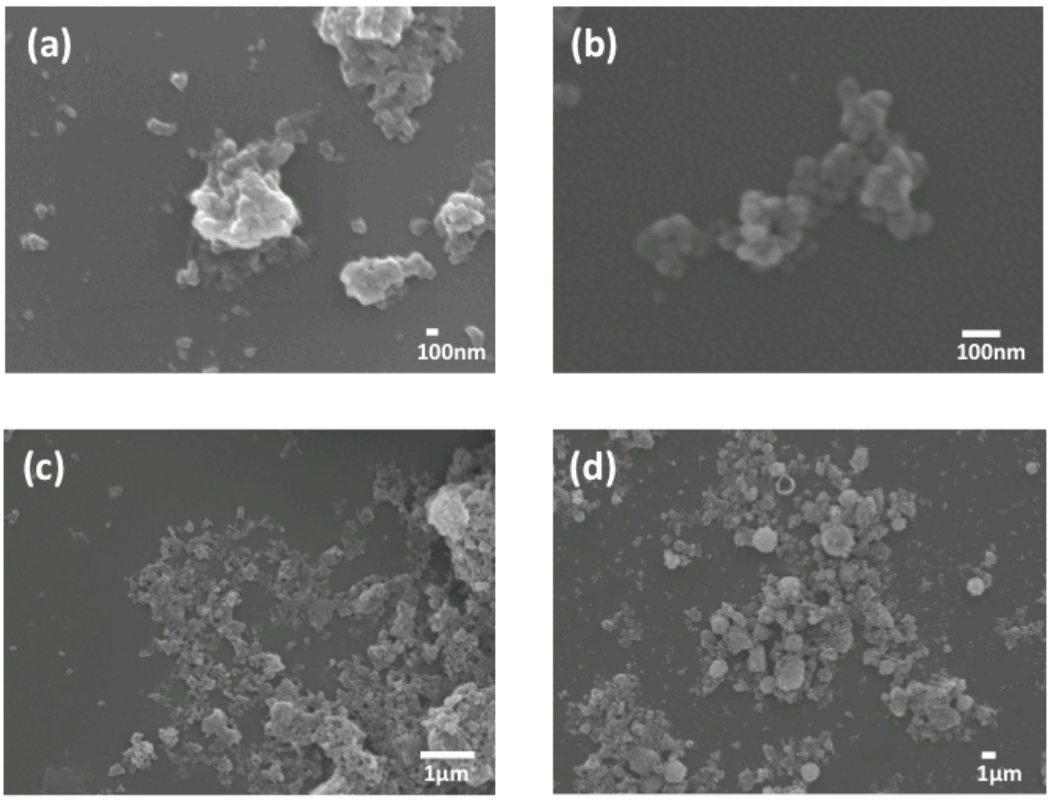


**Figure 4.21 SEM images of the ZIF-8 experiments performed in MeOH/$H_2O$ (1:1) at room temperature at different concentration of SPAN-80, respectively (a) 54, (b) 90, (c) 126, (d) 162 mg.**

PXRD patterns confirmed that all the experiments performed in water/MeOH lead to the formation of a pure ZIF-8 phase (Figure 4.20). Interestingly, when only 18 mg of SPAN-80 was employed, insufficient solid for PXRD analysis was obtained suggesting that at very low levels in mixed water/MeOH the SPAN-80 slowed down ZIF-8 formation. Further, the yield of the experiments increased on increasing the amount of SPAN-80 added to the synthesis (11, 12 and 15 mg respectively) indicating that perhaps counter-intuitively lower amounts of SPAN-80 had a stronger effect on slowing down the reaction. The supramolecular organization of the surfactant strongly depends on its concentration[185] therefore increasing the amount of SPAN-80 the surfactant might undergo to a mesophase transition which displays different interactions with the MOF precursors. However this is just a speculation since the behavior of SPAN-80 in water/MeOH mixtures is unknown.

SEM images of the experiment performed with 126 mg of SPAN-80 and below showed that just nanoparticles were formed, while in the experiment performed with 162 mg of SPAN-80 a few colloidosomes were detected (Figure 4.21). This was in contrast to those experiments performed wholly in water and suggested that the introduction of the second solvent changed the properties of the micellar solution,[189] limiting ZIF-8 colloidosome formation. This provided some evidence that the SPAN-80 aggregates were responsible for colloidosome formation.

Finally the premade ZIF-8 nanoparticles were investigated as a precursor for the formation of the hollow particles. The hexagonal ZIF-8 nanosize particles were synthesized following the reported synthesis[106] and characterized by PXRD pattern and SEM image, as shown respectively in Figure 4.22 a and Figure 4.23 a ). As before SPAN-80 was stirred for 5 hours at room temperature and then an aqueous solution of ZIF-8 particles was added and stirred for 2 hours at room temperature. PXRD pattern and SEM image are shown in Figure 4.22 b and Figure 4.23 b.

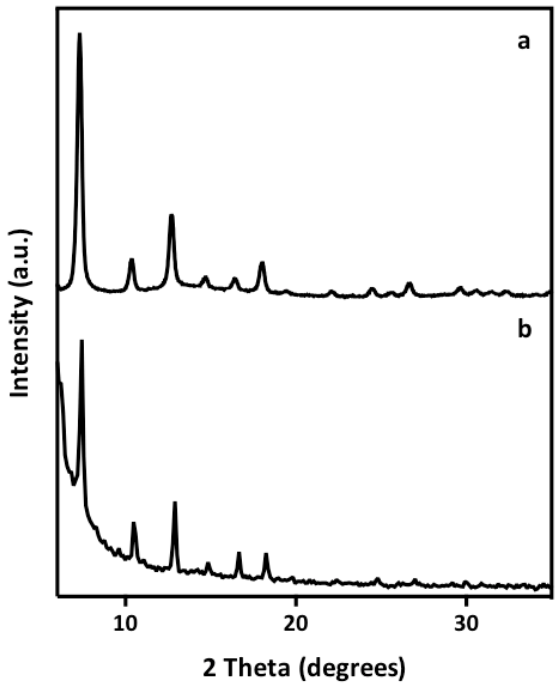


**Figure 4.22 PXRD patterns of preformed ZIF-8 particles: (a) as synthesis (b) after the experiments performed in aqueous solution at room temperature with SPAN-80.**

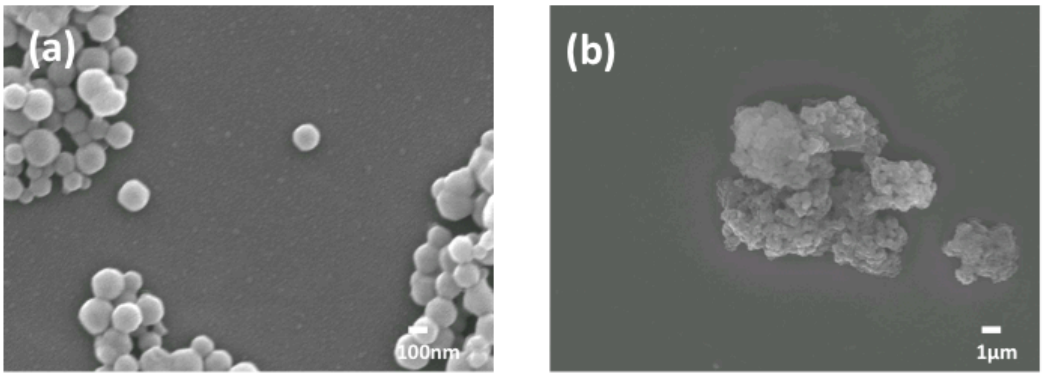


**Figure 4.23 SEM images of preformed ZIF-8 particles: (a) as synthesized, and (b) after the assembly experiments performed in aqueous solution at room temperature with SPAN-80.**

PXRD data and SEM images, respectively Figure 4.22 b and Figure 4.23 b, confirmed that the ZIF-8 phase was preserved but under these conditions SPAN-80 did not exert any effect on the superstructure assembly of ZIF-8 nanoparticles.

This agreed with the work from Huo *et al.*[175] (previously discussed in 4.1), where premade ZIF-8 nanoparticles stabilized Pickering emulsion in solution but they needed the support of a polymeric component to be isolated as solids.

This series of experiments was a first screening of the effect of the surfactant SPAN-80 on the ZIF-8 macroscopic structure. The reaction was designed in aqueous solvent and at room temperature[182] in order to favor surfactant mesophase formation. Initially the effect of the SPAN-80 concentration on the reaction was investigated. Interesting results were obtained at a SPAN-80 concentration of 90 mg in 5 mL (18 wt%) of $H_2O$ where, beside nanoparticles and rod-like particles, hollow capsules were observed. Following on from this, efforts were made in order to improve the surfactant effectiveness in hollow capsule formation. Despite the variation of a number of parameters, such as SPAN-80 dilution and stirring time and the combined effect of SPAN-80 with the surfactant CTAB in the emulsion step and the effect of the stirring and the addition of imidazole as a competitor ligand and compositional parameters such as solvent and MOF precursor in synthesis step, it appeared that a narrow range of conditions were optimal to obtain the ZIF-8 colloidosomes. In this regard the SPAN-80 stirring step was fundamental to the surfactant assembly, whereas during the ZIF-8 synthesis a lack of stirring facilitated the framework formation.

### 4.2.2 Studies with SPAN-80 and dodecane

Dodecane is an apolar molecule that readily forms oil-in-water emulsions, that have previously been exploited for the preparation of MOF-based colloidosomes from premade MOF nanoparticles via Pickering stabilisation.[175] Based on this key demonstration, dodecane was added to assist SPAN-80 in colloidosome formation by providing a well-defined hydrophobic droplet phase to further solubilise the aliphatic parts of the amphiphiles. In the present case, the nanoparticles were formed in situ during the reaction rather than being pre-prepared as reported by Huo *et al.*.[175] In a typical experiment dodecane and SPAN-80 were dissolved in an aqueous solution (90 mg in 5 mL of $H_2O$) and stirred for 5 hours in order to obtain an intimate aggregation of the two compounds. Hereafter the zinc nitrate solution (29 mg in 0.5 mL $dH_2O$) and methylimidazole solution (560 mg in 2 mL $dH_2O$) were added and the reaction carried out for 2 hours. Also in this case the reaction was classified by two steps: mixing dodecane and SPAN-80 in water, the emulsion step, and the addition of zinc and methylimidazole solution, the ZIF-8 synthesis step. The reaction was analysed under different aspects in order to find the best synthetic conditions, including: the effect of dodecane concentration, the effect of the stirring and the effect of dilution on SPAN-80/dodecane or the ZIF-8 precursors solutions related to the

emulsion step or the variation in the ratio zinc to methylimidazole and the influence of the time in ZIF-8 synthesis step were investigated.

#### 4.2.2.1 Emulsion step

The experiments were performed under different amounts of added dodecane (25, 50, 75 and 100 µL respectively) keeping the amount of SPAN-80 fixed at 90 mg, as previously determined as the optimum quantity (4.2.1). PXRD patterns and SEM images of the experiments are shown below (Figure 4.24 and Figure 4.25).

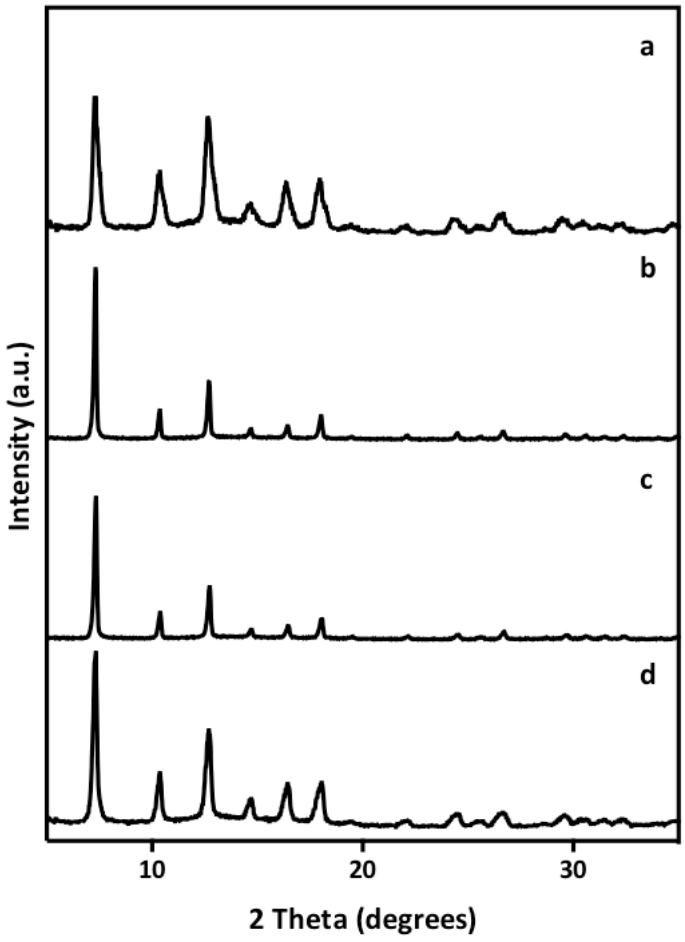


**Figure 4.24 PXRD patterns of the ZIF-8 experiments performed in aqueous solution at room temperature with 90 mg of SPAN-80 at different amount of dodecane: (a) 25 µL, (b) 50 µL, (c) 75 µL and (d) 100µL.**

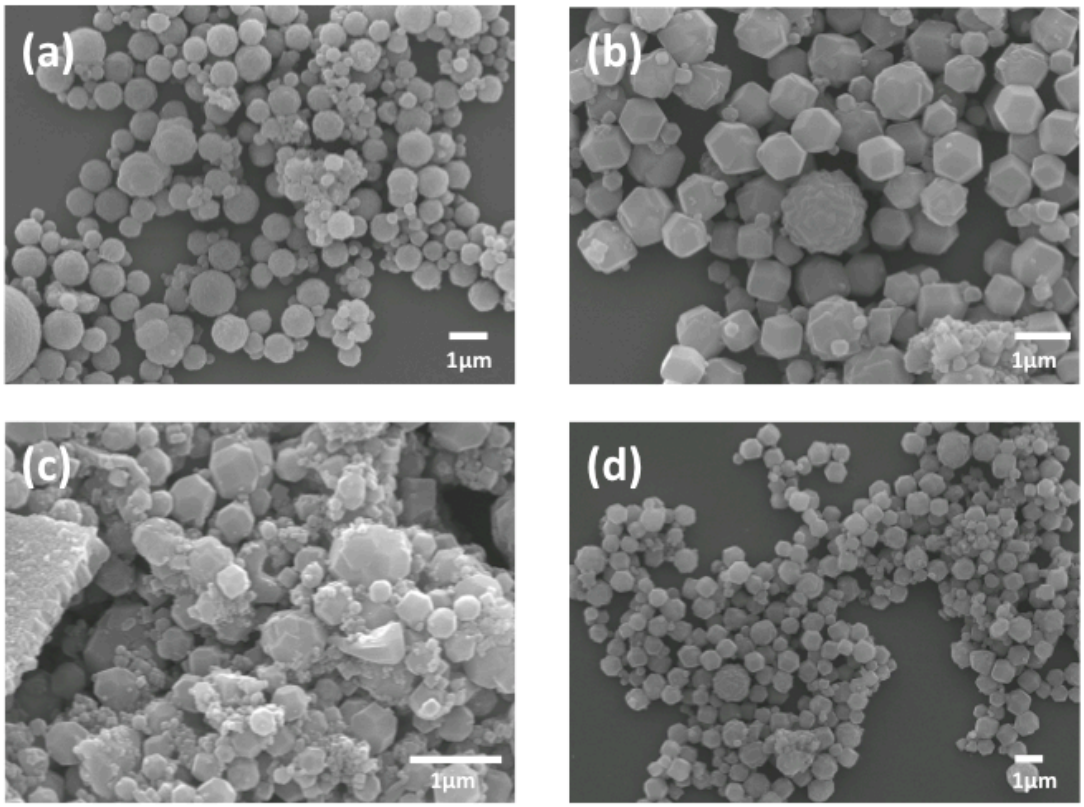


**Figure 4.25 SEM images of the ZIF-8 experiments performed in aqueous solution at room temperature with 90 mg of SPAN-80 at different amount of dodecane: (a) 25 µL, (b) 50 µL, (c) 75 µL and (d) 100µL.**

PXRD patterns showed a pure ZIF-8 phase formed in all the experiments, meaning that the addition of dodecane did not interfere with the MOF formation. However SEM images revealed an effect on the MOF macroscopic structure. When only 25 µL of dodecane were added to the synthesis mostly colloidosomes and a few unaggregated particles were detected. When the quantity of dodecane added reaches 50 µL and above fewer colloidosomes were observed but mostly micron-sized truncated rhombic dodecahedral crystals were formed.

Truncated rhombic dodecahedral crystals are the expected morphology for ZIF-8 based on the minimum total surface energy,[106] consistently also with the morphology of the crystals obtained in the ZIF-8 control experiment (Figure 4.26).

Therefore from the experiments it appeared that above 50 µL of dodecane the dodecane/SPAN-80 system was less effective as a templating agent, which might be related to a change in the emulsion phase present in solution,[190] as also observed for increased amounts of SPAN-80 (4.2.1).

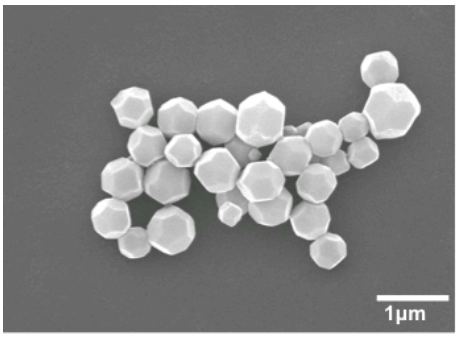


**Figure 4.26 SEM image of ZIF-8 crystal performed in aqueous solution at room temperature without any surfactant.**

Furthermore the stirring was evaluated as a parameter that can influence the macroscopic structure of ZIF-8, as also indicated from the experiments performed in the previous section. In particular the emulsion step should be stirred in order to form a stable emulsion, while probably the stirring was not that important in the ZIF-8 synthesis step, where for the longer stirring they might knock together and break up. The stirring effect was investigated at all stages of the process, stirring both or only one of the stages outlined above. PXRD patterns and SEM images are shown in Figure 4.27 and Figure 4.28.

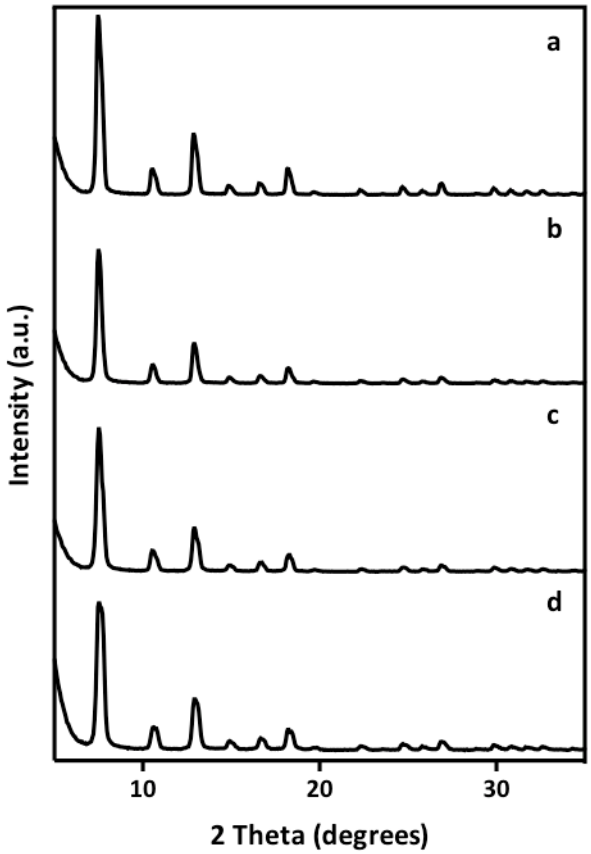


**Figure 4.27 PXRD patterns of the ZIF-8 experiments performed in aqueous solution at room temperature with SPAN-80 and dodecane at different stirring conditions: (a) both the emulsion and ZIF-8 synthesis step have not been stirred, (b) emulsion step has not been stirred and ZIF-8 synthesis step has been stirred, (c) emulsion step has been stirred and ZIF-8 synthesis step has not been stirred and (d) both the steps have been stirred.**

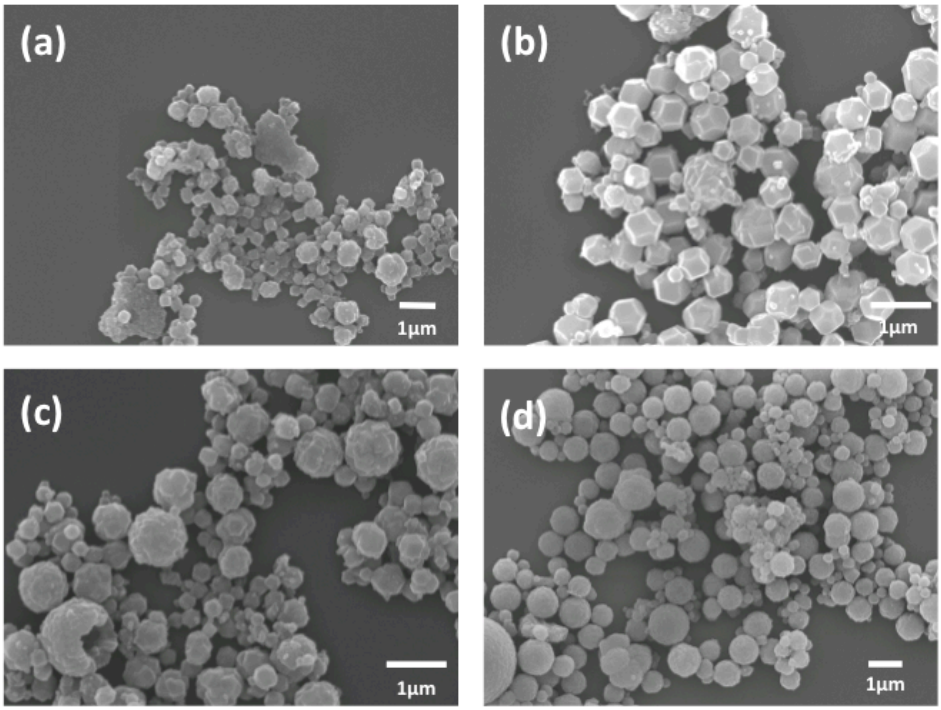


**Figure 4.28 SEM images of the ZIF-8 experiments performed in aqueous solution at room temperature with SPAN-80 and dodecane at different stirring conditions: (a) both the emulsion and ZIF-8 synthesis step have not been stirred, (b) emulsion step has not been stirred and ZIF-8 synthesis step has been stirred, (c) emulsion step has been stirred and ZIF-8 synthesis step has not been stirred and (d) both the steps have been stirred.**

PXRD patterns showed ZIF-8 formation in all the experiments (Figure 4.27). When the emulsion step was not stirred truncated rhombic dodecahedron ZIF-8 crystals were formed, as shown in SEM images (Figure 4.28 a and b). Due to the lack of stirring the emulsion was probably not formed and it could not template the macroscopic structure of ZIF-8, hence the energetically favoured ZIF-8 crystal morphology was formed. On the other hand when the emulsion step was stirred colloidosomes were formed. The stirring of the ZIF-8 synthesis step just slightly improved the result in terms of unaggregated particles (Figure 4.28 c and d for not stirred and stirred ZIF-8 synthesis step), unlike the stirring experiments performed in the preliminary experiments (4.2.1.2) where the stirring increases the number of unaggregated particles. Therefore the stirring of the immiscible water/dodecane system with SPAN-80 was vital to form a stable emulsion of well-defined droplets for the successful templating of hollow spherical ZIF-8 marcostructures at the o/w interface.

Furthermore the effect of the dilution of the starting solutions was also investigated: firstly the emulsion solution was dispersed in half or double amount of solvent, respectively 2.5 or 10 mL of $H_2O$. Secondly the ZIF-8 precursor solutions were dissolved in half or double amount of water: 0.25 mL for the zinc salt and 1 mL for methylimidazole or 1 mL for the zinc salt and 4 mL for methylimidazole solution respectively. The reaction was carried out as previously. PXRD patterns and SEM images are shown below in Figure 4.29 and Figure 4.30.

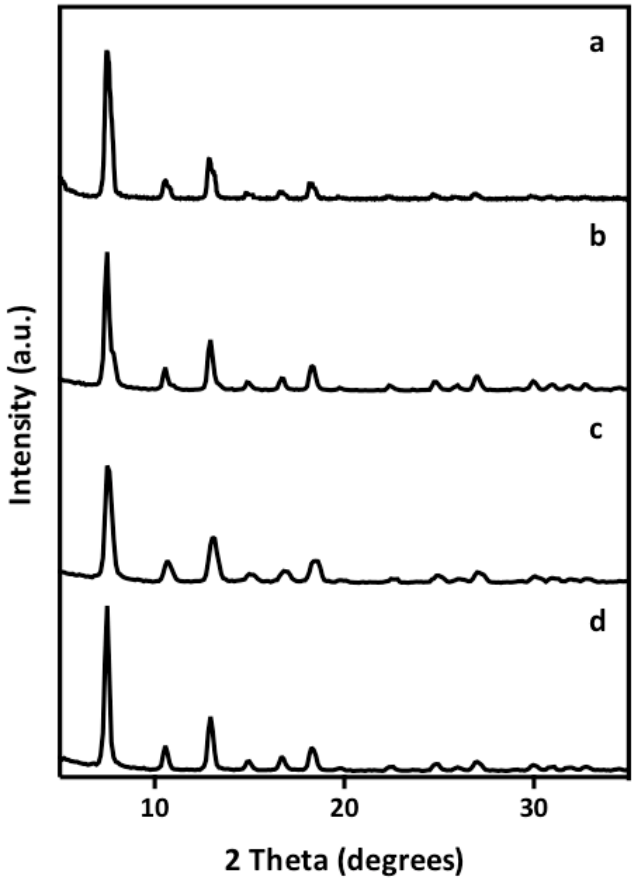


**Figure 4.29 PXRD patterns of the ZIF-8 experiments performed in aqueous solution at room temperature with SPAN-80 and dodecane at different dilution conditions: (a) SPAN-80 and dodecane dissolved in 2.5 mL of $dH_2O$, (b) SPAN-80 and dodecane dissolved in 10 mL of $dH_2O$ (c) Zn and MeIm dissolved in half amount of $dH_2O$, (d) Zn and MeIm dissolved in double amount of solvent $dH_2O$.**

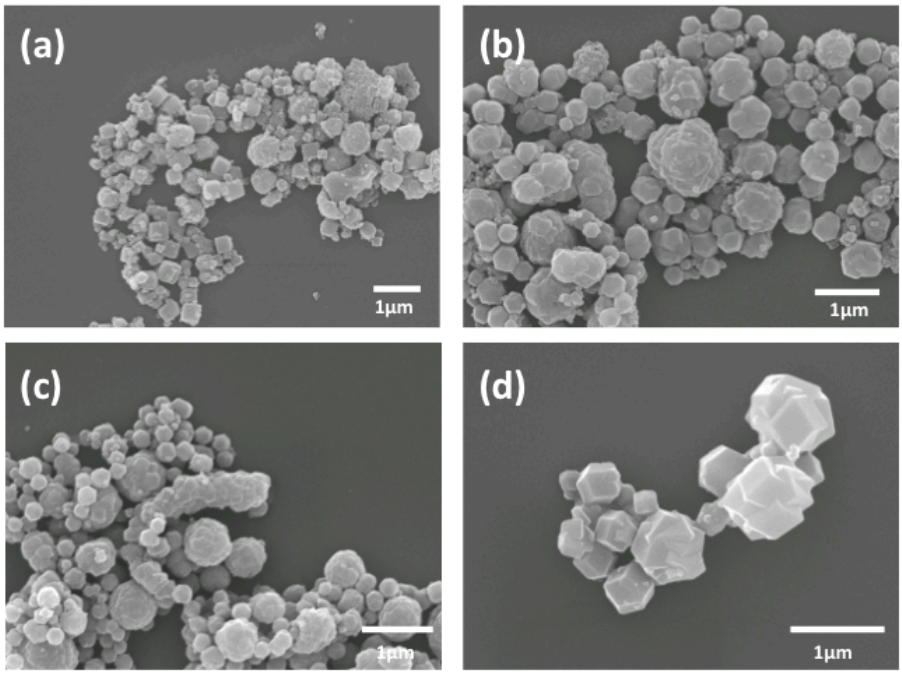


**Figure 4.30 SEM images of the ZIF-8 experiments performed in aqueous solution at room temperature with SPAN-80 and dodecane at different dilution conditions: (a) SPAN-80 and dodecane dissolved in 2.5 mL of $dH_2O$, (b) SPAN-80 and dodecane dissolved in 10 mL of $dH_2O$ (c) Zn and MeIm dissolved in half amount of $dH_2O$, (d) Zn and MeIm dissolved in double amount of solvent $dH_2O$.**

PXRD patterns confirmed that a pure phase of ZIF-8 was formed in all cases (Figure 4.29). SEM images of the experiments were comparable to each other and showed the presence of colloidosomes but also an increased number of truncated rhombic dodecahedral particles (Figure 4.30), where probably the greater dilution affected the macroscopic structure formation of the emulsion.

#### 4.2.2.2 Synthesis step

The previous experiments gave some indication about the emulsion step: both dodecane and SPAN-80 were involved in the emulsion formation where the optimum amount of dodecane to SPAN-80 = 25 µL and 90 mg in 5 mL of $H_2O$ which was then stirred for 5 hours for effective emulsion formation to template ZIF-8 colloidosomes. Starting from this optimum emulsion, other parameters in the ZIF-8 synthesis step in the process were explored, including the ratio of zinc to methylimidazole. In particular the adopted ratio zinc: methylimidazole of 1:70 was reduced to 1:35 and the reaction carried out for 2 hours. PXRD patterns and SEM images are shown below inFigure 4.31 and Figure 4.32.

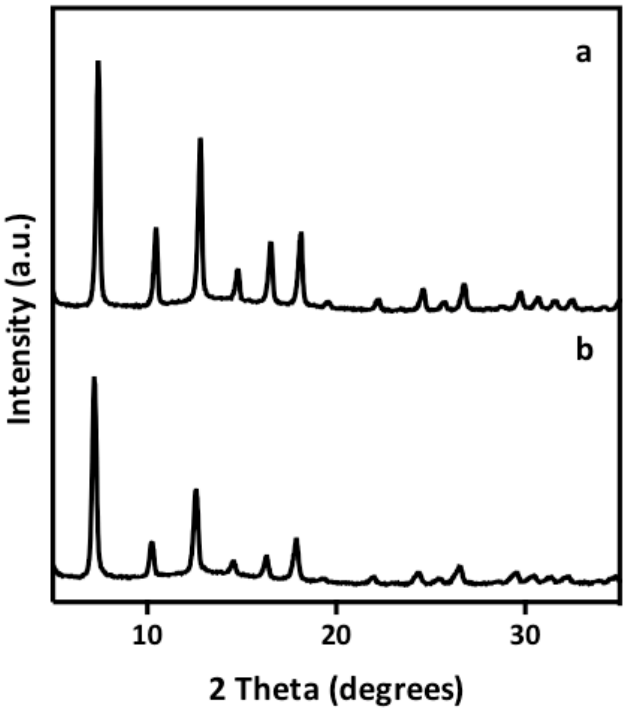


**Figure 4.31 PXRD patterns of the ZIF-8 experiments performed in aqueous solution at room temperature with SPAN-80 and dodecane at different at different metal to ligand ratio (a) $Zn^{2+}$:MeIm=1:35, (b) $Zn^{2+}$:MeIm=1:70.**

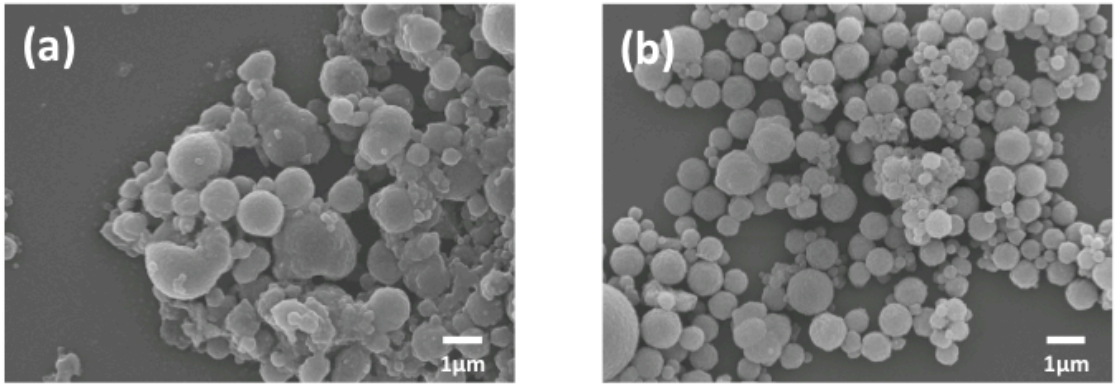


**Figure 4.32 SEM images of the ZIF-8 experiments performed in aqueous solution at room temperature with SPAN-80 and dodecane at different at different metal to ligand ratio (a) $Zn^{2+}$:MeIm=1:35, (b) $Zn^{2+}$:MeIm=1:70.**

PXRD patterns confirmed that a pure phase of ZIF-8 was formed in both cases (Figure 4.31) but SEM images clearly revealed that the decrease of the ligand concentration affected the homogeneity of the colloidosomes and increases the number of unaggregated particles formed (Figure 4.32 a). In the reported synthesis[182] the optimized value for the ratio Zn:MeIm is 1:70. However also the ratio 1:35 was studied[191] and the resulting crystals were comparable in terms of size and morphology and the main difference was in terms of yield. Therefore reducing the ratio Zn:MeIm might lead to a kinetic effect slowing down the ZIF-8 formation, which might finally affect the quality of the superstructure formed. Furthermore decreasing the ratio of metal to ligand to 1:35 also decreased the overall concentration of the solution to (Zn=[0.048],

MeIm=[1.7]). Comparing this with the experiment in which the concentration of both the Zn and MeIm were decreased (Zn=[0.024], MeIm=[1.7]) (Figure 4.32 d) it appeared that the reduction of the concentration of the zinc solution strongly affected the hollow capsule formation, which might indicate that the zinc is primarily involved with the dodecane superstructure.

Finally the reaction time was decreased at 0.25, 0.5, 0.75 and 1 hour in order to investigate its effect.

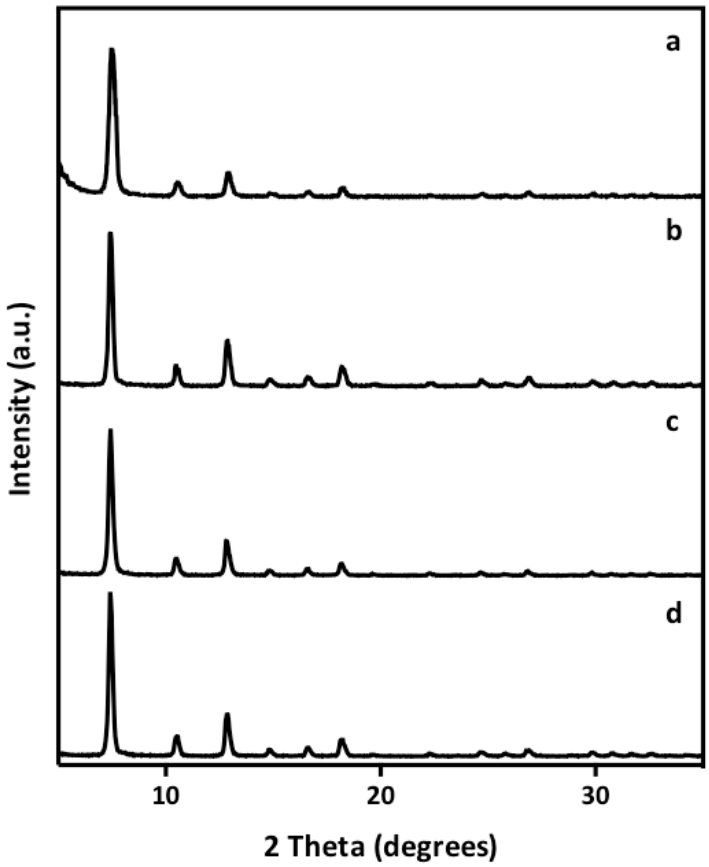


**Figure 4.33 PXRD patterns of the ZIF-8 experiments performed in aqueous solution at room temperature with SPAN-80 and dodecane at different ZIF-8 synthesis step time: (a) 0.25, (b) 0.5, (c) 0.75 and (d) 1 hour.**

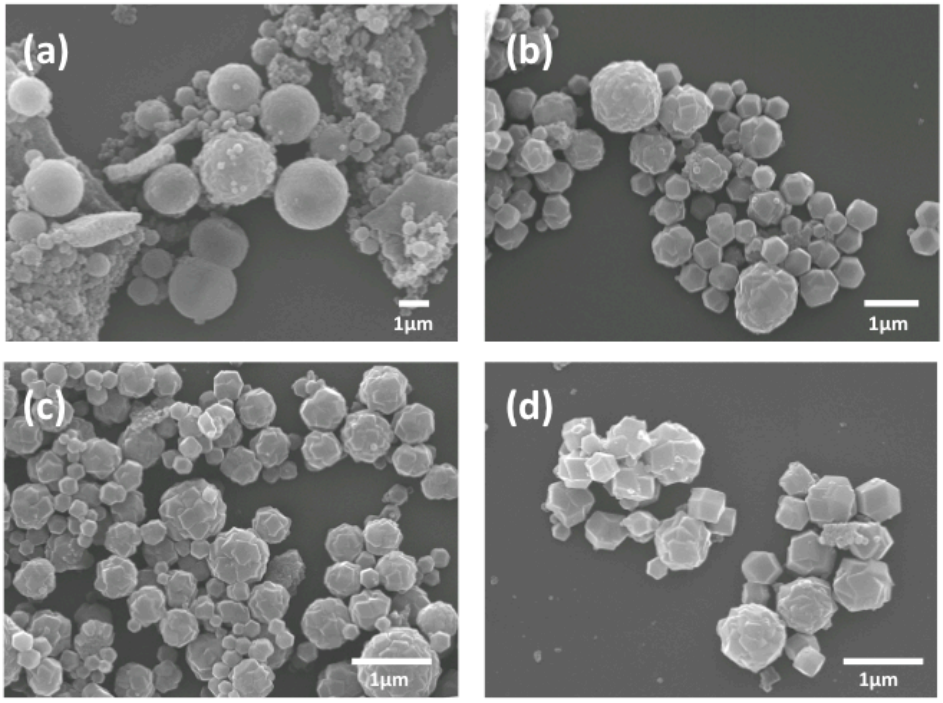


**Figure 4.34 SEM images of the ZIF-8 experiments performed in aqueous solution at room temperature with SPAN-80 and dodecane at different ZIF-8 synthesis step time: (a) 0.25, (b) 0.5, (c) 0.75 and (d) 1 hour.**

PXRD patterns confirmed that a pure phase of ZIF-8 was formed in all cases (Figure 4.33); SEM images of the experiments showed beside the colloidosomes, the presence of truncated rhombic dodecahedral particles in all the samples (Figure 4.34). Therefore, according to the preliminary experiments (4.2.1.2), the synthesis time was an important parameter in the hollow capsule formation. Probably before 2 hours time the nanoparticles had not yet interacted with the dodecane mesostructure and therefore they were still unaggregated.

Therefore the introduction of dodecane in the reaction improved the colloidosomes formation, even though, also in this case the reaction is strongly depended on the synthetic parameters used and little variations led to the formation of unaggregated particles.

The optimum amount of dodecane was 25 µL and, according with the preliminary experiments, the stirring of the emulsion step was crucial for the surfactant mesoscopic structure formation. While the stirring of the synthesis step slightly improved the hollow structure formation. The dilution of SPAN-80/dodecane solution or the ZIF-8 precursors solution also had an effect on the supramolecular organization of the surfactant and the quality of the hollow capsules and number of unaggregated particles present, here the optimum values were 5 mL of $dH_2O$ for the SPAN-80/ dodecane solution, 0.5 mL for the zinc salt and 2 mL for methylimidazole. Regarding the synthesis step, the two parameters ratio zinc: methylimidazole and the reaction time were investigated and the best result was found at ratio 1: 70 and at reaction time 2 hours.

### 4.2.3 Preparation of ZIF-8 hollow capsules by shear force instrument

The previous experiments, as a preliminary study, pointed out the importance of the synthetic parameters in the ZIF-8 superstructure formation; for instance they stressed the importance of the stirring process on the emulsion formation for effective templating of colloidosomes. Therefore a shear force instrument was employed in order to improve homogeneity of the surfactant-free water/dodecane and water/dodecane/SPAN-80 emulsion systems.

In general the synthesis was designed on the base of the best conditions found in the preliminary study: zinc nitrate (29 mg in 0.5 mL $dH_2O$) and methylimidazole (560 mg in 2 mL $dH_2O$), were added to a surfactant-free dodecane-in-water emulsion formed by agitation using a shear force instrument at 16500 rpm for 2 min and left at 4 °C for 3 hours. The oil-in-water emulsion was investigated by varying the amount of dodecane between 5 to 100 µL where the $dH_2O$ amount was held to 5 mL of as shown Table 4.1. PXRD patterns and SEM images of the resulting ZIF-8 hollow capsule formed are shown in Figure 4.35, Figure 4.36 and Figure 4.37.

| SAMPLE | a | b | c | d | e |
|---|---|---|---|---|---|
| DODECANE (µl) | 5 | 25 | 50 | 75 | 100 |

**Table 4.1 Amount of dodecane (µL) added to 5 mL of $H_2O$ for emulsion formation.**

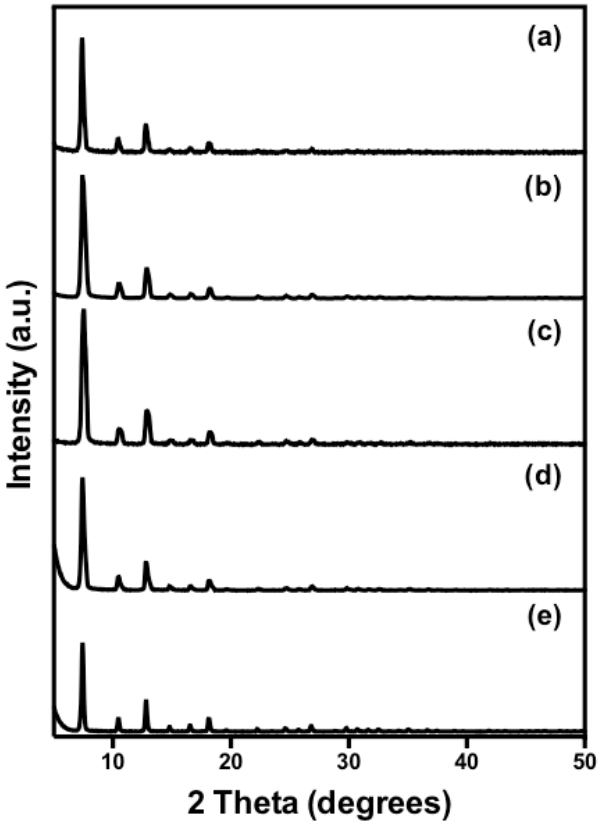


**Figure 4.35 PXRD patterns of the ZIF-8 samples formed in water in the presence of different amounts of added dodecane as the internal phase: (a) 5, (b) 25, (c) 50 (d) 75 and (e) 100 µL.**

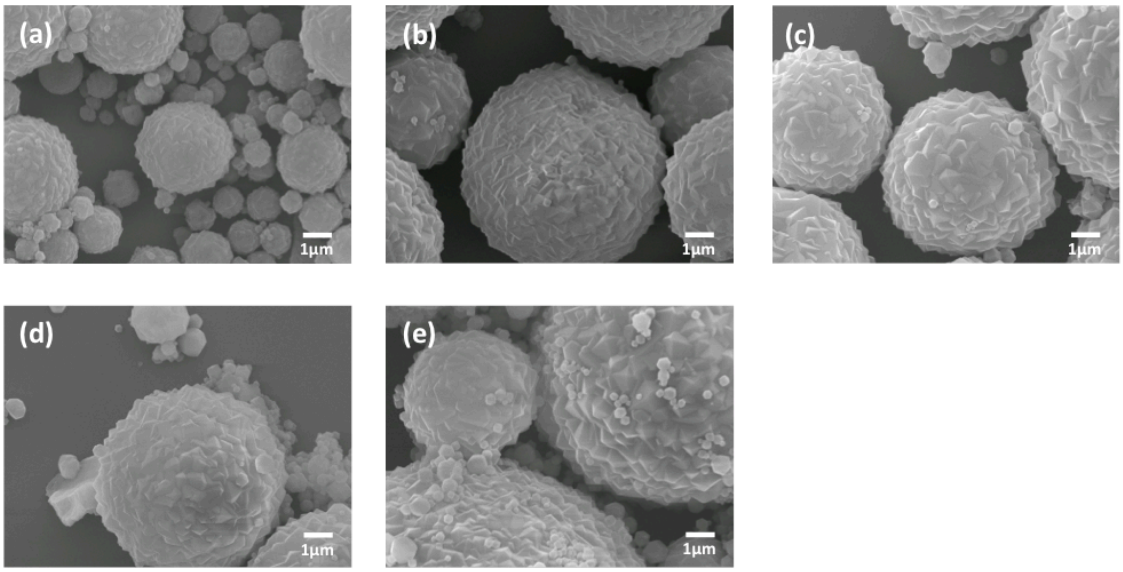


**Figure 4.36 SEM images of the ZIF-8 samples formed in water in the presence of different amounts of added dodecane as the internal phase: (a) 5, (b) 25, (c) 50 (d) 75 and (e) 100 µL (ZOOM IN).**

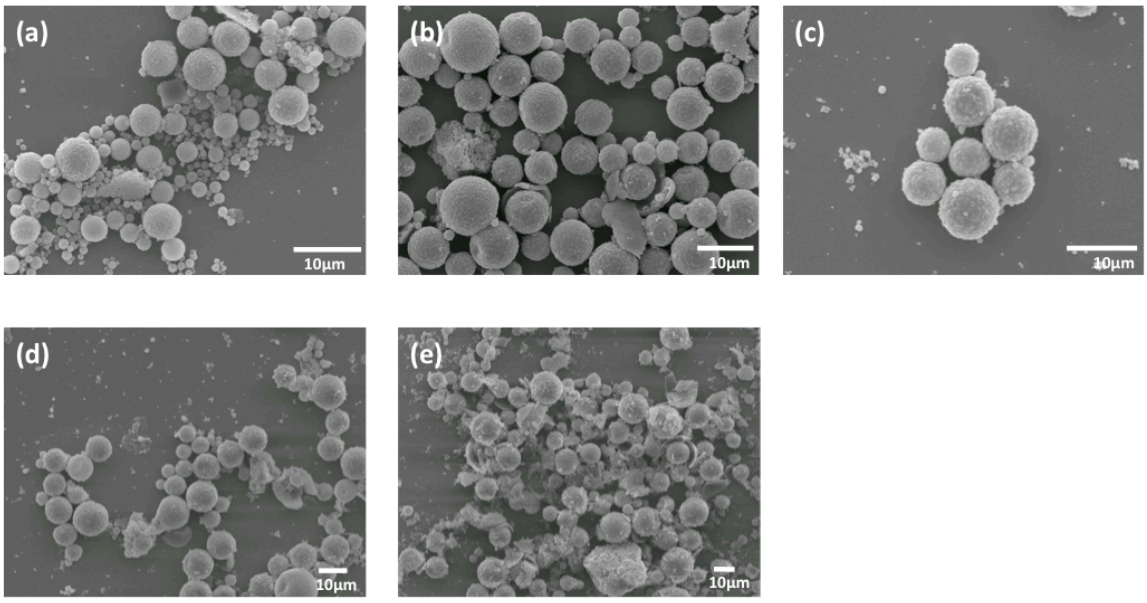


**Figure 4.37 SEM images of the ZIF-8 samples formed in water in the presence of different amounts of added dodecane as the internal phase: (a) 5, (b) 25, (c) 50 (d) 75 and (e) 100 µL (ZOOM OUT).**

The PXRD patterns confirmed that pure ZIF-8 was successfully synthesized (Figure 4.35) using a surfactant free dodecane in water emulsion. SEM images (Figure 4.36) clearly showed that hollow capsules were formed under all conditions investigated, meaning that a stable emulsion was formed at every dodecane concentration tested. However the variation of the dodecane concentration appeared to influence the monodispersity of the hollow capsules, their size and the amount of unaggregated (free) ZIF-8 particles present (Figure 4.37). When only 5 µL of dodecane was added polydisperse hollow capsules ranging in size from 500 nm to 5 µm, measured from SEM image, were formed (Figure 4.36 and Figure 4.37 a), which appeared to be more even in size when the internal phase was increased to 25 and 50 µL (Figure 4.36 and Figure 4.37 b, c) and only a small number of unaggregated particles were present. Finally when the internal phase reaches 75 µL and above the hollow capsules were again more polydisperse and there were numerous unaggregated ZIF-8 nanoparticles as shown in Figure 4.36 and Figure 4.37 d, e. However in general colloidosomes were formed, indicating that the surface of the ZIF-8 particles was sufficiently wettable by the dispersed oil phase to generate a stable Pickering emulsion, then the shell probably underwent further growth increasing its thickness and giving the observed hollow capsule.[175]

The experiment performed with dodecane concentration of 50 µL, hereafter named HC-50D-ZIF-8, where HC stands for hollow capsule and 50D is referred to the amount of dodecane in µL used for emulsion formation, was selected for full characterization (SEM, BET, TGA, IR). Further SEM images are shown below in Figure 4.38.

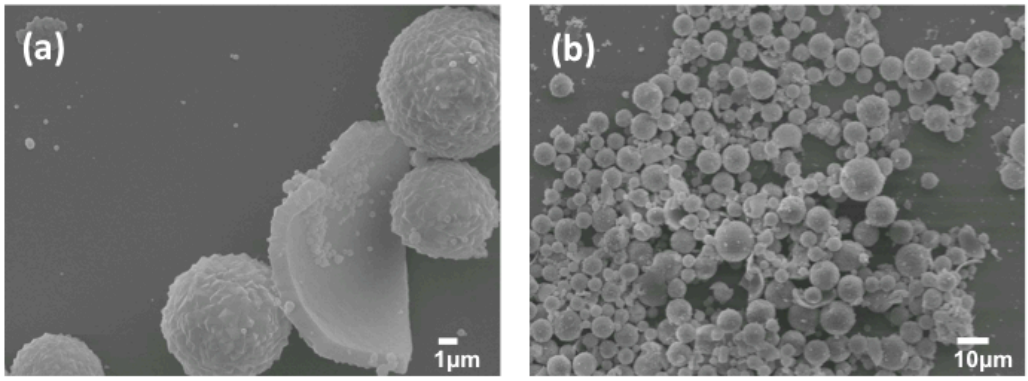


**Figure 4.38 SEM images at different magnitude of HC-50-ZIF-8.**

From the images the hollow capsules appeared enough homogeneous in size, where their size distribution is shown in Graph 4.1, varying from 4 to 17 µm, and just a few unaggregated particles are present.

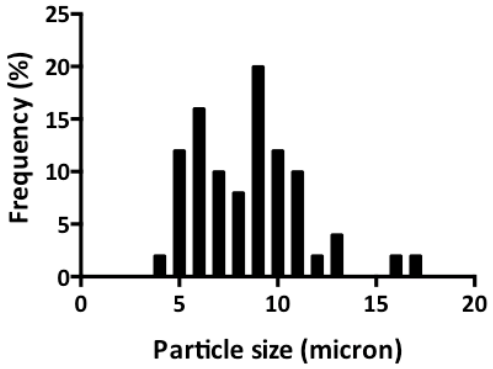


**Graph 4.1 Particle size distribution of HC-50D-ZIF-8 calculated after measuring 50 capsules and expressed in percentage.**

Figure 4.38 a showed the hollow nature of the hollow capsules, with shell thickness of about 1 µm, where the shell thickness might be an indication of the further growth of the shell following an initial pickering stabilisation as shell was thick and not made up of just aggregate of ZIF particles.

Nitrogen sorption analysis of HC-50D-ZIF-8 and ZIF-8 control experiment are shown below (Figure 4.39 and Figure 4.40)

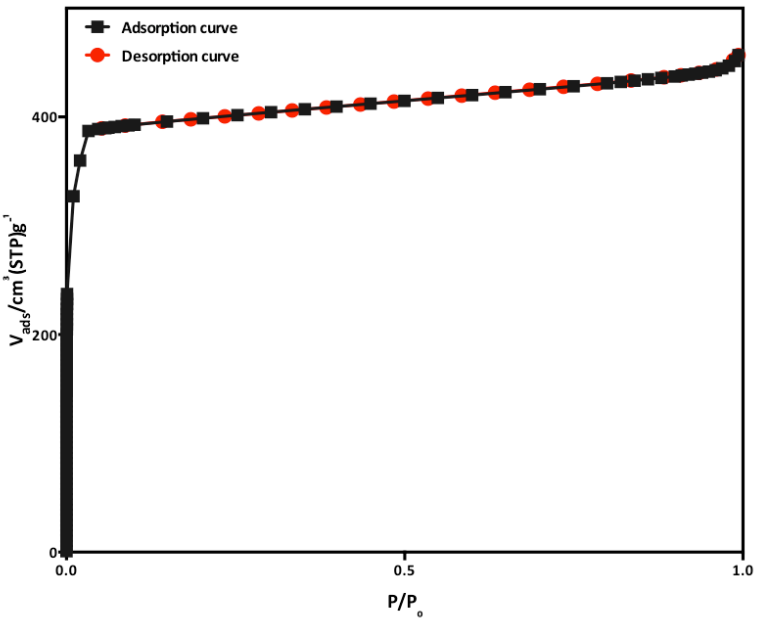


**Figure 4.39 Nitrogen sorption analysis determined at 77 K of HC-50D-ZIF-8.**

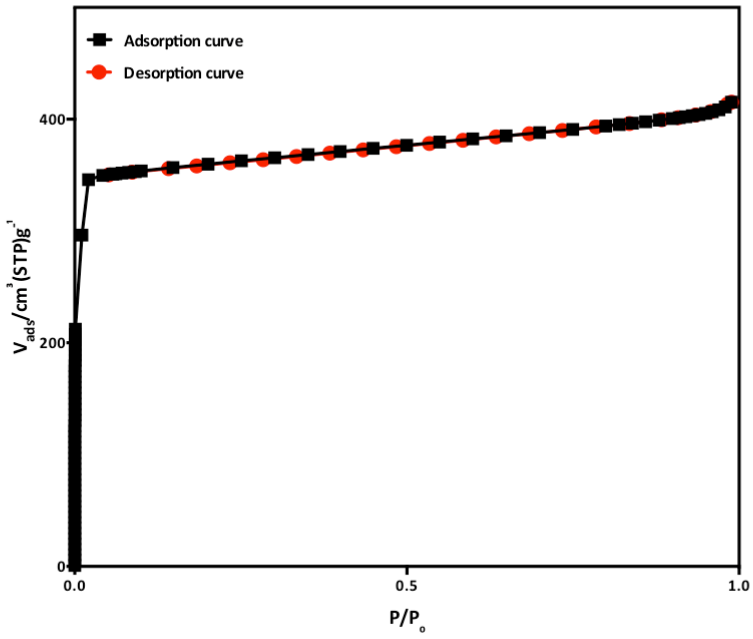


**Figure 4.40 Nitrogen sorption analysis determined at 77 K of ZIF-8 control experiment.**

The isotherm of HC-50D-ZIF-8 displayed a type I behaviour, with a large uptake at very low pressure related to the presence of micropores typical of ZIF-8, with a BET surface area of 1627 ± 0.5 $m^2/g$, which was higher then the other value detected in hollow ZIF-8 capsule[171, 192] and the ZIF-8 control experiment (1490 ± 0.3 $m^2/g$) but comparable to ZIF-8 obtained by solvothermal reaction.[70]

Below, in Figure 4.41 and Figure 4.42, infrared spectra and thermogravimetric analysis are shown.

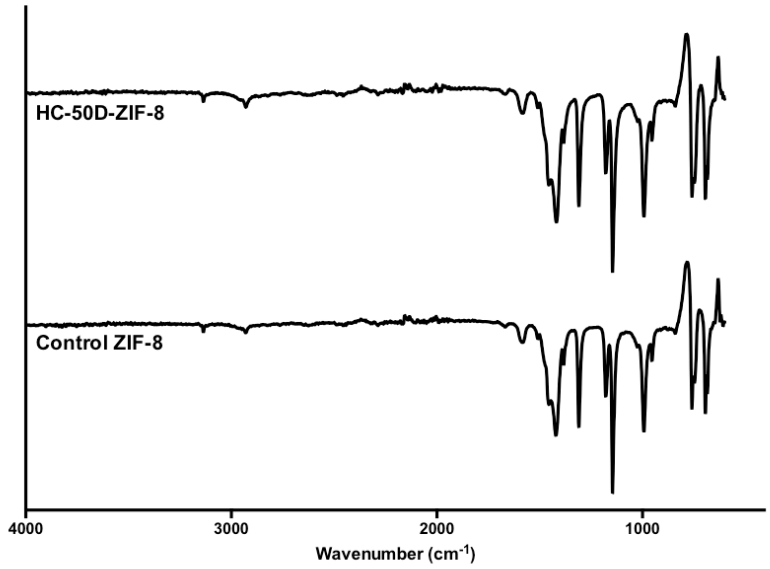


**Figure 4.41 IR spectra of the HC-50D-ZIF-8 and control ZIF-8.**

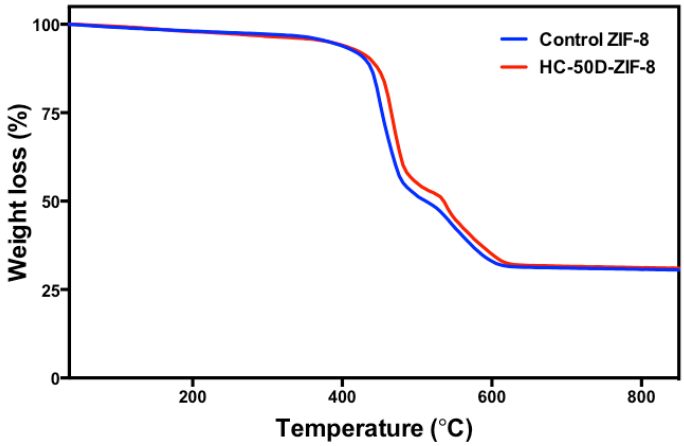


**Figure 4.42 Termo gravimetric analysis of the hollow capsules obtained at 50 µL of dodecane and control ZIF-8**

The IR spectrum showed the typical stretches associated with ZIF-8, where the bands at ~ 3150 and 3000 $cm^{-1}$ were attributed to the aromatic and the aliphatic C–H stretches of the methylimidazole linkers, respectively. The peak at 1600 $cm^{-1}$ can be assigned as the C=N stretching mode, whereas the intense and convoluted bands at 1350–1500 $cm^{-1}$ were associated with the entire ring stretching. The bands in the spectral region of 900–1350 $cm^{-1}$ referred to the in-plane bending of the ring while those below 800 $cm^{-1}$ were assigned as out-of-plane bending.[193] Finally the thermogravimetric analysis recorded that HC-50D-ZIF-8 was thermically stable until ~ 400 °C, then a mass loss of 71% related to the organic components in the range of temperature between ~ 400-600 °C occurred, which was consistent with the mass loss of the organic components expected for ZIF-8, which is 72%.

As mentioned before the influence of the addition of the surfactant SPAN-80 in the dodecane-in-water emulsion was investigated. In particular the amount of dodecane was kept constant, while

the amount of SPAN-80 was varied, as shown in Table 4.2. In a typical synthesis SPAN-80 and 25 µL of dodecane were dispersed in 5 mL of DI water by ultrasound for 10 min. A stable emulsion was generated by agitation using a shear force instrument at 16500 rpm for 2 min. Then a solution of $Zn(NO_3)_2.6H_2O$ (0.029g in 0.5 mL $dH_2O$) was added to the emulsion and stored at 4° C. After 3 hours a methyl imidazole solution (0.56g in 2 mL $dH_2O$) was further added and the emulsion stored at 4° C overnight. The white precipitate was recovered by centrifugation, washed twice with ethanol and dried overnight at room temperature. PXRD patterns and SEM images of the resulting ZIF-8 samples formed with different concentrations of SPAN-80 in the dodecane emulsion are shown below (Figure 4.43 and Figure 4.44).

| SAMPLE | a | b | c | d | e | f |
|---|---|---|---|---|---|---|
| DODECANE (µl) | 25 | 25 | 25 | 25 | 25 | 25 |
| SPAN-80 (mg) | 0 | 18 | 54 | 90 | 126 | 162 |

**Table 4.2 Amount of SPAN-80 and dodecane dissolved in 5 mL of $H_2O$ which undergoes to a shear force instrument for the emulsion formation.**

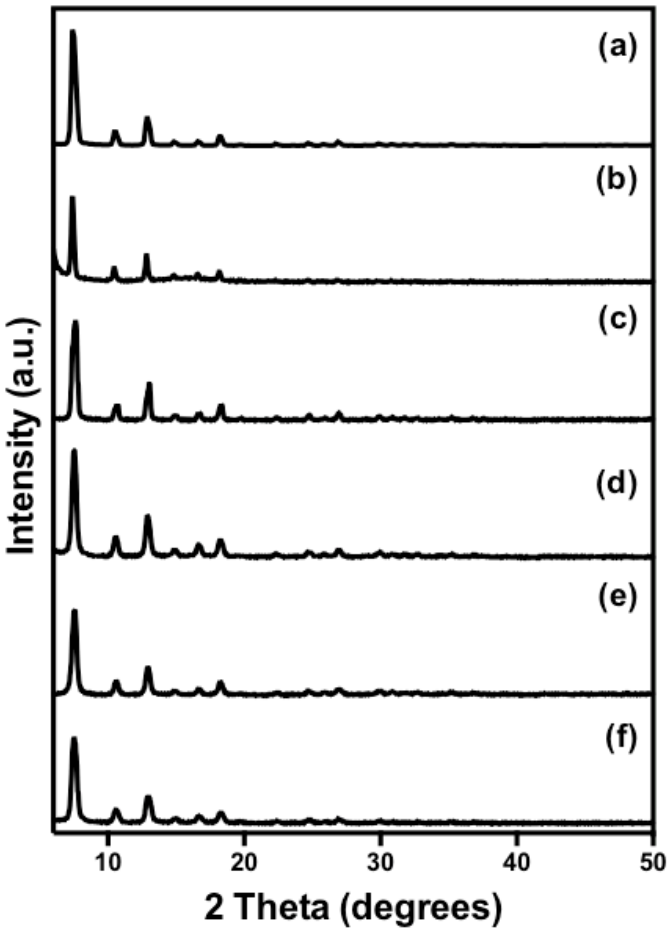


**Figure 4.43 PXRD patterns of ZIF-8 formed at different amounts of SPAN-80 keeping the dodecane at 25 µL: (a) 0, (b) 18, (c) 54, (d) 90, (e) 126 and (f) 162 mg.**

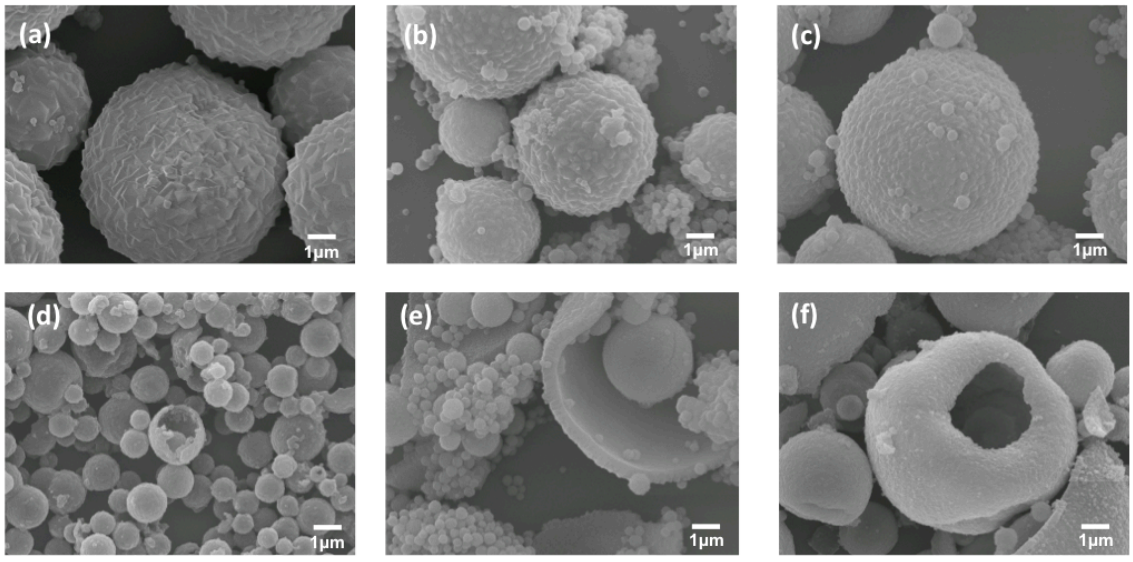


**Figure 4.44 SEM images of the samples performed at different amount of SPAN-80 keeping the dodecane at 25 µL: (a) 0, (b) 18, (c) 54, (d) 90, (e) 126 and (f) 162 mg respectively**

PXRD patterns confirmed that pure ZIF-8 was successfully synthesized in all the samples (Figure 4.43). SEM images showed that the introduction of SPAN-80 in the synthetic procedure still

allowed the hollow capsules formation. In particular its effect was concentration dependent: indeed the experiments performed in presence of 18 or 54 mg of SPAN-80 did not substantially differ from the one obtained in the emulsion formed just by dodecane (Figure 4.44 b and c and a respectively). When the amount of SPAN-80 was increased to 90 mg a visible decrement in the hollow capsules size was detected (Figure 4.44 d). Finally when the amount of SPAN-80 reached 126 mg and above unaggregated ZIF-8 particles and polydisperse hollow capsules were formed (Figure 4.44 e and f).

The experiment performed with 90 mg of SPAN-80 (Figure 4.44 d), thereafter named HC-25D-90S-ZIF-8, where HC stands for hollow capsule, 25D refers to the amount of dodecane in µL and 90 to the amount of SPAN-80 in milligrams, has been further characterized by SEM, BET, TGA and FTIR.

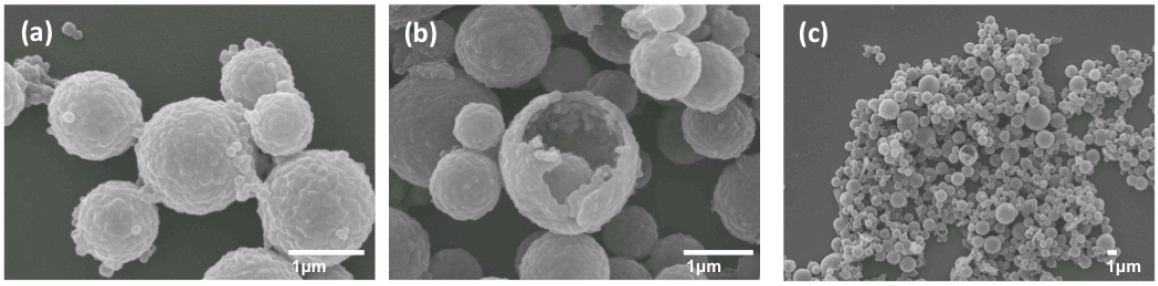


**Figure 4.45 SEM images of HC-25D-90S-ZIF-8.**

Figure 4.45 shows further SEM images of HC-25D-90S-ZIF-8 revealing that the size of the hollow capsules have an average diameter between 0.75 and 1.25 µm, as reported in Graph 4.2, which is approximately an order of magnitude smaller than when surfactant-free dodecane emulsions were used (Graph 4.1).

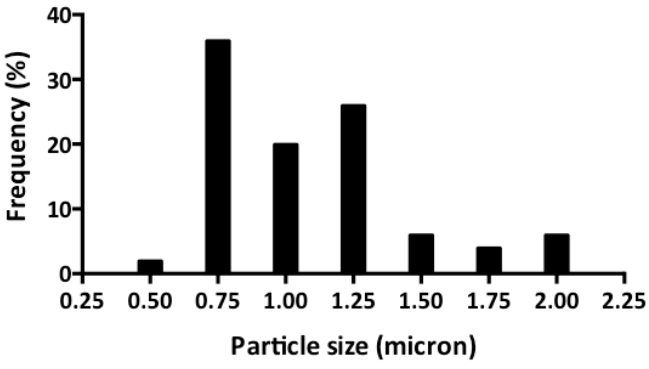


**Graph 4.2 Particle size distribution of HC-25D-90S-ZIF-8 calculated after measuring 50 capsules and expressed in percentage.**

Figure 4.45 b demonstrated the hollow nature of the capsules, with a shell thickness of about 100 nm. The nitrogen sorption analysis and pore size adsorption and desorption graphs are shown in Figure 4.46 and Figure 4.47, respectively.

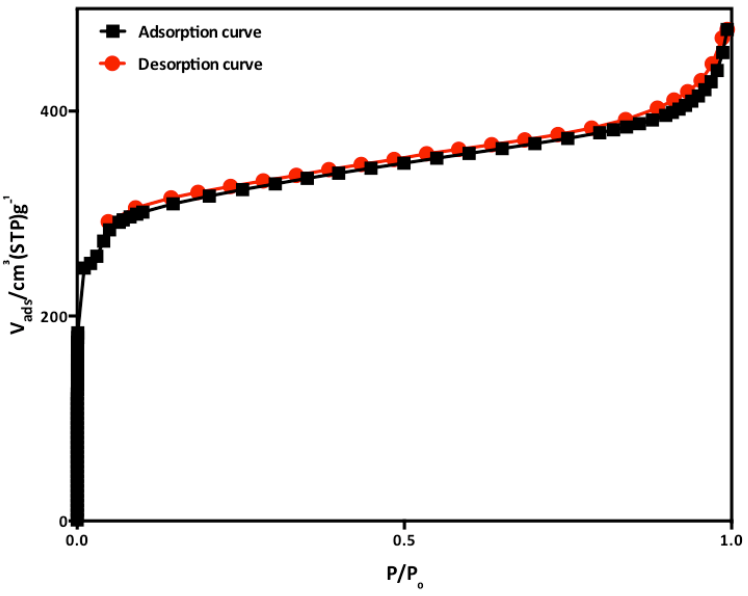


**Figure 4.46 Nitrogen sorption analysis of HC-25D-90S-ZIF-8 measured at 77 K**

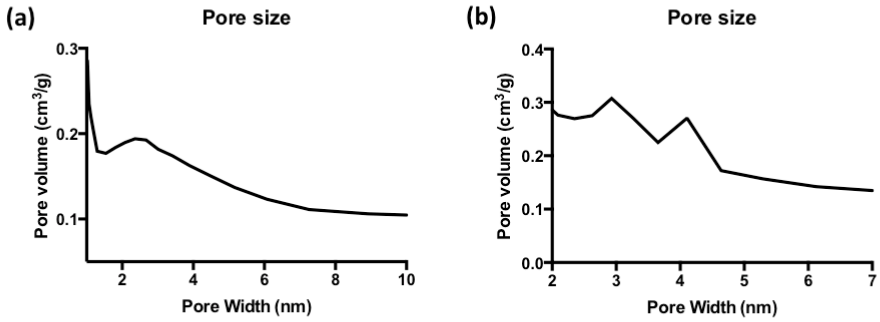


**Figure 4.47 The pore size determined by (a) BJH adsorption and (b) BJH desorption pore distribution**

The isotherm exhibited an intermediate behaviour between types I and IV, with a large uptake at low pressure and a hysteretic desorption profile. The large uptake at low pressure was related to the presence of the microporous ZIF-8, while the hysteresis in the desorption branch was characteristic of mesoporosity. In the present case this most likely arose from the voids between the particles forming the walls of the hollow capsule rather than templated mesopores and the capsule interiors which were on the macroporous scale would contribute to this. This was confirmed by the BJH adsorption and desorption graphs that showed a mesopore size of 3-4 nm, due to the voids left between the particles, which was not present in the control ZIF-8 experiment. The apparent BET surface area was reduced compared to the previous hollow capsules and with respect to the control experiments (Figure 4.40), which was consistent with the presence of mesoporosity (respectively 1180 ± 0.5 for HC-25D-90S-ZIF-8, 1627 for HC-50D-ZIF-8 and 1490 $m^2/g$ for the control experiment). Below infrared spectra and thermogravimetric analysis were shown (Figure 4.48 and Figure 4.49).

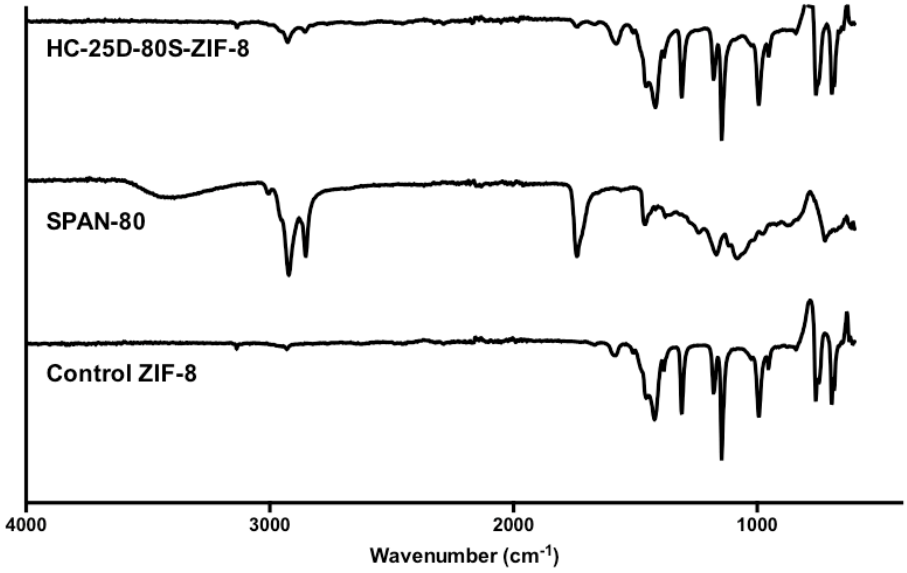


**Figure 4.48 IR spectra of HC-25D-90S-ZIF-8, the surfactant SPAN-80 and control ZIF-8.**

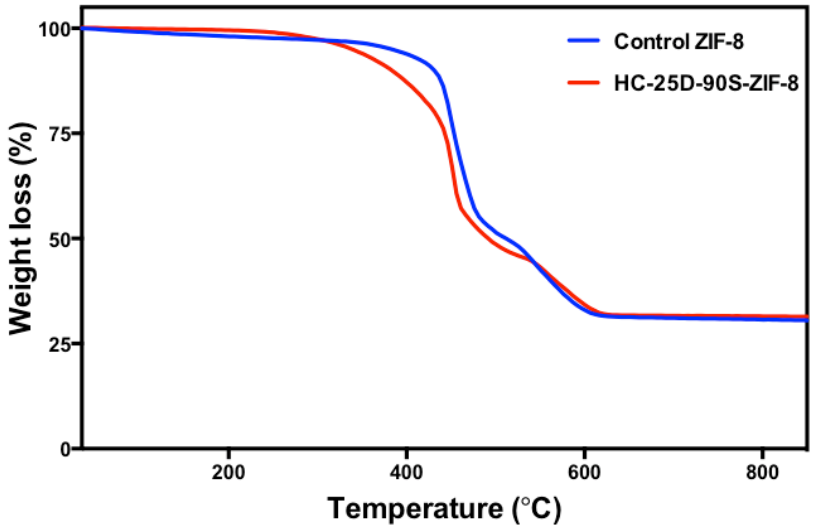


**Figure 4.49 Thermogravimetric analysis of HC-25D-90S-ZIF-8 and the control ZIF-8**

The IR spectrum of HC-25D-90S-ZIF-8 reported showed that, nevertheless the sample was repeatedly washed in ethanol, SPAN-80 still appeared to be present in the framework, as indicated by the bands at 2900, 2800 and 1750 $cm^{-1}$, which were not present in the IR spectrum of the ZIF-8 control. The presence of SPAN-80 in HC-25D-90S-ZIF-8 framework would suggest an intimate association between the two, implying the former had a role to play in colloidosome assembly.[194] Furthermore the drop in surface area might be related to the presence of SPAN-80 in the framework. However the TGA of HC-25D-90S-ZIF-8 did not show an increment in the organic percentage compared to the control ZIF-8, meaning that the amount of SPAN-80 included was likely limited.

HC-50D-ZIF-8 and HC-25D-90S-ZIF-8 were compared in terms of their external surface characteristics, shell thickness and overall size as shown in Figure 4.50.

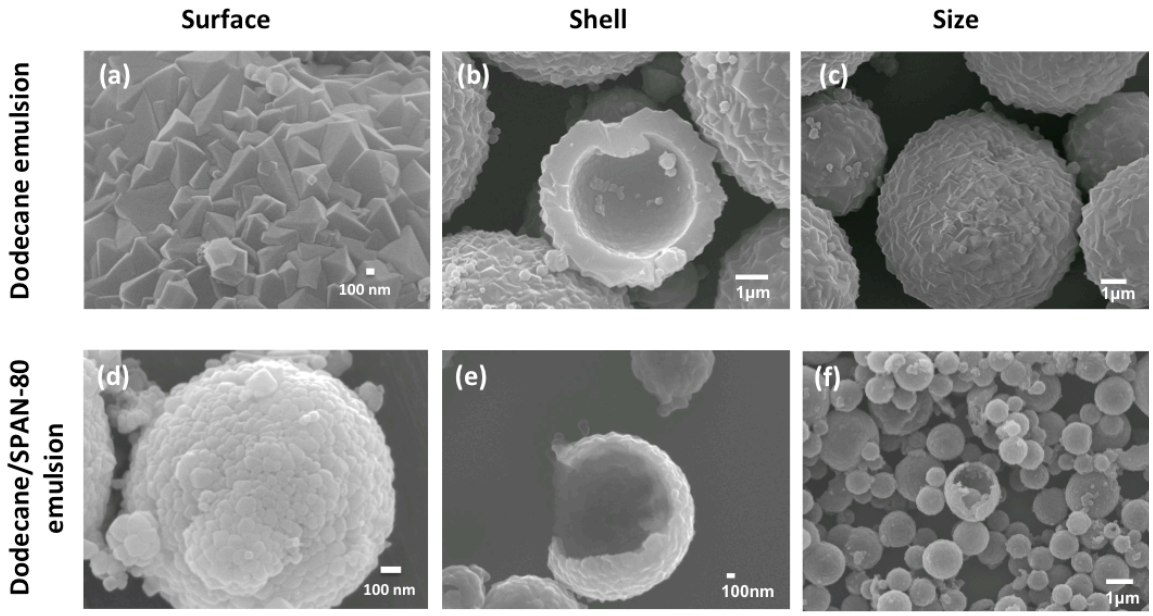


**Figure 4.50 Comparison in terms of surface, shell thickness and size of the hollow capsules obtained with the two different kind emulsions: (a), (b) and (c) from dodecane emulsion and (d), (e), (f) from dodecane/SPAN-80 emulsion**

The external surfaces of the hollow capsules appeared different in the two cases: the size of the crystals that made up the shell surface was much greater than 100 nm in HC-50D-ZIF-8, whereas those in HC-25D-90S-ZIF-8 were < 100 nm (Figure 4.50 a and d). Also the thickness of the shell was considerably different in the two samples: it was about 1 µm for HC-50D-ZIF-8 and about 100 nm for HC-25D-90S-ZIF-8, which was comparable to the dimensions of the ZIF-8 nanoparticles from which it was composed (Figure 4.50 b and e). Finally the dimension of the two hollow capsules was about 4 and 10 µm size for HC-50D-ZIF-8 and between 500 nm and 1 µm for HC-25D-90S-ZIF-8 (Figure 4.50 c and f).

The observed differences could arise from different mechanisms for the hollow capsule formation with and without the SPAN-80 emulsifier and further analysis were performed in order to investigate this. At first the as prepared emulsions obtained by the shear force instrument were analysed by optical microscopy as shown in Figure 4.51.

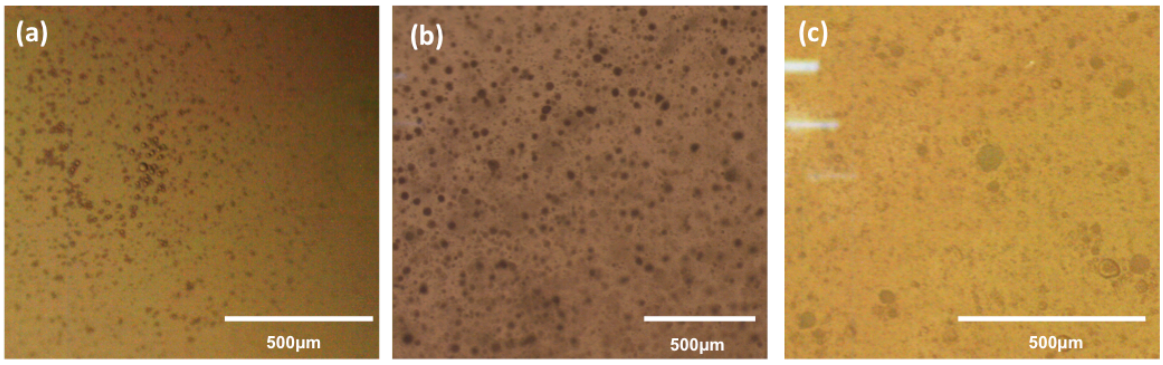


**Figure 4.51 Optical microscopy images of (a) dodecane, (b) dodecane/SPAN-80 and (c) SPAN-80 emulsions prepared by shear force instrument.**

The dodecane-in-water emulsions did not differ significantly whether the SPAN-80 was present or not; however, the water dispersion of SPAN-80 showed a reduction in homogeneity of the droplet size. The experiment was then performed in a SPAN-80 dispersion: PXRD pattern and SEM images were shown in Figure 4.52.

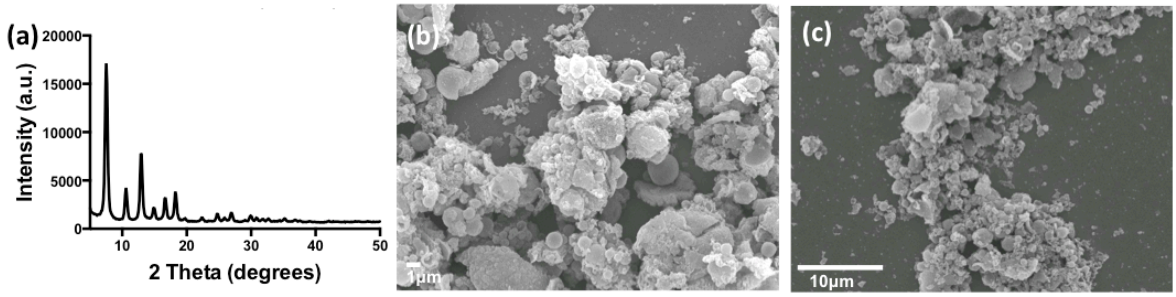


**Figure 4.52 (a) PXRD pattern and (b), (c) SEM images of experiment performed with SPAN-80 emulsion.**

ZIF-8 was successfully synthesized in the presence of SPAN-80 only, and SEM images showed that mainly nanoparticles were formed with very few hollow capsules being observed. This suggested that the assembly of SPAN-80 in the absence of an oil phase was not sufficiently stable to form well-defined hollow capsules of ZIF-8 under these conditions. On the other hand SPAN-80 had a clear affect on the ZIF-8 particle-size when compared to a control synthesis under the same conditions in the absence of the emulsifier as shown in Figure 4.53.

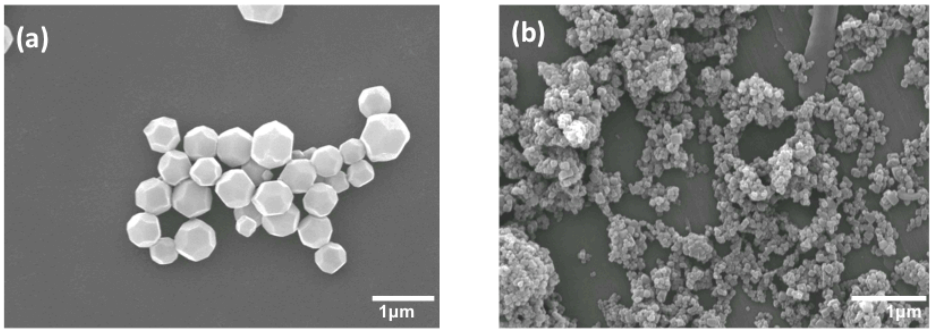


**Figure 4.53 SEM images of (a) control experiment and (b) unaggregated particles formed in the experiment performed with SPAN-80.**

The particle size was reduced from about 500 nm in the control experiments to about 100 nm, suggesting that SPAN-80 could modulate the particle size, which was already reported for the conjunction effect of SPAN-80 and TWEEN-80 in aqueous media[183] even though the synthetic conditions used in the reactions were different. In the reported literature the SPAN-80/TWEEN-80 emulsion was formed by sonication and the reaction conducted at 60 °C for 1 hour and the relative ratio $Zn^{2+}$:SPAN-80:TWEEN-80:MeIm:$H_2O$ =1:0.06:0.08:2:1234, while in the experiments performed here the ratio $Zn^{2+}$:SPAN-80:MeIm:$H_2O$ was 1:2.3:70:4294. The reported mechanism of the process involved the formation of surfactant micelles in which the ZIF-8 nanocrystals were formed. While H-MeIm molecules and Zn-MeIm intermediates enriched inside the micelle, $OH^-$ was largely excluded due to the less hydrophilic nature, preventing the competition with the organic ligand. This effect stabilized the Zn−MeIM intermediates from the attack of $OH^-$ groups, which resulted in formation of pure ZIF-8 nanocrystals. Furthermore the ZIF-8 crystal morphology and size were tailored using the surfactant CTAB as capping agent, as further discussed in the introduction;[106] in this case the ratio of zinc precursor to MeIm and the dilution of the solutions were comparable ($Zn^{2+}$:MeIm:$H_2O$=1:56:4581) but the reaction was carried out under solvothermal conditions and using lower amounts of CTAB (range between 0.0055 and 0.055 mmol versus 0.21 mmol in the present work). Increasing the amount of surfactant to 0.055 mmol the crystal size decreases to ca. 110 nm obtaining particles with truncated cubic morphology. In this case the long hydrocarbon chain of the surfactant was reported to play a crucial role in changing the morphology and the particles size of ZIF-8 crystals. Finally Xing *et al.* successfully modulated the ZIF-8 particle size into the nanorange in the presence of non-ionic triblock copolymers P123 and F127 in aqueous solution under microwave irradiation.[195] The reaction was heated in a microwave oven at 120 °C for 30 minutes using a relative ratio $Zn^{2+}$:P123:F127:MeIm:$H_2O$=1:0.005-0.07:0.0007-0.01:4:1110. The proposed mechanism for the formation of ZIF-8 nanocrystals was the following: PEO–PPO–PEO type amphiphilic triblock copolymers P123 and F127 formed surfactant micelles in aqueous solution, in which a core was presumably dominated by PPO and a corona was dominated by hydrated PEO blocks. These

oxygen atoms on PEO blocks could electrostatically interact with metal ions which would compete with the coordination equilibrium between MeIm and metal ions under microwave irradiation. The evenly distributed $Zn^{2+}$ with PEO–PPO–PEO type surfactants would facilitate the formation process of the ZIF-8 structure acting as seeds for the nucleation during the microwave irradiation. More seeds led to faster growth and higher yields with narrow size distribution. In light of this, SPAN-80 might downsize the ZIF-8 particles forming micelles, since its amount was comparable to the SPAN-80/TWEEN-80 synthesis or maybe just through the attachment of long hydrocarbon chains on the ZIF-8 crystal faces, in a similar manner reported for CTAB.[106]

Based on the experimental differences in the surface, shell thickness and the size of the hollow capsules obtained from dodecane-only and dodecane/SPAN-80 emulsions and the effect of SPAN-80 on ZIF-8 particle size, two different mechanisms were hypothesized. The proposed mechanism for the dodecane emulsion system was the following: applying the shear force the dodecane-in-water emulsion was formed, the two ZIF-8 precursors were added, and rapidly formed ZIF-8 particles stabilise the emulsion droplets via a Pickering-type interaction as they had appropriate wettability.[175] The Pickering-stabilised droplet then acted as a substrate for further MOF growth allowing the completion and deposition of the observed thick MOF shell as shown in Scheme 4.2.

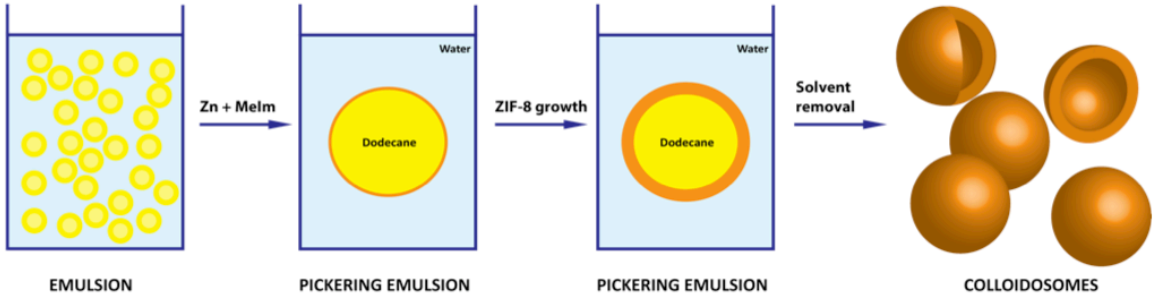


**Scheme 4.2 Illustration of the HC-50D-ZIF-8 formation mechanism. Dodecane emulsion is formed by applying a shear force and when the two ZIF-8 precursors are added the ZIF-8 particles form and stabilise the emulsion droplets via Pickering emulsion forming the hollow capsules.**

In the case of the dodecane/SPAN-80 system probably SPAN-80 acted as an emulsifying agent to provide a greater initial stabilisation of the dodecane emulsion and presumably its outward-facing polar headgroup promoted nucleation of small ZIF-8 nanoparticles over their growth hence particles in the resulting shell were much smaller than in the previous case, as shown in Scheme 4.3.

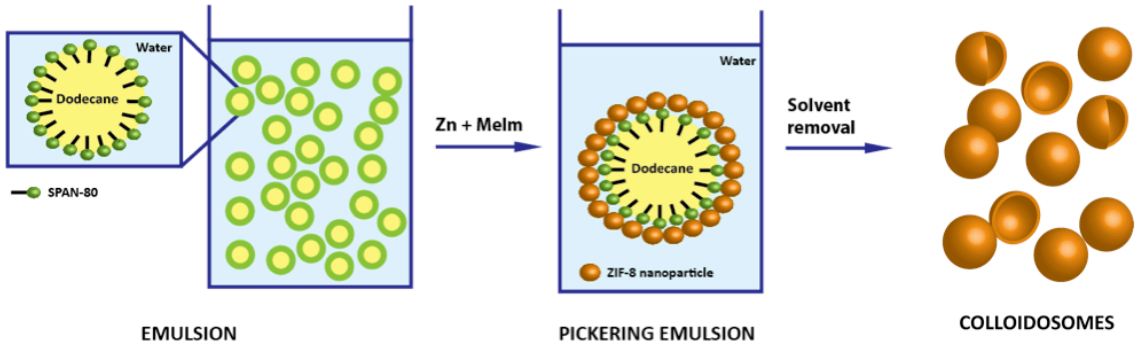


**Scheme 4.3 Illustration of the HC-25D-90S-ZIF-8 formation mechanism in dodecane/SPAN-80 emulsion. SPAN-80 tailor the particle size into the nanorange, which are self-assembled around the dodecane droplet forming the colloidosomes.**

Furthermore the resulting colloidosomes HC-25D-90S-ZIF-8 showed a decrement in the size of about one order of magnitude compared to the HC-50D-ZIF-8. Considering that the dodecane and dodecane/SPAN-80 as-prepared emulsions had comparable size (Figure 4.51 a, b) the size decrement of HC-25D-90S-ZIF-8 might be related to the decrement in the ZIF-8 building blocks due to the presence of SPAN-80.

The experiments were also performed in the presence of dodecane/TWEEN-85 and dodecane/SPAN-20 emulsion systems to further evaluate the specific role of SPAN-80. Despite the similarity of these two emulsifiers with SPAN-80 these two emulsions did not lead to the formation of colloidosomes. In dodecane/TWEEN-85 emulsion no precipitate was detected implying the suppression of ZIF-8 formation. Probably under these conditions TWEEN interacted too strongly with the MOF precursors, as in the mentioned case of CTAB,[156] or it might just slow down the reaction, so having a kinetic effect on ZIF-8 formation. Dodecane/SPAN-20 emulsion led to the formation of even smaller ZIF-8 nanoparticles, as shown from the PXRD pattern and the SEM image of Figure 4.54.

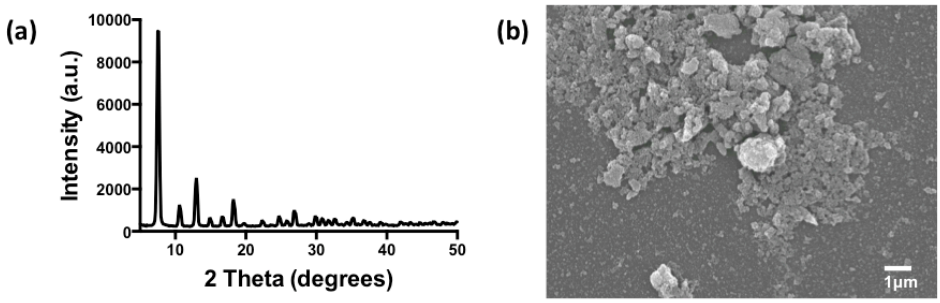


**Figure 4.54 Experiment performed with dodecane/SPAN-20 emulsion:(a) PXRD pattern and (b) SEM image.**

Therefore the decrement in the particle size promote by SPAN-20 might prevent the colloidosomes formation[173] or SPAN-20 might not stabilise the dodecane emulsion as efficiently

as SPAN-80. Indeed according to their hydrophilic-lipophilic balance (HLB) values (Table 4.3, Appendix A), SPAN-20 and TWEEN-85 were more soluble in aqueous solution then SPAN-80.

| Product name | Chemical identity | HLB value |
|---|---|---|
| SPAN-20 | Sorbitan monolaurate | 8.6 |
| SPAN-80 | Sorbitan monooleate | 4.3 |
| SPAN-85 | Sorbitan trioleate | 1.8 |
| TWEEN-85 | Polyethylene glycol sorbitan trioleate | 11 |

**Table 4.3 Product name, chemical identity and HLB value of the SPAN and TWEEN surfactant employed.**

This indicates they were less suitable to stabilize the emulsion.

### 4.2.4 Hollow capsules treated with imidazole

HC-50D-ZIF-8 was further treated with imidazole. As previously reported imidazole can change the ZIF-8 morphology and topology, therefore the effect of the organic ligand was investigated also starting from the hollow capsule. Typically 0.46 g of imidazole were dissolved in 7 ml of water and then added to 15 mg of premade colloidosomes. The solution was sonicated for 2 minutes and left for respectively 5, 10, 15 minutes or 2 hours and then centrifuged, washed twice with ethanol and left to dry overnight at room temperature. PXRD patterns and SEM images are shown below in Figure 4.55 and Figure 4.56.

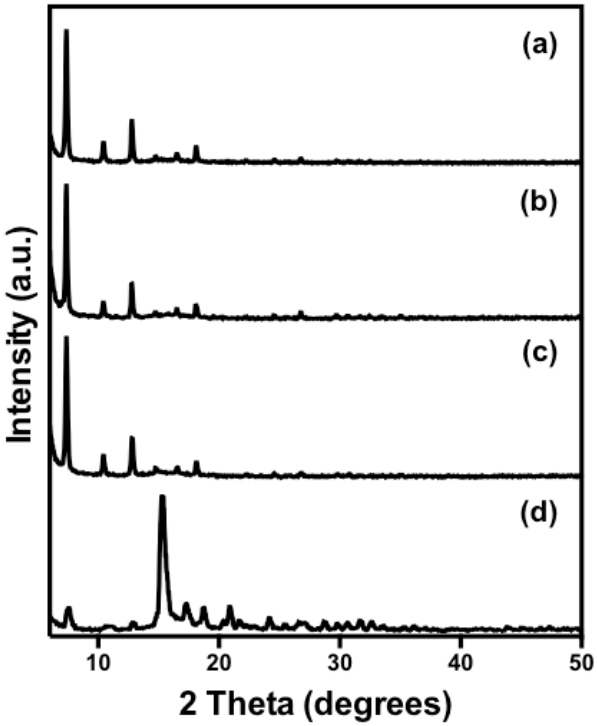


**Figure 4.55 PXRD patterns of time experiments after imidazole addition: (a) 5 minutes, (b) 10 minutes, (c) 15 minutes and (d) 2 hours.**

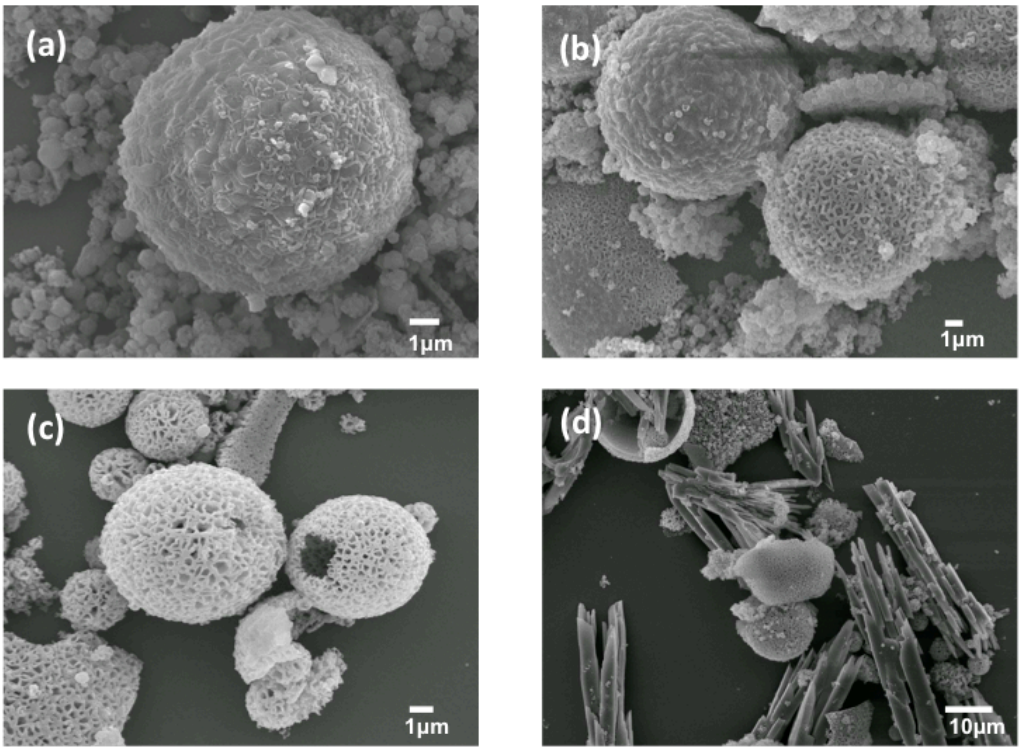


**Figure 4.56 SEM images of time experiments after imidazole addition: (a) 5 minutes, (b) 10 minutes, (c) 15 minutes and (d) 2 hours.**

PXRD patterns showed a time dependent conversion from ZIF-8 to ZIF-61, transforming from an open sodalite (**sod**) network to a dense **zni** phase, which would be more extensively discussed in

Chapter 5. SEM images of the samples at different time intervals showed that imidazole etches the surface of the hollow capsules. The effect was visible after only 5 minutes and it was complete after 15 minutes, where the hollow capsule shell wall presented holes on their surface, as in flower-like microcapsules.[196] Longer reaction times led to the complete conversion of the ZIF-8 phase into ZIF-61, which was visible in both the PXRD pattern and the clear change in morphology from spheres to rod-like particles in Figure 4.55 d.

The sample at 15 minutes, named Im-HC-50D-ZIF-8 was further analysed by SEM.

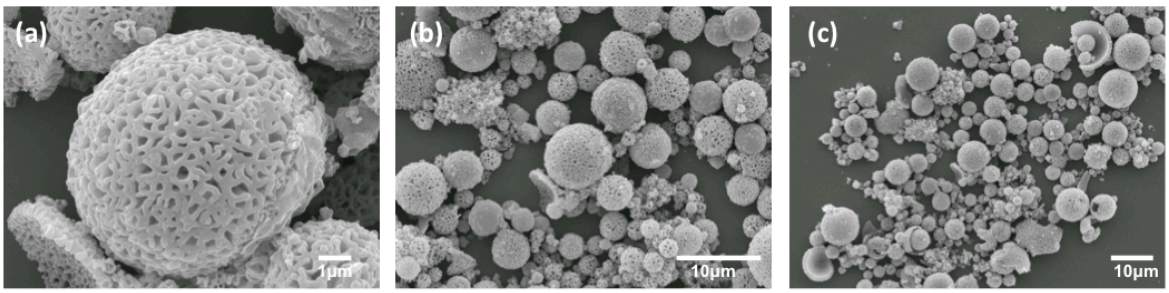


**Figure 4.57 SEM images of Im-HC-50D-ZIF-8 flower-like microcapsule obtained by treatment of with imidazole.**

SEM images showed that the shape of the hollow capsules was retained, while their surface was etched by imidazole into rounded features of a few hundred nanometers in size, which appeared to penetrate all the way through the shell wall (Figure 4.57).

Furthermore, HC-25D-90S-ZIF-8 was also treated with imidazole following a similar procedure: 0.46 g of imidazole were dissolved in 7 ml of water and then added to 15 mg of premade colloidosomes. The solution was sonicated for 2 minutes and left for 15 minutes and then centrifuged, washed twice with ethanol and dried overnight at room temperature. PXRD patterns and SEM images were shown below (Figure 4.58).

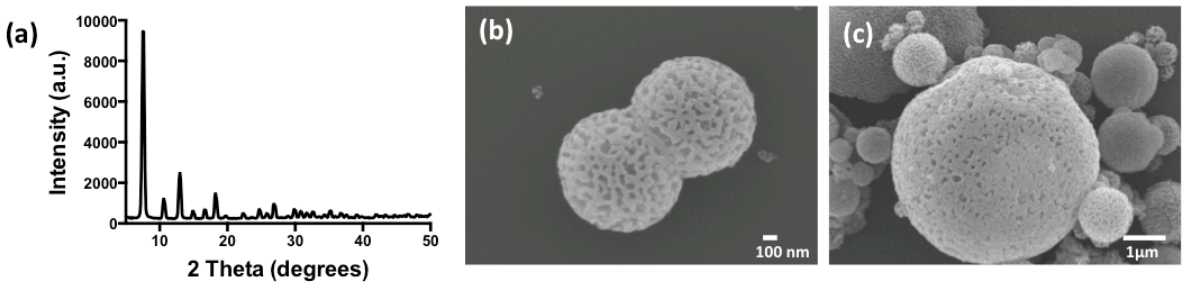


**Figure 4.58 HC-25D-90S-ZIF-8 treated with imidazole: (a) PXRD patterns and (b-c) SEM images.**

Also in this case PXRD pattern showed the SOD topology has been maintained and the imidazole had the same effect in etching the surface of HC-25D-90S-ZIF-8.

These kind of features were not new in the literature, and were obtained from biomimetic mineralization approaches,[196-197] where phosphate-type microflowers (e.g. $Cu_3(PO_4)_2$, $Ca_3(PO_4)_2$) were used as templates for the preparation of flower-like microcapsule. However the hollow capsules etched by imidazole was more likely to follow the same path as the Prussian blue (PB) hollow particles fabricated by controlled self-etching reaction in the presence of PVP,[198] where the etching solution diffused into the core of the PB mesocrystals (mesoscopically-structured crystals) through the small pores (or defects) of the aggregated PB nanocrystals leading to the formation of an interior hollow cavity with the retention of the original PB crystallinity. Similarly the defects between the ZIF-8 crystals that comprised the shell might be the point from which imidazole started its etching. Furthermore the transformation from a smooth surface to extremely rough highly increased the exposed surface area, which increased the potential application of the material for instance in catalysis. On the other hand a related etching effect was reported in MOF chemistry by Maspoch *et al.*.[199] In their approach simple acid-base reactions were used for metal ion sequestration. In particular colloidal aqueous solution of ZIF-8 or ZIF-67 crystals were mixed with an aqueous solution containing the weak acid xylenol orange (XO) whose pH was adjusted using HCl or NaOH. Mixing the two solutions the MeIm linkers became protonated, which respectively breaks the Zn/Co-MeIm bonds and slowly and preferentially carved those external crystal surfaces having the highest density of Zn/Co-MeIm bonds (that was, carved in the <100> and/or <211> directions). Simultaneously, XO also acted as a chelating agent chelating the liberated $Zn^{2+}$ and $Co^{2+}$ ions to form the well-known, stable, and water-soluble Zn–XO and Co–XO complexes respectively, which sequestered the metal ions, preventing any further reaction.

## 4.3 Conclusions

In this chapter the directional self-assembly properties of ZIF-8 in aqueous media at room temperature for the formation of hollow capsules and colloidosomes were investigated. A few preliminary studies were performed stirring the reaction under magnetic stirring using SPAN-80 or SPAN-80/dodecane emulsions. Even though colloidosomes were formed, the experiments performed stressed the importance of a stable emulsion for the hollow capsule formation, which was optimized using a shear force instrument. Therefore two kinds of emulsions were selected: dodecane-in-water and dodecane/SPAN-80-in-water. Both emulsions were suitable for the formation of hollow capsules; thereafter the conditions were optimized in order to obtain monodisperse hollow capsules without any unorganized (free) nanoparticles. It was important to underline that the type of emulsion used influences the process though the hollow capsules were

assembled, as suggested by the differences in surface, shell thickness and size of the two kinds of hollow capsules.

In the case of the dodecane-only emulsion probably ZIF-8 particles formed and stabilised the emulsion droplets via Pickering type, this can then act as a substrate for further MOF growth giving rise to the hollow capsule. On the other hand, when the emulsion was formed by dodecane/SPAN-80 the resulting hollow capsules had different characteristics. In this system the role of SPAN-80 was two-fold: acting as an emulsifying agent in the dodecane emulsion and promoting the nucleation of ZIF-8 nanoparticles over their growth at the oil-in-water interface. This led to colloidosomes with smaller shell compared to the previous case. Finally HC-50D-ZIF-8 and HC-25D-90S-ZIF-8 significantly differed in size. It might be related to the decrement in the ZIF-8 building blocks due to the presence of SPAN-80, rather than the as-prepared emulsion.

The hollow capsules were further treated with imidazole, indeed the organic linker influenced the morphology and topology of ZIF-8. HC-50D-ZIF-8 was dispersed in an aqueous solution of imidazole for a period between 5 minutes and two hours. The introduction of imidazole led to the conversion from ZIF-8 to ZIF-61, further discussed in Chapter 5, which was detected by PXRD patterns and a morphological change of the particles from spherical to rod-like. More interestingly, before the conversion occurred, imidazole etched the surface of the hollow capsules leaving characteristic features on their surface similarly to flower-like microcapsule. The etching solution was supposed to diffuse from the defect of the crystals composing the surface, leading to visible holes in the shell structures. Furthermore also HC-25D-90S-ZIF-8 were treated with an aqueous solution of imidazole for 15 minutes giving rise to similar features on the surface and keeping the original topology.

## 4.4 Experimental part

**SYNTHETIC PROCEDURE FOR THE SYNTHESIS OF ZIF-8 WITH SPAN-80 UNDER MAGNETIC STIRRING:** SPAN-80 (90 mg, 0.21 mmol) was dissolved in 5 mL of water and stirred for 1 or 5 hours at room temperature, solutions of $Zn(NO_3)_2.6H_2O$ (0.029g in 0.5 mL $dH_2O$) and methyl imidazole (0.56g in 2 mL $dH_2O$) were sequentially added and the let under stirring for an other two hours. The white precipitate was recovered by centrifugation, washed twice with ethanol and dried overnight at room temperature. Yield= 15 mg.

**SYNTHETIC PROCEDURE FOR PREMADE ZIF-8 PARTICLES WITH SPAN-80 UNDER MAGNETIC STIRRING** SPAN-80 (90 mg, 0.21 mmol) was dissolved in 5 mL of water and stirred for 5 hours at room temperature and then an aqueous solution of ZIF-8 particles (15 mg in 2.5 mL of $H_2O$) was added and stirred for 2 hours at room temperature. The white precipitate was recovered by

centrifugation, washed twice with ethanol and dried overnight at room temperature. Yield= 15 mg.

**SYNTHETIC PROCEDURE FOR THE SYNTHESIS OF ZIF-8 WITH SPAN-80/DODECANE UNDER MAGNETIC STIRRING:** Dodecane and SPAN-80 were dissolved in an aqueous solution (respectively 25 µL and 90 mg in 5 mL of $H_2O$) and stirred for 5 hours in order to obtain an intimate aggregation of the two compounds. Hereafter the zinc nitrate solution (0.029g in 0.5 mL $dH_2O$) and methylimidazole solution (0.56g in 2 mL $dH_2O$) were added and the reaction carried out for 2 hours. The white precipitate was recovered by centrifugation, washed twice with ethanol and dried overnight at room temperature. Yield= 15 mg.

**SYNTHETIC PROCEDURE FOR THE SYNTHESIS OF ZIF-8 COLLOIDOSOMES, DODECANE EMULSION WITH SHEAR FORCE INSTRUMENT:** 50 µL of dodecane were dispersed in 5 mL of DI water by ultrasound for 10 min. A stable Pickering emulsion was generated by agitation using a shear force instrument at 16500 rpm for 2 min. Then solutions of $Zn(NO_3)_2.6H_2O$ (0.029g in 0.5 mL $dH_2O$) and methyl imidazole (0.56g in 2 mL $dH_2O$) were sequentially added to the emulsion and stored at 4° C for 3 hours. The white precipitate was recovered by centrifugation at 5000 rpm, washed twice with ethanol and dried overnight at room temperature. Yield= 15 mg.

**SYNTHETIC PROCEDURE FOR THE SYNTHESIS OF ZIF-8 COLLOIDOSOMES, SPAN-80/DODECANE WITH SHEAR FORCE INSTRUMENT:** SPAN-80 (90 mg) and 25 µL of dodecane were dispersed in 5 mL of DI water by ultrasound for 10 min. A stable emulsion was generated by agitation using a shear force instrument at 16500 rpm for 2 min. Then a solution of $Zn(NO_3)_2.6H_2O$ (0.029g in 0.5 mL $dH_2O$) was added to the emulsion and stored at 4° C. After 3 hours a 2-methylimidazole solution (0.56g in 2 mL $dH_2O$) was further added and the emulsion stored at 4° C overnight. The white precipitate was recovered by centrifugation at 5000 rpm, washed twice with ethanol and dried overnight at room temperature. Yield= 15 mg.

**SYNTHETIC PROCEDURE FOR THE SYNTHESIS OF ZIF-8 WITH SPAN-80 WITH SHEAR FORCE INSTRUMENT:** SPAN-80 (90 mg) was dispersed in 5 mL of DI water by ultrasound for 10 min. The dispersion underwent to agitation by using a shear force instrument at 16500 rpm for 2 min. Then solutions of $Zn(NO_3)_2.6H_2O$ (0.029g in 0.5 mL $dH_2O$) and methyl imidazole (0.56g in 2 mL $dH_2O$) were sequentially added to the emulsion and stored at 4° C for 3 hours. The white precipitate was recovered by centrifugation at 5000 rpm, washed twice with ethanol and dried overnight at room temperature. Yield= 15 mg.

**SYNTHETIC PROCEDURE FOR THE SYNTHESIS OF ZIF-8 COLLOIDOSOMES, SPAN-20 or TWEEN-85 and DODECANE WITH SHEAR FORCE INSTRUMENT:** SPAN-20 or TWEEN-85 (0.21 mmol) and

25 µL of dodecane were dispersed in 5 mL of DI water by ultrasound for 10 min. A stable emulsion was generated by agitation using a shear force instrument at 16500 rpm for 2 min. Then a solution of $Zn(NO_3)_2.6H_2O$ (0.029g in 0.5 mL $dH_2O$) was added to the emulsion and stored at 4° C. After 3 hours a 2-methylimidazole solution (0.56g in 2 mL $dH_2O$) was further added and the emulsion stored at 4° C overnight. The white precipitate was recovered by centrifugation at 5000 rpm, washed twice with ethanol and dried overnight at room temperature. Yield: no precipitate with TWEEN-85, 10 mg with SPAN-20.

**SYNTHETIC PROCEDURE FOR THE TREATMENT OF COLLOIDOSOMES WITH IMIDAZOLE:** 0.46 g of imidazole where dissolved in 7 ml of water and then added to 15 mg of colloidosomes (HC-50D-ZIF-8 or HC-25D-90S-ZIF-8). The solution was sonicated for 2 minutes and let for respectively 5, 10, 15 minutes or 2 hours and then centrifuged, washed twice with ethanol and let dried overnight at room temperature. Yield= 2 mg

**SYNTHETIC PROCEDURE FOR ZIF-8 CONTROL EXPERIMENT:** A solution of $Zn(NO_3)_2.6H_2O$ (0.029g in 5.5 mL $dH_2O$) was mixed with a solution of methyl imidazole (0.56g in 2 mL $dH_2O$) and stored at 4° C overnight. The white precipitate was recovered by centrifugation at 5000 rpm, washed twice with ethanol and dried overnight at room temperature. Yield= 15 mg.

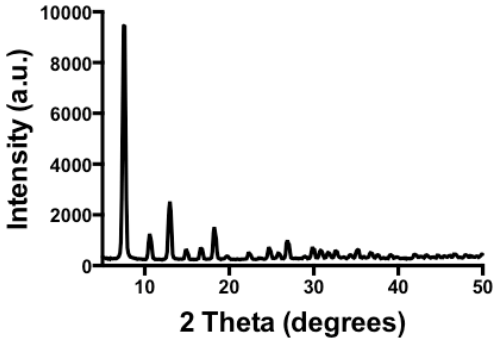


**Figure 4.**59 **PXRD pattern of ZIF-8 control experiment.**

All the experiments where performed at least 3 times in order to ensure reproducibility.

# Chapter 5: Surfactants effect on topology

## 5.1 Introduction

Zeolitic imidazolate frameworks (ZIFs) are a subclass of MOF materials formed by tetrahedral metal centres bridged by imidazolate linkers forming network structures analogous to zeolites.[70-73] Due to their wide structural diversity and relative thermal and chemical stability, ZIFs are promising materials which have been employed for different applications such as gas storage, separation, and catalysis.[75-76, 200-201] ZIFs are structurally classified on the basis of their topology,[82, 202] designated by a *bold-lowercase-three-letter* symbol, where some of them are based on zeotype topologies and others are new topologies, which have not been discovered in zeolites. Properties such as framework density and porosity are functions of the topology; therefore driving the connectivity of the building blocks to the desired topology should lead to control over the properties of the material. In this regards experimental and computational studies were performed, demonstrating that the topology of ZIFs could be tailored by the synthetic conditions[70] or by a ligand directed strategy.[73, 203] For instance ZIF-7 and ZIF-11 are characterized by the same chemical formula $Zn(PhIm)_2$ (PhIm= benzimidazolate) but displayed distinct topologies, **sod** and **rho** respectively, which were obtained by employing different synthetic conditions: ZIF-7 was synthesized in N,N-dimethylformamide (DMF) using a molar ratio $Zn^{2+}$:PhIm:DMF=1:0.74:87 from a solvothermal reaction at 130 °C for 48 hours, while ZIF-11 was synthetised in N,N-diethylformamaide (DEF) using a molar ratio $Zn^{2+}$:PhIm:DEF=1:15:1695 from a solvothermal reaction at 100 °C for 96 hours.[70] Furthermore small changes on parts of the imidazolate-type linker not involved in metal binding positions can make a difference in terms of favoured topology: it was the case of the work of *Yaghi et al.*, where replacing carbon with nitrogen at key positions of PhIm linker determined the topology of the resulting ZIF frameworks between **sod**, **rho**, **dia** or **lta**,[79] and the work of *Chen et al.* where reactions carried out under the same synthetic conditions, but employing 2-methylimidazole, ethylimidazole or a mixture of both as linkers led to the formation of **sod**, **ana** or topological $4^36$ supercages respectively, as shown in Figure 5.1.[80]

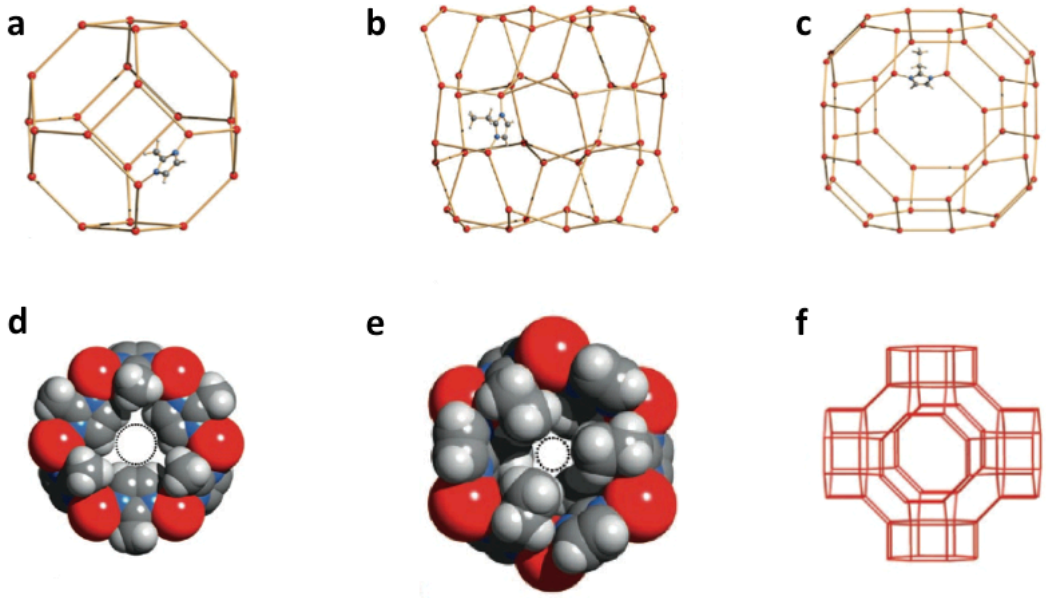


**Figure 5.1 Illustration of (a) topological sodalite (sod) net and (d) related space-filling diagram; (b) topological analcime (ANA) net and (e) related space-filling diagram; (c) truncated cuboctahedron and (f) the topological $4^3$6 supercage constructed from six eight-membered rings, eight six-membered rings, and twelve four-membered rings, and surrounded by six topological $4^2$8$^2$ cages, each constructed from two eight-membered rings and eight four-membered rings. Color code: Zn red, N blue, C gray, H white. Figure adapted with permission from ref.[80]**

Even more interestingly topological evolution of ZIFs through thermal treatment or solution mediated phase transformations within the same system were reported.[204-206] Whereas in the first case the thermal treatment of a 1-dimensional chain structure with formula [Zn(Im)(HIm)$_2$(OAc)] (HIm= imidazole, OAc= carboxylate) in a closed system led to a topological transformation to **zni** and then to **coi** topology,[204] while examples of the second case were the conversion of the Co-imidazolate based ZIF CoNIm (NIm= 2-nitroimidazole) from **rho** topology to the **sod** with increasing the reaction time[205] and ZIF-71 nanocrystals ([Zn(dcIm)$_2$], dcIm= 4,5-dichloroimidazolate) which underwent transformation from **rho** to **sod** and then **lcs** topology (ZIF-72) when kept in the mother solution.[206]

Moreover MOFs with mixed ligands possess an additional degree of complexity where the variability in the topology could also depend on the relative ratio of the two organic components incorporated into the framework.[207-208] In this regard the work from Oh *et al.* was significant: herein the morphology and the structure of MOF particles changed with the ratio of the two organic linkers.

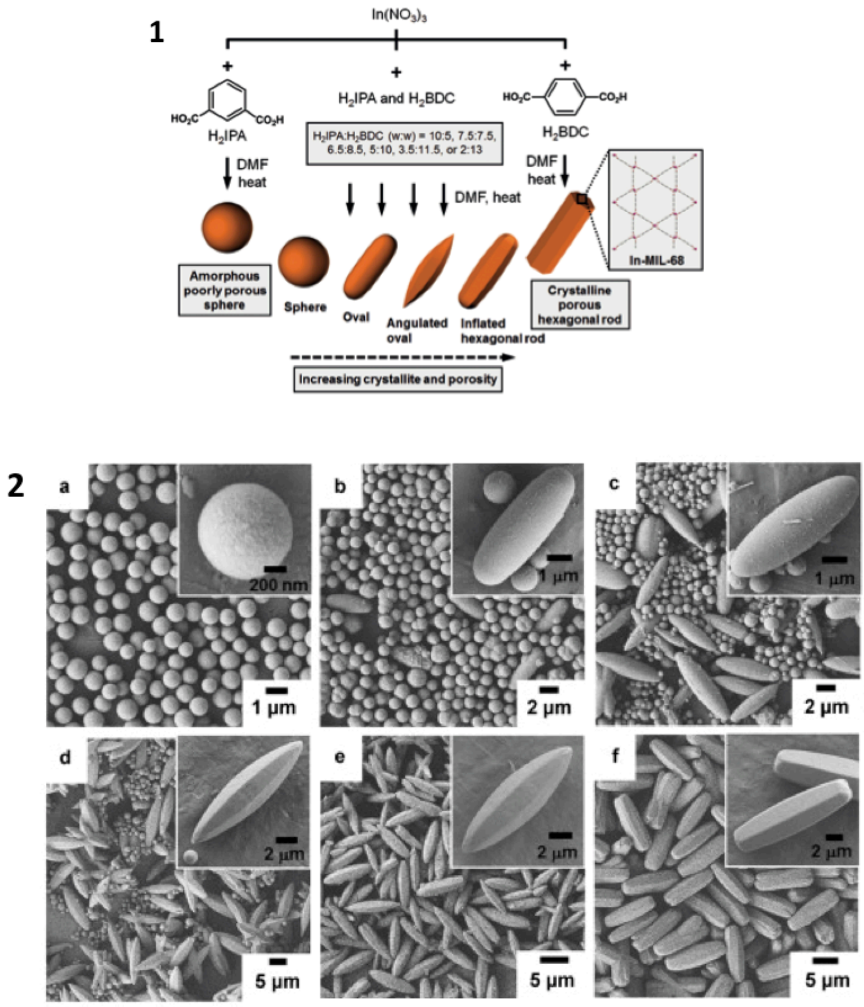


**Figure 5.2 (1) Schematic illustration of the morphological evolution of MOF particles constructed from the solvothermal reactions of $In(NO_3)_3$ in the presence of $H_2IPA$ and/or $H_2BDC$, (2) corresponding SEM images showing the morphological evolution of MOF particles constructed at different $H_2IPA$:$H_2BDC$ (w:w) ratio, respectively (a) 10:5, (b) 7.5 :7.5, (c) 6.5 :8.5, (d) 5 :10, (e) 3.5 :11.5, and (f ) 2 :13. Figure adapted with permission from ref.[208]**

The solvothermal reactions were carried out using $In(NO_3)_3$, isophthalic acid ($H_2IPA$) and/or 1,4-benzenedicarboxylic acid ($H_2BDC$) in different ratios (Figure 5.2 1). Interesting morphological and structural evolutions of the resulting MOFs according to the degree of contribution of the two organic linkers, determined from the starting conditions, occurred during the MOF particle construction (Figure 5.2 2). In particular highly crystalline porous MOF particles were generated when the contribution of BDC linkers within the framework was superior and amorphous non-porous MOF particles resulted when the contribution of the IPA linkers was dominant. Therefore the relative amounts of the two organic linkers incorporated within MOF particles determined the resulting morphological features, the porosity and the structure of the MOF particles. Moreover the work of Feng *at al.* was explanatory for mixed ligand systems of the ZIF class, where the topology of the ZIFs synthesized was determined by the ratio of the two imidazolates incorporated in the framework, which again was strongly dependent on the synthetic conditions employed (Figure 5.3). For example, TIF-2 ($[Zn(Im)_{1.1}(MBim)_{0.9}]\cdot$~2.5($C_6H_6$), MBim= 5-

methylbenzimidazole) was synthesized in (±)-2-amino-1-butanol and benzene using a molar ratio $Zn^{2+}$:MBIm:Im:(±)-2-amino-1-butanol:benzene=1:1:1.2:80:75 from a solvothermal reaction for 5 days at at 150 °C, TIF-3 ($[Zn(Im)_x(MBim)_y]\cdot(G_z)$, (x+y=2)) was synthesized in (±)-2-amino-1-butanol and benzene using a molar ratio $Zn^{2+}$:MBIm:Im:(±)-2-amino-1-butanol:benzene=1:1:1.1:80:8.5 from a solvothermal reaction for 6 days at at 150 °C and TIF-4 ($[Zn(Im)_{1.5}(MBim)_{0.5}]\cdot 0.5(C_6H_6)$ was synthesized in 3-amino-1-propanol and benzene using a molar ratio $Zn^{2+}$:MBIm:Im:3-amino-1-propanol:benzene=1:0.4:1.6:100:72 from a solvothermal reaction for 5 days at at 150 °C.[209]

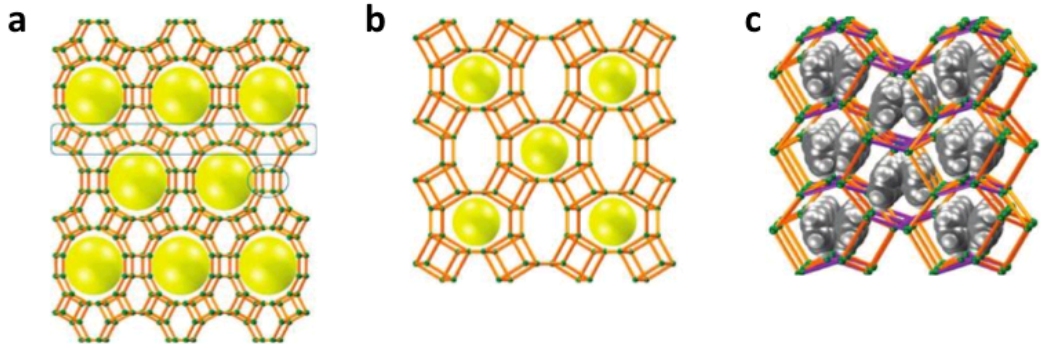


**Figure 5.3 Topology of (a) TIF-2, (b) TIF-3 and (c) TIF-4 viewed along [001] direction. Figure adapted with permission from ref. [209]**

So far a mixed ligand ZIF system in which the framework evolved with time from a metastable topology to a more stable topology depending on the ratio of the ligands incorporated in the framework within the same reaction has not been reported. The topological evolution of the system would clarify the influence of the ligands in the stabilization of the topologies in the energy landscape and more widely speaking a system able to change its topology in response to an external stimulus, such as an organic molecule (linker), might be useful for applications, such as sensing.

In this chapter the system zinc: methylimidazole: imidazole and the two related ZIFs formed, with topology **sod** and **zni,** were investigated. The **sod** and **zni** topologies had the building blocks but they differed in terms of the ratio between the two organic linkers included. The mixed-linker **sod** topology was previously reported in the literature as SALEM-2,[210] it is analogous to ZIF-8 ($Zn(MeIm)_2$), where some of the 2-methylimidazole linkers were partially substituted by the imidazole ones, which led to a material with large voids, unobstructed apertures and appreciable surface area and it has been synthesized by solvent-assisted linker exchange[55] via solvothermal reaction for 7 days in butanol at 100° C (Figure 5.4).

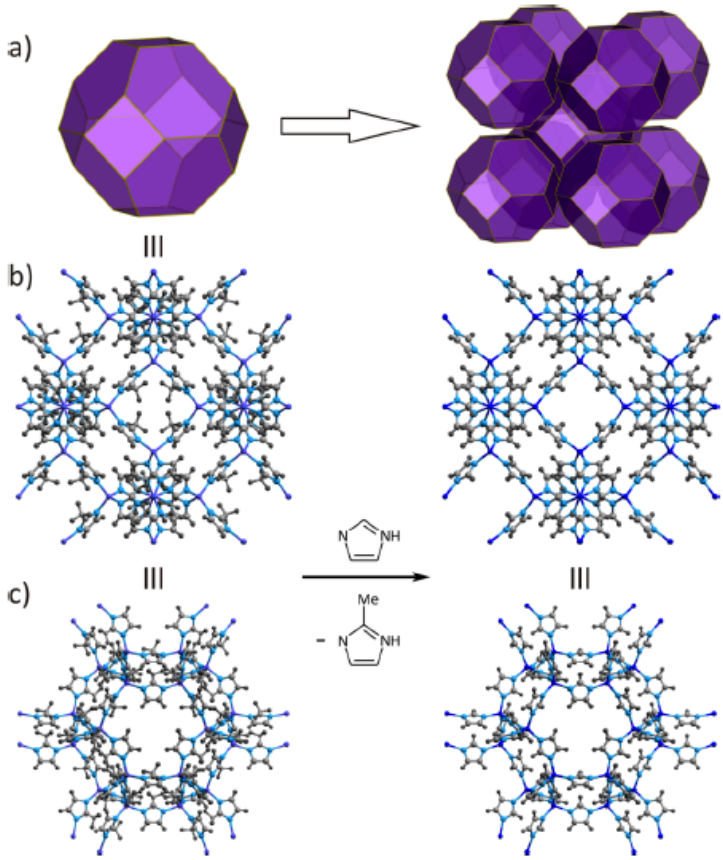


**Figure 5.4 (a) 3D Representation of the Tiling of the SOD Topology; (b) View along the Crystallographic a Axis; and (c) View along [111] Direction of ZIF-8 (Left) and SALEM- 2 (Right). Reprinted with permission from ref.[210]**

The **zni** topology, also named ZIF-61, is the most dense and thermodynamically stable of the ZIF family,[211-212] where $M^{2+}$ cations (M= Zn or Co) are bridged by imidazolate anions to afford a neutral uninodal 4-connected net possessing five-ring structures, as shown in Figure 5.5.

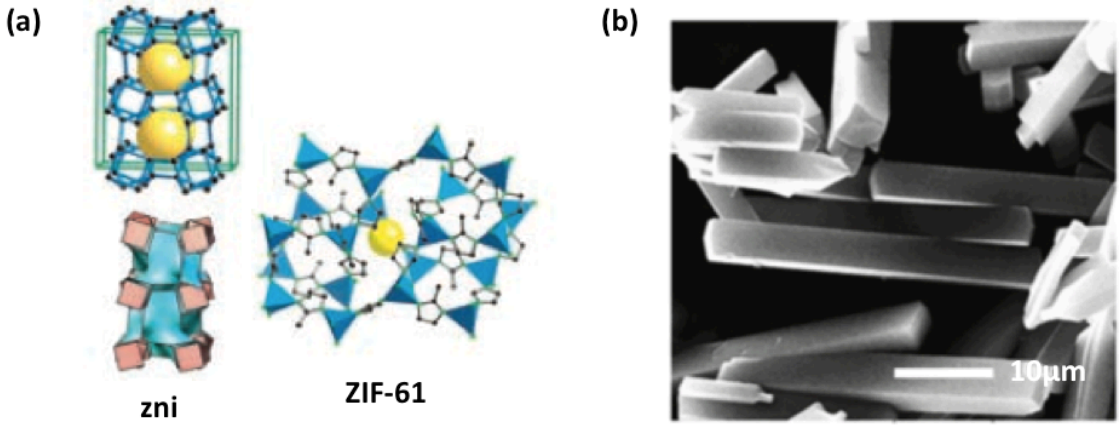


**Figure 5.5 (a) Schematic representation of ZIF-61 structure and topology: up left as stick diagrams of the nets, down left the same structures decomposed into tiles (generalized polyhedral or cages that combine to completely fill space) and the largest cage in the real structure on the right, the yellow balls are placed in the structure for clarity and to indicate space in the cage. (b) SEM images of ZIF-61 crystals. Figure adapted with permission from ref.[213]**

The **zni** phase is composed by three isomorphous compounds, namely Zn(Im)(MeIm), $Zn(Im)_2$ and $Co(Im)_2$[71, 74, 214] and it has been synthesized solvothermally,[72] by microwave,[213] solvent free reactions via thermal-mediated transformation,[204] heating a structural isomers of ZIF-4[215-216] and ionothermally.[217] It is characterized by lozenge-shaped particles (Figure 5.5 b) but, due to the dense topology, its surface area is very low compared to other ZIFs (5 $m^2/g$). For this reason it has not been intensively studied even though it shows application in catalysis[213] and clathrate hydrate formation.[218]

Nevertheless the mixed ligands system $Zn(MeIm)_x(Im)_{(1-x)}$ with **sod** topology was preferred because of the intrinsic properties of the material, it was experimentally found that often the **zni** was synthesized instead. Therefore, in order to have a complete view of the system at first the synthesis of the **zni** phase was investigated and optimized carrying out the reaction in aqueous media at room temperature. As previously reported (4.2.1.2) SPAN-80 promotes the topological, morphological and chemical evolution of the mixed ligands system $Zn(MeIm)_x(Im)_{(1-x)}$, from **sod** ($Zn(MeIm)_{1.1}(Im)_{0.9}$) to **zni** topology ($Zn(MeIm)_{0.7}(Im)_{1.3}$), which was further investigated in this chapter. Finally, in order to further study the thermodynamics of the system, conversion experiments from premade ZIF-8 (**sod**) and **zni** phase and about the variation of the zinc: methylimidazole: imidazole ratio were investigated.

## 5.2 Results and discussion

### 5.2.1 Synthesis of zni phase

The **zni** topology was synthesized at room temperature by mixing a solution of $Zn(NO_3)_2$ (29 mg in 0.5 mL $H_2O$) with a solution of methyl imidazole (570 mg in 2 mL $H_2O$) and a solution of imidazole (480 mg in 2 mL $H_2O$) giving a total molar ratio of $Zn^{2+}$:MeIm:Im=1:70:70. The reaction was studied at different times, respectively 0.5, 2 and 24 hours, leading to an increment in the yield with increasing time to 24 hours from 54 to 68%. The experiments were characterized by PXRD, NMR and TGA (Figure 5.6, Figure 5.7 and Figure 5.8).

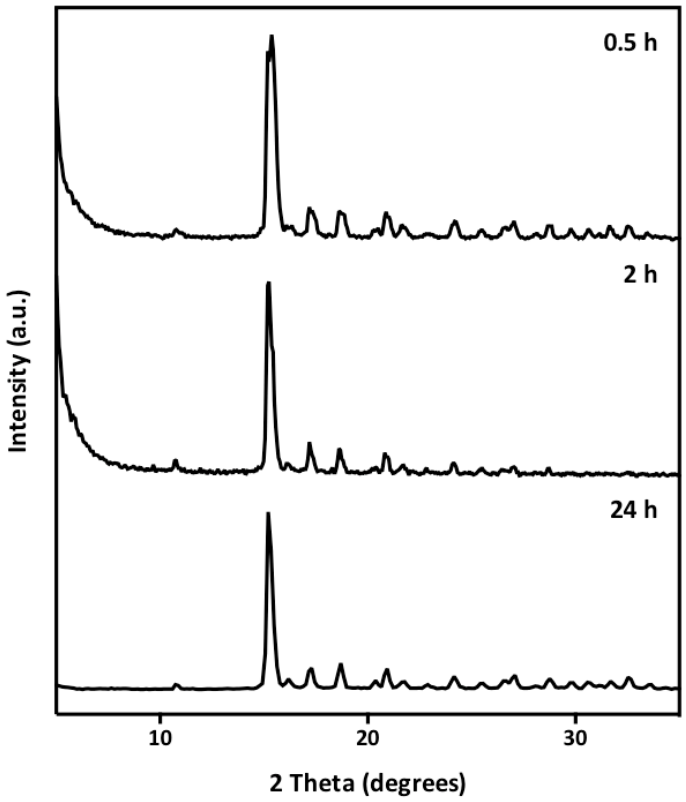


**Figure 5.6 PXRD patterns of ZIF-61 zni phase obtained at room temperature in aqueous media at time 0.5, 2 and 24 hours.**

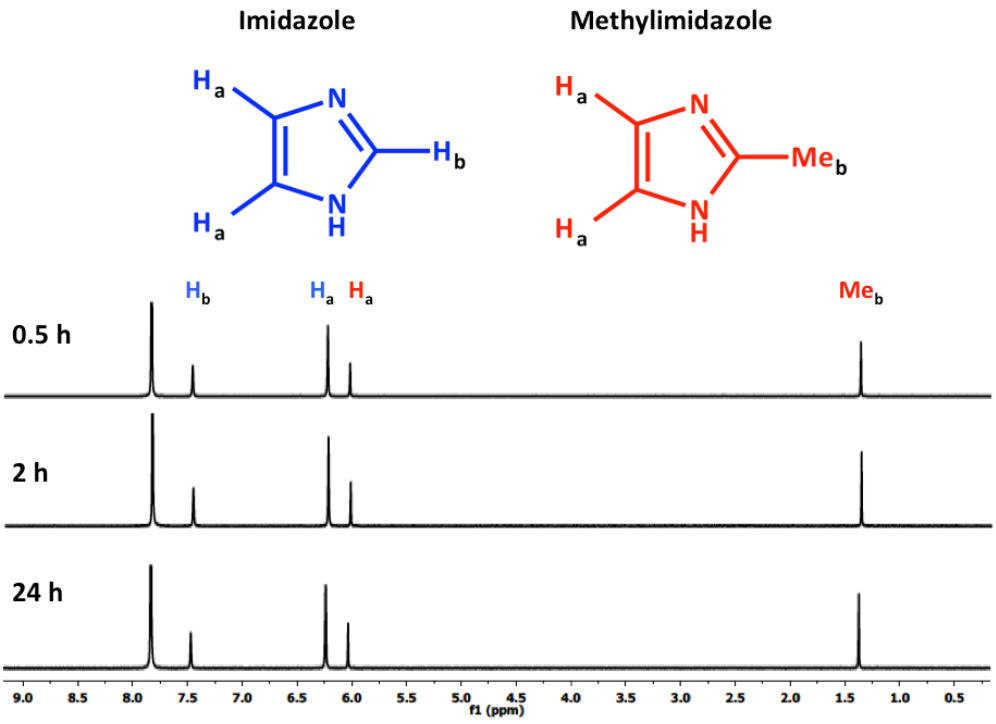


**Figure 5.7 $^{1}$H-NMR spectra of ZIF-61 zni phase obtained at room temperature in aqueous media at time 0.5, 2 and 24 hours.**

| Time [hours] | $CH_a$ *Im* | $CH_b$ *Im* | $CH_a$ *MeIm* | $Me_b$ *MeIm* | Ratio MeIm:Im |
|---|---|---|---|---|---|
| 0.5 | 2.3 | 1.2 | 1 | 1.5 | 30:70 |
| 2 | 2.5 | 1.3 | 1 | 1.5 | 30:70 |
| 24 | 2.3 | 1.2 | 1 | 1.5 | 30:70 |

**Table 5.1 Integral related to $^1$H-NMR spectra of ZIF-61 zni phase obtained at room temperature in aqueous media at time 0.5, 2 and 24 hours.**

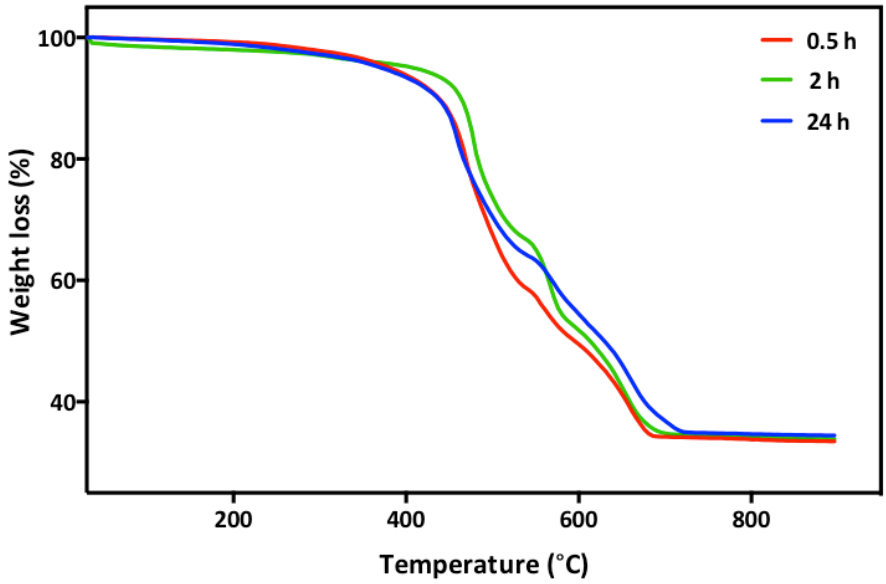


**Figure 5.8 Thermogravimetric analysis (TGA) of ZIF-61 zni phase obtained at room temperature in aqueous media at time 0.5, 2 and 24 hours.**

The PXRD patterns Figure 5.6 showed that the **zni** phase was obtained as a pure phase with the characteristic most intense peak at 2Θ = 15°, which corresponded to the 004 reflection. The chemical composition of the materials with respect to linker ratio was verified by $^1$H-NMR spectroscopy following digestion of the framework in 35% DCl solution (Figure 5.7). The chemical shift at δ=1.4 and 6.1 ppm were related to methylimidazole, respectively the three hydrogens of $Me_b$ and the two hydrogens $H_a$, while the chemical shift at δ=6.3 and 7.5 ppm were related to the imidazole, respectively the two hydrogens $H_a$ and $H_b$. The relative ratio between the two linkers was calculated by comparing the chemical shifts at δ=6.1, related to the two hydrogen $H_a$ of methylimidazole and the corresponding chemical shift at δ=6.3 related to the 2 hydrogen $H_a$ of imidazole. Table 5.1 showed the $^1$H-NMR peak integrals and the ratio between methylimidazole and imidazole included in the framework in each experiment, which was stable at a ratio of MeIm:Im=30:70. In the literature the **zni** phase was previously observed as three isomorphous

compounds, namely Zn(Im)(MeIm), $Zn(Im)_2$ and $Co(Im)_2$,[74, 214, 218] however this study is just focused on the mixed ligand isomorph, which was characterized by Banerjee *et al.* with a relative linker ratio of 50:50.[71] The reaction was carried out in a mixed DMF/DEF solvent system by mixing a solution of Im with one of MeIm and then with a $Zn(NO_3)_2 \cdot 4H_2O$ solution in ratio $Zn^{2+}$:MeIm:Im= 1:2:2 and allowed to react solvothermally at 100 °C for 96 hours. The solvothermal synthesis and the higher ratio of $Zn^{2+}$:MeIm:Im used by Banerjee might permit increased incorporation of the methylimidazole linker into the framework. The thermogravimetric analysis (Figure 5.8) indicated the samples decompose in three shallow steps in the range 300-700 °C, which was related to the presence of Im and MeIm in the framework, and the organic percentage reported was consistent with the mass loss expected for the **zni** phase (respectively 65 and 64%) and with proportion of organic linkers determined by $^1$H-NMR (64%). Finally the **zni** phase was essentially non-porous in line with the reported literature for the related Zn(Im)(MeIm) isomorph ($5m^2/g$).[213]

SEM images of the three experiments at 0.5, 2 and 24 hrs were shown below and compared with **zni** particles of Zn(Im)(MeIm) obtained in the literature (Figure 5.9).[213]

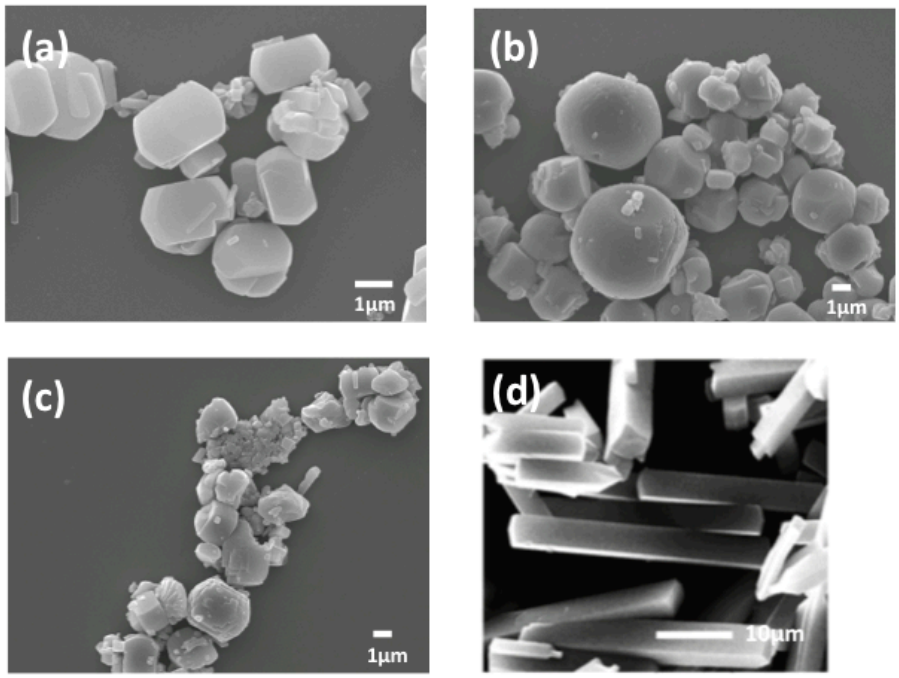


**Figure 5.9 Time evolution of the zni particles morphology (a) 0.5 hours, (b) 2 hours and (c) 24 hours reaction, (d) lozenge-like particles obtained by microwave ionothermal reaction. Figure (d) adapted with permission from ref.[213]**

The morphology of the **zni** phase slightly changed with reaction time from lozenge-like particles at time 0.5 hours to more rounded ones at time 2 and 24 hours, while the microwave ionothermal reaction reported in the literature reported lozenge-like particles even though the size was an order of magnitude greater.[213]

### 5.2.2 sod→zni conversion

#### 5.2.2.1 SPAN-80 as surfactant

Recently a soft-templating approach was used in order to gain control over the macroscopic structure or physical form such as crystal size, morphology and crystal superstructure of MOF materials.[99] Due to the morphological evolution of the **zni** phase in the absence of any surfactant, it seemed a good candidate for morphological studies, therefore the influence of the surfactant SPAN-80 was investigated. Furthermore in the previous chapter it was shown that the use of SPAN-80 in the $Zn^{2+}$:Im:MeIm system (4.2.1.2) leads to the coexistence of two phases, namely **zni** and **sod**, which was further investigated here.

The reaction was carried out in a large excess of the linkers ($Zn^{2+}$:MeIm:Im=1:70:70) following the reported synthetic procedure for ZIF-8 formation in water[182] and in the presence of the surfactant SPAN-80 (90 mg, 2.1 mmol, ratio $Zn^{2+}$:SPAN-80=1:2.3). In a typical synthesis SPAN-80 surfactant was stirred for 5 hours in 5 mL of $H_2O$ at room temperature. Then solutions of $Zn(NO_3)_2.6H_2O$ (29 mg in 0.5 mL $H_2O$), 2-methylimidazole (560 mg in 2 mL $H_2O$) and imidazole (490 mg in 2 mL $H_2O$) were added consequently to the SPAN-80 solution and stirred for different times (from 0.25 to 24 hours) at room temperature.

PXRD was used in order to monitor the topological changes of the material during the reaction (Figure 5.10).

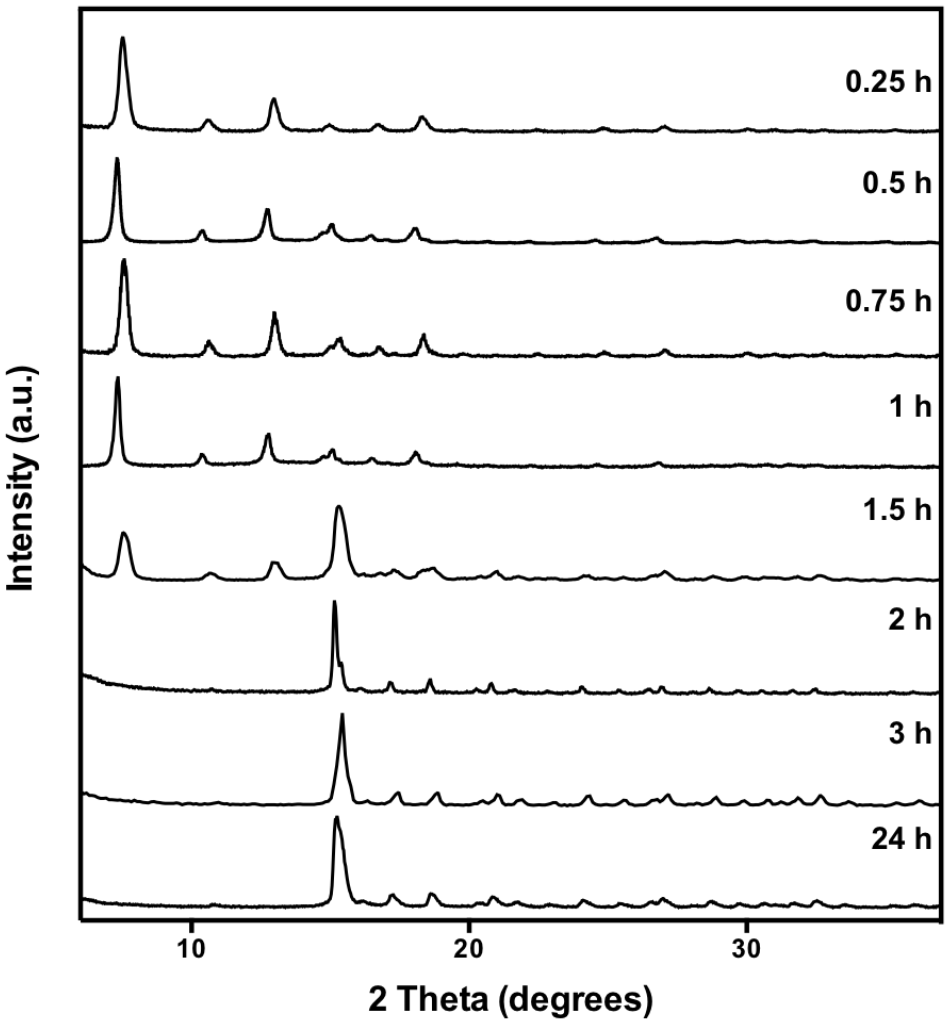


**Figure 5.10 PXRD patterns of the experiments performed in presence of SPAN-80 from time 0.25 to 24 hours, which shows the topological conversion from the sod to the zni net.**

In particular the sample at 0.25 hours showed the patterns corresponding to only the **sod** topology, which was in contrast to those mixed-linker ZIF syntheses conducted in the absence of SPAN-80 where the **zni** phase was formed from the outset. Samples isolated following 0.5, 0.75, 1 and 1.5 hours of reaction also showed the **sod** topology but the presence of a Bragg reflection at 2Θ = 15° characteristic of the **zni** topology was observed, which clearly increased in intensity with reaction time. The **zni** phase was the only one present for all samples isolated after reaction times > 2 hours, suggesting that the SPAN-80 may have a role in initially forming a metastable **sod** topology which fully transformed to **zni** within a few hours during the reaction. SEM images of all the samples were presented in Figure 5.11.

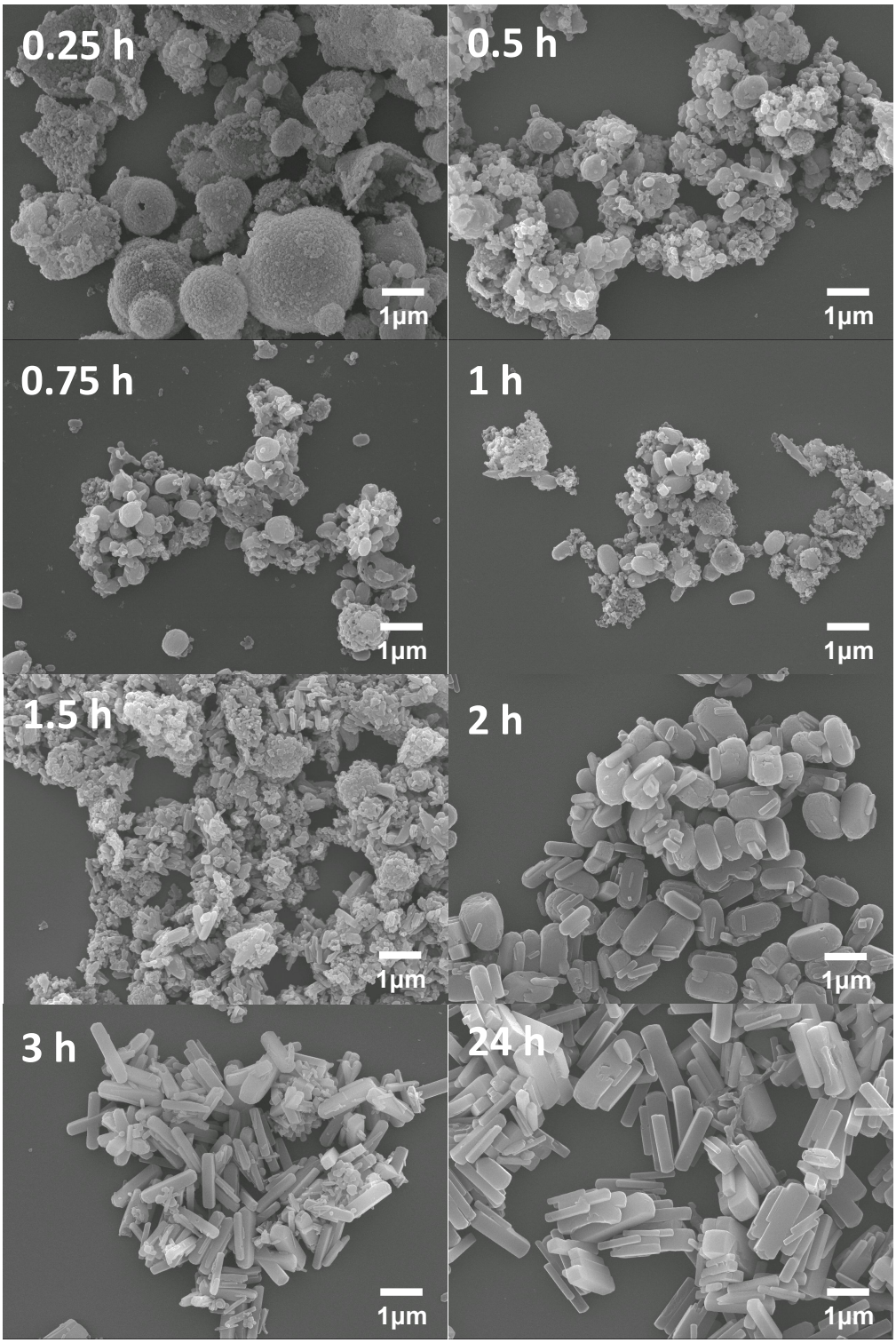


**Figure 5.11 SEM images showing the morphological evolution of the particles from nano-crystals and colloidosomes related to SALEM-2 to tetragonal rectangular shape particles related to the zni phase.**

They showed that the topological change was also accompanied by a morphological change of the particles. The **sod** topology was present as nano-crystals (about 100 nm diameter size), comparable with the particles obtained in the reference synthesis,[182] and as micron sized hollow spherical superstructures composed of aggregated nanocrystals related to the colloidosomes,[176] which were formed through the template effect of a surfactant mesophase as outlined in Chapter

4.[213] SEM images of the samples at 0.25 hours showed colloidosomes and nano-crystals of **sod** topology, whereas those at 0.5 to 1.5 hours showed the presence of an increasing number of particles corresponding to the **zni** phase, which also appeared to increase in size with reaction time. SEM images after 2 hours or more of reaction time all revealed particles with a lozenge-type morphology, where the thickness of the crystals decreased with the reaction time, consistent with the presence of only the **zni** topology as confirmed by PXRD (Figure 5.10).

The chemical composition of all the samples was verified by $^{1}$H-NMR spectroscopy, following digestion in 35% DCl solution (Figure 5.12), and the relative ratio between the two linkers was calculated as in zni (5.2.1). Table 5.2 showed the $^{1}$H-NMR peak integrals, the MeIm:Im ratio included in the framework after the defined reaction time and the topology present in each experiment determined from PXRD.

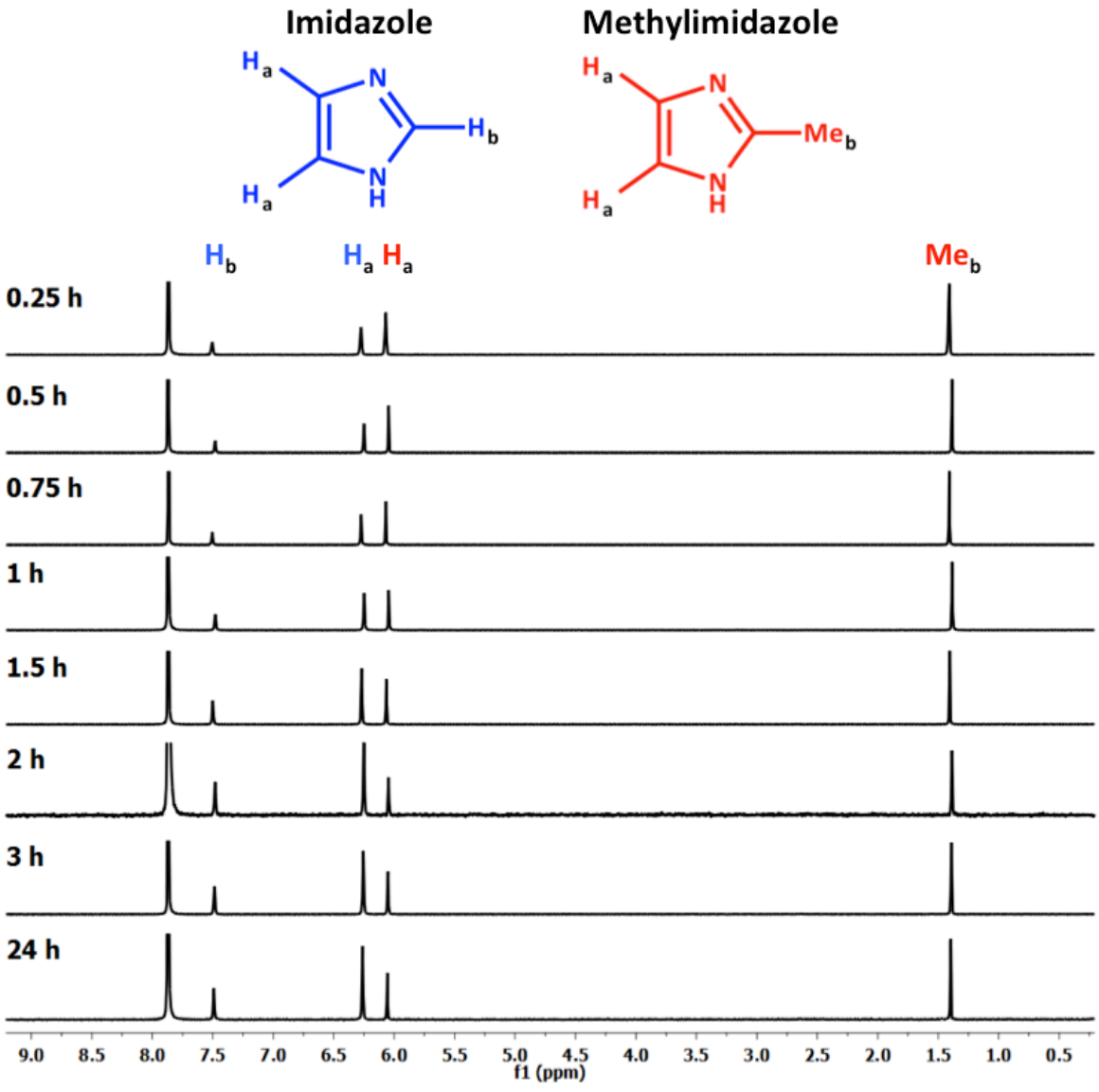


**Figure 5.12 $^{1}$H-NMR spectra of the different time experiments with chemical shift assigned.**

| Time [hours] | $CH_a$ *Im* | $CH_b$ *Im* | $CH_a$ *MeIm* | $Me_b$ *MeIm* | Ratio MeIm:Im | Topology |
|---|---|---|---|---|---|---|
| 0.25 | 0.8 | 0.4 | 1 | 1.6 | 56:44 | sod |
| 0.5 | 0.9 | 0.5 | 1 | 1.5 | 52:48 | sod/zni |
| 0.75 | 1 | 0.5 | 1 | 1.5 | 50:50 | sod/zni |
| 1 | 1.2 | 0.6 | 1 | 1.5 | 45:55 | sod/zni |
| 1.5 | 1.9 | 0.9 | 1 | 1.6 | 35:65 | sod/zni |
| 2 | 2.1 | 1.1 | 1 | 1.7 | 35:65 | zni |
| 3 | 1.9 | 0.9 | 1 | 1.5 | 35:65 | zni |
| 24 | 2.1 | 1.1 | 1 | 1.5 | 35:65 | zni |
| zni phase | 2.3 | 1.2 | 1 | 1.5 | 30:70 | zni |

**Table 5.2 $^1$H-NMR peak integrals, ratio between 2-methylimidazole and imidazole included in the framework and the related topologies (from PXRD data) formed at the different time experiments vs. the control zni phase.**

It is clear that increasing the reaction time the content of imidazole in the framework increased from 44% (0.25 hours) to 65% (24 hours). The sample at 0.25 hours was the only pure **sod** topology and it showed 44% of Im incorporation. This value was significantly lower than previously reported for mixed ligand ZIFs with the **sod** topology $Zn(Im)_{(1-x)}(MeIm)_x$ (SALEM-2) where ~ 85% ligand exchange was achieved, but employing more extreme conditions (7 days in butanol at 100° C),[210] however the authors pointed out the importance of the solvent in the SALE synthesis, where solvents such as N,N-dimethylformamide and N,N-dimethylacetamide, led to the degradation of the **sod** framework. Furthermore they demonstrated that SALEM-2 remained crystalline after 24 hours in boiling water, similarly to ZIF-8 and the **zni** phase.[71] The samples from 0.5 to 1.5 hours showed the presence of both **sod** and **zni** phases, and although the general trend was an increase in the Im percentage it was not possible to assign the relative contribution of Im in the framework to each topology. The samples from 2 to 24 hours showed a pure **zni** phase with Im inclusion of 65%, which was consistent with the control **zni** phase in which the percentage of Im inclusion was 70% at all the time experiments (Table 5.2 and Figure 5.12). However ZIF -8 has been demonstrated as capable of including small molecules in its pore,[86] therefore it might be that a portion of MeIm is included as a guest rather than into the framework of ZIF-8.

The IR spectra of the samples exhibited similar characteristic peaks, as shown in Figure 5.13.

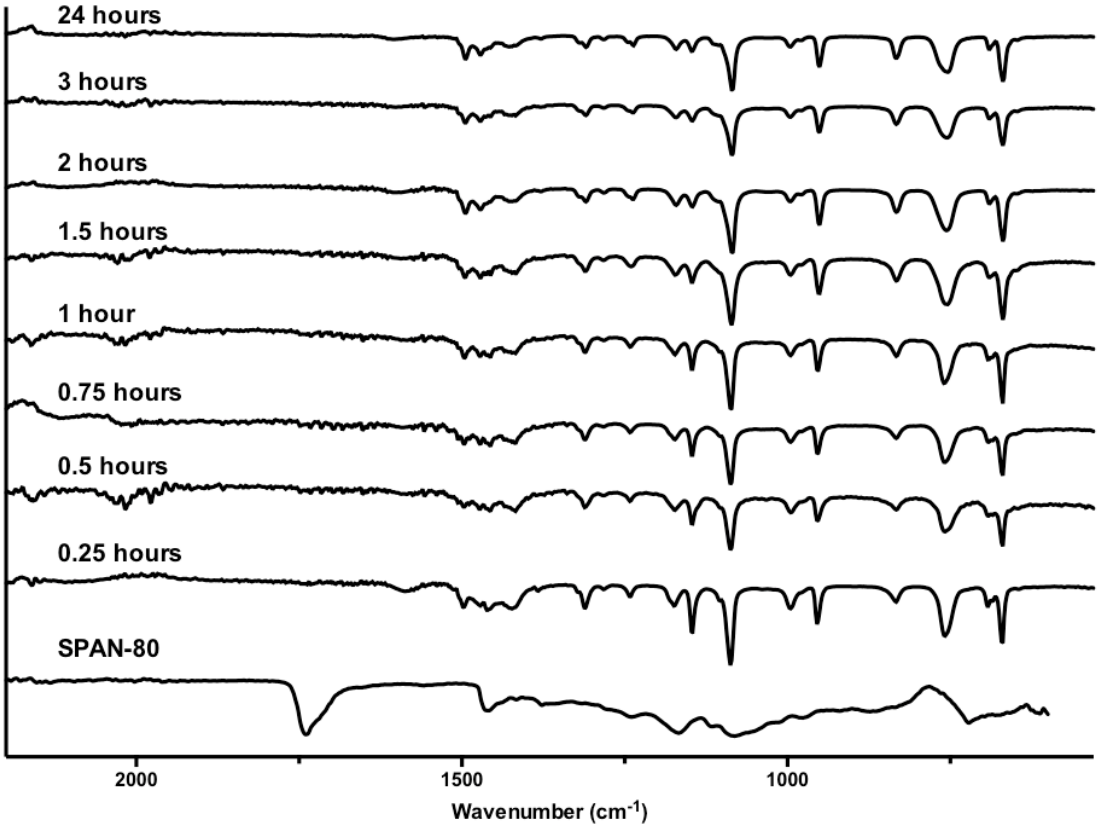


**Figure 5.13 IR spectra of the different time reaction experiments and SPAN-80 surfactant.**

The IR spectra showed typical stretches of the imidazolate-based frameworks and even though it was difficult to distinguish between the two linkers due to their similarity, the weak peak at about 1600 $cm^{-1}$ could be assigned as the C=N stretching mode, while the intense and convoluted bands at 1350–1500 $cm^{-1}$ were associated with the entire ring stretching of both the ligands. The bands in the spectral region of 900–1350 $cm^{-1}$ were for the in-plane bending of the (methyl)imidazole rings while those below 800 $cm^{-1}$ were assigned as out-of-plane bending.[193] Furthermore the IR spectra were compared with the IR spectrum of SPAN-80, which showed a strong broad band at 1750 $cm^{-1}$ which was clearly absent from the mixed-imidazole ZIFs across all reaction times investigated, indicating that the surfactant was removed from the samples following washing.

Thermogravimetric analysis (TGA) indicated the samples were thermally stable until ~ 300 °C, then they decomposed in different steps in the range ~ 300-700 °C, which should be related to the presence of Im and MeIm in the framework (Figure 5.14).

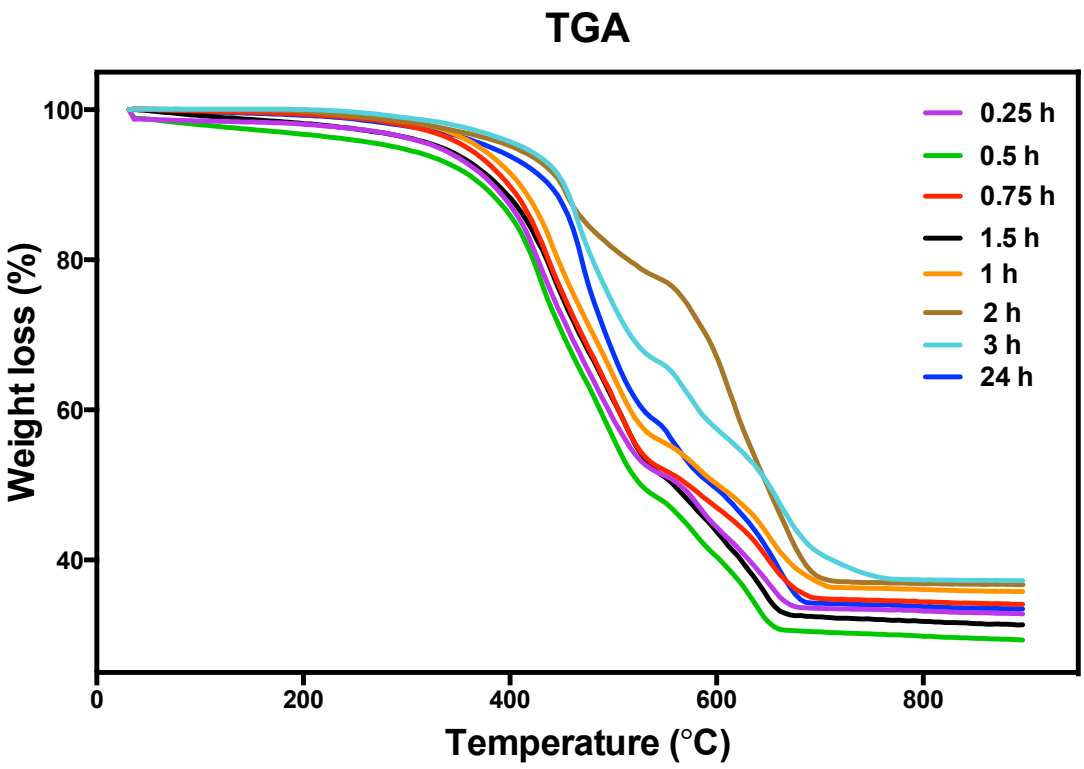


**Figure 5.14 Thermogravimetric analysis of the different time reaction experiments.**

The organic percentage of the experiments performed at time 0.25, 1.5 and 24 hours recorded was 64.7, 64 and 63.5% which was consistent with the proportion of organic linkers incorporated in the framework determined by $^{1}$H-NMR (65% for sample at 0.25 hours and 64% for the samples at time 1.5 and 24 hours). Finally the residual amounts of ZnO were in the range 30-40 wt% consistent with the expected value for the inorganic phase. The porosity of the all the samples was investigated by nitrogen sorption analysis (Figure 5.15).

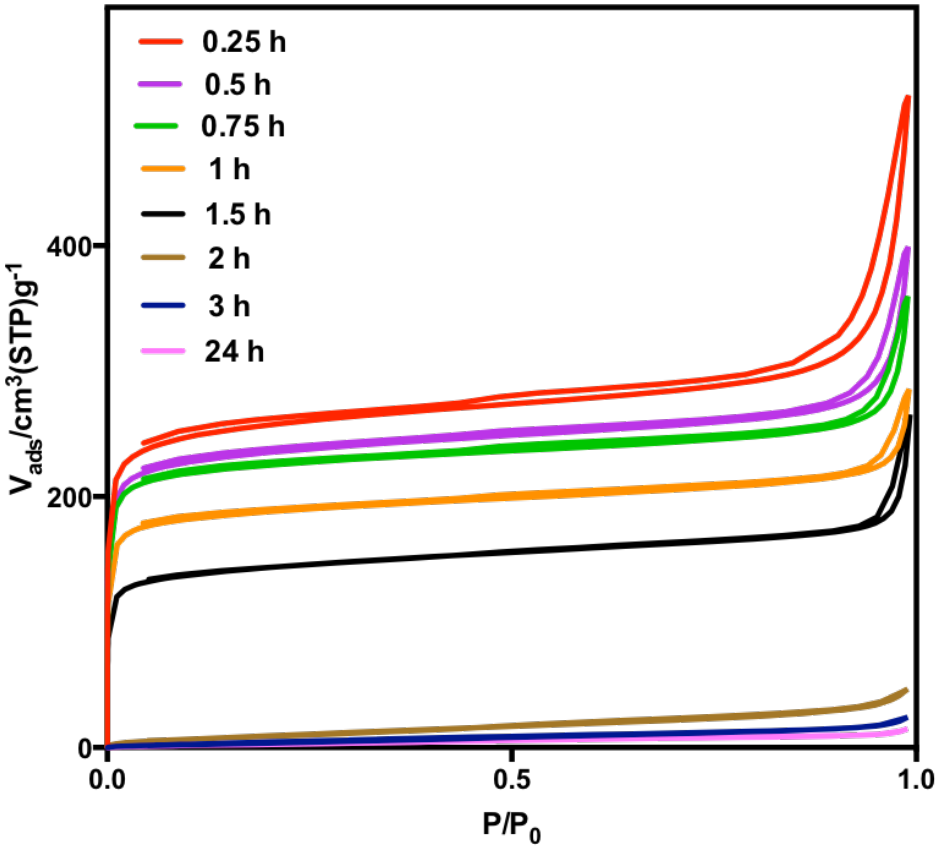


**Figure 5.15 Nitrogen sorption isotherms of mixed-imidazole ZIFs measured at 77 K on samples obtained at different reaction times.**

The trend showed a decrement of porosity with increasing reaction time, which correlates with the increasing amounts of the denser **zni** topology. The sample recovered after 0.25 h of reaction time showed the highest porosity with an apparent BET surface area of 990 ± 0.4 $m^2/g$, which was directly comparable to the BET surface area of pure ZIF-8 phases obtained under the same reaction conditions (952 ± 0.3 $m^2/g$, Figure 5.16 and Figure 5.17) and with the related literature.[156, 210]

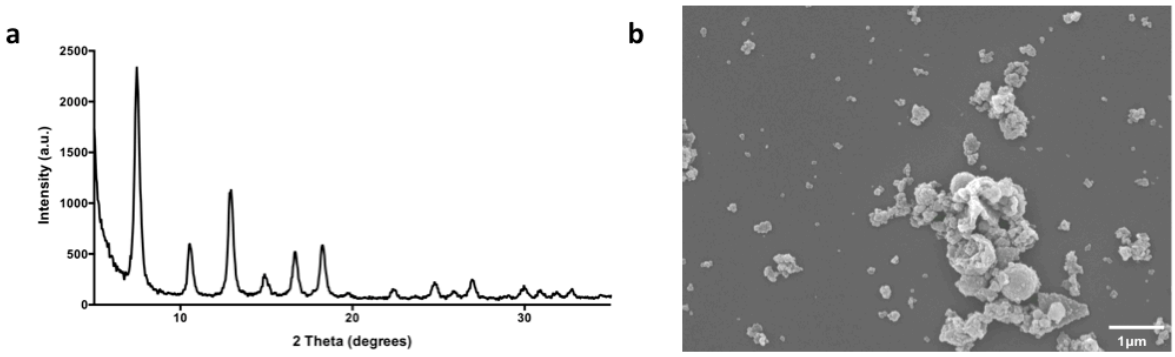


**Figure 5.16 ZIF-8 synthesized with SPAN-80 (a) PXRD pattern and (b) SEM image.**

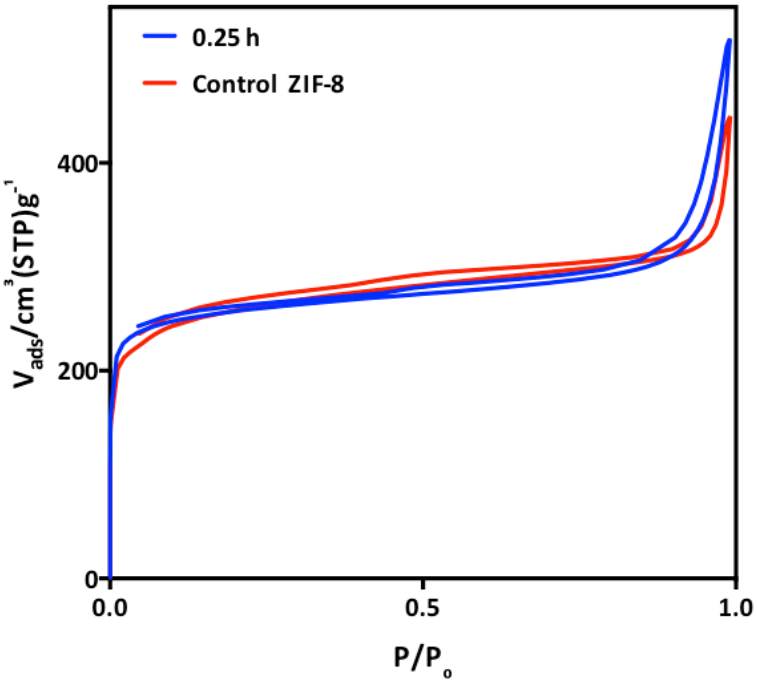


**Figure 5.17 Nitrogen sorption isotherms of mixed-imidazole ZIF experiment performed at 0.25 hours and control ZIF-8 measured at 77 K.**

BET surface areas for the samples prepared after 0.5 and 0.75 hours were slightly lower at 915 ± 0.6 and 882 ± 0.3 $m^2/g$, respectively, arising from the presence of a small amount of the non-porous **zni** topology. However, the samples after 1 and 1.5 hours of reaction showed a dramatic decrease in BET surface area to 735 ± 0.5 and 549 ± 0.4 $m^2/g$, respectively. In all cases the adsorption isotherms showed a marked increase in uptake at relative pressures > 0.90, consistent with aggregates of small ZIF particles.[137] As the conversion proceeded further even lower values were recorded (BET surface area of 41 ± 0.2 , 24 ± 0.2 and 23 ± 0.05 $m^2/g$ for 2, 3 and 24 hours samples) consistent with a pure **zni** phase.

### 5.2.2.2 Reaction investigated with other surfactants

In order to gain further insight into the role of SPAN-80, the time evolution of the topology was also investigated in the presence of cetyltrimethylammonium bromide (CTAB), sodium dodecyl sulphate (SDS), sorbitan monolaurate (SPAN-20), sorbitan trioleate (SPAN-85) and polyethylene glycol sorbitan trioleate (TWEEN-85) (Figure 5.18 and outlined in Appendix A). CTAB and SDS were respectively cationic and anionic surfactants, while SPAN-20, SPAN-80, SPAN-85 and TWEEN-85 were all non-ionic and derived from sorbitol. SPAN-20 and SPAN-80 had a single chain, of respectively 11 and 17 carbon atoms, while SPAN-85 and TWEEN-85 had three chains of 17 carbons atoms and differ from each other as TWEEN surfactants were ethoxylated analogues of SPAN.

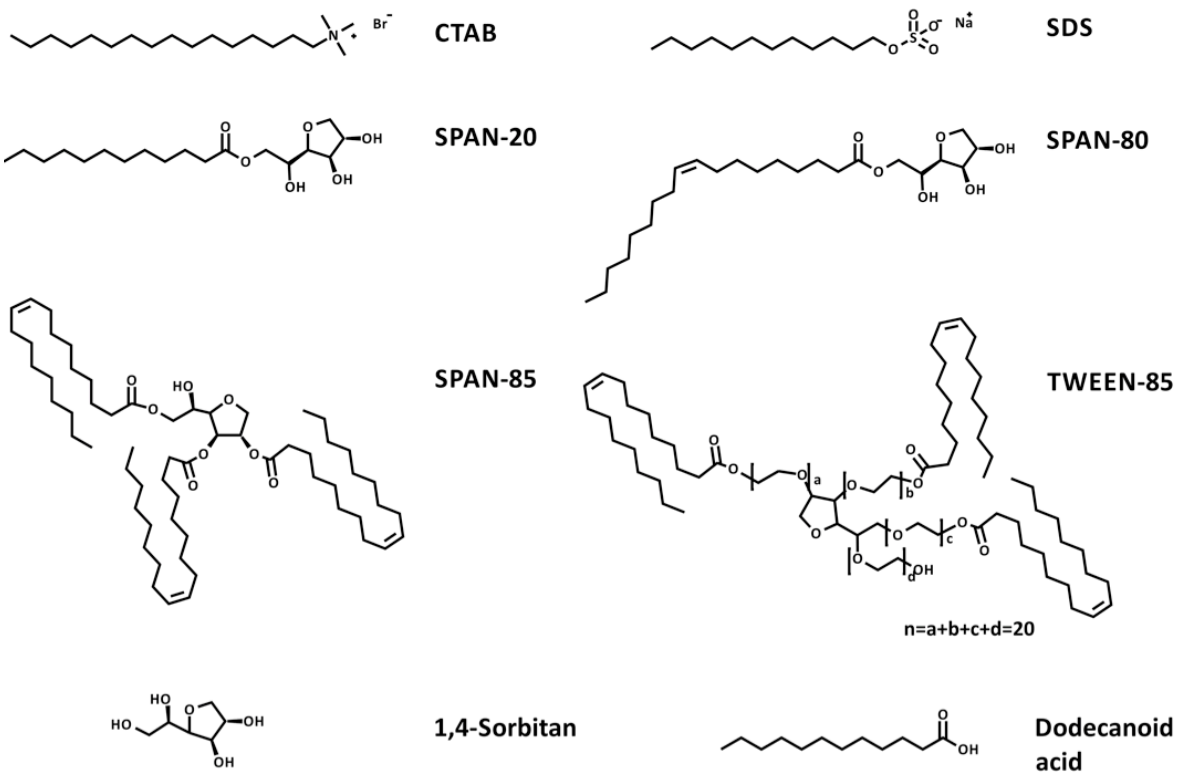


**Figure 5.18 Illustration of the surfactants used in the zni morphological and topological experiments.**

All surfactants replaced SPAN-80 directly in the aqueous synthesis and were kept in the same molar ratio and the reactions analysed at times of 0.5, 2 and 24 hours. CTAB appeared to suppress ZIF formation under these conditions yielding only a clear and transparent solution. As discussed in Chapter 4 and supported by Wang *et al.* at room temperature stronger interactions between the cationic surfactant and the deprotonated MeIm might form, preventing the network formation,[156] or the metal ion might react with $Br^-$ forming $ZnBr_2$. When employing anionic SDS however, the reaction led directly to the formation of the **zni** topology even after 0.5 hours as shown from the PXRD pattern in Figure 5.19.

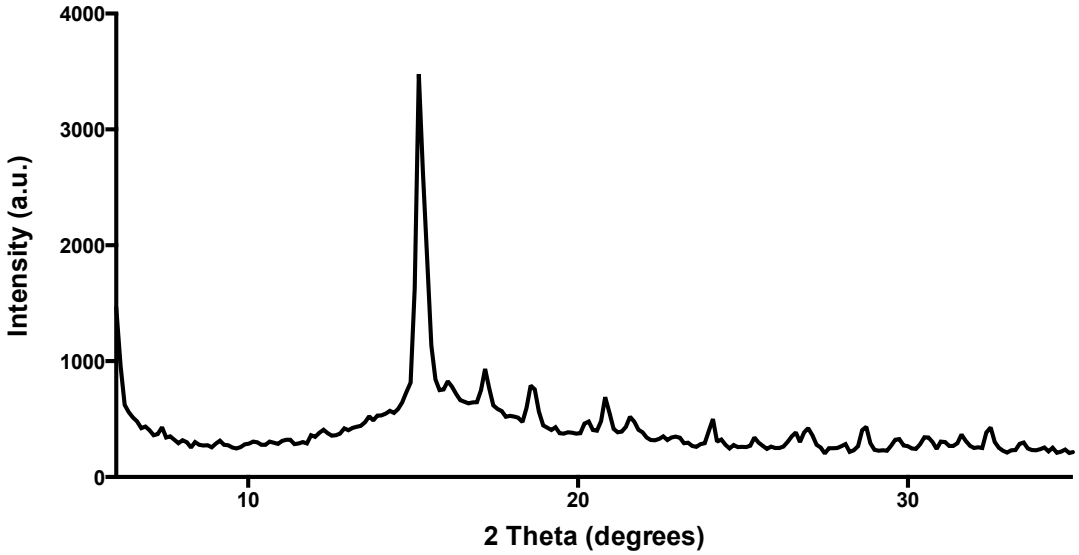


**Figure 5.19 PXRD pattern of the experiment performed with the surfactant SDS.**

SPAN-20, SPAN-85 and TWEEN-85 (Figure 5.20) all had a similar effect to SPAN-80 on the reaction differing just in terms of the **sod**-to-**zni** conversion time, which appeared to depend on the solubility of the surfactant.

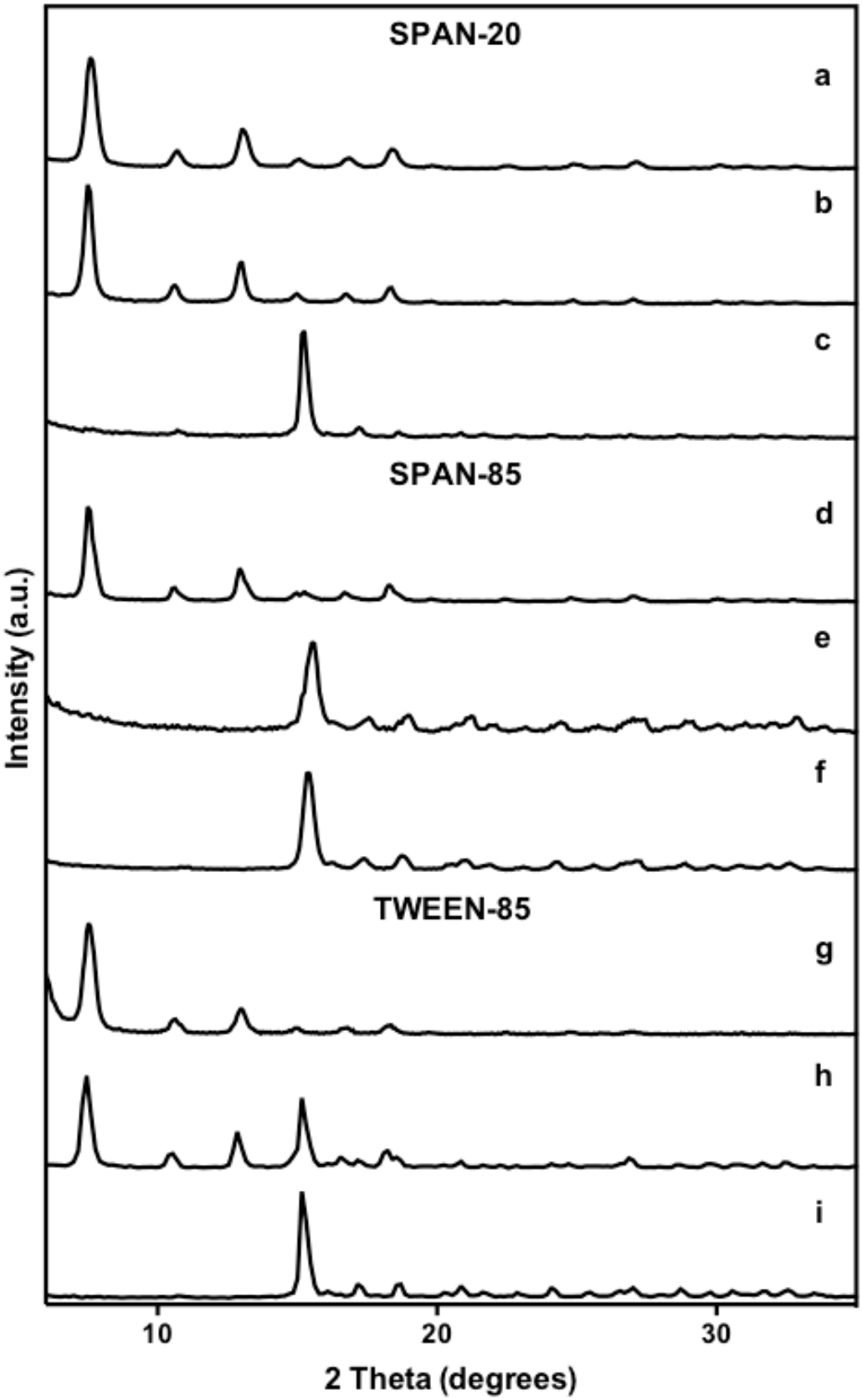


**Figure 5.20 PXRD patterns of the experiments performed with the surfactant SPAN-20 at time (a) 0.25 hours, (b) 2 hours and (c) 24 hours, with the surfactant SPAN-85 at time (d) 0.25 hours, (e) 2 hours and (f) 24 hours and with the surfactant TWEEN-85 at time (g) 0.25 hours, (h) 2 hours and (i) 24 hours.**

According to their hydrophilic-lipophilic balance (HLB) values (Table 5.3).

| Product name | Chemical identity | HLB value |
|---|---|---|
| SPAN-20 | Sorbitan monolaurate | 8.6 |
| SPAN-80 | Sorbitan monooleate | 4.3 |
| SPAN-85 | Sorbitan trioleate | 1.8 |
| TWEEN-85 | Polyethylene glycol sorbitan trioleate | 11 |

**Table 5.3 Product name, chemical identity and HLB value of the SPAN and TWEEN surfactant employed.**

SPAN-20 and TWEEN-85, which were more soluble in aqueous solution than SPAN-80, did not present a complete **sod→zni** conversion within 2 hours of reaction (Figure 5.20 b for SPAN-20, h for TWEEN-85 and Figure 5.10 for SPAN-80), while SPAN-85, which was less soluble and therefore less available, appeared to accelerate the conversion; indeed the PXRD patterns of the sample at 0.5 h already showed peaks for the **zni** phase (Figure 5.20 d).

SEM images of the time experiments conducted with the surfactants are shown below in Figure 5.21.

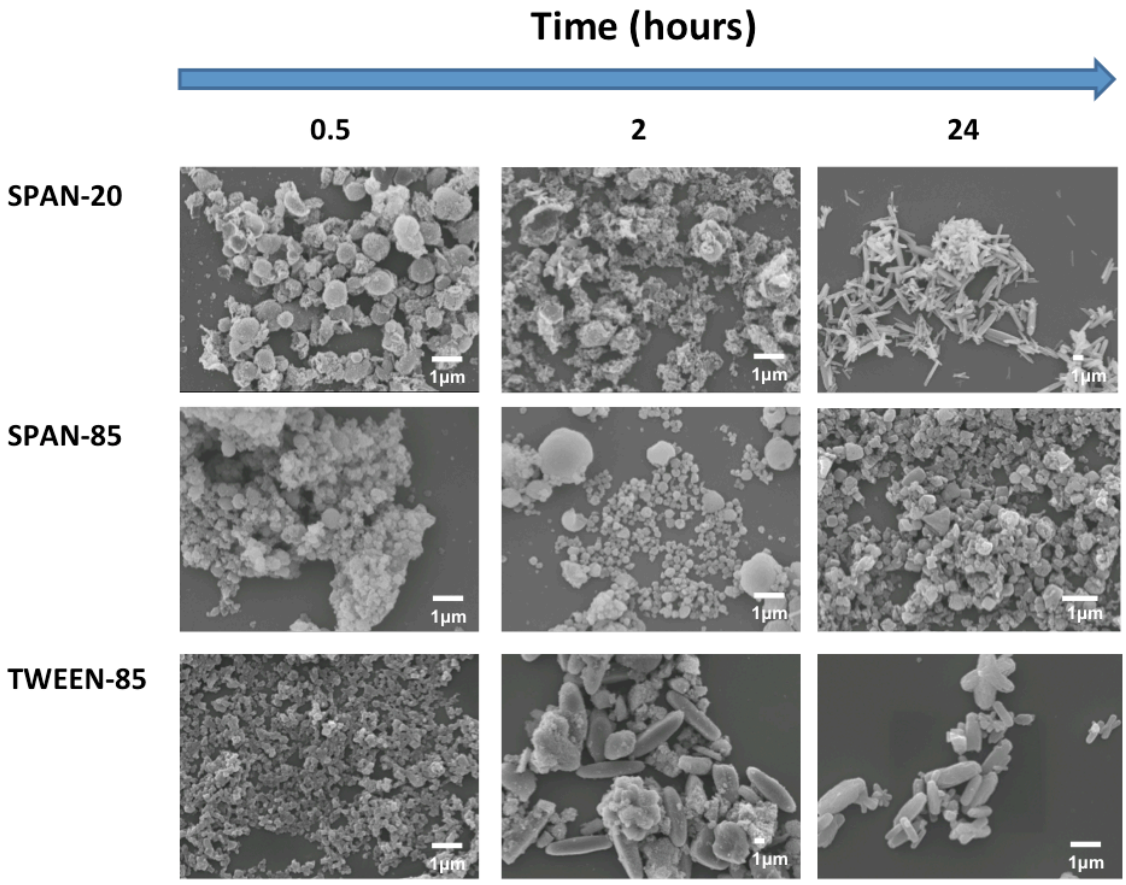


**Figure 5.21 SEM images of the experiments performed with the surfactant SPAN-20 at time 0.25 hours, 2 hours and 24 hours, with the surfactant SPAN-85 at time 0.25 hours, 2 hours and 24 hours and with the surfactant TWEEN-85 at time 0.25 hours, 2 hours and 24 hours.**

Even though PXRD patterns showed that the experiments carried out with the three different surfactants SPAN-20, SPAN-85 and TWEEN-85 followed the same topological path, the morphology of the crystals changed in consistently different ways depending on the surfactant used: SPAN-20 showed similar morphological effects to SPAN-80, forming **sod** ZIF colloidosomes at time 0.5 hours, which were broken into the resulting **sod** nanoparticles at time 2 hours and were finally converted into **zni** rod-like or lozenge-like particles after 24 hours (Figure 5.21). SPAN-85 formed an aggregation of **sod** particles at time 0.5 hours, which were converted in **zni** rounded-like particle of various dimensions (from few micron to hundreds of nanometers) at time 2 hours and downsized to the nanorange with increasing the reaction time to 24 hours (Figure 5.21). TWEEN-85 did not appear to stabilize any colloidosome-like aggregates but formed directly **sod** nanoparticles at time 0.5 hours, according to the PXRD pattern at time 2 hours both **sod** and **zni** phase were present, indeed the SEM images confirmed the presence of both **sod** nanoparticles and lozenge-like particles typical of the **zni** phase. Finally at time 24 hours, just lozenge-like particles were detected with TWEEN-85 (Figure 5.21).

Finally the different surfactants promoted different effects on the crystal size and morphologies. Regarding the **sod** phase all the surfactants formed particles with dimensions in the nanorange but just SPAN-20 is able to stabilize colloidosomes. Regarding the **zni** phase SPAN-20 and TWEEN-85 formed lozenge-like particles comparable in size and morphology, while SPAN-85 formed rounded-like particles with smaller dimensions. Since the HLB value of the surfactants SPAN-20 and TWEEN-85 were similar, we could speculate they were present under the same mesophase, which justified the effect on the **zni** particles. However it did not explain the different behaviour on the **sod** phase. Therefore it might be that different parts of the surfactant were involved in forming the macroscopic structure of the two phases.

#### 5.2.2.3 Reaction investigated with 1,4-Sorbitan and dodecanoic

Even though these experiments indicated the importance of the neutrality of the surfactant on the appearance of an initial **sod** phase they did not completely clarify which part of the amphiphile was involved in the conversion. 1,4-Sorbitan and dodecanoic acid mimic respectively the hydrophilic and the lipophilic part of SPAN-80 and were selected to perform further experiments at time 0.5, 2 and 24 hours (Figure 5.22) in an attempt to delineate the roles of the SPAN-80 tail and headgroup.

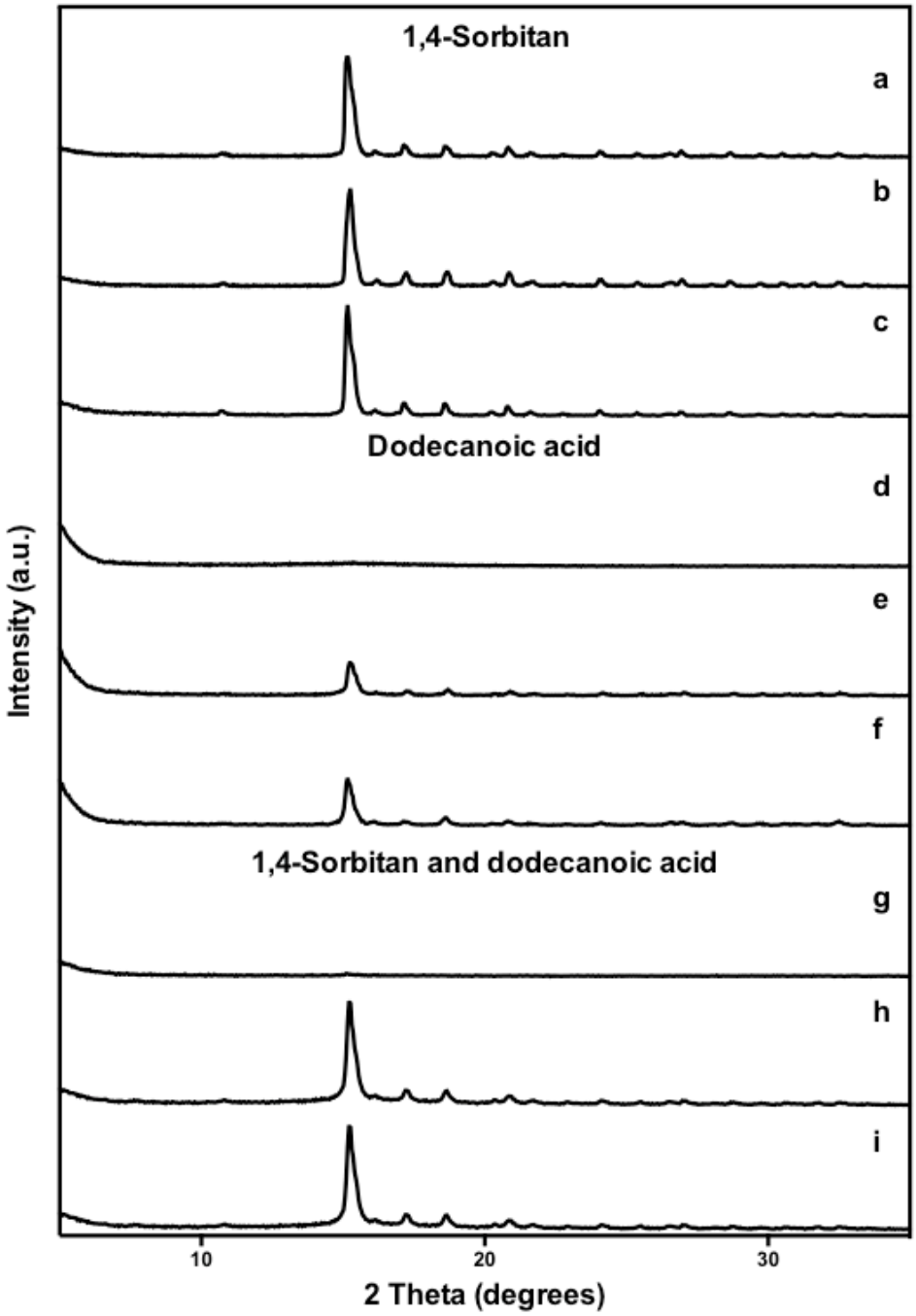


**Figure 5.22 PXRD patterns of the experiments performed with the 1,4-Sorbitan at time (a) 0.5 hours, (b) 2 hours and (c) 24 hours, with dodecanoic acid at time (d) 0.5 hours, (e) 2 hours and (f) 24 hours and with 1,4-Sorbitan and dodecanoic acid together at time (g) 0.5 hours, (h) 2 hours and (i) 24 hours.**

Used separately, both 1,4-sorbitan and dodecanoic acid led directly to the formation of the dense **zni** phase, although the latter appeared to slow down the reaction to about 2 hours. A similar effect was observed when the two components were used together (Figure 5.22), which was discussed in the next paragraph. SEM images of the products were shown below in Figure 5.23, where the image for dodecanoic acid and dodecanoic acid with 1,4-Sorbitan at reaction times of 0.5 hours were not presented since no solid was formed under these conditions.

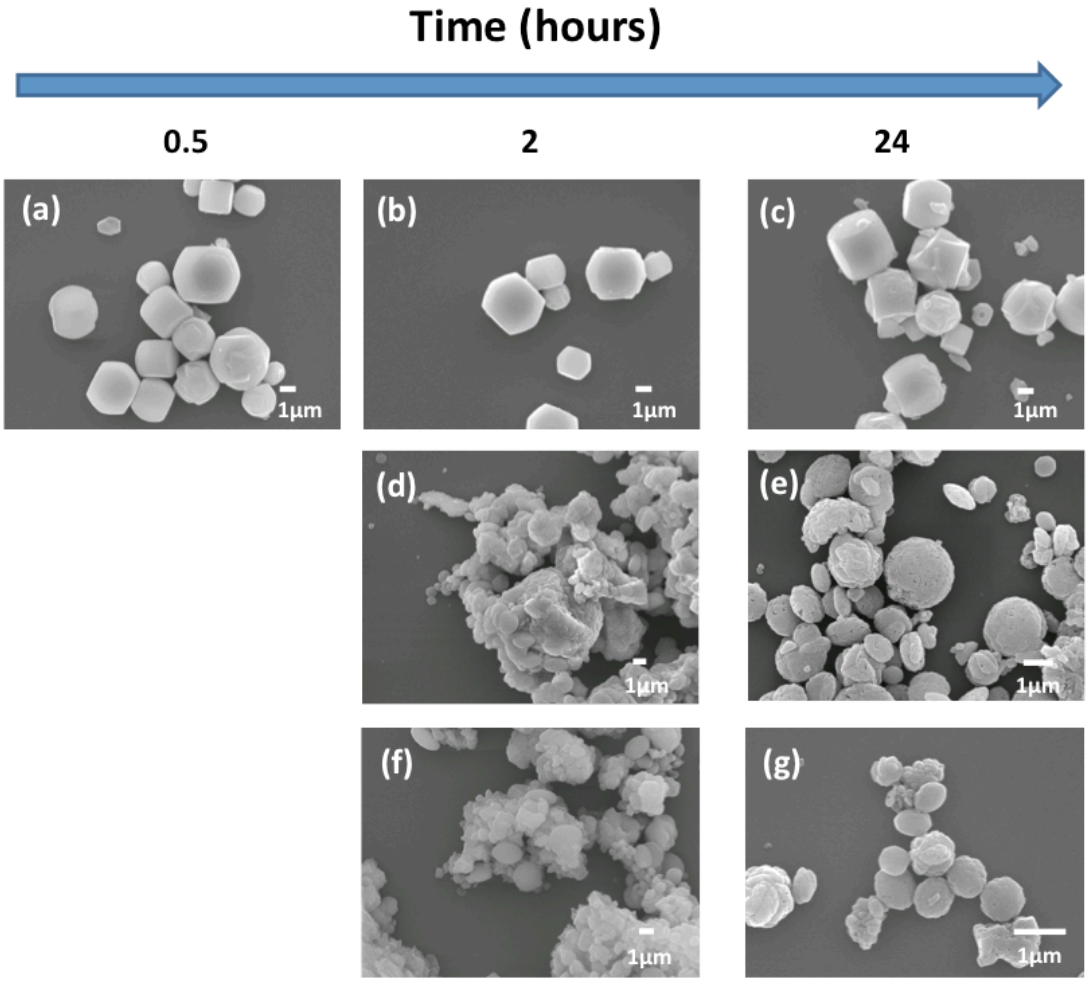


**Figure 5.23 SEM images of the experiments performed with the 1,4-Sorbitan at time (a) 0.5 hours, (b) 2 hours and (c) 24 hours, with dodecanoic acid at time (d) 2 hours and (e) 24 hours and with 1,4-Sorbitan and dodecanoic acid together at time (f) 2 hours and (g) 24 hours.**

1,4-Sorbitan did not appear to act on the morphology of the **zni** particles, indeed the particles were comparable with the **zni** particles obtained without any surfactant showed in Figure 5.9 a-c. Dodecanoic acid and the combined used of dodecanoic acid and 1,4-Sorbitan on the other hand led to the formation of aggregated particles after 2 hours, which then evolved into rounded-like particles.

In light of the experiments performed it was clear that SPAN-80 had many effects on the reaction including: the colloidosomes formation, the initial stabilization of **sod** phase and/or the conversion from **sod** to **zni** as shown in 5.2.2.1. The colloidosomes formation was analogous to the template effect of the surfactant that had been widely discussed in Chapter 4. Concerning the stabilization of the initial **sod** phase rather than direct formation of **zni**, it was demonstrated that this only occurred in the presence of the surfactant SPAN-80 (5.2.2.1) or related sorbitan-derived amphiphiles (5.2.2.2), and those experiments performed without SPAN-80 immediately resulted in the **zni** phase (5.2.1). The role of SPAN-80 was further analysed by performing the reaction with

molecules that mimic respectively the hydrophilic and the lipophilic part of the surfactant, i.e. 1,4-Sorbitan and dodecanoic acid (5.2.2.3). It was noted that when these components were used together or separately as additives the **sod** topology did not form. In particular, the experiments showed that 1,4-Sorbitan did not have any particular effect on the reaction, leading directly to the **zni** phase, while, when dodecanoic acid was employed in the synthesis, alone or in conjunction to 1,4-Sorbitan, it slowed the **zni** phase formation.

This at first may indicate that the effect of dodecanoic acid was dominant over 1,4-Sorbitan, as supported from the PXRD patterns of the time experiments performed with 1,4-Sorbitan and/or dodecanoic acid (Figure 5.22). Then we can speculate about how dodecanoic acid slowed down the growth of the **zni** phase. For example, the carboxylic moiety might interact with $Zn^{2+}$ ions, as in the case of MOF-5,[107] which may lower their chemical potential or it might be due to the lipophilic tail, as reported for the effect of CTAB with ZIF-8.[106]

Therefore SPAN-80 might act similarly to dodecanoic acid, slowing down the **zni** formation and at the same time stabilizing or promoting the **sod** topology arising from the connection of the sorbitol moiety to the hydrocarbon chain. Indeed the PXRD patterns of the time experiments performed with SPAN-80 indicated that the **zni** phase started appearing after 0.5 hours (Figure 5.10), so its formation is slowed down as in the case of dodecanoic acid (Figure 5.22). However, PXRD patterns of the experiments performed with SPAN-80 also showed the presence of the **sod** phase at 0.25 hours, while dodecanoic acid did not form any solid product before the **zni** phase at 2 hours time. It is possible that the presence of SPAN-80 initially favoured **sod** formation given that the MeIm linker was more hydrophobic than Im, promoting the inclusion of MeIm into the framework leading to an initial **sod** phase. According to the literature[183] **sod** nanocrystals might form into the surfactant micelles. While H-MeIm molecules and Zn-MeIm intermediates enriched inside the micelle, Im would be largely excluded due to the less hydrophilic nature, therefore promoting the formation of the **sod** phase. Even though the mechanism of why **sod** formed first in the presence of SPAN-80 is still not clear, the **sod** phase was clearly metastable under the aqueous conditions investigated and underwent conversion into the **zni** phase, as demonstrated from the PXRD patterns of the time experiments performed with SPAN-80 (Figure 5.10).

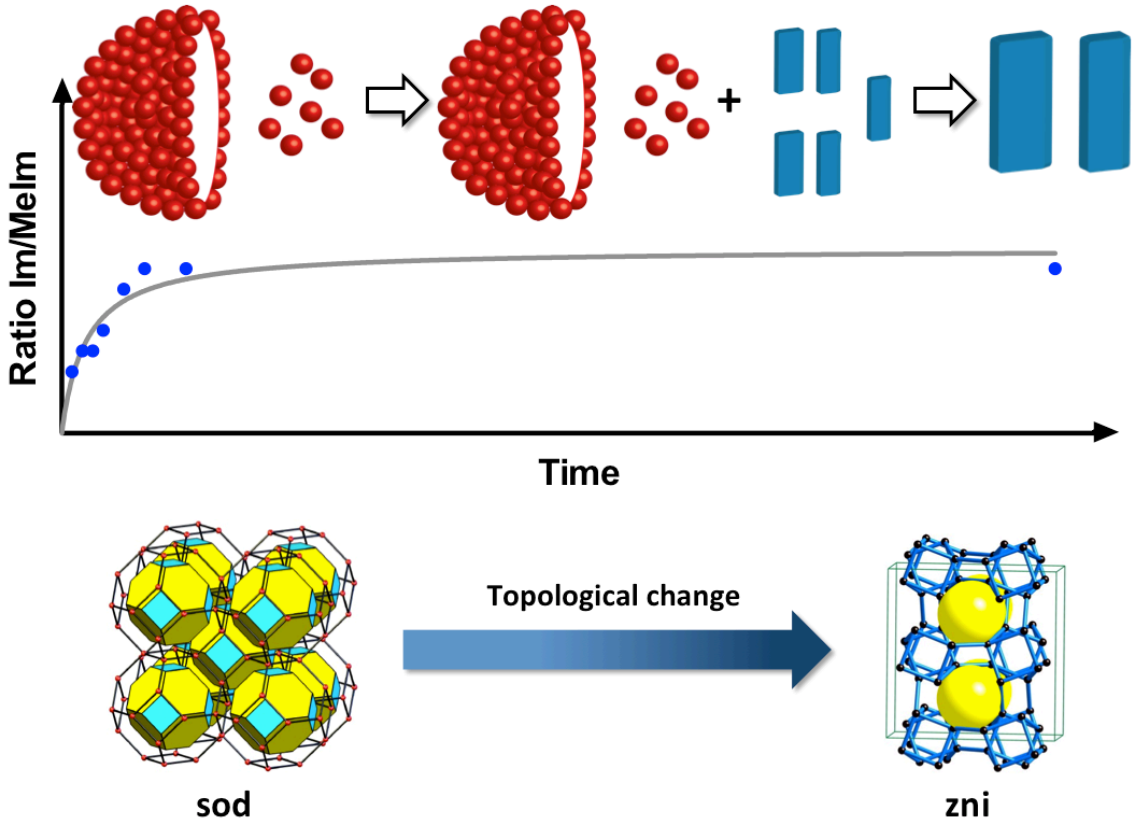


**Scheme 5.1 Morphological evolution of the framework from nano-crystals and colloidosomes (related nanocrystals superstructures) typical of SALEM-2 to tetragonal rectangular shape particles typical of ZIF-61. The conversion involves a topological change from the highly porous sod net to the more dense zni one due to the change in the imidazole to 2-methylimidazole ratio in the framework.**

As the reaction preceded the conversion from **sod** to **zni** phase increased. The topological change from **sod** to **zni** topology *prima facie* appeared to depend on the replacement of MeIm linkers in the initially deposited framework by increasing amounts of Im (Scheme 5.1). Ligand-ligand interactions played a crucial role in the topological diversity of ZIFs[73, 79, 203, 209] as do the nature of any substituents on the imidazole ring. For instance, the **zni** topology is more energetically stable than the **sod** topology and it is the favoured one for the $Zn(Im)_2$ system[211], but because of steric effects and the rules of optimal space partitioning of the methyl groups, it has not been reported for the pure $Zn(MeIm)_2$ system, which tends to assemble into the significantly more open **sod** network.[79-80, 219] Therefore the relative content of each ligand probably affects the final topology of the framework. According to this, experimental data showed that while MeIm was in excess the **sod** topology was stabilized, but when the relative proportions of the Im component increased in the mixed-linker ZIF the more dense **zni** topology started to appear. Furthermore the topological conversion was also followed by a morphological change of the particles: the nanoparticles and colloidosomes belonging to the **sod** phase were indeed replaced by **zni** lozenge-like particles, which size increased with the reaction time. It is still unclear how the morphological change occurs, it might be that the incorporation of imidazole in the framework caused the

breaking down of the colloidosomes or that the colloidosomes would break down anyhow and then the lozenge-like particles form. Finally the lozenge-like particles appeared to increase in size with time, possibly via an Ostwald ripening mechanism.[220]

Essentially the reaction seemed to follow different paths depending on the presence or not of the surfactant: when SPAN-80 was not present the more thermodynamically stable **zni** phase was directly formed (or at least at the time-scale in which the experiments were performed), while when the amphiphile was present a metastable **sod** phase was initially formed and then converted to a more stable **zni** phase.

### 5.2.3 Conversion from premade ZIFs

The role of SPAN-80 on the thermodynamics of the reaction was further studied starting from premade ZIF-8 (**sod**, $Zn(MeIm)_2$) or **zni** phase ($Zn(MeIm)_{0.6}(Im)_{1.4}$) instead of directly in the synthesis. It was hoped that these experiments would confirm or otherwise the chemical stability of ZIF-8 in the presence of imidazole and the reversibility of the conversion from **sod** to **zni** topology and vice versa. The conversion was performed starting from premade ZIF-8 or **zni** phases respectively in the presence of an excess of Im or MeIm in the presence and absence of SPAN-80 and the reactions carried out for 24 hours. The experiments without surfactant were performed in order to check the stability of the starting phase and to demonstrate the decisive role of SPAN-80 in the conversion. Figure 5.24 and Figure 5.25 show respectively the PXRD patterns and the SEM images of the premade ZIFs and the related experiments.

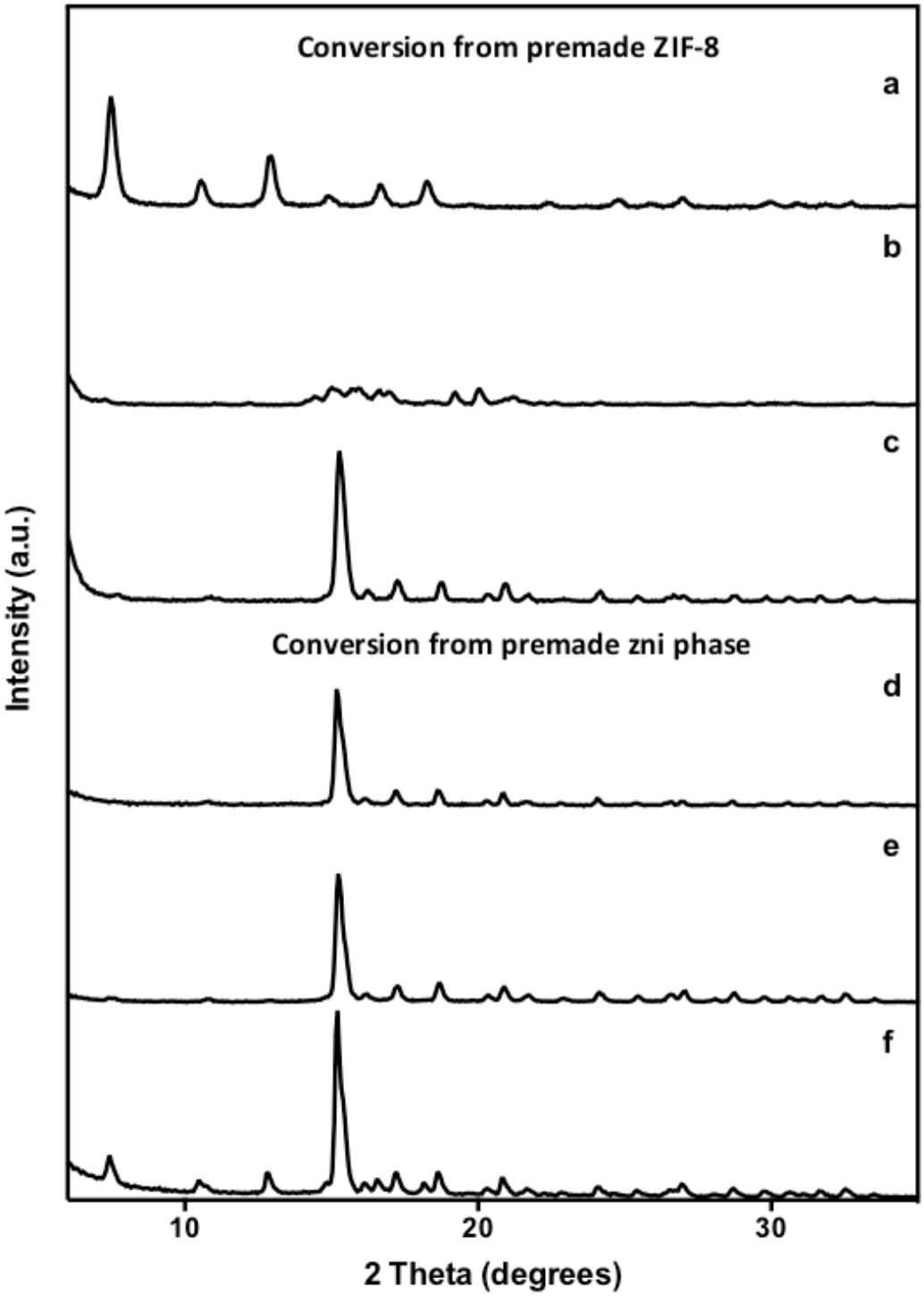


**Figure 5.24 PXRD patterns of conversion experiments from premade ZIFs: (a) premade ZIF-8 (b) premade ZIF-8 with imidazole at time 24 hours, (c) premade ZIF-8 with imidazole and SPAN-80 at time 24 hours, (d) premade zni phase (e) premade zni phase with methylimidazole at time 24 hours (f) premade zni phase with methylimidazole and SPAN-80 at time 24 hours.**

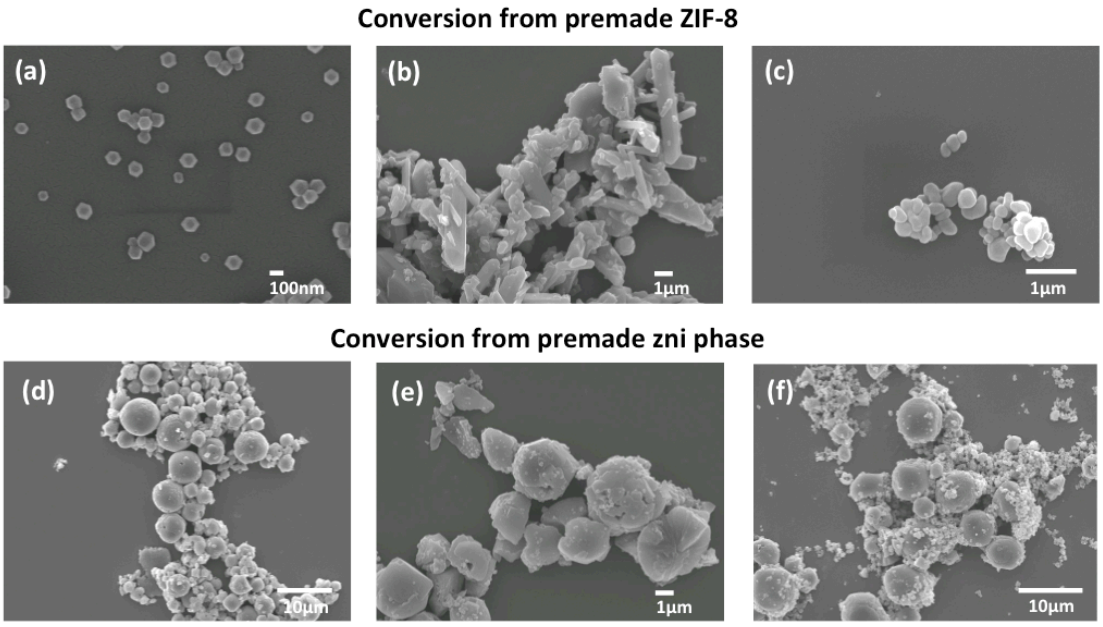


**Figure 5.25 SEM images of conversion experiments from premade ZIFs: (a) premade ZIF-8 (b) premade ZIF-8 with imidazole at time 24 hours, (c) premade ZIF-8 with imidazole and SPAN-80 at time 24 hours, (d) premade ZIF-61 (e) premade ZIF-61 with methylimidazole at time 24 hours (f) premade zni phase with methylimidazole and SPAN-80 at time 24 hours.**

Starting from premade ZIF-8 an amorphous phase was formed in the presence of an excess of imidazole in water, which also occurred using DMF or DMA as solvent in the solvothermal reaction,[210] while it was totally converted to **zni** phase in the presence of an excess of imidazole and SPAN-80 (respectively Figure 5.24 b and c). Sample c was further investigated by $^{1}$H NMR spectroscopy using the outlined method, which quantifies the ratio imidazole to methylimidazole to 90:10 (Figure 5.26).

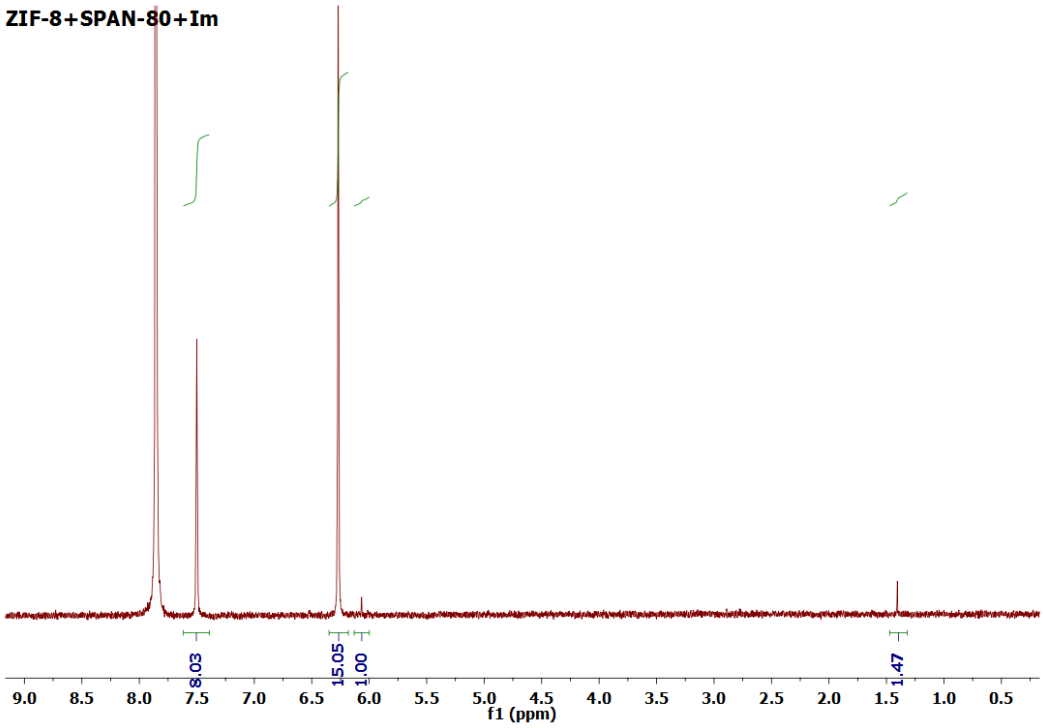


**Figure 5.26 $^{1}$H-NMR spectrum of the reaction of ZIF-8 with imidazole and SPAN-80 at time 24 hours showing the methylimidazole to imidazole content.**

This ratio was considerably higher than in the direct synthesis or in the conversion promoted by SPAN-80 at a comparable reaction time (respectively 70 to 30 and 65 to 35). It might be partially due to the nanosize of the ZIF-8 particles used but also to the fact that the ratio of zinc to Im was maintained at 1:70 as in the direct synthesis, meaning that it was 35 times in excess compared to the MeIm in the framework, which might reasonably be expected to lead to a higher incorporation of Im. These results demonstrated the instability of **sod** ZIF-8 in the presence of Im in water, which appeared to collapse to an amorphous phase, and confirmed further that SPAN-80 drove the topological conversion to the **zni** phase (Figure 5.24 b and c).

On the other hand the effect of imidazole on HC-50D-ZIF-8 or HC-25D-90S-ZIF-8 led to the formation of flower-like microcapsules with **sod** topology, which converted with time into rod-like particles with **zni** topology (4.2.4). Nevertheless the starting conditions employed were comparable (ratio Zn:Im = 1:70 and Im:MeIm = 35), in the latter cases the reactions were carried out up to 2 hours instead of 24 hours, which might indicate that ZIF-8 undergoes conversion before collapsing to an amorphous phase. Furthermore HC-25D-90S-ZIF-8 still presented traces of SPAN-80, as proved by the IR spectrum (Figure 4.48) and therefore it agreed with the experiment performed starting from premade ZIF-8 with imidazole and SPAN-80.

The experiments performed starting from a premade **zni** phase showed that it was stable in the presence of methylimidazole, while it was just partially converted to the **sod** topology with SPAN-

80 and methylimidazole (respectively Figure 5.24 e and f), indicating both the higher stability of **zni** compared to the **sod** topology and again the fundamental role of SPAN-80 in the conversion. SEM images revealed the morphological evolution of the particles due to the addition of additives in the synthesis. The ZIF-8 starting material was characterized by hexagonal nanoparticles,[182] which were converted to amorphous rod-like particles by introducing imidazole in water. On the other hand, when imidazole was used in the presence of SPAN-80 the well-defined ZIF-8 crystals were fully converted into nanosized **zni** particles, where the particle downsize was probably due to the size of the starting ZIF-8 material. **zni** starting material was characterized by rounded-like particles, and in this case the addition of MeIm or MeIm/SPAN-80 did not change the morphology of the starting material although it was clear there was some break-up.

### 5.2.4 Ratio between the two ligands

Two factors were fundamental for the conversion from **sod** to **zni** topology when using a mixed MeIm/Im ligand system: the presence of the SPAN-80 surfactant and the ratio of the ligands. While the SPAN-80 appeared to initially favour and partially stabilise the **sod** topology, the replacement of methylimidazole by imidazole linkers with time led to a conversion to the **zni** topology (paragraph 5.2.2). Therefore the starting ratio of methylimidazole to imidazole could exert an influence on the reaction kinetics, in particular increasing the relative amount of methylimidazole in the starting ratio the conversion from **sod** to **zni** topology could be decelerated and vice versa increasing the relative amount of imidazole in the ratio the conversion should be enhanced.

Starting from this observation a series of experiments which took into account both methylimidazole to imidazole relative ratio and reaction time were performed: the reactions were carried out in aqueous media, but while in the previous experiments the ratio $Zn^{2+}$:MeIm:Im was 1:70:70, here it was kept $Zn^{2+}$:(MeIm+Im)=1:70. The reactions were performed in presence of the surfactant SPAN-80 (0.21 mmol, ratio $Zn^{2+}$:SPAN-80=1:2.3) and monitored at time 2 and 24 hours.[182] While the sum of the two linkers is 70 times in excess compared to the zinc, their relative amount was varied according to the following percentages: MeIm:Im= 100:0, 75:25, 50:50, 25:75, 0:100. PXRD patterns of the experiments are shown below in Figure 5.27,

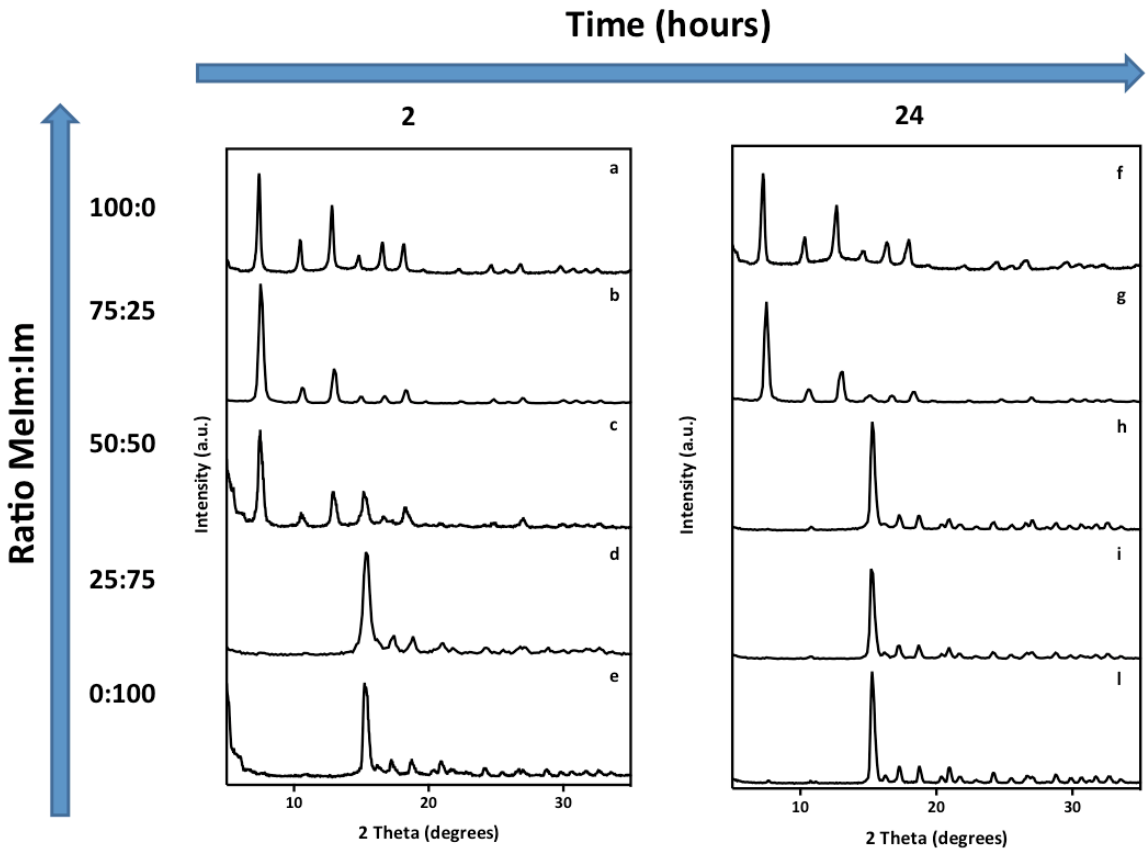


**Figure 5.27 PXRD patterns of the experiment performed in the presence of SPAN-80 at 2 hours reaction time at ratio MeIm:Im= (a) 100:0, (b) 75:25, (c) 50:50, (d) 25:75, (e) 0:100 and at 24 hours reaction time at ratio MeIm:Im= (f) 100:0, (g) 75:25, (h) 50:50, (i) 25:75, (l) 0:100.**

As expected the variation of MeIm:Im ratio and the reaction time appeared to influence the topology of the resulting ZIFs. When only methylimidazole was used (MeIm:Im=100:0) or this was in excess (75:25) a pure **sod** phase was formed after a reaction time of 2 hours, which did not appear to undergo further conversion even after 24 hours. However, when methylimidazole to imidazole were present in equal quantities at the start of the synthesis (50:50) the reaction time played a crucial role: at time 2 hours the **sod** topology was present and the emergence of a peak at 2Θ = 15° indicated **zni** was also forming, which underwent full conversion to the **zni** phase following 24 hours. Finally when imidazole was present in excess (MeIm:Im=25:75) the **zni** topology was formed within 2 hrs despite the presence of SPAN-80.

SEM images of these experiments are presented in Figure 5.28, ordered by reaction time and methylimidazole to imidazole ratio.

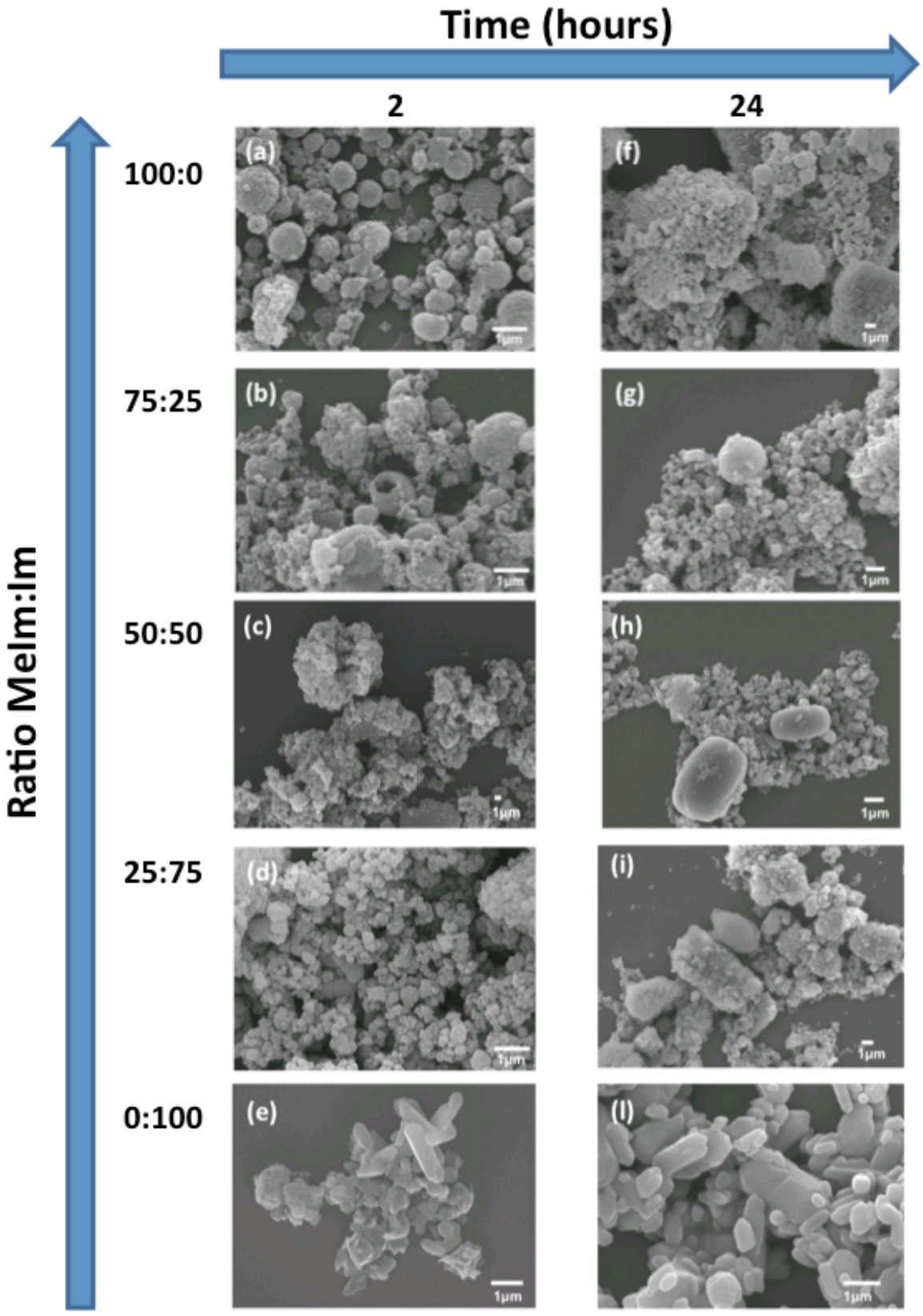


**Figure 5.28 SEM images of the experiment performed at 2 hours reaction time at ratio MeIm:Im= (a) 100:0, (b) 75:25, (c) 50:50, (d) 25:75, (e) 0:100 and at 24 hours reaction time at ratio MeIm:Im= (f) 100:0, (g) 75:25, (h) 50:50, (i) 25:75, (l) 0:100.**

Figure 5.28 revealed the effect of the time and the starting methylimidazole to imidazole ratio on the morphology of the resulting ZIFs. In agreement with the PXRD pattenrs, when methylimidazole was in large excess (MeIm:Im=100:0 or 75:25) **sod** colloidosomes, which were then broken into the resulting nanoparticles with time were formed. At an even methylimidazole to imidazole ratio **sod** nanoparticles were detected at time 2 hours, and some bigger particles characteristic of the **zni** topology were detected at 24 hours. Finally in an excess of imidazole (MeIm:Im=25:75 or 0:100) just typical **zni** particles were detected. Here the particle size appeared to increase with increasing the imidazole content and the reaction time from the nanorange at ratio MeIm:Im=25:75 at time 2 hours to micron range at ratio MeIm:Im=0:100 at time 24 hours. Notably the morphology of the **zni** isomorph $Zn(Im)_2$ was recognizable from the Zn(MeIm)(Im) isomorph presented in 5.2.1. Finally thermogravimetric analyses of all the experiments are reported (Figure 5.29) and the data summarized in Table 5.4.

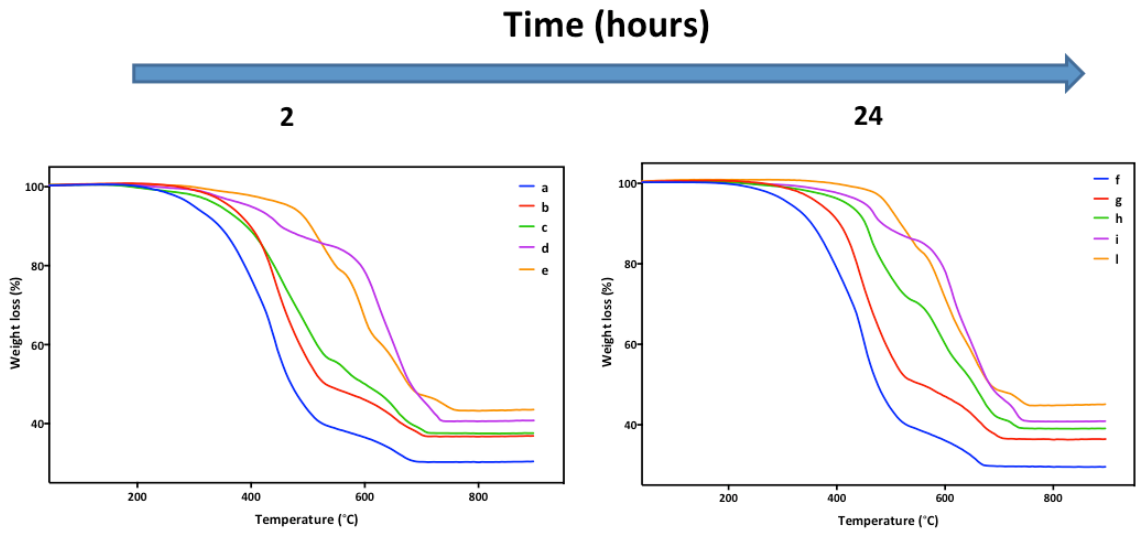


**Figure 5.29 Thermogravimetric analysis of the experiment performed at 2 hours reaction time at ratio MeIm:Im= (a) 100:0, (b) 75:25, (c) 50:50, (d) 25:75, (e) 0:100 and at 24 hours reaction time at ratio MeIm:Im= (f) 100:0, (g) 75:25, (h) 50:50, (i) 25:75, (l) 0:100.**

| Starting MeIm:Im ratio | 2 hours reaction | | | 24 hours reaction | | |
|---|---|---|---|---|---|---|
| | Organic % | Ratio MeIm:Im | Topology | Organic % | Ratio MeIm:Im | Topology |
| 100:0 | 70 | 100:0 | sod | 70 | 100:0 | sod |
| 75:25 | 64 | $60:40_{(e)}$ | sod | 64 | $60:40_{(e)}$ | sod |
| 50:50 | 63 | $50:50_{(e)}$ | sod/zni | 61 | $65:35_{(e)}$ | zni |
| 25:75 | 60 | $25:75_{(e)}$ | zni | 60 | $25:75_{(e)}$ | zni |
| 0:100 | 57 | 0:100 | zni | 56 | 0:100 | zni |

**Table 5.4 Organic content (expressed in percentage) included in the framework, ratio MeIm:Im included in the framework (subscript (e) stands for estimated) and the related topologies formed at the different ligands ratio experiments.**

Table 5.4 reported the organic percentage obtained from the different composition experiments, the estimate ratio methylimidazole to imidazole included in the framework and the related topology. The general trend was that decreasing the MeIm:Im ratio the resulting organic percentage decreases, which indicated an higher incorporation of imidazole in the framework. In large excess of methylimidazole (MeIm:Im=100:0 and 75:25), where **sod** topology was formed, the organic percentage of the corresponding time experiments following 2 and 24 hours were exactly the same, respectively 70% for MeIm:Im=100:0 and 64% for MeIm:Im=75:25. Interestingly, the two experiments at ratio MeIm:Im=50:50 recorded a decrease of the organic percentage from 63 to 61% from 2 to 24 hours, respectively for the **sod** and **zni** topology. Finally in excess of imidazole (MeIm:Im=25:75 or 0:100), where only the **zni** topology was accessible, the organic percentage of the corresponding time experiment were comparable, respectively 60% for MeIm:Im=25:75 and 57 and 56% for MeIm:Im=0:100. In general the expercted mass loss for $Zn(MeIm)_2$ was 71.2%, which agrees with the experiments performed with ratio MeIm:Im = 100:0 with organic percentage = 70%, while for $Zn(Im)_2$ the expected mass loss was 62%, higher than compared to the experiments performed at ratio MeIm:Im = 0:100 (57 and 56%), probably related to the error in the measurement or the presence of impurities. However considering the organic percentage obtained at MeIm:im=100:0 and 0:100 as reference values (respectively 70 and 56%) it was possible to estimate the ratio methylimidazole to imidazole in the framework: considering the experiment performed at reaction time 2 hours the final ratio MeIm:Im was 100:0, 60:40, 50:50, 75:25 and 0:100 and for the experiments performed at reaction time 24 hours it was 100:0, 60:40, 65:35, 75:25 and 0:100 respectively for starting ratio 100:0, 75:25, 50:50, 75:25 and 0:100. Therefore generally the degree of incorporation of the ligands in the framework was related to the starting ratio MeIm:Im where the appearance of **sod** phase was determined by a higher

presence of methylimidazole in the framework, while the **zni** phase by a higher presence of imidazole. The only exception was given by the experiment with starting ratio MeIm:Im=50:50 where the conversion **sod** to **zni** phase occurred and the estimate final ratio MeIm:Im changed from 50:50 to 65:35 respectively for 2 and 24 hours reaction, which again proved that the thermodynamics of the process led to the **zni** topology formation as function of the increment of imidazole in the framework and the reaction time.

## 5.3 Conclusions

Herein the system zinc: methylimidazole: imidazole was studied under different conditions. At first the **zni** phase with composition $Zn(MeIm)_{0.6}(Im)_{1.4}$ was synthesized in aqueous media at room temperature by simple mixing of the three precursor solutions in a ratio of $Zn^{2+}$:MeIm:Im=1:70:70.

Furthermore the synthesis of the **zni** phase in the presence of SPAN-80 was investigated as a function of time. It was experimentally found that SPAN-80 initially promote the formation of a **sod** phase in water under conditions where the **zni** phase would otherwise form, but the **sod** network was apparently metastable and readily transforms into the dense and more thermodynamically stable **zni** phase as the MeIm linkers were successively replaced by Im, from a starting composition of $Zn(MeIm)_{1.1}(Im)_{0.9}$ (**sod**) to $Zn(MeIm)_{0.7}(Im)_{1.3}$ (**zni**) (Scheme 5.2). The conversion was monitored at different times and characterized by PXRD, SEM, $^{1}$H-NMR, IR, TGA and nitrogen sorption analysis.

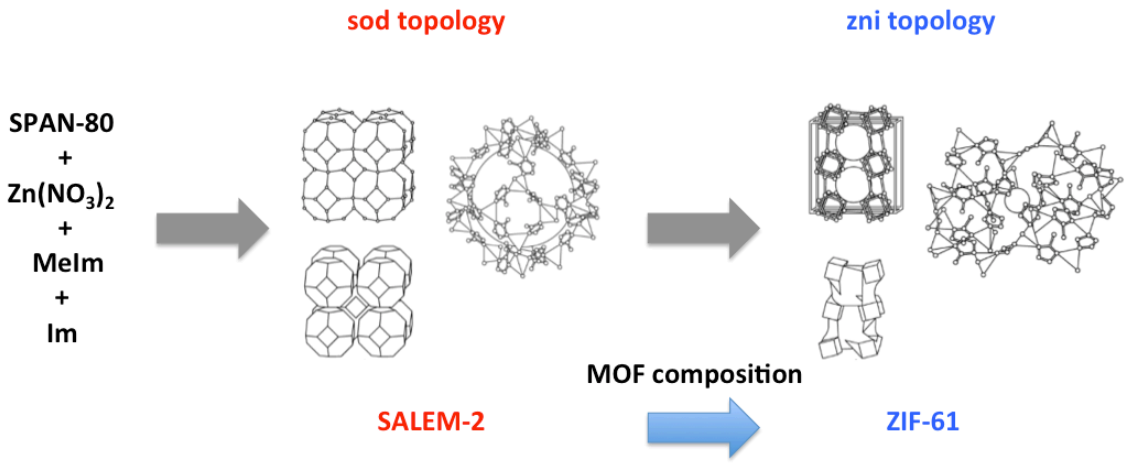


**Scheme 5.2 Representation of the topological conversion from the open sod topology of mixed-linker SALEM-2 to the dense zni topology of ZIF-61.**

In order to gain further insight into the role of SPAN-80, the reaction was performed under the same conditions but in the presence of other surfactants including CTAB, SDS, SPAN-20, SPAN-80, SPAN-85 and TWEEN-85. Using SDS the reaction led directly to the formation of the **zni** topology,

while CTAB appeared to suppress any ZIF formation. SPAN-20, SPAN-85 and TWEEN-85 all had a similar effect to SPAN-80 on the reaction differing just in terms of the **sod**-to-**zni** conversion time, which depended on the solubility of the surfactant in water. Finally 1,4-Sorbitan and dodecanoic acid, which mimic respectively the hydrophilic and the lipophilic part of SPAN-80, were chosen to perform further experiments in order to clarify which part of the surfactant was involved in the conversion: used separately, both of them led directly to the formation of the dense **zni** phase but dodecanoic acid slowed down the reaction and when they were used together the reaction was also slower.

In light of the results reported in this chapter a conversion mechanism was tentatively proposed. While the formation of the **zni** phase was slowed down probably by the surfactant the **sod** topology was promoted. **sod** nanocrystals might form into the surfactant micelles where the presence of MeIm is favoured compared to Im due to the more hydrophilic nature of the former. Then the topological change from **sod** topology to **zni** topology occurred, which was driven by the replacement of 2-methylimidazole linkers in the initially deposited framework by increasing amounts of Im. Therefore while MeIm was in excess the **sod** topology was stabilized, until the relative proportions of the Im component increased in the mixed-linker ZIF the more dense **zni** topology started to appear. In terms of reaction time **zni** phase started appearing after 0.5 hours and became the only phase present after 2 hours. Furthermore the topological conversion was also accompanied by a morphological change from **sod** nanoparticles and colloidosomes to **zni** lozenge-like particles.

The role of SPAN-80 on the thermodynamics of the reaction was further studied in the conversion from premade ZIF-8 (**sod**) or ZIF-61 (**zni**) respectively in the presence of an excess of imidazole or methylimidazole without or with SPAN-80 for 24 hours. Starting from premade ZIF-8 an amorphous phase was formed without SPAN-80 while it was totally converted to **zni** phase in the presence of the surfactant on the other hand premade **zni** phase was stable without any surfactant and it was just partially converted to the **sod** phase with SPAN-80, indicating the chemical instability of ZIF-8 in water in the presence of imidazole, and the higher stability of the **zni** topology and the fundamental role of SPAN-80.

Finally the ratio $Zn^{2+}$:MeIm:Im together with the time were further analysed as parameters that could exert an influence on the reaction kinetics of the **sod**→**zni** conversion. As expected the variation of MeIm:Im ratio and the reaction time appeared to influence the topology of the resulting ZIFs and while in the case of large excess of methylimidazole of imidazole respectively **sod** or **zni** phase were formed, at even ratio methylimidazole to imidazole (50:50) the time played a crucial role, indeed at time 2 hours **sod** topology was favoured, while at time 24 hours **zni**

topology was formed, also according with the increment of degree of imidazole linker in the framework. Therefore those experiments further proved that the thermodynamics of the process led to the **zni** topology formation as function of the increment of imidazole in the framework and the reaction time.

## 5.4 Experimental part

**Synthesis of zni phase.** Solutions of $Zn(NO_3)_2.6H_2O$ (0.029g in 0.5 mL $H_2O$), 2-methylimidazole (0.57 g in 2 mL $H_2O$) and imidazole (0.48 g in 2 mL $H_2O$) were mixed together and stirred for different time (0.25, 0.5, 0.75, 1, 1.5, 2, 3 and 24 hours) at room temperature. The white precipitate was centrifuged, washed twice with ethanol and dried overnight in air. Yield= 15mg.

**Synthesis of zni phase with surfactants.** 2.1 mmol of surfactant (SDS, CTAB, SPAN-20, SPAN-80, SPAN-85, TWEEN-85, 1,4 Sorbitan, dodecanoic acid, 1,4 Sorbitan:dodecanoic acid= 1:1) were stirred for 5 hours in 5 mL of $H_2O$ at room temperature. Solutions of $Zn(NO_3)_2.6H_2O$ (0.029g in 0.5 mL $H_2O$), 2-methylimidazole (0.56g in 2 mL $H_2O$) and imidazole (0.49g in 2 mL $H_2O$) added consequently at the SPAN-80 solution and stirred for different time (from 0.25 to 24 hours) at room temperature. The white precipitate was centrifuged, washed twice with ethanol and dried overnight in air. Yield= 15mg.

**Synthetic procedures of ZIF-8 with SPAN-80.** SPAN-80 (90 mg, 2.1 mol) was stirred for 5 hours in 5 mL of $H_2O$ at room temperature. Solutions of $Zn(NO_3)_2.6H_2O$ (0.029g in 0.5 mL $H_2O$) and methyl imidazole (1.12g in 4 mL $H_2O$) added to the SPAN-80 solution and stirred for 2 hours at room temperature. The white precipitate was centrifuged, washed twice with ethanol and dried overnight in air. Yield= 15mg.

**Synthetic procedures for premade ZIF-8 with imidazole.** 16 mg of ZIF-8 were added in 2.5 mL of $dH_2O$, then a solution of 0.49 g of Im in 2 mL of $dH_2O$ was added and left under stirring for 24 h. The white precipitate was centrifuged, washed twice with ethanol and dried overnight in air. Yield= 16mg.

**Synthetic procedures for premade ZIF-8 with SPAN-80 and imidazole.** 90 mg of SPAN-80 stirred for 5 hours in $dH_2O$ then 16 mg of ZIF-8 were added in 2.5 mL of $dH_2O$, then a solution of 0.49 g of Im in 2 mL of $dH_2O$ was added and left under stirring for 24 h. The white precipitate was centrifuged, washed twice with ethanol and dried overnight in air. Yield= 16mg.

**Synthetic procedures for premade zni phase with methylimidazole.** 16 mg of ZIF-61 were added in 2.5 mL of $dH_2O$, then a solution of 0.56 g of MeIm in 2 mL of $dH_2O$ was added and left under

stirring for 24 h. The white precipitate was centrifuged, washed twice with ethanol and dried overnight in air. Yield= 16mg.

**Synthetic procedures for premade zni phase with SPAN-80 and methylimidazole.** 90 mg of SPAN-80 stirred for 5 hours in $dH_2O$ then 16 mg of ZIF-61 were added in 2.5 mL of $dH_2O$, then a solution of 0.56 g of MeIm in 2 mL of $dH_2O$ was added and left under stirring for 24 h. The white precipitate was centrifuged, washed twice with ethanol and dried overnight in air. Yield= 16mg.

**Synthetic procedure for the sod→ zni conversion varying the ligands ratio.**

2.1 mmol of SPAN-80 surfactant (90 mg) were stirred for 5 hours in 5 mL of $H_2O$ at room temperature. Solutions of $Zn(NO_3)_2.6H_2O$ (0.029g in 0.5 mL $H_2O$), 2-methylimidazole (x g in 2 mL $H_2O$) and imidazole (y g in 2 mL $H_2O$) added consequently at the SPAN-80 solution and stirred for different time (2 and 24 hours) at room temperature. Ratio $Zn^{2+}$:(Me+Im)=1:70, ratio Me:Im= 100:0, 75:25, 50:50, 25:75, 0:100, respectively MeIm=0.56g, MeIm=0.42g and Im=0.12g, MeIm=0.28g and Im=0.245g, MeIm=0.14g and Im=0.36g, Im+0.49g. The white precipitate was centrifuged, washed twice with ethanol and dried overnight in air. Yield= 10mg.

All the experiments where performed at least 3 times in order to ensure reproducibility.

# Chapter 6: Conclusions and outlook

Within this thesis several aspects of MOF macroscopic structure formation, starting from the three prototypical MOFs HKUST-1, ZIF-8 and ZIF-61, were investigated. A summary of obtained results and an outlook to future work are outlined below.

## 6.1 Conclusions

Using HKUST-1, it has been demonstrated that the formation of mesostructured phases depends on the co-assembly between the surfactant mesophase and the MOF precursors. Therefore the strength and nature of the interactions and of the surfactant itself and the synthetic parameters, such as salt precursors, pH, solvent and reaction temperature are fundamental.

The crucially of the nature of the surfactant and the co-assembly between surfactant mesophase and MOF precursors through specific interactions was demonstrated using Pluronic-P123 block copolymers or carboxylic acid-derived surfactants, namely octanoic acid or dodecanoic acid. Pluronic-P123, which did not form any specific interactions with the MOF precursors, acted only to reduce the particle size, while carboxylic acids, which displayed modulator properties, acted on the particle morphology and mesoporosity, forming worm-like structures or mesoporous rounded HKUST-1 particles (rp-HKUST-1, rp= rounded particles).

On the other hand the synthetic parameters strongly influenced the MOF nucleation and formation process, the reaction kinetics and the resulting Cu-BTC phase(s) formed. The templating effect of the mesostructure occurred during the MOF formation, therefore slowing down the reaction kinetics, using mild conditions and more structurally suitable precursors, helped on manipulating the physical form of the MOF.

These results represent an overview of the effect of surfactants on the synthesis and assembly of HKUST-1 and indicate that in the high variability of the MOF synthesis a careful design is needed in order to promote a macroscopic structure formation. In the specific case of intraparticle mesoporosity, both effect of surfactant and synthetic condition had to be taken in account.

Further the directional self-assembly properties of ZIF-8 for the formation of superstructures, such as hollow capsules and colloidosomes was investigated. Preliminary studies performed using SPAN-80 or SPAN-80/dodecane systems stressed the importance of a stable emulsion for the templating of hollow capsule structures. Thereafter dodecane-in-water and dodecane/SPAN-80-in-water emulsions were tested for the formation of hollow capsules with a shear force

instrument and the conditions were optimized in order to obtain relatively monodisperse hollow capsules without the presence of any bulk MOF nanoparticles.

It is important to underline that the type of emulsion used strongly influences the process, and the hollow capsules that were assembled displayed differences in surface roughness, shell thickness and overall size. In the case of dodecane-only emulsions the ZIF-8 hollow capsules were formed by a Pickering emulsion type mechanism. When dodecane/SPAN-80 system is employed the SPAN-80 acted as an emulsifying agent stabilising the dodecane emulsion and tailoring the size of the particles into the nanorange, therefore the resulting hollow capsules had different characteristics, such as a smaller dimension and smoother external surfaces.

Finally the hollow capsules were treated with imidazole. As further discussed in Chapter 5 the introduction of imidazole led to the conversion from ZIF-8 to ZIF-61 or an open **sod** to the dense **zni** topology with time. However the morphological effects of imidazole on the hollow capsules prior to the topological transformation was enhanced by their starting superstructure, giving rise to flower-like microcapsules with visible holes that were etched in the shell structure.

In the last chapter the **zni** phase (ZIF-61, $Zn(MeIm)_{0.6}(Im)_{1.4}$) was systematically investigated and its synthesis optimized under environmentally friendly conditions.

Furthermore the synthesis of the **zni** phase in the presence of SPAN-80 was investigated as a function of time. It has been experimentally found that SPAN-80 promoted a conversion from the **sod** to the **zni** phase. However the initially formed **sod** topology was only metastable and readily transformed into the dense and more thermodynamically stable **zni** phase as the MeIm linkers are successively replaced by Im, changing the composition from $Zn(MeIm)_{1.1}(Im)_{0.9}$ for the **sod** phase to $Zn(MeIm)_{0.7}(Im)_{1.3}$ for the **zni** phase.

The conversion mechanism proposed contemplates that formation of the **zni** phase was retarded by the surfactant, and therefore the **sod** topology was promoted. Then the topological change from **sod** topology to **zni** topology occurred, which appears to be driven by the replacement of 2-methylimidazole linkers in the initially deposited framework by increasing amounts of imidazole. Therefore when methylimidazole was in excess the **sod** topology was promoted, while when the relative proportions of the imidazole component increased in the mixed-linker ZIF the more dense **zni** topology started to appear. Furthermore the topological conversion is also accompanied by a morphological change from **sod** nanoparticles and colloidosomes to **zni** lozenge-like particles.

Further experiments were performed that indicated the chemical instability of ZIF-8 in the presence of imidazole in water, suggesting that the process was thermodynamically driven from

**sod** to **zni** topology as a function of the increased imidazole in the framework and reaction time and the fundamental role of SPAN-80 in the topological conversion.

Finally, envisioning a control over the macroscopic structure of MOFs, this thesis gives an overview of the importance of structural features of the starting MOF, surfactant nature and synthetic conditions employed. The relation between starting MOF, surfactant and synthetic conditions was fundamental and typical for every system and just carefully tuning it was possible to be effective in the templating effect.

## 6.2 Outlook to future work

HKUST-1 is already known as a Lewis acid catalyst, such as for the isomerization of terpene derivatives, the rearrangement of α-pinene oxide to campholenic aldehyde and the cyclization of citronellal to isopulegol[52] among others. The mesoporous rpHKUST-1 described in Chapter 3 is promising for catalytic applications, where both the mesostructure and the reduction of particle size should increase its performance in terms of diffusion of substrates and products and availability of catalytically active sites when compared to the bulk material. In this sense further experiments should be performed in order to compare the catalytic activity of bulk HKUST-1 and rp-HKUST-1 and clarify if the mesoporous structure and particle size affect the catalytic performances of the material.

A drug carrier is defined as any substrate used in the process of drug delivery, which improves the selectivity, effectiveness and/or safety of drug administration. A wide variety of drug carrier system have been developed and studied, such as liposomes, polymeric micelles, nanoparticles and microspheres. In particular microspheres are hollow, micron-size carriers in which the active drug is encapsulate for delivery. Drug release is normally achieved by diffusion through pore in the microsphere structure or by degradation of the microsphere shell. In addition recently MOFs have been recognized as attractive potential drug carriers.[221] For instance hollow ZIF-8 nanoworms were used as drug carrier for the model anticancer drug doxorubicin (DOX) with a pH-trigged release, also exhibiting a high loading capacity.[181] Therefore ZIF-8 colloidosomes showed in Chapter 4 could find an application as drug delivery system, due to the suitable shape and size (9 or 0.75 micron for HC-50D-ZIF-8 and HC-25D-90S-ZIF-8 respectively) and the biocompatibility in the body.

Finally there are still open questions about how the morphological and topological conversion from **sod** to **zni** topology described in Chapter 5 occurred. Beside the role of the surfactant, it would be interesting to investigate also the mechanism through which the replacement of MeIm by Im occurred. Terahertz time-domain spectroscopy (THz-TDS) has been previously used to study

the chemical and structural properties of a variety of system, and between them also MOFs. In particular the swing and gate-opening motions in ZIFs fall within the terahertz frequency region[222] and further THz-TDS was used to probe the terahertz vibrational modes of ZIF-8 (**sod**).[223] Therefore THz-TDS might be employed in order to monitor the conversion from **sod** to **zni** topology. Since THz can detect the swing and gate-opening motions, it would also clarify if the incorporation of the imidazole occurred in the pre-existing **sod** crystal or it occurred by a dissolution/reprecipitation process.

# Appendices

# Appendix A

SPAN (Sorbitan esters) and TWEEN (polyethoxylated sorbitan esters) are a range of mild non-ionic surfactants with high stability, formulating flexibility and wider compatibility. They are stable in mild acids, alkalis and electrolytes and do not react with ionic ingredients or actives, furthermore they are highly effective solubilisers, dispersing agent and wetting aids.[224]

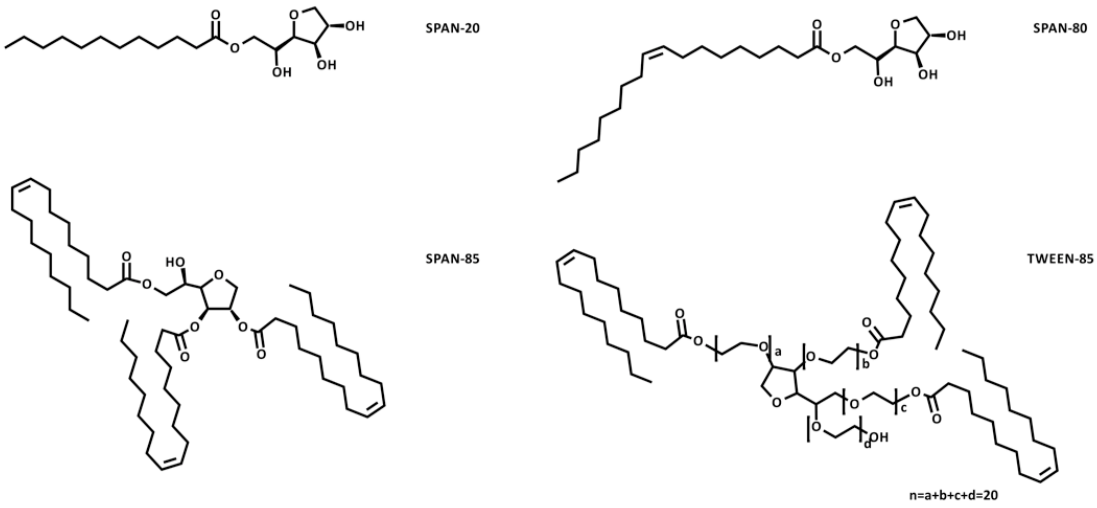


**Figure A1 Illustration of SPAN-20, SPAN-80, SPAN-85 and TWEEN-85.**

| Product name | Chemical identity | HLB value |
|---|---|---|
| SPAN-20 | Sorbitan monolaurate | 8.6 |
| SPAN-80 | Sorbitan monooleate | 4.3 |
| SPAN-85 | Sorbitan trioleate | 1.8 |
| TWEEN-85 | Polyethylene glycol sorbitan trioleate | 11 |

**Table A1 Product name, chemical identity and HLB value of the SPAN and TWEEN surfactant employed.**

# Bibliography

**Uncategorized References**


[1] J. Rouquerol, D. Avnir, C. W. Fairbridge, D. H. Everett, J. H. Haynes, N. Pericone, J. D. F. Ramsay, K. S. W. Sing, K. K. Unger, *Pure Appl. Chem.* **1994**, *66*, 1739-1758.

[2] *IUPAC Manual of Symbols and Terminology, Appendix 2, Pt. 1, Colloid and Surface Chemistry [Pure Appl. Chem. 1972, 31, 578] .*

[3] P. B. Venuto, E. T. Habib, *Jr., Chemical Industries* **1979**, *1*.

[4] C. J. Adams, A. Araya, S. W. Carr, A. P. Chapple, K. R. Franklin, P. Graham, A. R. Minihan, T. J. Osinga, J. A. Stuart, *Stud. Surf. Sci. Catal.* **1997**, *105B*, 1667.

[5] C. G. Coe, *Gas Separation Technology*, **1990**.

[6] L. J. Murray, M. Dinca, J. R. Long, *Chem. Soc. Rev.* **2009**, *38*, 1294-1314.

[7] J. Lee, O. K. Farha, J. Roberts, K. A. Scheidt, S. T. Nguyen, J. T. Hupp, *Chem. Soc. Rev.* **2009**, *38*, 1450-1459.

[8] J. S. Beck, W. J. Roth, M. E. Leonowicz, J. C. Vartuli, C. T. Kresge, K. D. Schmitt, C. T-W. Chu, D. H. Olson, E. W. Sheppard, S. B. McCullen, J. B. Higgins, J. L. Schlenkert, *J. Am. Chem. Soc.* **1992**, *114*, 10834-10843.

[9] C.T. Kresge, W. J. Roth, J.C. Vatuli, M. E. Leonowicz, J. S. Beck, *Nature* **1992**, *359*, 710-712.

[10] M. D. Jones, M. J. Duer, S. Hermans, Y. Z. Khimyak, B. F. G. Johnson, J. M. Thomas, *Angew. Chem. Int. Edit.* **2002**, *41*, 4726-4729.

[11] M. Hartmann, *Chem. Mat.* **2005**, *17*, 4577-4593.

[12] Z. Zhang, T. J. Pinnavaia, *J. Am. Chem. Soc.* **2002**, *124*, 12294- 12301.

[13] Z. Zhang, R. W. Hicks, T. R. Pauly, T. J. Pinnavaia, *J. Am. Chem. Soc.* **2002**, *124*, 1592-1593.

[14] W. Zhang, T. J. Pinnavaia, *Chem. Commun.* **1998**, 1185-1186.

[15] R. W. Hicks, T. J. Pinnavaia, *Chem. Mater.* **2003**, *15*, 78-82.

[16] W.J. Zhang, Y.Q. He, Q. Qi, *Mater. Chem. Phys.* **2005**, *93*, 508–515.

[17] P. Monneyron, M.H. Manero, J.N. Foussard, F. Benoit-Marquié, M. T. Maurette, *Chem. Eng. Sci.* **2003**, *58*, 971–978.

[18] G.K. Mor, O.K. Varghese, M. Paulose, K. Shankar, C. A. Grimes, *Sol. Energy Mater. Sol. Cells* **2006**, *90*, 2011–2075.

[19] B. F. H. Brendan F. Abrahams, and, R. Robson, *J. Am. Chem. Soc.* **1991**, *113*, 3606-3607.

[20] B. F. Hoskins, R. Robson, *J. Am. Chem. Soc.* **1990**, *112*, 1546-1554.

[21] C. Wang, D. Liu, W. Lin, *J. Am. Chem. Soc.* **2013**, *135*, 13222-13234.

[22] G. Ferey, *Chem. Soc. Rev.* **2008**, *37*, 191-214.

[23] T. R. Cook, Y. R. Zheng, P. J. Stang, *Chem. Rev.* **2013**, *113*, 734-777.

[24] H. Li, M. Eddaoudi, M. O'Keeffe, O. M. Yaghi, *Nature* **1999**, *402*, 276-279.

[25] M. Eddaoudi, J. Kim, N. Rosi, D. Vodak, J. Wachter, M. O'Keeffe, O. M. Yaghi, *Science* **2002**, *295*, 469-472.

[26] O. M. Yaghi, M. O'Keeffe, N. W. Ockwig, H. K. Chae, M. Eddaoudi, J. Kim, *Nature* **2003**, *423*, 705-714.

[27] D. J. Tranchemontagne, J. L. Mendoza-Cortes, M. O'Keeffe, O. M. Yaghi, *Chem. Soc. Rev.* **2009**, *38*, 1257-1283.

[28] O. K. Farha, J. T. Hupp, *Acc. Chem. Res.* **2012**, *43*, 1166.

[29] C. Janiak, J. K. Vieth, *New J. Chem.* **2010**, *34*, 2366.

[30] Z. Wang, S. M. Cohen, *Chem. Soc. Rev.* **2009**, *38*, 1315-1329.

[31] S. Kitagawa, R. Kitaura, S. Noro, *Angew. Chem. Int. Ed. Engl.* **2004**, *43*, 2334-2375.

[32] N. Stock, S. Biswas, *Chem. Rev.* **2012**, *112*, 933-969.

[33] S. T. Meek, J. A. Greathouse, M. D. Allendorf, *Adv. Mater.* **2011**, *23*, 249-267.

[34] C. Janiak, *Dalton Trans.* **2003**, 2781–2804.

[35] S. L. James, *Chem. Soc. Rev.* **2003**, *32*, 276.

[36] M. D. Allendorf, C. A. Bauer, R. K. Bhakta, R. J. Houk, *Chem. Soc. Rev.* **2009**, *38*, 1330-1352.

[37] A. U. Czaja, N. Trukhan, U. Muller, *Chem. Soc. Rev.* **2009**, *38*, 1284-1293.

[38] V. Stavila, A. A. Talin, M. D. Allendorf, *Chem. Soc. Rev.* **2014**, *43*, 5994-6010.

[39] J. L. C. Rowsell, O. M. Yaghi, *Microporous Mesoporous Mater.* **2004**, *73*, 3-14.

[40] M. Eddaoudi, D. B. Moler, H. Li, B. Chen, T. M. Reineke, M. O'Keeffe, O. M. Yaghi, *American Chemical Society* **2001**, *34*, 319-330.

[41] S. S.-Y. Chui, S. M.-F. Lo, J. P. H. Charmant, A. G. Orpen, I. D. Williams, *Science* **1999**, *283*, 1148-1150.

[42] https://commons.wikimedia.org/wiki/File:HKUST-1_activated.png.

[43] Y.-K. Seo, G. Hundal, I. T. Jang, Y. K. Hwang, C.-H. Jun, J.-S. Chang, *Microporous Mesoporous Mater.* **2009**, *119*, 331-337.

[44] M. Schlesinger, S. Schulze, M. Hietschold, M. Mehring, *Microporous Mesoporous Mater.* **2010**, *132*, 121-127.

[45] N. Campagnol, T. Van Assche, T. Boudewijns, J. Denayer, K. Binnemans, D. De Vos, J. Fransaer, *Journal of Materials Chemistry A* **2013**, *1*, 5827.

[46] J. L. Rowsell, O. M. Yaghi, *Angew. Chem. Int. Ed. Engl.* **2005**, *44*, 4670-4679.

[47] A. R. Millward, O. M. Yaghi, *J. Am. Chem. Soc.* **2005**, *127*, 17998-17999.

[48] C. Petit, B. Mendoza, D. O'Donnell, T. J. Bandosz, *Langmuir* **2011**, *27*, 10234-10242.

[49] C. Petit, B. Levasseur, B. Mendoza, T. J. Bandosz, *Microporous Mesoporous Mater.* **2012**, *154*.

[50] P. Chowdhury, C. Bikkina, D. Meister, F. Dreisbach, S. Gumma, *Microporous Mesoporous Mater.* **2009**, *117*, 406-413.

[51] A. Sachse, R. Ameloot, B. Coq, F. Fajula, B. Coasne, D. De Vos, A. Galarneau, *Chem. Commun.* **2012**, *48*.

[52] L. Alaerts, E. Seguin, H. Poelman, F. Thibault-Starzyk, P. A. Jacobs, D. E. De Vos, *Chem. Eur. J.* **2006**, *12*, 7353-7363.

[53] L. Alaerts, F. Thibault-Starzyk, E. Seguin, J. F. M. Denayer, P. A. Jacobs, D. E. D. Vos, *Stud. Surf. Sci. Catal.* **2007**, *170*.

[54] F. R. Kogler, M. Jupa, M. Puchberger, U. Schubert, *J. Mater. Chem.* **2004**, *14*, 3133–3138.

[55] J. H. Cavka, S. Jakobsen, U. Olsbye, N. Guillou, C. Lamberti, S. Bordiga, K. P. Lillerud, *J. Am. Chem. Soc.* **2008**, *130*, 13850-13851.

[56] M. Kim, S. M. Cohen, *CrystEngComm* **2012**, *14*, 4096-4104.

[57] N. Chang, X.-P. Yan, *J. Chromatogr. A* **2012**, *1257*, 116-124.

[58] G. E. Cmarik, M. Kim, S. M. Cohen, K. S. Walton, *Langmuir* **2012**, *28*, 15606-15613.

[59] S. Chavan, J. G. Vitillo, M. J. Uddin, F. Bonino, C. Lamberti, E. Groppo, K.-P. Lillerud, S. Bordiga, *Chem. Mater.* **2010**, *22*, 4602-4611.

[60] C. Gomes Silva, I. Luz, F. X. Llabrés i Xamena, A. Corma, H. García, *Chem. Eur. J.* **2010**, *16*, 11133–11138.

[61] F. Vermoortele, R. Ameloot, A. Vimont, C. Serre, D. De Vos, *Chem. Commun.* **2011**, *47*, 1521-1523.

[62] C. Serre, F. Millange, C. Thouvenot, M. Nogues, G. Marsolier, D. Louer, G. Ferey, *J. Am. Chem. Soc.* **2002**, *124*, 13519.

[63] G. Ferey, C. Mellot-Draznieks, C. Serre, F. Millange, J. Dutour, S. Surble, I. Margiolaki, *Science* **2005**, *309*, 2040-2042.

[64] A. Boutin, F.-X. Coudert, M.-A. Springuel-Huet, A. V. Neimark, G. Férey, A. H. Fuchs, *The Journal of Physical Chemistry C* **2010**, *114*, 22237-22244.

[65] K. Hunger, N. Schmeling, H. B. T. Jeazet, C. Janiak, C. Staudt, K. Kleinermanns, *Membranes* **2012**, *2*, 727-763.

[66] P. Horcajada, T. Chalati, C. Serre, B. Gillet, C. Sebrie, T. Baati, J. F. Eubank, D. Heurtaux, P. Clayette, C. Kreuz, J.S. Chang, Y. K. Hwang, V. Marsaud, P.N. Bories, L. Cynober, S. Gil, G. Ferey, P. Couvreur, R. Gref, *Nat. Mater.* **2010**, *9*, 172–178.

[67] A. Henschel, K. Gedrich, R. Kraehnertb, S. Kaskel, *Chem. Commun.* **2008**, 4192–4194.

[68] V. Finsy, L. Ma, L. Alaerts, D. E. De Vos, G. V. Baron, J. F. M. Denayer, *Microporous Mesoporous Mater.* **2009**, *120*, 221-227.

[69] J. J. Du, Y. P. Yuan, J. X. Sun, F. M. Peng, X. Jiang, L. G. Qiu, J. F. Zhu, *J. Hazard. Mater.* **2011**, *190*, 945-951.

[70] K. S. Park, Z. Ni, A. P. Cote, J. Y. Choi, R. Huang, F. J. Uribe-Romo, H. K. Chae, M. O'Keeffe, O. M. Yaghi, *Proc Natl Acad Sci U S A* **2006**, *103*, 10186-10191.

[71] R. Banerjee, A. Phan, B. Wang, C. Knobler, H. Furukawa, M. O'Keeffe, O. M. Yaghi, *Science* **2008**, *319*, 939.

[72] O. M. Yaghi, H. Furukawa, B. Wang, **2013**.

[73] J. P. Zhang, Y. B. Zhang, J. B. Lin, X. M. Chen, *Chem. Rev.* **2012**, *112*, 1001-1033.

[74] Y. Q. Tian, C. X. Cai, X. M. Ren, C. Y. Duan, Y. Xu, S. Gao, X. Z. You, *Chem. Eur. J.* **2003**, *9*, 5673-5685.

[75] Y. Q. Tian, Y. M. Zhao, Z. X. Chen, G. N. Zhang, L. H. Weng, D. Y. Zhao, *Chemistry* **2007**, *13*, 4146-4154.

[76] A. Phan, C. J. Doonan, F. J. Uribe-Romo, C. B. Knobler, M. O'Keeffe, O. M. Yaghi, *Acc. Chem. Res.* **2010**, *43*.

[77] R. Banerjee, H. Furukawa, D. Britt, C. Knobler, M. O'Keeffe, O. M. Yaghi, *J. Am. Chem. Soc.* **2009**, *131*, 3875–3877.

[78] B. Wang, A. P. Cote, H. Furukawa, M. O'Keeffe, O. M. Yaghi, *Nature* **2008**, *453*, 207-211.

[79] H. Hayashi, A. P. Cote, H. Furukawa, M. O'Keeffe, O. M. Yaghi, *Nat Mater* **2007**, *6*, 501-506.

[80] X. C. Huang, Y. Y. Lin, J. P. Zhang, X. M. Chen, *Angew. Chem. Int. Ed.* **2006**, *45*, 1557-1559.

[81] D. W. Breck, *Zeolite Molecular Sieves, Wiley, New York,* **1974**.

[82] *IZA Structure Commission.* http://izasc.ethz.ch/fmi/xsl/IZA-SC/ft.xsl.

[83] Hui Wu, Wei Zhou, T. Yildirim, *J. Am. Chem. Soc.* **2007**, *129*, 5314-5315.

[84] R. Ostermann, J. Cravillon, C. Weidmann, M. Wiebcke, B. M. Smarsly, *Chem Commun (Camb)* **2011**, *47*, 442-444.

[85] A. Demessence, C. Boissière, D. Grosso, P. Horcajada, C. Serre, G. Férey, G. J. A. A. Soler-Illia, C. Sanchez, *J. Mater. Chem.* **2010**, *20*, 7676.

[86] H. Bux, F. Liang, Y. Li, J. Cravillon, M. Wiebcke, J. Caro, *J. Am. Chem. Soc.* **2009**, *131*, 16000–16001.

[87] H. Bux, A. Feldhoff, J. Cravillon, M. Wiebcke, Y.-S. Li, J. Caro, *Chem. Mater.* **2011**, *23*, 2262-2269.

[88] N. Chang, Z.-Y. Gu, X.-P. Yan, *J. Am. Chem. Soc.* **2010**, *132*, 13645–13647.

[89] A. Corma, H. Garcia, F. X. Llabres i Xamena, *Chem. Rev.* **2010**, *110*, 4606-4655.

[90] A. Ahmed, N. Hodgson, M. Barrow, R. Clowes, C. Robertson, A. Steiner, P. McKeown, D. Bradshaw, P. Myers, H. Zhang, *J. Mater. Chem. A* **2014**, *2*, 9085-9090.

[91] O. Shekhah, H. Wang, M. Paradinas, C. Ocal, B. Schüpbach, A. Terfort, D. Zacher, R. A. Fischer, C. Wöll, *Nature Materials* **2009**, *8*, 481-484.

[92] D. Bradshaw, S. El-Hankari, L. Lupica-Spagnolo, *Chem. Soc. Rev.* **2014**, *43*, 5431-5443.

[93] B. Seoane, S. Castellanos, A. Dikhtiarenko, F. Kapteijn, J. Gascon, *Coord. Chem. Rev.* **2016**, *307*, 147-187.

[94] Y. Sakata, S. Furukawa, M. Kondo, K. Hirai, N. Horike, Y. Takashima, H. Uehara, N. Louvain, M. Meilikhov, T. Tsuruoka, S. Isoda, W. Kosaka, O. Sakata, S. Kitagawa, *Science* **2013**, *339*, 193-196.

[95] A. D. Dinsmore, M. F. Hsu, M. G. Nikolaides, M. Marquez, A. R. Bausch, D. A. Weitz, *Science* **2002**, *298*, 1006-1009.

[96] M. D. Allendorf, A. Schwartzberg, V. Stavila, A. A. Talin, *Chem. Eur. J.* **2011**, *17*, 11372–11388.

[97] L. E. Kreno, K. Leong, O. K. Farha, M. Allendorf, R. P. Van Duyne, J. T. Hupp, *Chem. Rev.* **2012**, *112*, 1105–1125.

[98] A. Carne-Sanchez, I. Imaz, K. C. Stylianou, D. Maspoch, *Chemistry* **2014**, *20*, 5192-5201.

[99] S. Furukawa, J. Reboul, S. Diring, K. Sumida, S. Kitagawa, *Chem. Soc. Rev.* **2014**, *43*, 5700-5734.

[100] Z. Zhanga, M. J. Zaworotko, *Chem. Soc. Rev.* **2014**, *43*, 5444-5455.

[101] S. Mann, *Nature* **1993**, *365*, 499-505.

[102] A. Thomas, F. Goettmann, M. Antonietti, *Chem. Mater.* **2008**, *20*, 738–755.

[103] E. A. Flugel, A. Ranft, F. Haaseab, B. V. Lotsch, *J. Mater. Chem.* **2012**, *22*, 10119–10133.

[104] T. Tsuruoka, S. Furukawa, Y. Takashima, K. Yoshida, S. Isoda, S. Kitagawa, *Angew. Chem. Int. Ed. Engl.* **2009**, *48*, 4739-4743.

[105] S. Diring, S. Furukawa, Y. Takashima, T. Tsuruoka, S. Kitagawa, *Chem. Mater.* **2010**, *22*, 4531-4538.

[106] Y. Pan, D. Heryadi, F. Zhou, L. Zhao, G. Lestari, H. Su, Z. Lai, *Cryst. Eng. Comm.* **2011**, *13*, 6937.

[107] K. M. Choi, H. J. Jeon, J. K. Kang, O. M. Yaghi, *J. Am. Chem. Soc.* **2011**, *133*, 11920-11923.

[108] L. H. Wee, C. Wiktor, S. Turner, W. Vanderlinden, N. Janssens, S. R. Bajpe, K. Houthoofd, G. Van Tendeloo, S. De Feyter, C. E. Kirschhock, J. A. Martens, *J. Am. Chem. Soc.* **2012**, *134*, 10911-10919.

[109] G. Lu, J. T. Hupp, *J. Am. Chem. Soc.* **2010**, *132*, 7832–7833.

[110] W. J. Rieter, K. M. L. Taylor, H. An, W. Lin, W. Lin, *J. Am. Chem. Soc.* **2006**, 9024-9025.

[111] A. Schejn, L. Balan, V. Falk, L. Aranda, G. Medjahdi, R. Schneider, *CrystEngComm* **2014**, *16*, 4493.

[112] E. L. Bustamante, J. L. Fernandez, J. M. Zamaro, *J. Colloid Interface Sci.* **2014**, *424*, 37-43.

[113] H. Guo, Y. Zhu, S. Wang, S. Su, L. Zhou, H. Zhang, *Chem. Mater.* **2012**, *24*, 444-450.

[114] A. Garai, W. Shepherd, J. Huo, D. Bradshaw, *Journal of Materials Chemistry B* **2013**, *1*, 3678.

[115] W. Sun, X. Zhai, L. Zhao, *Chem. Eng. J.* **2016**, *289*, 59-64.

[116] K. M. L. Taylor, A. Jin, W. Lin, *Angew. Chem. Int. Ed.* **2008**, *47*, 7722 –7725.

[117] F. Hoffmann, M. Cornelius, J. Morell, M. Froba, *Angew. Chem. Int. Ed. Engl.* **2006**, *45*, 3216-3251.

[118] X. Roy, M. J. MacLachlan, *Chemistry* **2009**, *15*, 6552-6559.

[119] M.-H. Pham, G.-T. Vuong, F.-G. Fontaine, T.-O. Do, *Crystal Growth & Design* **2012**, *12*, 1008-1013.

[120] Y. Zhao, J. Zhang, B. Han, J. Song, J. Li, Q. Wang, *Angew. Chem. Int. Ed. Engl.* **2011**, *50*, 636-639.

[121] H. Colfen, M. Antonietti, *Angew. Chem. Int. Ed. Engl.* **2005**, *44*, 5576-5591.

[122] N. Yanai, M. Sindoro, J. Yan, S. Granick, *J. Am. Chem. Soc.* **2013**, *135*, 34-37.

[123] M. Sindoro, N. Yanai, A.-Y Jee, S. Granick, *Acc. Chem. Res.* **2014**, *47*, 459-469.

[124] O. Sato, T. Lyoda, A. Fujishima, K. Hashimoto, *Science* **1996**, *271*.

[125] E. Manuel, M. Evangelisti, *Phys. Rev. B* **2006**, *73*.

[126] S. Wu, X. Shen, Z. Xu, J. Wu, C. Gao, *Appl. Surf. Sci.* **2009**, *255*, 9182–9185.

[127] M. Pang, A. J. Cairns, Y. Liu, Y. Belmabkhout, H. C. Zeng, M. Eddaoudi, *J. Am. Chem. Soc.* **2012**, *134*, 13176–13179.

[128] Y. Yue, Z.-A. Qiao, P. F. Fulvio, A. J. Binder, C. Tian, J. Chen, K. M. Nelson, X. Zhu, S. Dai, *J. Am. Chem. Soc.* **2013**, *135*, 9572−9575.

[129] H. Wang, W. Zhu, J. Li, T. Tian, Y. Lan, N. Gao, C. Wang, M. Zhang, C. F. J. Faulb, G. Li, *Chem. Sci.* **2015**, *6*, 1910–1916.

[130] J. Reboul, S. Furukawa, N. Horike, M. Tsotsalas, K. Hirai, H. Uehara, M. Kondo, N. Louvain, O. Sakata, S. Kitagawa, *Nat. Mater.* **2012**, *11*, 717-723.

[131] A. Guinier, *X-Ray diffraction In Crystal, Imperfect Crystals, and Amorphous Bodies*, W. H. Freeman and Company, San Francisco **1963**.

[132] G. Will, *Powder Diffraction*, Springer-Verlag, Heidelberg, **2006**.

[133] M. F. Toney, *Encyclopedia of materials characterization - Surfaces, Interfaces, Thin Films; XRD - X-Ray Diffraction*, Manning Publications, Greenwich, **1992**.

[134] J. B. Bindell, *Encyclopedia of materials characterization - Surfaces, Interfaces, Thin Films; SEM - Scanning Electron Microscopy*, Manning Publications, Greenwich, **1992**.

[135] K. E. Sickafus, *Encyclopedia of materials characterization - Surfaces, Interfaces, Thin Films; TEM - Transmission Electron Microscopy*, Manning Publications, Greenwich, **1992**.

[136] W. Zhou, R. P. Apkarian, Z. L. Wang, D. Joy, *Scanning Microscopy for Nanotechnology: Techniques and Applications (Eds.: W. Zhou, Z. L. Wang)* Springer, New York, **2006**.

[137] K. S. W. Sing, D. H. Everett, R. A. W. Haul, L. Moscou, R. A. Pierotti, Rouquerol, S. J., *Pure Appl. Chem.* **1985**, *57*, 603-619.

[138] S. Brunauer, P. H. Emmett, E. Teller, *J. Am. Chem. Soc.* **1940**, *62*, 1723.

[139] B. D. Zdravkov, J. J. Čermák, M. Šefara, J. Janků, *Central European Journal of Chemistry* **2007**, *5*, 385-395.

[140] A. W. Adamson, A. P. Gast, *Physical Chemistry of Surfaces*, John Wiley & Sons, New York, **1997**.

[141] F. R. Hung, B. Coasne, K. E. Gubbins, F. R. Siperstein, M. Thommes, M. Sliwinska-Bartkowiak, in *Stud. Surf. Sci. Catal., Vol. Volume 160* (Eds.: F. R.-R. J. R. P.L. Llewellyn, N. Seaton), Elsevier, **2007**, pp. 153-160.

[142] F. Rouquerol, J. Rouquerol, K. S. W. Sing, G. Maurin, P. Llewellyn, in *Adsorption by Powders and Porous Solids (Second Edition)*, Academic Press, Oxford, **2014**, pp. 1-24.

[143] E. P. J. Barrett, L. G.; Halenda, P. P., *J. Am. Chem. Soc.* **1951**, *73*, 373-380.

[144] Z. Xue, J. Zhang, L. Peng, B. Han, T. Mu, J. Li, G. Yang, *Chemphyschem* **2014**, *15*, 85-89.

[145] L. G. Qiu, T. Xu, Z. Q. Li, W. Wang, Y. Wu, X. Jiang, X. Y. Tian, L. D. Zhang, *Angew. Chem. Int. Ed. Engl.* **2008**, *47*, 9487-9491.

[146] Y. Li, D. Zhang, Y. N. Guo, B. Guan, D. Tang, Y. Liu, Q. Huo, *Chem Commun (Camb)* **2011**, *47*, 7809-7811.

[147] L. B. Sun, J. R. Li, J. Park, H. C. Zhou, *J. Am. Chem. Soc.* **2012**, *134*, 126-129.

[148] E. Biemmi, S. Christian, N. Stock, T. Bein, *Microporous Mesoporous Mater.* **2009**, *117*, 111-117.

[149] J. Gascon, S. Aguado, F. Kapteijn, *Microporous Mesoporous Mater.* **2008**, *113*, 132-138.

[150] R. Ameloot, E. Gobechiya, H. Uji-i, J. A. Martens, J. Hofkens, L. Alaerts, B. F. Sels, D. E. De Vos, *Adv. Mater.* **2010**, *22*, 2685-2688.

[151] A. M. Walker, B. Slater, *CrystEngComm* **2008**, *10*, 790-791.

[152] S. El-Hankari, J. Huo, A. Ahmed, H. Zhang, D. Bradshaw, *Journal of Materials Chemistry A* **2014**, *2*, 13479-13485.

[153] P.F. Fulvio, S. Pikus, M. Jaroniec, *J. Colloid Interf. Sci.* **2005**, *287*, 717.

[154] D. Zhao, J. Feng, Q. Huo, N. Melosh, G. H. C. Fredrickson, Bradley F., G. D. Stucky, *Science* **1998**, *279*, 548-552.

[155] X.-X. Huang, L.-G. Qiu, W. Zhang, Y.-P. Yuan, X. Jiang, A.-J. Xie, Y.-H. Shen, J.-F. Zhu, *CrystEngComm* **2012**, *14*, 1613.

[156] J. Yao, M. He, K. Wang, R. Chen, Z. Zhong, H. Wang, *CrystEngComm* **2013**, *15*, 3601.

[157] X.-D. Do, V.-T. Hoang, S. Kaliaguine, *Microporous Mesoporous Mater.* **2011**, *141*, 135-139.

[158] M. Ma, D. Zacher, X. Zhang, R. A. Fischer, N. Metzler-Nolte, *Crystal Growth & Design* **2011**, *11*, 185-189.

[159] G. Férey, *Chem. Mater.* **2001**, *13*, 3084-3098.

[160] N. J. Manin, D. V. Baranov, V. P. Korolev, *Russ. J. Inorg. Chem.* **2003**, *48*, 288 – 293.

[161] O. Shekhah, H. Wang, D. Zacher, R. A. Fischer, C. Woll, *Angew. Chem. Int. Ed. Engl.* **2009**, *48*, 5038-5041.

[162] Stephan Hermes, Thomas Witte, Todor Hikov, Denise Zacher, Stefan Bahnmuller, Gerhard Langstein, Klaus Huber, R. A. Fischer, *J. Am. Chem. Soc.* **2007**, *129*, 5324-5325.

[163] a. L. S. Yiyin Mao, a Hubiao Huang,a Qing Yu,a Zhizhen Yeab and Xinsheng Peng, *CrystEngComm* **2013**, *15*, 265-270.

[164] H. Uehara, S. Diring, S. Furukawa, Z. Kalay, M. Tsotsalas, M. Nakahama, K. Hirai, M. Kondo, O. Sakata, S. Kitagawa, *J. Am. Chem. Soc.* **2011**, *133*, 11932-11935.

[165] Chunling Xin, Haijuan Zhan, Xin Huang, Hongguang Li, Ning Zhao, Fukui Xiao, W. Wei, Y. Sun, *RSC Adv.* **2015**, *5*, 27901–27911.

[166] Q. H. Dongyuan Zhao, Jianglin Feng, Bradley F. Chmelka, and Galen D. Stucky, *J. Am. Chem. Soc.* **1998**, *120*, 6024-6036.

[167] O. D. Velev, K. Furusawa, K. Nagayama, *Langmuir* **1996**, *12*, 2374.

[168] J. Huo, J. Aguilera-Sigalat, S. El-Hankari, D. Bradshaw, *Chemical Science* **2015**, *6*, 1938-1943.

[169] Y. Yang, F. Wang, Q. Yang, Y. Hu, H. Yan, Y. Z. Chen, H. Liu, G. Zhang, J. Lu, H. L. Jiang, H. Xu, *ACS Appl Mater Interfaces* **2014**, *6*, 18163-18171.

[170] H. J. Lee, W. Cho, M. Oh, *Chem. Commun.* **2012**, *48*, 221-223.

[171] C. H. Kuo, Y. Tang, L. Y. Chou, B. T. Sneed, C. N. Brodsky, Z. Zhao, C. K. Tsung, *J. Am. Chem. Soc.* **2012**, *134*, 14345-14348.

[172] X. Cao, L. Dai, L. Wang, J. Liu, J. Lei, *Mater. Lett.* **2015**, *161*, 682-685.

[173] Y. Chevalier, M. Bolzinger, *Colloids and Surfaces A: Physicochemical and Engineering Aspects* **2013**, *439*, 23-34.

[174] K. L. Thompson, M. Williams, S. P. Armes, *J. Colloid Interface Sci.* **2015**, *447*, 217-228.

[175] J. Huo, M. Marcello, A. Garai, D. Bradshaw, *Advanced Matererials* **2013**, *25*, 2717-2722.

[176] M. Pang, A. J. Cairns, Y. Liu, Y. Belmabkhout, H. C. Zeng, M. Eddaoudi, *J. Am. Chem. Soc.* **2013**, *135*, 10234-10237.

[177] C. Boissiere, D. Grosso, A. Chaumonnot, L. Nicole, C. Sanchez, *Adv. Mater.* **2011**, *23*, 599-623.

[178] A. Carne-Sanchez, I. Imaz, M. Cano-Sarabia, D. Maspoch, *Nat Chem* **2013**, *5*, 203-211.

[179] R. Ameloot, F. Vermoortele, W. Vanhove, M. B. Roeffaers, B. F. Sels, D. E. De Vos, *Nat Chem* **2011**, *3*, 382-387.

[180] N. Yanai, S. Granick, *Angew. Chem. Int. Ed. Engl.* **2012**, *51*, 5638-5641.

[181] H. Yu, X. Qiu, P. Neelakanda, L. Deng, N. M. Khashab, S. P. Nunes, K. V. Peinemann, *Sci Rep* **2015**, *5*, 15275.

[182] Y. Pan, Y. Liu, G. Zeng, L. Zhao, Z. Lai, *Chem. Commun.* **2011**, *47*, 2071-2073.

[183] X. Fan, W. Wang, W. Li, J. Zhou, B. Wang, J. Zheng, X. Li, *ACS Appl Mater Interfaces* **2014**, *6*, 14994-14999.

[184] R. G. Laughlin, *The Aqueous Phase Behaviour of Surfactants*, **1996**

[185] Milton J. Rosen, J. T. Kunjappu, *Surfactants and interfacial Phenomena Fourth Edition*, Wiley, **2012**.

[186] P. M. Holland, D. N. Rubingh, *American Chemical Society* **1992**, *501*, 2-30.

[187] J. Cravillon, R. Nayuk, S. Springer, A. Feldhoff, K. Huber, M. Wiebcke, *Chem. Mater.* **2011**, *23*, 2130-2141.

[188] J. Cravillon, S. Munzer, S. J. Lohmeier, A. Feldhoff, K. Huber, M. Wiebcke, *Chem. Mater.* **2009**, *21*, 1410–1412.

[189] R. J. Farn, *Chemistry and technology of surfactants.*, Blackwell publishing ltd, Oxford, **2006**.

[190] Mason TG, Wilking JN, Meleson K, Chang CB, G. SM, *J. Phys.: Condens. Matter* **2006**, *18*, 41.

[191] M. Jian, B. Liu, R. Liu, J. Qu, H. Wang, X. Zhang, *RSC Adv.* **2015**, *5*, 48433-48441.

[192] C. Rosler, A. Aijaz, S. Turner, M. Filippousi, A. Shahabi, W. Xia, G. Van Tendeloo, M. Muhler, R. A. Fischer, *Chem. Eur. J.* **2016**, *22*, 1 – 9.

[193] Y. Hu, H. Kazemian, S. Rohani, Y. Huang, Y. Song, *Chem. Commun.* **2011**, *47*, 12694-12696.

[194] H. Colfen, S. Mann, *Angew. Chem. Int. Ed. Engl.* **2003**, *42*, 2350-2365.

[195] T. Xing, Y. Lou, Q. Bao, J. Chen, *CrystEngComm* **2014**, *16*, 8994-9000.

[196] J. Shi, S. Zhang, X. Wang, C. Yang, Z. Jiang, *Journal of Materials Chemistry B* **2014**, *2*, 4289.

[197] F. Nudelman, N. A. Sommerdijk, *Angew. Chem. Int. Ed. Engl.* **2012**, *51*, 6582-6596.

[198] M. Hu, S. Furukawa, R. Ohtani, H. Sukegawa, Y. Nemoto, J. Reboul, S. Kitagawa, Y. Yamauchi, *Angew. Chem. Int. Ed. Engl.* **2012**, *51*, 984-988.

[199] C. Avci, J. Arinez-Soriano, A. Carne-S anchez, V. Guillerm, C. Carbonell, I. Imaz, D. Maspoch, *Angew. Chem. Int. Ed.* **2015**, *54*, 14417 –14421.

[200] J. C. Tan, T. D. Bennett, A. K. Cheetham, *Proc Natl Acad Sci U S A* **2010**, *107*, 9938-9943.

[201] e. a. Li KH, *J. Am. Chem. Soc.* **2009**, *131,*, 10368–10369.

[202] M. O'Keeffe, M. A. Peskov, S. J. Ramsden, O. M. Yaghi, *Acc. Chem. Res.* **2008**, *41*, 1782-1789.

[203] C. Mellot-Draznieks, B. Kerkeni, *Molecular Simulation* **2013**, *40*, 25-32.

[204] Q. Shi, F. Wang, X. Kang, J. Xu, Y. Huang, J. Li, J. Dong, *CrystEngComm* **2015**, *17*, 3998-4005.

[205] B. P. Biswal, T. Panda, R. Banerjee, *Chem Commun (Camb)* **2012**, *48*, 11868-11870.

[206] M. E. Schweinefuss, S. Springer, I. A. Baburin, T. Hikov, K. Huber, S. Leoni, M. Wiebcke, *Dalton transactions* **2014**, *43*, 3528-3536.

[207] K. Koh, A. G. Wong-Foy, A. J. Matzger, *Angew. Chem. Int. Ed. Engl.* **2008**, *47*, 677-680.

[208] H. J. Lee, J. We, J. O. Kim, D. Kim, W. Cha, E. Lee, J. Sohn, M. Oh, *Angew. Chem. Int. Ed. Engl.* **2015**, *54*, 10564-10568.

[209] Tao Wu, Xianhui Bu, Jian Zhang, P. Feng, *Chem. Mater.* **2008**, *20*, 7377–7382.

[210] O. Karagiaridi, M. B. Lalonde, W. Bury, A. A. Sarjeant, O. K. Farha, J. T. Hupp, *J. Am. Chem. Soc.* **2012**, *134*, 18790-18796.

[211] D. W. Lewis, A. R. Ruiz-Salvador, A. Gómez, L. M. Rodriguez-Albelo, F.-X. Coudert, B. Slater, A. K. Cheetham, C. Mellot-Draznieks, *CrystEngComm* **2009**, *11*, 2272.

[212] J. T. Hughes, T. D. Bennett, A. K. Cheetham, A. Navrotsky, *J. Am. Chem. Soc.* **2013**, *135*, 598-601.

[213] Z. Lian, L. Huimin, Y. Lisha, *Mater. Lett.* **2014**, *125*, 59-62.

[214] Z. R. Lehnert and F. Z. Seel, *Anorg. Allg. Chem.* **1980**, *464*, 187-194.

[215] T. D. Bennett, D. A. Keen, J. C. Tan, E. R. Barney, A. L. Goodwin, A. K. Cheetham, *Angew. Chem. Int. Ed. Engl.* **2011**, *50*, 3067-3071.

[216] T. D. Bennett, A. L. Goodwin, M. T. Dove, D. A. Keen, M. G. Tucker, E. R. Barney, A. K. Soper, E. G. Bithell, J. C. Tan, A. K. Cheetham, *Phys. Rev. Lett.* **2010**, *104*, 115503.

[217] Y. Wang, Y. Xu, D. Li, H. Liu, X. Li, S. Tao, Z. Tian, *Chinese Journal of Catalysis* **2015**, *36*, 855-865.

[218] Y. Wang, X. Lang, S. Fan, *Journal of Natural Gas Chemistry* **2012**, *21*, 299-301.

[219] I. A. Baburin, S. Leoni, *J. Mater. Chem.* **2012**, *22*, 10152.

[220] IUPAC, *Compendium of Chemical Terminology, The Gold Book*, 2nd ed., **1997**.

[221] C.-Y. Sun, Qin, C., Wang, X.-L. & Su, Z.-M. , *Expert Opin. Drug Deliv.* **2013**, *10*, 89–101.

[222] M. R. Ryder, B. Civalleri, T. D. Bennett, S. Henke, S. Rudic, G. Cinque, F. Fernandez-Alonso, J. C. Tan, *Phys. Rev. Lett.* **2014**, *113*, 215502.

[223] N. Y. Tan, M. T. Ruggiero, C. Orellana-Tavra, T. Tian, A. D. Bond, T. M. Korter, D. Fairen-Jimenez, J. A. Zeitler, *Chem Commun (Camb)* **2015**, *51*, 16037-16040.

[224] http://www.corda.com/europe.